DOCTOR OF PHILOSOPHY

Operational Ocean Modelling: a Critical Evaluation of Published Works

Siddorn, John

Award date:
2016

Awarding institution:
Bangor University

[Link to publication](#)

Operational Ocean Modelling: a Critical Evaluation of Published Works

John Siddorn

Head of Ocean Forecasting R&D, Met Office

School of Ocean Sciences
Bangor University

This dissertation is submitted for the degree of Doctor of Philosophy

January 2016

Summary

This thesis presents a subset of the author's published works, and describes the impact his work has had on ocean forecasting systems. This impact can be broadly divided into two themes, the underpinning development of ocean forecasting models and the implementation, tuning and evaluation of those models to ensure they provide skilful products, with value to users. The systems described in this dissertation are recognised as amongst the best available, and are being used by commercial operators, military decisions makers and governmental organisations, as well as research users. They also form the basis on which future systems will be developed, meeting the challenges and addressing the priorities discussed in the thesis. The author expects to have a substantive impact on driving the research agenda in these areas over the coming years.

Contents

Acknowledgements

First and foremost, I would like to express my thanks to the School of Ocean Sciences, University of Wales, Bangor. It is no exaggeration to say that studying in Menai Bridge many years ago as a postgraduate changed me, mainly for the better. The warmth with which I and my compatriots were welcomed into the world of Oceanography is unique to Menai. I will always be grateful, in particular, for the kindness shown me by Prof Dave Bowers, who always had the time and patience to support me through my thesis. It always struck me how he was able to break problems down in a way that showed such clear thinking. I hope even a little of that has rubbed off on me.

Prof Icarus Allen of Plymouth Marine Laboratory also deserves particular recognition for giving me my first research job despite me not having a PhD, and supporting me in my research and paper writing. I should also thank my numerous colleagues and friends at the Met Office, with whom I have worked for the bulk of my career and where most of my publications have been written. Recognition should also go to my wife Lin, to whom I owe so much, and without whom I wouldn't be able to do all this.

Which takes me full circle back to Menai Bridge and to Dave Bowers (again), who supported me when I originally approached him about doing a PhD by published works. His advice on preparing this dissertation has been invaluable, as has that of Prof Tom Rippeth, whose critique of the first draft served to improve it significantly.

1. Introduction

Operational ocean forecasting and monitoring services provide information to marine users in support of the safety of life at sea convention (SOLAS, 1974), marine security, commercial operations, marine operations' licensing, marine environmental monitoring and numerical weather prediction. These services are based on the use of models to complement and incorporate marine observations, which cannot be used alone. Given that predicting or monitoring the marine environment is inherently difficult, for a range of reasons discussed later in this work, there is a need for active and high quality research activities to underpin these services.

Early operational forecasts were implemented to respond to catastrophic surge events, such as the 1953 storm that resulted in a surge event killing several hundred people in the UK (Baxter, 2005). Surge forecasting services were subsequently implemented at the Met Office, and are a factor in ensuring that subsequent storms of comparable magnitude have not had the same catastrophic impact (Lewis, 2015). Wave models have been run operationally, also for a number of decades, and are used to forecast the sea state for mariners and commercial operators. They are also used in combination with surge modelling to forecast coastal flooding, providing a well established basis for predicting and monitoring extreme weather events (see e.g. Slingo et al., 2014).

More recently ocean forecast and monitoring services have expanded from solving essentially two-dimensional wave equations to include the fully three-dimensional state (hydrodynamics) of the ocean. This was primarily driven initially by the Royal Navy, with their requirement to understand the depth resolved currents (for diver operations, mine hunting and vessel operations) and the depth varying density (for submarine operations and detection). A number of other users have since become reliant on ocean analysis and forecast services, including seasonal forecasting (which relies on daily high quality ocean state analyses for initialisation of their forecasts), oil and gas and renewable industries, and search and rescue operations.

Complementing the physical forecasting of waves, surges and hydrodynamics, the capability to monitor and forecast the marine lower trophic levels and biogeochemistry is increasingly being required. The capability to model marine biogeochemistry in an operational context was originally developed to provide subsurface visibility for military purposes, but is increasingly being driven by the legislative and licensing requirements to maintain healthy marine environments, including most importantly the requirements in Europe to monitor in support of the Marine Strategy Framework

Directive (MSFD). The poor skill in biogeochemistry models is a concern for providers of marine environmental information and is a major priority area for research.

The Ocean Forecasting R&D (OFR&D) department, which is led by the author, has a team of approximately 35 scientists responsible for developing and supporting the above capabilities, and has an international scientific profile. There are several research elements that are required to develop a world-leading forecasting capability;

- models processes and parameterisations;
- observational datasets collection, quality assurance and error characterisation
- data assimilation methodologies
- forecast skill verification and communication

All of the above are significant areas of research which are undertaken in OFR&D, in collaboration with national and international partners. Significant advances are being continuously being made in all these areas, and as the growth in computing power allows increasingly complex, high-resolution modelling systems to be developed significant advances (and challenges) can be expected for the foreseeable future.

The author's primary area of expertise is in developing and improving upon shelf seas models used for operational ocean forecasting (i.e. the first of the above research elements). His early career was as an ocean modeller at Plymouth Marine Laboratory, developing coastal-scale hydrodynamic models coupled to a biogeochemistry model. He then continued developing expertise in marine modelling with his work on shelf seas hydrodynamics and biogeochemistry at the Met Office, with the focus on producing skilful forecasts from these systems. He has led teams working on the science of ocean prediction, including data assimilation at one stage, on domains ranging from shelf to global scale, but predominantly focusing on modelling of the European North-West Shelf using NEMO.

This dissertation will demonstrate the author has contributed substantially to ocean modelling and its use in the operational context. He was responsible for developing the world's first operational short-range marine biogeochemistry forecast, developed for the Royal Navy and since used extensively for monitoring the health of the marine environment. He has since led the Met Office and joint Met Office/NERC ocean model development programmes for a number of years. The ordering of the chapters is thematic, rather than chronological, and starts with the author's contribution to underpinning science for the ocean and biogeochemistry models (Chapter 2), follows

with the contributions to developing and evaluating forecast systems (Chapters 3 and 4). The work finishes with a look at the priorities and challenges for science developments in ocean forecasting (Chapter 5).
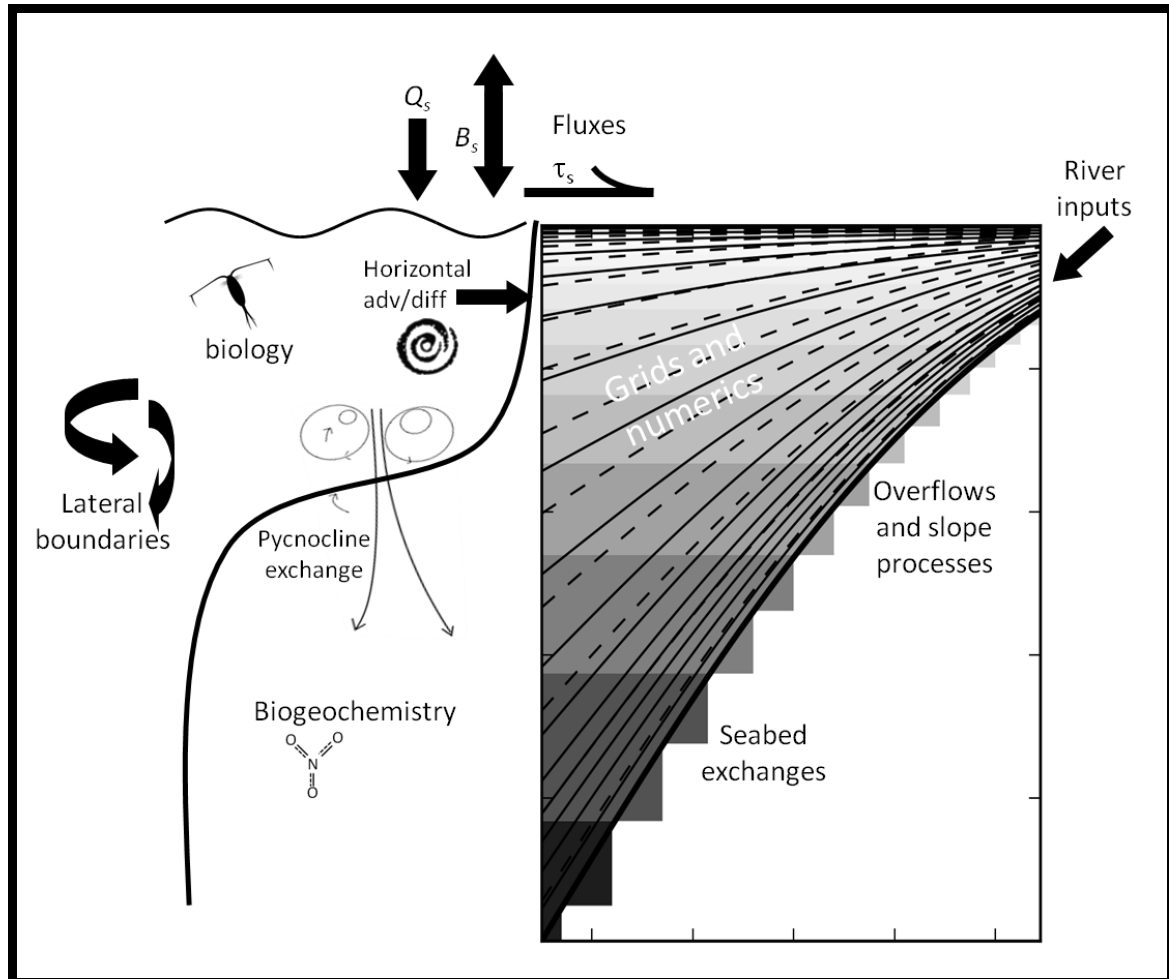
A schematic of an ocean model highlighting the important elements of the system, and processes that must be well represented or parameterised to ensure ocean forecasts are skilful.

Paper	Ref	Theme
Siddorn, J.R. and Furner, F. (2013) An analytical stretching function that combines the best attributes of geopotential and terrain-following vertical coordinates, *Ocean Modelling*, 66, 1–13, doi:10.1016/j.ocemod.2013.02.001.	R-1-I	Model Develop-ment
Siddorn, J.R. and Allen, J.I. (2003). Surface heat fluxes and ecosystem function in the Cretan Sea (eastern Mediterranean): a modelling study. *Annales Geophysicae*, 21, 377-389, doi:10.5194/angeo-21-377-2003.	R-1-II	
Allen, J.I., **Siddorn, J.R.,** Blackford, J.C. and Gilbert, F.J. (2004), Turbulence as a control on the microbial loop in a temperate seasonally stratified marine systems model, *J. Sea Res.*, 52(1), 1-20, doi:10.1016/S0924-7963(02)00072-6.	R-1-III	
Siddorn, J.R., Allen, J.I., Blackford, J.C., Gilbert,F.J., Holt, J.T., Holt, M.W., Osborne, J.P., Proctor, R.,Mills, D.K. (2007). Modelling the hydrodynamics and ecosystem of the North-West European continental shelf for operational oceanography *J. Mar. Sys.*, 65, 417-429, doi:10.1016/j.jmarsys.2006.01.018.	R-2-I	Shelf Seas Forecasts
Allen, J.I., Smyth, T.J., **Siddorn, J.R**. and Holt, M. (2008) How well can we forecast high biomass algal bloom events in a eutrophic coastal sea? *Harmful Algae*. doi:10.1016/j.hal.2008.08.024	R-2-II	
O'Dea, E.J., Arnold, A.K., Edwards, K.P., Furner, R., Hyder, P., Martin, M.J., **Siddorn, J.R.**, Storkey, D., While, J., Holt, J.T. and Liu, H. (2012) An operational ocean forecast system incorporating NEMO and SST data assimilation for the tidally driven European North-West shelf. *J. Op. Oc.*, 5, 3-17, doi:10.1080/1755876X.2012.11020128	R-2-III	
Storkey, D. , Blockley, E.W., Furner, R., Guiavarc'h, C., Lea, D., Martin, M.J., Barciela, R.M., Hines, A., Hyder, P. and **Siddorn, J.R.** (2010), Forecasting the ocean state using NEMO: The new FOAM system. *J. Op. Oc.*, 3, 3-15, doi:10.1080/1755876X.2010.11020109.	R-3-I	Global/ Basin Scale Forecasts
Hyder, P., Storkey, D., Blockley, E., Guiavarc'h, C., **Siddorn, J.,** Martin, M. and Lea, D. (2012) Assessing equatorial surface currents in the FOAM Global and Indian Ocean models against observations from the global tropical moored buoy array. *J. Op. Oc.,* 5(2), 25-39, doi:10.1080/1755876x.2012.11020136.	R-3-II	
Megann, A., Storkey, D., Aksenov, Y., Alderson, S., Calvert, D., Graham, T., Hyder, P., **Siddorn, J.,** and Sinha, B. (2014) GO5.0: The joint NERC-Met Office NEMO global ocean model for use in coupled and forced applications, *Geosci. Model Dev.,* 7, 1069–1092, doi:10.5194/gmd-7-1069-2014.	R-3-III	

List of papers presented for the PhD by published works, grouped by theme.

2. Forecast model development

Shelf seas are shallow regions bounded by the shelf slope, exchanges across which dictate the interaction with the deep ocean. Being shallow, interaction with the seabed is important, not least due to the impact friction has upon the flows in these regions. Models for shelf seas forecasting tend to be similar in their fundamentals, with the vast majority being finite difference models solving the Navier-Stokes equations for motion, simplified by applying the Boussinesq, incompressibility, and hydrostatic approximations. Density is calculated using an equation of state, which links the active tracers (temperature and salinity) and the fluid dynamics. Scales at which the shelf seas are modelled are of the order kilometres in the horizontal and tens of metres in the vertical, motivating scale separation between the horizontal and vertical solutions. Vertical turbulent motions are approximated by turbulent closure schemes, and horizontal sub-grid scale turbulent motions (mesoscale and/or submesoscale features) and the associated energy cascades are it not resolved and therefore require the use of laplacian and/or bilaplacian diffusion operators. For the sake of computational efficiency these models also separate the barotropic motions associated with the fast moving tides and (slower) baroclinic motions. Given the importance of the seabed interactions for the shelf seas dynamics the choice of vertical coordinate is predominantly terrain-following, allowing both good resolution of the near-bed waters and proper representation of the bottom kinematic boundary condition (which requires the model coordinate to lie parallel to the seabed). Despite the use of terrain-following coordinates, the models do not fully resolve the bottom log layer, and so the effects of friction on the horizontal momentum are parameterised by a (generally) quadratic function of the near bed velocities scaled by a drag coefficient.

2.1. The vertical coordinate

Hydrodynamic forecast models have historically been developed in separate communities that can broadly divided into three groups; the coastal, the shelf seas and the basin/global scale. The coastal community tends to use finite element or finite volume solutions that are well suited to low aspect-ratio problems (for example using TELEMAC, Galland et al., 1991) where the separation of horizontal and vertical scales is not required or desirable. The shelf seas and basin/global scale modelling communities tend both to work in finite difference modelling frameworks, and have scale separated solutions in the horizontal and vertical dimensions. Even so, shelf seas and deep ocean systems have developed different solutions, albeit increasingly in the same modelling framework, due both to the differing science problems and the differing communities they serve (predominantly the coupled

ocean-atmosphere modelling of climate prediction and seasonally forecasting at the global scale, and short-range ocean forecasting and reanalysis/hindcast at the shelf scale). This is the case for the discretisation of the grid in the vertical. Shelf seas systems require a vertical discretisation that resolves the bottom topography, whilst numerically satisfying the bottom kinematic boundary condition, to ensure topographic steering and the friction effects of the sea bed are well represented. A terrain-following coordinate is therefore the most commonly used approach. This is less important in global scale applications, where resolving the surface exchanges and the cross-pycnocline fluxes are a higher priority. Resolving the surface mixed layer and minimising spurious numerical diffusion is thus a key consideration. This has led to the domination of geopotential and/or isopycnic models to solve basin and global scale modelling requirements.

This separation of the global and shelf seas is increasingly being challenged (e.g. Holt et al., 2013), primarily because global models are now approaching the resolution that allows (albeit crudely) the shelves to be represented. This raises the prospect of being able to upscale from the shelf to the basin scale and vice versa. This requires that shelf seas are adequately represented both in terms of resolution (horizontal and vertical) and numerics in global models. If this is to be done in a single domain (other options exist, for example by using two-way nesting techniques) then a prerequisite is to have both horizontal and vertical grids defined in such a way as to meet the requirements of both the deep and shelf waters. In other words, geopotential vertical coordinates across the whole domain is not the ideal solution.

Additionally, there is a growing interest in high-resolution regional (i.e. shelf seas) scale air-wave-ocean coupled systems both for coupled Numerical Weather Prediction (NWP) and for ocean forecasting (for more details, see Section 5.2). The use of traditional (even stretched) terrain following coordinates leads to significant differences in the surface grid box depth within a model domain, resulting in the imprinting of the bathymetry upon the air-sea fluxes. This is clearly unsatisfactory both scientifically and with respect to provision of model based services, and is particularly a problem in coupled modelling systems where the ocean/atmosphere components remain free to evolve without the constraint of a prescribed atmosphere/ocean boundary condition.

The research described in Paper R-1-I was undertaken to satisfy this need to have a more flexible vertical coordinate for both global models representing shelf-seas and to improve the representation of air-sea exchange in shelf seas models, with an eye on the developing regional coupled systems. Geopotential coordinates are normally defined in real space (i.e. in units of

distance from a reference point) but can be defined in computational space (i.e. dimensionless units from a reference point). This opens up the possibility to define a geopotential set of levels within a stretched terrain-following framework, and hence combine the benefits of both geopotential and terrain-following coordinate systems. Paper R-1-I provides a function for discretising the vertical coordinate in ocean models that is designed to allow the user to define a fixed surface resolution, as one can in geopotential coordinate models, whilst retaining the benefits of terrain-following coordinates. This formulation has been termed the γ-stretching function and provides a solution that keeps the numerics of the terrain-following system at the seabed whilst allowing the coordinate to remain relatively flat in the surface waters. Options such as that of Shapiro et al. (2013) hybridize the terrain-following and geopotential methods and go some way to solving the problem, but often at a cost; for example the S-upon-Z has a staircase bathymetry over a large part of the domain and therefore does not represent seabed numerics well, and also has a large number of inactive vertical cells in the shallower waters, making it computationally inefficient.

The early part of R-1-I describes the theoretical framework of the method. Following this a series of steps that are required to effectively implement the coordinate are described, and a seamount test case based upon that published in Beckmann and Haidvogel (1993) is used to investigate the impact upon the model numerics. This shows the new stretching to have improved slope and hydrostatic consistency parameters compared with the frequently used scheme of Song and Haidvogel (1994). As would therefore be expected the stretching results in reduced horizontal pressure gradient (HPG) errors in the test case.

Moving to realistic configurations, the paper describes the implementation for a model for the European North-West Shelf, the Forecasting Ocean Assimilation Model (FOAM) Atlantic Margin Model (AMM7). Slope currents are particularly important in the European North-West Shelf, given their role in controlling exchanges between the shelf and open ocean (Huthnance et al., 2009). Shelf slope processes are particularly complex, and our modelling of them is further hampered by the prevalence of horizontal pressure gradient (HPG) errors in terrain-following coordinate models. HPG errors are minimised when the model coordinate surface is aligned with the isopycnal surface. The paper shows that an important side benefit of using the γ-stretching function is a flattening of the model surfaces over the slope and hence a significant reduction in HPG errors. The benefits of a constant and shallow box for air–sea exchange are also demonstrated in the paper, with the new setup giving enhanced diurnal ranges and shallower mixed layer depths, all key to improving the near-surface properties of the forecasts using the model.

This coordinate is now accepted as the standard terrain-following coordinate in NEMO, and is used by default by shelf seas modellers using NEMO. The so called CO5 version of the AMM7 (O'Dea et al., in prep) uses the vertical discretisation described in this paper, and hence this work has had a direct impact upon services, amongst others, to the Royal Navy and the Copernicus Marine Environmental Monitoring Services.

2.2. Modelling ocean physical-biological interactions

As discussed in the introduction, shelf seas forecasting services are expected to include a marine biogeochemistry component coupled to the hydrodynamic forcing. This allows the monitoring of ecosystem health and allows the UK to meet our international obligations under the Oslo Paris Convention (OSPAR, 2010). It also allows a response to legislation such as the Marine Strategy Framework Directive (MSFD) and Water Framework Directive (WFD). Early work by government to respond to MSFD includes model based outputs developed by the author (e.g. Defra, 2010). It also allows predictions of underwater visibility for marine (including Naval) operations, as well as forecasts of eutrophication and algae blooms for commercial aquaculture ventures. This coupling of the hydrodynamic forecasts with the biogeochemistry models provides a critical test of the hard-to-validate advective and diffusive flux terms from the hydrodynamic models, and can prove helpful in highlighting their deficiencies.

Physical control upon biological function can be considered on two scales. On the turbulent scale physical motions influence individual plankton through, for example, turbulent control upon the availability of nutrients in the immediate vicinity of individual organisms (e.g. Peters et al., 2006) or the rate of contact between organisms and its influence upon predation rates . These scales are too small for ocean models to resolve and hence including the affects of the turbulence upon plankton processes is the domain of the biological model parameterisations. Mixing processes are also important at the grid scale and larger (order metres in the vertical for most ocean models), and at larger scales changes to the general circulation patterns can influence the biota (Lévy et al., 2012). It is also worth noting that the presence of biota has an impact upon the physical properties of seawater through shading (and hence an impact upon the downwelling radiation) and the effect of plankton upon viscosity (e.g. Seuront et al., 2006) but this is not considered here.

The classic Sverdrup (1953) paradigm postulates that incident light intensities and mixed layer depth determine phytoplankton growth. Studies stretching back to Pingree et al., 1977 have explored the relationship between vertical mixing and biogeochemistry of our shelf seas. Sharples and Tett (1994)

showed through modelling studies that after the initial bloom the presence of a deep chlorophyll maximum was best explained through the diffusion of nutrients from below the thermocline into the mixed layer induced by wind induced mixing events. A number of subsequent works (for example Waniek, 2003, Kelly-Gerreyn et al., 2004, Sharples et al. 2001, 2007 and Rippeth et al., 2009) explored further the influence of mixing upon primary productivity, either due to the influence of meteorology deepening the mixed layer or dynamical processes such as internal wave breaking or shear spiking creating exchange across the pycnocline.

R-1-II explores the dependence of lower trophic level ecosystem function upon air-sea exchanges using a 1D implementation of the Princeton Ocean Model (POM; Blumberg and Mellor, 1987) coupled to the European Regional Seas Ecosystem Model (ERSEM; Baretta et al., 1995) in the Cretan Sea. It shows that modelled ecosystem behaviour can be defined as having periods where physical forcing controls the solution and periods where the system is far less sensitive to the physical environment, and details of the biological model behaviour control the solution.

Small errors or changes in the physical forcing (either through errors in the input fluxes or in the air-sea exchange formulations used) can lead to significant changes to the ecosystem solution around times of the onset of stratification. This paper also shows that the spring bloom can occur a long-time before the onset of stratification in the oligotrophic waters of the Mediterranean, following the critical turbulence theory of Huisman et al. (1999). R-1-II, slightly surprisingly, highlights the importance of accurate atmospheric humidity to the ecosystem simulations, through its influence on the surface heat flux, which affects the turbulence of the surface waters. Changes in turbulence impact upon, firstly, the transport of phosphate up from deeper waters and secondly the residence time of phytoplankton in the surface, euphotic waters. The impact of temporal frequency of the forcing upon the mean biological state of the system is limited.

The paper therefore highlights the importance of the air-sea exchange formulation, and the accuracy of the atmospheric forcing, upon the biological system in the periods under physical control. Subtle changes in the physics parameterisations, which have seemingly insignificant impacts on the physical state solution, have significant impacts upon the biological state in coupled ocean-biogeochemistry models (as also shown in e.g. Brasseur et al., 2009). This amplification effect is a significant issue for producing forecasts of biogeochemistry, and creates difficulties in the process of developing forecast systems. The correlation characteristics required for the data assimilation are a function of the model mixing processes, and ultimately the vertical mixing characteristics which a biogeochemistry

model is exposed to, is a function of both the model mixing scheme and the methods used for assimilating physical parameters. This can be useful in that it highlights issues with the physical model or assimilation not otherwise noticed (a notable case being the enhanced cross-pycnocline fluxes due to vertical temperature and salinity profile assimilation). It also puts considerable constraints upon the model developers, with the biogeochemistry model needing evaluation and (normally) re-tuning after even seemingly minor updates to the ocean model and/or data assimilation system.

R-1-III extends this work to investigate the role of turbulence and light upon lower trophic level ecosystem function, again using the ERSEM model coupled to a 1D physical model, this time the General Ocean Turbulence Model (GOTM; Umlauf and Burchard, 2003). A number of idealised experiments showed that short-term variability in ecosystem properties is dominated by the influence of light and primary productivity, explaining two thirds of the variability in primary production seen in the model. However, the bulk properties of biomass and production on seasonal and longer timescales is controlled by the strength of stratification which determines the seasonal variation in nutrient availability in the surface waters. The interplay between light, mixing and primary productivity leads to predictable cycles in production and lysis which gives rise to regimes that are either dominated by bacteria, phytoplankton or zooplankton. This transition between the regimes is physically mediated and clearly shows periodicity at relatively short timescales (following the spring-neap cycle) and at seasonal timescales (following the annual variations in light). This study gives us insight into the biological processes that may be important under different physical regimes, as well as providing a process based understanding of the biological system that proves useful when analysing the results from biological simulations.

3. Shelf seas reanalysis and forecast systems

Shelf seas environments present a number challenges to modellers (see e.g. Delhez et al., 2004 or Golbeck et al., 2015 for examples of the uncertainty in ocean predictions on the shelf). Firstly, they are dynamic regions where a range of processes need to be represented if realistic simulations are to be achieved. Wind and buoyancy driven residual circulation is superimposed upon the tidal circulation. The difficulty in representing the relatively poorly understood dynamics of shelf-slopes, including mesoscale and submesoscale processes, means cross-shelf exchanges can be particularly difficult to model. This is compounded by enhanced numerical errors in regions where the model grid is not aligned well with isopycnals (as discussed previously). Small scale (turbulent) processes

are important in determining exchanges across interfaces, most notably vertically in seasonally and tidally stratified waters but also horizontally, for example in determining the horizontal extent of the influence of freshwater discharges as the freshwater is mixed with adjacent waters by baroclinic instabilities.

Shelf seas environments also present particular challenges in that they are significantly influenced by the deep ocean, land, sea-bed and air boundaries. Not only therefore do the relevant dynamical processes need to be well represented but the inputs to the system also need to be well specified. Poor river sources of freshwater can have a dramatic effect upon the model solution. Good quality bathymetry and coastlines still remains a limitation, exacerbated by the difficulty in defining a bottom roughness length in an environment that not only has highly spatially variable bottom types that are poorly monitored, but may also have rapidly evolving changes to the bed morphology. Compounding this, air-sea exchange parameterisations tend to be based upon empirical formulations derived in regimes far removed from those being modelled, and the atmospheric models used to provide atmospheric boundary information are imperfect and primarily tuned to give the best solutions over land where the dominant societal impact is to be found.

R-2-I describes an ocean model configuration developed for real-time ocean forecasting in the European North-West Shelf. This was the first system to operationally produce analyses and forecasts of the hydrodynamics and biogeochemistry. It was implemented primarily for the use of the Royal Navy which requires information about the vertical density gradients (for sonar purposes), the currents (primarily for diver operations including mine clearance) and the visibility (both for submarine detection and for diver operations). There is also significant interest in this type of service from agencies such as the Department of Energy and Climate Change (DECC), the Department for Environment, Food and Rural Affairs (Defra), the Environment Agency (EA) and the Maritime and Coastguard Agency (MCA), for marine monitoring and response activities. R-2-I details the methodology behind the operational system, which was based on a version of the Proudman Oceanography Laboratory Coastal Ocean Modelling System (POLCOMS) physical model developed at Proudman Oceanographic Laboratory (now the National Oceanography Centre, NOC) and the ERSEM biogeochemistry model developed at Plymouth Marine Laboratory (PML), in part by the author (e.g. Allen et al., 2001). The quality of both the physical and biogeochemistry components of the system were evaluated in paper R-2-I, but the focus was on the biogeochemistry as this was the novel aspect of the system.

R-2-II followed the work in R-2-I, looking in detail at the operational skill in predicting algal bloom events, a significant issue both for agencies responsible for monitoring and maintaining coastal health (EA and local councils) and for commercial fisheries and aquaculture operators. The assessment used categorical metrics which convert measurements to a binary number (1/0) by means of a threshold. This method is widely used in the atmospheric community (e.g. Jolliffe and Stephenson, 2011) as it enables scientists to describe skill in a way that is meaningful for users of the data. The binary nature makes it possible to locate and define specific events. Contingency tables are created, which place each data point into true or false hits or misses, giving a two-by-two matrix. A "classification rate" (Brown and Davis, 2006), the sum of the correct true hits and misses divided by the number of events, combined with the bias shows the model to have some (but limited) skill in predicting discrete events. This sort of comparison, however, is in some ways unfair for algal bloom events which can be well-predicted but be offset slightly in space and time to give poor skill scores against standard metrics. Stow et al. (2009) provide a good description of how more advanced metrics that take into account spatial or temporal phase mismatches could be used.

As already discussed elsewhere in this work, ocean modelling systems have traditionally evolved separately for global and basin scale solutions to those for the relatively shallow water environments of the shelf seas. However, this has disadvantages both scientifically and from a resourcing perspective. Despite the different science drivers, there are also many solutions being developed for global models that may have benefits for shelf seas models, and vice versa. This is most obvious in the context of operational forecasting in the potential use of data assimilation systems that have primarily been developed for global modelling. More prosaically, maintaining a unified modelling framework generates less overhead than maintaining two. It was therefore decided a number of years ago at the Met Office, and with the support of NOC, that the functionality that at the time was present in the POLCOMS would be added to the Nucleus for European Modelling of the Ocean (NEMO; Madec, 2014). In doing so the shelf seas models used to produce reanalyses and forecasts would benefit from the numerics and parameterisations, as well as data assimilation capability, developed for use in global and basin scale models, and vice versa.

Following the implementation of the system described in R-2-I and R-2-II, the shelf seas forecasting was transitioned to use NEMO. This allowed, amongst other things, a data assimilation capability to be implemented. The short time and space scales in the shelf seas, with respect to the data availability, make assimilating data here a particular challenge. However, progress is being made and assimilation of subsurface temperature and salinity data and sea surface height data (King and

Martin, 2013) will become operationally viable within the next couple of years. Research on ocean colour assimilation has also shown promise, although considerably more development is required before this is ready for operational implementation.

R-2-III describes the operational implementation of the FOAM (Forecasting Ocean Assimilation Model) AMM7 (Atlantic Margin Model) at ~7 km resolution. This is the successor to the forecasting system detailed in R-2-I. The purpose of R-2-III was firstly to document the model and data assimilation configurations used in FOAM-AMM7 and secondly to provide evidence of the skill in the system. This paper serves as the initial documentation of shelf seas functionality in NEMO. The challenge in the development work behind R-2-III was to ensure that, despite its origin as an open ocean model, NEMO could be used in shelf-seas (tidal) simulations to give similar or better model skill to the options already available. The subsequent challenge was to demonstrate that the data assimilation functionality that therefore became available to the shelf seas forecasting team could be applied in the shelf seas environment, where the time and space scales are very different from those in the open ocean. The model has now been consistently shown to be as good as or better than its predecessor, and was for example shown by O'Neill et al. (2012) to outperform a significantly higher resolution POLCOMS equivalent for the Liverpool Bay region. Increasingly NEMO is now being used for operational oceanography in tidal/shelf environments, and this work contributed to developments in other operational systems including for the Irish-Biscay-Iberian region (Maraldi et al., 2013), in the Arabian Gulf (Hyder et al., 2012) and in the Black Sea (Shapiro et al., 2013) as well as for research (e.g. Wobus et al., 2013).

4. Operational basin scale and global reanalysis and forecast systems

In Section 3 the evolution of the shelf seas forecasting systems is described, including the transition from the POLCOMS to the NEMO physical model environment. A similar transition happened several years ahead for the FOAM deep ocean models. Once both systems were transitioned to using NEMO the development of both was consolidated into one team, led by the author. This Section describes some of the work done in developing the deep ocean configurations during that time.

R-3-I describes the first implementation of an operational forecasting system using NEMO at the Met Office. The primary configuration implemented was a global system based upon the $1/4^{\circ}$ ORCA grid (Drévillon et al., 2008), a tripolar, curvilinear discretisation that allows the poles to be placed over land and gives enhanced resolution at high latitudes. Three other basin scale configurations for

regions of particular user interest (the Mediterranean, the North Atlantic and the Indian Ocean) were also implemented on regular lat-lon grids (rotated in the case of the North Atlantic model to give a more regular grid) at higher (1/12°) resolution, giving a suite of forecast systems that was eddy permitting over the globe and eddy resolving in key basins. The paper describes the skill of the system and compares it to the previous operational models. The requirement from the work was that the new system would at least match its predecessor (given its implementation was primarily an enabler for future science pull-through) and the paper demonstrates it comfortably met these aims.

One of the primary uses of the FOAM system is in the prediction of currents, both for military and commercial purposes, but it is relatively difficult to assess the quality of ocean current forecasts because of the limited data availability. The large gyre circulations are generally well represented, but constraining the mesoscale is difficult both because of the chaotic nature of these flows and because of the resolution of both the models (which are not always eddy permitting) and the observations used in the assimilation (altimetry not providing the required space or time resolution). It is also difficult to evaluate ocean currents due to the scarcity of in situ measurements of currents and the poor quality of satellite derived current measures. The paper R-3-II provides an evaluation of the Indian Ocean model, with a focus upon the equatorial currents. These are only partially constrained by the altimetry assimilation due to the limited impact of geostrophy at low latitude. They are to some extent controlled by the profile assimilation of temperature and salinity, although corrections to density profiles in the presence of erroneous wind forcing fields give rise to spurious currents. Tropical currents and their evaluation is therefore of particular interest. This paper showed that the zonal flows, dominated by seasonal to interranual changes in density and Tropical Instability Waves (with timescales of the order of weeks) are reasonably well represented. Meridional currents, which are dominated by mesoscale features with shorter space and timescales, are simulated with significantly poorer skill.

R-3-III describes a successor system to that described in R-3-I. It was developed as part of the Joint Met-Office NERC Ocean Modelling Programme (JOMP), led by the author. JOMP introduced formalism to the system development process, with science development (new parameterisations or schemes) being followed by trials and systematic evaluation of the changes prior to release and testing in operational configurations. This is now accepted as the norm and critical for effective pull-through of scientific developments into improved predictive skill. The paper documents clearly both the present configuration and the changes implemented since the previous versions of the model, evaluates the quality both qualitatively and quantitatively, and attributes the changes in the quality

to the science changes implemented. The most significant science changes were to the vertical mixing scheme, which were updated on the basis of the tuning performed in Calvert and Siddorn (2013).

5. Science challenges and priorities for operational ocean forecasting

Operational ocean forecasting is still relatively immature, and there is therefore research needed to fill the gaps in, and improve the quality of, ocean services. Understanding the priorities for Ocean Forecasting Research is important at any time, but never more so than at the moment when fundamental changes in both the scientific capability and the user drive provide significant opportunities. Alongside the traditional needs for surface waves, currents and profiles of temperature and density, the increasing emphasis on monitoring the marine environment under legislation such as the Marine Strategy Framework Directive (MSFD) is driving the need to monitor the marine environment at levels not presently achievable. MSFD requires that EU member states have a marine strategy in place by 2020 that defines how they intend to monitor their marine waters, and therefore ensure that they can maintain Good Environmental Status (GES).

Observations alone cannot, without enormous and unrealistic investment, provide the spatial or temporal coverage required for a marine monitoring capability, and are limited to a subset of the parameters that are required. It is therefore clear that ocean modelling, with the appropriate assimilation of good quality observations, of the physical environment, the marine chemistry and the lower trophic level marine biology, is required to support these user needs.

Progress is needed to ensure models used for these purposes are of sufficient quality. Producing operational simulations that have skill requires model developers to balance the desire to improve the model through improved numerics and parameterisations with the need to well prescribe the inputs to the system.

Ocean models (especially biogeochemistry models) are still at a level of maturity where significant improvements to skill can be found from improving the process representation within the models.

Improving atmospheric, riverine or lateral boundary inputs is often overlooked as an important driver for improved skill, and can give substantial benefits for relatively minor investments of time and computing power. However, there is a limit to the availability of good quality input data and often there is a limit to which datasets that can be used (especially in real-time forecasting mode)

without creating undesirable dependencies. The potential to better represent some of the interface exchanges may be possible with the advent of coupled systems which allow the ocean to directly interact with the atmosphere and the land. These systems are presently being developed, with one of the most advanced being the UK Environmental Prediction system (discussed below), a joint NERC and Met Office activity led from the Ocean Forecasting group at the Met Office. Increased complexity systems can often be helpful in informing the model development process even if not incorporated as part of the final production solution. Climate researchers have used coupled models for a number of years, but due to the latency in the ocean system it has not until recently been considered of interest to the numerical weather prediction community. However, as weather models increase in resolution, and the focus on hazards prediction increases, the potential for air-land-sea coupling systems is increasingly driving research activity.

5.1. Model improvements

Vertical mixing schemes in ocean models are presently dependent upon empirical parameterisations and constant background constant diffusivity/viscosity terms that poorly represent the real mixing processes. Errors in vertical mixing develop quickly and are responsible for rapid degradations in the skill over a short-range forecast. They are therefore amongst the most immediate causes of poor forecast skill in the subsurface ocean. They are also important over longer timescales as spurious diapycnal mixing of scalar properties (nutrients and salt/temperature) is not necessarily constrained by the initialisation of the model and can lead to long-term drifts in the solution. This is a particular problem for any coupled forecasting systems where the surface properties of the ocean are unconstrained by the atmospheric model forcing, and atmosphere/ocean feedbacks can lead to rapidly growing biases. Improving upon the vertical mixing properties in ocean models is therefore a priority for the ocean forecasting community. Mixing errors are important a) within the surface mixed layer, particularly because of the impact upon air-sea exchanges, b) across the thermocline, because of the impact on nutrients in the surface waters and the accurate representation of density structure in the near-surface waters and c) in quiescent regions, because of the impact spurious numerical mixing this has on maintaining water masses.

Present schemes are often dominated by pragmatic tuning options that dominate the mixing and result in mixing schemes that poorly represent the real processes. NEMO for example relies on both a constant background minimum viscosity and diffusivity and an additional wind related penetration of turbulent kinetic energy below the mixed layer to compensate for a lack of explicitly included

16

processes. The exchange of scalar properties from the surface to deep waters and vice versa is therefore dominated by a number of tunable parameters which have limited tracability to the true physical processes. Calvert and Siddorn (2013) describes a series of tuning experiments used to produce reasonable mixing in the ocean surface boundary layer. This is essentially a curve fitting exercise, given the present schemes do not properly represent, for example, the effects of Langmuir turbulence (D'Asaro, 2015; Belcher et al., 2012), internal wave breaking (Gargett and Hollaway, 1984) and shear spiking (Rippeth et al., 2009). Despite it being possible to (more or less) fit the models to the observations, the underlying physical processes are clearly not being properly represented. The OSMOSIS project is seeking to redress this problem by incorporating a more realistic set of processes into a mixed layer model that will couple to a more traditional two-equation model below the mixed layer. There is still more to be done to move from the idealised to the real application, for example to address how the OSMOSIS mixed layer model will behave under ice and in shelf seas where the bottom and surface boundary layers can overlap. However, in the medium term this has the potential to redress some of the shortcomings in this area.

As our understanding and parameterisation of mixing processes improves we will increasingly be adding new explicit terms for mixing into our models. This further highlights the issue of spurious numerical mixing, especially for quiescent regions. Vertical coordinate can be chosen to align the model coordinate with isopyncal surfaces and hence to minimise the spurious diffusion, as discussed in Chapter 3. The extreme of this is to define the vertical coordinate on isopycnal surfaces which essentially limits the cross-isopycnal exchange to that defined by the vertical mixing scheme and "vertical" advection scheme. Isopycnal models, however, have disadvantages, especially in the surface mixed layer and as the water column shallows. Hybrid schemes have therefore been developed which show promise. The isopycnic and geopotential schema start to converge in the use of Arbitrary Lagrangian-Eulerian coordinates (ALE). Leclair and Madec (2011) developed an ALE capability for the NEMO model (termed the $z^\sim$ coordinate) that applies the lagrangian component (i.e. grid adaptation) in response to fast moving waves only. This neatly allows the model to limit the amount of adaptation required whilst removing the primary source of spurious vertical mixing. Petersen et al. (2015) described the impact of a range of vertical coordinates, including fully ALE and the $z^\sim$ subset of ALE and concluded that the use these coordinates worked well at reducing mixing under many scenarios. These formulations show promise and should be introduced into operational configurations once they are sufficiently mature.

Improving the advection/diffusion schemes to have improved properties is very much business as usual for the ocean model development community and will undoubtedly continue. However, the numerical properties of any modelling framework are inextricably tied to the numerical framework within which they are coded. Work being done on grids for atmosphere modelling, where it is a pressing problem, will in the not too distant future provide insight into the optimal approach to take. For example, the USA's MPAS project (Ringler et al. 2013) and the UK's GungHo project (Thuburn and Cotter, 2015) have both developed new grid frameworks and appropriate numerical schemes that have improved properties for geophysical modelling (Cotter and Thuburn, 2014). There may be significant benefit for the ocean modelling community to follow the lead of these projects, but it should be noted one of the key drivers for these activities is the polar singularity issue which in ocean models can be hidden through placing poles over land. The present consensus is that the most promising numerical approach probably lies in C-grid finite volume methods like those implemented in MPAS rather than finite elements based discretizations (Danilov 2013) which have been tried for the low aspect ratio ocean problems (for example the ICOM model) but without great success to date. As most ocean models are based upon C-grid finite difference methods, the pressure for change is relatively low in the ocean community. However, as computing infrastructures change the benefits to move to unstructured, finite volume or element solutions may increase.

There are fundamental scales in the ocean that need to be considered when deciding at which resolution to develop model configurations. At the smallest scales turbulent motions are clearly not resolvable and so these are parameterised, in the vertical using turbulence closure models and in the horizontal through diffusion operators. In the recent past mesoscale processes have not been resolved, and so methods for parameterising the impacts of mesoscale motions upon vertical restratification have been included in global models (e.g. Gent and McWilliams, 1990). We are now entering a period when computing power is such that operational modelling systems are under development at resolutions that can in the main resolve the mesoscale (of the order $1/15^{o}$ globally and 1 km in mid-latitude shelf regions). At these resolutions the challenge is to parameterise turbulent motions at the (smaller) grid scales, including sub-mesoscale eddies and filaments.

Increasingly there is a drive for forecasting and monitoring of the whole earth system, including the marine biogeochemistry. Presently the skill of biogeochemistry models is limited for forecasting bloom events. Allen et al. (2010) gives an interesting oversight of the challenges confronting the developers of biogeochemsitry systems. As discussed previously, the biogeochemistry accentuates physical model errors, and therefore particular attention needs to be paid to the hydrodynamic

modelling framework (including assimilation) errors in the context of their implications for biological function. We are still at the stage in the biological modelling community of trying to understand what modelling tools give the best trade off between complexity (costly, but potentially overfitted) and simplicity (inexpensive, but missing key processes). Developing well-posed biogeochemistry models is therefore still an area that needs active research. The use of data assimilation techniques to constrain the biogeochemistry simulations is also only just reaching the maturity required for operational forecasting purposes. The poor quality and range of data to constrain the system, allied with the complex interdependencies of the assimilated parameters with non-assimilated state variables, makes biogeochemistry assimilation a considerable challenge.

5.2. Coupled forecasting systems

The importance of air-sea interaction in both the modelling of the ocean and atmosphere has been recognised for many years. The timescales on which these interactions have traditionally been considered important has limited the use of coupled models to studies or prediction systems for monthly and longer timescales and while the need to represent feedbacks between different components of the environment is well understood and mature for climate prediction, the use of coupled approaches is not as well developed on shorter timescales. However there have been several vision papers (e.g. Brunet et al., 2010) and workshops relevant to this area, and the importance of coupling is becoming increasingly recognised for weather timescales. The need to accelerate progress in Earth System prediction across all scales (climate and weather, global and local) is discussed by Shapiro et al. (2010).

The GODAE OceanView (GOV) Science Team, recognizing the need to explore the potential benefit to both oceanic and atmospheric forecasting, formed the Short-to Medium-Range Coupled Prediction Task Team (SMRCP-TT). The progress made by the communities involved in the SMRCP-TT since its inception on understanding coupled modelling, its challenges and benefits, and in building coupled systems, is detailed in Brassington et al. (2015).

The Met Office strategy for weather and ocean forecasting is to focus upon a two system approach, one global and one for the UK. The coupling activities follow the same approach, and two science teams to lead the research activities in this area have been created within the author's group. The strategy for seamless prediction (Met Office Science Strategy, 2015) is increasingly bringing the weather and a climate system in closer alignment and because of this significant progress is being made in coupled modelling on weather timescales. Nonetheless the move to coupled forecasting

presents significant technical, scientific and resourcing challenges. Presently the use of coupled systems in weather forecasting is in its research phase, but planning for the operational phase for global systems has begun.

The leading order impact of including an interactive ocean model as part of a coupled operational NWP system is that the atmosphere will see a more realistic evolving sea surface temperature (SST) during the forecast period. It is therefore expected that the main benefits for global models will be in regions where there is a large diurnal SST range (particularly the tropics) or where ocean surface temperatures can change rapidly due to large heat fluxes or strong ocean mixing processes. Previous work (e.g. Kim et al. 2010) has shown that permitting high frequency SST variability (by coupling atmosphere and ocean components at least every few hours) has significant benefits in the tropics by allowing a better phase relationship between SSTs and convection, and increasing the ability of models to forecast the spatial and temporal evolution of the Madden-Julian Oscillation (MJO). Indications of improved MJO predictions have already been seen in Met Office coupled systems (Shelly et al., 2014). There is also evidence that mid-latitude storm generation and evolution can be better predicted in a forecast model with an interactive ocean and atmosphere. Such benefits are expected to be more fully realised once the ocean model resolution is high enough to provide a detailed representation of the sharp SST gradients (associated with, for example, eddies) which can then strongly influence the atmospheric boundary layer. A number of studies (e.g. Janssen et al. 2013) have shown that using a coupled system has an impact on the evolution of slow moving tropical cyclones due to cooling of SSTs as heat is removed from the surface ocean. This is expected to correctly reduce the tendency of atmosphere-only models to otherwise over-develop such systems, particularly as the resolution increases.

Validation of global coupled forecasts for provision of the Copernicus Marine Service forecasts showed improvements in some regions over (which benefits from higher resolution atmosphere forcing), although differences are relatively small (Guiavarc'h, pers comms). Given the ocean and atmosphere forecasting systems are well-tuned and have been shown to perform extremely well when compared with international partners (e.g. Ryan et al., 2015) this is encouraging and one would expect significant benefits to be realised as the system matures.

Coupled regional prediction systems have been applied in research mode to improve the representation of air-sea interactions on, for example, Bora winds over the Adriatic (e.g. Pullen et al., 2006), on the evolution of Mediterranean storms (e.g. Renault et al., 2012) and on hurricane

formation and development (e.g. Warner et al., 2010). Given these results it seems likely that coupling would lead to better representation of the surface wind/pressures in extra-tropical storms could lead to improved surges, a key feature of the hydrodynamics in the North-West European Shelf, and improved representation of the ocean surface boundary layer. Additionally, air-ocean-land coupling has the potential to improve the hydrological cycle, a major shortcoming in ocean models that have significant riverine input. The development of a flexible and collaborative modelling framework for coupled land-surface and hydrological models (Pietroniro et al., 2007; Deacu et al., 2012) has enabled better understanding of the behaviour of different land-surface models and objective testing of different schemes to improve the representation and accuracy of the regional water budget. Also important for the Met Office, in its role as the UK's weather service, the ability to simulate land-sea-breeze circulation and the formation of coastal fog, all of which can be expected to be improved by coupled modelling.

There is already evidence of the benefit of coupled prediction for improving weather forecast skill. For example, coupled atmosphere-ice-ocean forecasts are now operational at the Canadian Meteorological Centre for the Gulf of St Lawrence region in Canada, with evaluation demonstrating significant improvement in the skill of both atmospheric and ice forecasts (Smith et al., 2013 and others).

6. Summary

This dissertation presents a subset of the author's published works, and describes the impact his work has had on ocean forecasting systems. This impact can be broadly divided into two themes, the underpinning development of ocean forecasting models and the implementation, tuning and evaluation of those models to ensure they provide skilful products, with value to users. The systems described in this dissertation are recognised as amongst the best available, and are being used by commercial operators, military decisions makers and governmental organisations, as well as research users. They also form the basis on which future systems will be developed, meeting the challenges and addressing the priorities discussed in Section 5. The author expects to have a substantive impact on driving the research agenda in these areas over the coming years.

7. References

Allen, J.I., Blackford, J., Holt, J., Proctor, R., Ashworth, M., Siddorn, J. (2001) "A highly spatially resolved ecosystem model for the North West European Continental Shelf", Sarsia, 86(6), 423-440.

Allen, J.I., Aiken, J., Anderson, T.R., Buitenhuis, E., Cornell, S., Geider, S.J, Haines, K, Hirata, T., Holt, J., Le Quéré, C., Hardman-Mountford, N., Ross, O.N., Sinha, B., While, J. (2010) "Marine ecosystem models for earth systems applications: The MarQUEST experience", Journal of Marine Systems, 81(1–2), 19-33.

Baretta, J.W., Ebenhöh, W., Ruardij P. (1995) "The European regional Seas Ecosystem Model, a complex marine ecosystem model", Neth. J. Sea Res. 33, 233-246.

Baxter, P.J. (2005) "The east coast Big Flood, 31 January–1 February 1953: a summary of the human disaster", Phil. Trans. R. Soc. A 363, 1293–1312.

Beckmann, A. and Haidvogel, D.B. (1993) "Numerical simulation of flow around a tall isolated seamount. Part I: Problem formulation and model accuracy", Journal of Physical Oceanography 23, 1736–1753.

Belcher, S. E., Grant, A. L. M., Hanley, K. E., Fox-Kemper, B., Van Roekel, L., Sullivan, P. P., Large, W. G., Brown, A., Hines, A., Calvert, D., Rutgersson, A., Pettersson, H., Bidlot, J.-R., Janssen, P. A. E. M., & Polton, J. A. (2012) "A global perspective on langmuir turbulence in the ocean surface boundary layer", Geophys. Res. Lett., 39 (18), L18605+.

Blumberg, A. F. and Mellor, G. L. (1997) A description of a three-dimensional coastal ocean circulation model, Three-Dimensional Coastal Ocean Models, (Ed) Heaps, N., AGU, Washington, D.C.

Brasseur, P., Gruber, N., Barciela, R., Brander, K., Doron, M., El Moussaoui, A., Hobday, A. J., Huret, M., Kremeur, A.-S., Lehodey, P., Matear, R., Moulin, C., Murtugudde, R., Senina, I., Svendsen, E. (2009) "Integrating biogeochemistry and ecology into ocean data assimilation systems", Oceanography, 22(3), 206-215.

Brassington, G., Martin, M.J., Tolman, H.L., Akella, S., Balmeseda, M., Chambers, C.R.S., Chassignet, E., Cummings, J.A., Drillet, Y., Jansen, P.A.E.M., Laloyaux, P., Lea, D., Mehra, A., Mirouze, I., Ritchie, H., Samson, G., Sandery, P.A., Smith, G.C., Suarez M., Todling, R. (2015) "Progress and challenges in short- to medium-range coupled prediction", Journal of Operational Oceanography, 8, s239-s258.

Brown, C.D. and Davis, H.T. (2006) "Receiver operating characteristics curves and related decision measures: a tutorial", Chemometrics Intell. Lab. Syst. 80, 24–38.

Brunet, G., Shapiro, M., Hoskins, B., Moncrieff, M., Dole, R., Kiladis, G. N., Kirtman, B., Lorenc, A., Mills, B., Morss, R., Polavarapu, S., Rogers, D., Schaake, J., Shukla, J. (2010) "Collaboration of the weather and climate communities to advance Subseasonal-to-Seasonal prediction", Bull. Amer. Meteor. Soc., 91 (10), 1397-1406.

Calvert, D. and Siddorn, J. (2013) "Revised vertical mixing parameters for the UK community standard configuration of the global NEMO ocean model", Hadley Centre Technical Note 95, 74 pp, Met Office, Exeter, UK.

Cotter, C.J. and Thuburn, J. (2014) "A finite element exterior calculus framework for the rotating shallow-water equations", Journal of Computational Physics, 257, 1506-1526.

Danilov, S. (2013) "Ocean modeling on unstructured meshes", Ocean Modelling, 69 , 195-210.

Deacu, D., Fortin, V., Klyszejko, E. (2012) "Predicting the net basin supply to the Great Lakes with a hydrometeorological model", J. Hydrometeorol., 13, 1739-1759.

D'Asaro, E. A. (2014) "Turbulence in the Upper-Ocean mixed layer", Annual Review of Marine Science, 6 (1), 101-115.

Delhez, É. J. M., Damm, P., de Goede, E., de Kok, J. M., Dumas, F., Gerritsen, H., Jones, J. E., Ozer, J., Pohlmann, T., Rasch, P. S., Skogen, M., Proctor, R. (2004) "Variability of shelf-seas hydrodynamic models: lessons from the NOMADS2 project", Journal of Marine Systems, 45 (1-2), 39-53.

Department for Environment, Fisheries and Rural Affairs (Defra) (2010) "Charting progress 2", http://webarchive.nationalarchives.gov.uk/20141203181034/http://chartingprogress.defra.gov.uk/about, last retrieved 25th January 2016, Defra, London, UK.

Drévillon, M., Bourdallé-Badie, R., Derval, C., Drillet, Y., Lellouche, J.M., Rémy, E., Tranchant, B., Benkiran, M., Greiner, E., Guinhut, S., Verbrugge, N., Garric, G., Testut, C.E., Laborie, M., Nouel, L., Bahurel, P., Bricaud, C., Crosnier, L., Dombrowsky, E., Durand, E., Ferry, N., Hernandez, F., Le Galloudec, O., Messal, F., Parent, L. (2008) "The GODAE/Mercator-Océan global ocean forecasting system: results, applications and prospects", J. Operational Ocean., 1 (1), 51–57.

Galland, J.C., Goutal, N., Hervouet, J.M. (1991) "TELEMAC: A New Numerical Model for Solving Shallow Water Equations", Adv. Water Resources, 14 (3), 138–148.

Gargett, A. E. and Holloway, G. (1984) "Dissipation and diffusion by internal wave breaking", Journal of Marine Research, 42 (1), 15-27.

Gent, P.R. and McWilliams, J.C. (1990) "Isopycnal mixing in ocean circulation models", J. Phys. Oceanogr., 20, 150–155.

Golbeck, I., Li, X., Janssen, F., Brüning, T., Nielsen, J., Huess, V., Söderkvist, J., Büchmann, B., Siiriä, S.-M., Vähä-Piikkiö, O., Hackett, B., Kristensen, N., Engedahl, H., Blockley, E., Sellar, A., Lagemaa, P., Ozer, J., Legrand, S., Ljungemyr, P., Axell, L. (2015) "Uncertainty estimation for operational ocean forecast products—a multi-model ensemble for the north sea and the baltic sea", Ocean Dynamics, 65(12), 1603-163.

Holt, J., New, A., Liu, H., Coward, A., Ashworth, M., Pickles, S., Harle, J., Siddorn, J. (2013) "Prospects for improving the representation of coastal and shelf seas in global ocean models", In EGU General Assembly Conference Abstracts, volume 15 of EGU General Assembly Conference Abstracts, pages 10755+.

Huisman, J., van Oostveen, P., Weissing, F. J. (1999) "Critical depth and critical turbulence: two different mechanisms for the development of phytoplankton blooms", Limnol. Oceangr., 44(7),1781–1787.

Huthnance, J. M., Holt, J. T., Wakelin, S. L. (2009) "Deep ocean exchange with west-european shelf seas", Ocean Science, 5 (4), 621-634.

Hyder, P., While, J., Arnold, A., O'Dea, E., Furner, R., Siddorn, J., Martin, M. and Sykes, P. (2012) "Evaluating a new NEMO-based Persian/Arabian Gulf tidal operational model", Journal of Operational Oceanography, 6(1), 3-16.

Janssen, P.A.E.M., Breivik, Ø., Mogensen, K., Vitart, F., Balmaseda, M., Bidlot, J.-R., Keeley, S., Leutbecher, M., Magnusson, L., Molteni, F. (2013) "Air-sea interaction and surface waves", ECMWF Technical Memorandum 712, ECMWF, Reading, UK.

Jolliffe, I.T. and Stephenson, D.B (Eds.) (2011) *Forecast Verification: A Practitioner's Guide in Atmospheric Science*, Wiley, New York, pp. 292.

Kelly-Gerreyn, B.A., Anderson, T.R., Holt, J.T., Gowen, R.J., Proctor, R. (2004) "Phytoplankton community structure at contrasting sites in the Irish Sea: a modelling investigation", Estuarine and Coastal Shelf Science 59, 363–383.

Kim, H.-M., Hoyos, C.D., Webster, P.J., Kang, I.-S. (2010) "Ocean-atmosphere coupling and the boreal winter MJO", Climate Dynamics. 35, 771-784.

King, R.R and Martin, M. (2013) "Comparing satellite altimetry with ocean models of the North-West Shelf Forecasting", Research Technical Report No: 581, Met Office, Exeter UK.

Leclair., M and Madec, G. (2011) "Z~-Coordinate, an Arbitrary Lagrangian–Eulerian coordinate separating high and low frequency motions", Ocean Modelling, 37, 139–152.

Lewis, H., Mittermaier, M., Mylne, K., Norman, K., Scaife, A., Neal, R., Pierce, C., Harrison, D., Jewell, S., Kendon, M., Saunders, R., Brunet, G., Golding, B., Kitchen, M., Davies, P., Pilling, C. (2015) "From months to minutes – exploring the value of high-resolution rainfall observation and prediction during the UK winter storms of 2013/2014", Met. Apps, 22, 90–104.

Lévy, M., Iovino, D., Resplandy, L., Klein, P., Madec, G., Tréguier,A.-M. Masson, S., Takahashi, K. (2012) "Large-scale impacts of submesoscale dynamics on phytoplankton: Local and remote effects", Ocean Modelling, 43–44,77-93.

Madec G. (2014) "NEMO ocean engine", Note du Pôle de modélisation, Institut Pierre-Simon Laplace (IPSL), Paris, France, No 27 ISSN No 1288-1619.

Maraldi, C., Chanut, J., Levier, B., Ayoub, N., De Mey, P., Reffray, G., Lyard, F., Cailleau, S., Drévillon, M., Fanjul, E. A., Sotillo, M. G., Marsaleix, P., the Mercator Research & Development Team (2013) "NEMO on the shelf: assessment of the Iberia-Biscay-Ireland configuration", Ocean Science, 9(4), 745-771.

Met Office (2015) "Science Strategy: 2016-2021. Delivering science with impact", Met Office, Exeter, UK, pp 42.

O'Dea, E., Siddorn, J.R., Furner, F., While, J., Sykes, P, King, R.R, Holt, J.T., Wakelin, S. (in prep) "Version CO5 of the 7km Atlantic Margin Model (AMM7) reanalysis system: Part 1, Ocean model Component", Geophysical Model Development.

O'Neill, C. K., Polton, J. A., Holt, J. T., O'Dea, E. J. (2012) "Modelling temperature and salinity in Liverpool Bay and the Irish Sea: sensitivity to model type and surface forcing", Ocean Science, 8 (5), 903-913, 2012.

OSPAR (2010) "Quality Status Report 2010", http://qsr2010.ospar.org/en/index.html, last retrieved 25th January 2016, OSPAR, London, UK.

Peters, F., Arin, L., Marrasé, C., Berdalet, E., Sala, M.M. (2006) "Effects of small-scale turbulence on the growth of two diatoms of different size in a phosphorus-limited medium", Journal of Marine Systems, 61(3–4), 134-148.

Petersen, M.R., Jacobsen, D.W., Ringler, T.D., Hecht, M.W., Maltrud, M.E. (2015) "Evaluation of the arbitrary Lagrangian–Eulerian vertical coordinate method in the MPAS-Ocean model", Ocean Modelling, 86, 93-113.

Pietroniro, A., Fortin, V., Kouwen, N., Neal, C., Turcotte, R., Davison, B., Verseghy, D., Soulis, E.D., Caldwell, R., Evora, N., Pellerin, P. (2007) "Development of the MESH modelling system for hydrological ensemble forecasting of the Laurentian Great Lakes at the regional scale", Hydrol. Earth Syst. Sci., 11, 1279-1294.

Pingree, R.D., Maddock, L., Butler, E.I. (1977) "The influence of biological activity and physical stability in determining the chemical distributions of inorganic phosphate, silicate and nitrate", Journal of the Marine Biological Association of the UK 57, 1065–1073.

Pullen, J., Doyle, J., Signell, R.P. (2006) "Two-way air-sea coupling: a study of the Adriatic", Mon. Weather Rev. 134: 1465-1483.

Renault, L., Chiggiaro, J., Warner, J.C., Gomez, M., Vizoso, G., Tintoré, J. (2012) "Coupled atmosphere-ocean-wave simulations of a storm event over the Gulf of Lion and Balearic Sea", J. Geophys. Res., 117, C09019.

Ringler, T., Petersen, M., Higdon, R. L., Jacobsen, D., Jones, P. W., Maltrud, M. (2013) "A Multi-Resolution Approach to Global Ocean Modeling. Ocean Modelling", 69(C), 211–232. doi:10.1016/j.ocemod.2013.04.01

Rippeth, T.P., Wiles, P., Palmer, M.R., Sharples, J., Tweddle, J. (2009) "The diapcynal nutrient flux and shear-induced diapcynal mixing in the seasonally stratified western Irish Sea", Continental Shelf Research, 29, 1580–1587.

Ryan, A.G., Regnier, C., Divakaran, P., Spindler, T., Mehra, A., Smith, G.C., Davidson, F., Hernandez, F., Maksymczuk, J., Liu, Y. (2015) "GODAE OceanView class 4 forecast verification framework: global ocean inter-comparison", Journal of Operational Oceanography, 8, s98-s111.

Seuront, L., Vincent, D., Mitchell, J.G. (2006) "Biologically induced modification of seawater viscosity in the Eastern English Channel during a Phaeocystis globosa spring bloom", Journal of Marine Systems, 61(3–4), 118-133.

Shapiro, G., Luneva, M., Pickering, J. Storkey, D. (2013) "The effect of various vertical discretization schemes and horizontal diffusion parameterization on the performance of a 3-D ocean model: the Black Sea case study", Ocean Science, 9(2), 377-390.

Shapiro, M., Shukla, J., Brunet, G., Nobre, C., Beland, M., Dole, R., Tremberth, K., Anthes, R., Asrar, G., Barrie, L., Bougeault, P., Brasseur, G., Burridge, D., Busalacchi, A., Caughey, J., Chen, D., Church, B., Enomoto, T., Hoskins, B., Hov, Ø., Laing, A., Le Treut, H., Marotzke, J., McBean, G., Meehl, G., Miller, M., Mills, B., Mitchell, J., Moncrieff, M., Nakazawa, T., Olafsson, H., Palmer, T., Parson, D., Rogers, D., Simmons, A., Troccoli, A., Toth, Z., Uccellini, L., Velden, C., Wallace, J.M. (2010) "An Earth-System prediction initiative for the 21st Century", Bull. Am. Meteorol. Soc. 91: 1377-1388.

Sharples, J. and Tett, P. (1994) "Modelling observations of the seasonal cycle of primary productivity: the importance of short-term physical variability", Journal of Marine Research, 52, 219–238.

Sharples, J., Moore, C.M., Abraham, E.R. (2001) "Internal tide dissipation, mixing, and vertical nitrate flux at the shelf edge of NE New Zealand", J. Geophys. Res., 106, 14069–14081.

Sharples, J., Tweddle, J.F., Green, J.A.M., Palmer, M.R., Kim, Y.-N., Hickman, A.E., Holligan, P.M., Moore, C.M., Rippeth, T.P., Simpson, J.H., Krivtsov, V. (2007) "Spring-neap modulation of internal tide mixing and vertical nitrate fluxes at a shelf edge in summer", Limnol. Oceanogr., 52(5), 1735-1747.

Shelly, A., Xavier, P., Copsey, D., Johns, T., Rodriguez, J.M., Milton, S., Klingaman, N. (2014) "Coupled versus uncoupled hindcast simulations of the Madden-Julian Oscillation in the Year of Tropical Convection", Geophys. Res. Lett., 41, 5670–5677.

Smith, G.C., Roy, F., Brasnett, B. (2013) "Evaluation of an operational ice-ocean analysis and forecasting system for the Gulf of St Lawrence", Q. J. R. Meteorol. Soc., 139, 419-433.

Slingo, J.L. et al. (2014) "The Recent Storms and Floods in the UK", http://www.metoffice.gov.uk/media/pdf/n/i/Recent_Storms_Briefing_Final_07023.pdf, last retrieved 4th January 2016, Met Office, Exeter, UK.

SOLAS (1974), "International Convention for the Safety of Life at Sea", http://www.imo.org/About/Conventions/ListOfConventions/Pages/International-Convention-for-the-Safety-of-Life-at-Sea-(SOLAS),-1974.aspx, last retrieved 4th January 2016, International Maritime Organization (IMO), London, UK.

Song, Y. and Haidvogel, D.B. (1994) "A semi-implicit ocean circulation model using a generalized topography-following coordinate system", Journal of Computational Physics, 115, 228–244.

Stow, C.A., Jolliff, J., McGillicuddy, D.J., Doney, S.C., Allen, J.I., Friedrichs, M.A.M., Rose, K.A., Wallhead, P. (2009) "Skill assessment for coupled biological/physical models of marine systems.", Journal of Marine Systems 76 (1-2) 4–15.

Sverdrup, H.U. (1935) "On conditions for the vernal blooming of phytoplankton", J. Counc. 18, 287 – 295.

Thuburn, J., Cotter, C.J. (2015) "A primal-dual mimetic finite element scheme for the rotating shallow water equations on polygonal spherical meshes", Journal of Computational Physics, 290, 274-297.

Umlauf, L. and Burchard, H. (2003) "A generic length-scale equation for geophysical turbulence models", Journal of Marine Research, 61 (2), 235-265.

Waniek, J.J. (2003) "The role of physical forcing in initiation of spring blooms in the northeast Atlantic", Journal of Marine Systems 39, 57–82.

Warner, J.C., Armstrong, B., He, R., Zambon, J.B. (2010) "Development of a coupled ocean-atmosphere-wave-sediment transport (COAWST) modelling system", Ocean Modelling, 35, 230-244.

Wobus, F., Shapiro, G.I., Huthnance, J.M., Maqueda, M.A.M. Aksenov, Y. (2013) "Tidally induced lateral dispersion of the Storfjorden overflow plume", Ocean Sci., 9, 885–899.

Annex A: Contributions as Co-author

R-I-III and R-2-I

Contributions of John Siddorn to Papers by Prof Icarus Allen

The papers considered are:

Allen, J.I., Siddorn, J.R., Blackford, J.C. and Gilbert, F.J. (2004), Turbulence as a control on the microbial loop in a temperate seasonally stratified marine systems model, Journal of Sea Research, 52(1), 1-20.

and

Allen, J.I., Smyth, T.J., Siddorn, J.R. and Holt, M. (2008) How well can we forecast high biomass algal bloom events in a eutrophic coastal sea? Harmful Algae. doi:10.1016/j.hal.2008.08.024

In Allen et al 2004 John constructed the water column model system used. He co-designed the numerical experiment and ran the simulations. He validated the models and co-designed the analysis. He made a significant contribution to the writing of the paper.

In Allen et al 2008 he set up the coupled POLCOMS-ERSEM model used in this paper (the Met Office operational model also used for research purposes). He ran and evaluated the experiments on which this work was based.

Prof Icarus Allen

Plymouth Marine Laboratory
Head of Science - Marine ecosystem models and predictions

R-2-III

Hi John,

I am sketching some words (see attached) with regards to the paper contribution.

So far it's an extremely short sketch and general rather than in being in anyway specific, but maybe that is all that is needed?

Or do you feel they want things to be more elaborated where I go point by point (the other extreme)

through the paper about where you fit in?

I can't comment on the data assimilation part of the paper as that was Jame's work.

Cheers,
Enda.

John Siddorn's contribution to:

O'Dea, E.J., Arnold, A.K., Edwards, K.P., Furner, R., Hyder, P., Martin, M.J., Siddorn, J.R., Storkey, D., While, J., Holt, J.T. and Liu, H. (2012) An operational ocean forecast system incorporating NEMO and SST data assimilation for the tidally driven European North-West shelf. Journal of Operational Oceanography, 5, 3-17

John Siddorn's contribution to the paper was twofold both supervisory and technical. John's oversight helped to guide the experimental design of the model runs that underpin this paper. He also acted as the primary reviser of the text facilitating the evolution of a coherent, succinct and clear story for publication.

With respect to the model runs, not only did John participate in guiding the overall experimental plan for the broad brush strokes of the work but also helped overcome individual technical matters in the details as and when the need arose.

John's broader and longer background in ocean sciences was particularly valuable in the writing stage which helped me precipitate my nebulous thoughts and arguments into a logical self contained configuration paper that has since acted as a point of reference for many subsequent studies.

Ref: Hyder et al 2012

1) Hyder, P., Storkey, D., Blockley, E., Guiavarc'h, C., Siddorn, J., Martin, M. and Lea, D. (2012) Assessing equatorial surface currents in the FOAM Global and Indian Ocean models against observations from the global tropical moored buoy array. Journal of Operational Oceanography, 5(2), 25-39.

John provided an invaluable contribution to this paper concerning advice on: Equatorial dynamics and its representation in ocean models; Potential sources of model forcing error; Sampling and observational uncertainty; Inferences derived from model errors; and Structure and wording for the paper. He was the team scientific manager at the time of the work.

2) P Hyder; J While; A Arnold; E O'Dea; R Furner; J Siddorn; M Martin; P Sykes (2013). Evaluating a new NEMO-based Persian/Arabian Gulf tidal operational model. Journal of Operational Oceanography, 6(1) 3-16.

John provided an invaluable contribution to this paper concerning advice on Persian Gulf tidal and non-tidal dynamics and their representation in ocean models; Potential sources of model forcing error; Sampling and observational uncertainty; Inferences derived from model errors; and Structure and wording for the paper. He was the team scientific manager at the time of the work.

Dr Patrick Hyder
Senior Scientist, Ocean Modelling

R-3-I

Hi John,

Is this OK? Let me know if you need it in Word format or something.

Cheers,

Dave

Storkey, D., Blockley, E. W., Furner, R., Guiavarc'h, C., Lea, D., Martin, M. J., Barciela, R. M., Hines, A., Hyder, P., and Siddorn, J. R.: *Forecasting the ocean state using NEMO: the new FOAM system*, Journal of Operational Oceanography, 3, 3–15, 2010.

This paper describes the first version of the FOAM system based on the NEMO ocean model. John was scientific leader of the team that transitioned the FOAM system to using NEMO and hence was ultimately responsible for the scientific choices made in the set up of the system and described in the paper. He also provided invaluable advice on the structure and contents of the paper and provided helpful comments in the review process before it was submitted.

R-3-III

Hi John,

I hope you are well. i have been very busy here running and evaluating the prototype GO6.0 run and a few sensitivity runs, and hopefully will have a chance to do some of my own science again soon...

How about this:

John Siddorn's role in the GO5.0 evaluation paper

John was the overall manager of the JOMP project, which generated the GMD GO5.0 paper (see below). This meant that he took a leading role in planning the sensitivity experiments described in the paper, and had the main responsibility for decisions on the final GO5.0 model configuration. He had a significant input in the development of the structure of the paper, particularly in the section on attribution, and played an important role in gathering together the contributions of the Met Office authors.

Megann, A., Storkey, D., Aksenov, Y., Alderson, S., Calvert, D., Graham, T., Hyder, P., Siddorn, J., and Sinha, B. (2014) GO5.0: The joint NERC-Met Office NEMO global ocean model for use in coupled and forced applications, *Geosci. Model Dev.,* **7**, 1069–1092, doi:10.5194/gmd-7-1069-2014.

Regards,

Alex

Annex B: Contributing Papers

Ocean Modelling

An analytical stretching function that combines the best attributes of geopotential and terrain-following vertical coordinates

J.R. Siddorn *, R. Furner

Met Office, FitzRoy Road, Exeter EX1 3PB, United Kingdom

ABSTRACT

This work provides a function for discretising the vertical coordinate in ocean models that is designed to allow the user to define a fixed surface resolution, as one can in geopotential coordinate models, whilst retaining the benefits of terrain-following coordinates. This formulation has been termed the γ stretching function and provides an analytical solution that, in contrast with hybrid schemes, allows gradual coordinate changes in the vertical and horizontal. The early part of the paper describes the theoretical framework in which this can be done. Following this a series of steps that are required to effectively implement the coordinate have been described, and a full description of the implementation for a shelf model, the Forecasting Ocean Assimilation Model (FOAM) Atlantic Margin Model (AMM7), is given.

This implementation is then used to quantify the impact of the γ stretching compared with the current stretching scheme. This shows the new stretching to have improved slope and hydrostatic consistency parameters. As would therefore be expected the γ stretching is shown to give rise to reduced horizontal pressure gradient errors in an idealised seamount test case. The benefits of a constant and shallow box for air–sea exchange are demonstrated, with the γ stretching giving enhanced diurnal ranges, increased sea surface temperatures and shallower mixed layer depths where the FOAM AMM7 is presently unable to well represent these properties.

Crown Copyright © 2013 Published by Elsevier Ltd. All rights reserved.

1. Introduction

Oceanic processes are either explicitly modelled or implicitly parameterised depending upon whether they are resolved by the model. This requires ocean model scales to be consistent with the natural length-scales of the ocean. If this is not the case then formulations and parameterisations can become ill-posed. These length-scales vary in both space and time, and one of the challenges for ocean modellers is to choose appropriate grids to allow the model scales to match those in the real world for the processes being modelled. If the model scales vary they should do so consistently with the natural scales of the ocean, otherwise the model solution becomes inconsistent. Although considerable effort is made to improve the way we formulate ocean processes in our models, when considering the impact upon the quality of ocean model simulations the choice of vertical coordinate is the single most important factor (Chassignet et al., 2000; Haidvogel and Beckmann, 1999; Griffies et al., 2000). This paper describes a novel method for defining ocean model vertical coordinates that is designed to improve this alignment of scales between the ocean model and the real ocean.

Ocean models can be discretized in the vertical using geopotential, terrain-following, isopycnal or pressure-coordinate systems. A useful description of vertical coordinates is available in Song and Hou (2006). The aim of this work is to improve simulations using the Nucleus for European Modelling of the Ocean model (NEMO; Madec, 2008) and will therefore only consider geopotential and terrain-following coordinates, with isopycnal and pressure coordinates not being available in the NEMO framework. In particular, the aim is to improve the Met Office short-range forecasting model of the North–West European Continental Shelf (NWS), the Forecasting Ocean Assimilation Model Atlantic Margin Model at approximately 7 km (the FOAM AMM7, Fig. 1). A full description of the model is given in O'Dea et al. (2012). This is a three-dimensional baroclinic model using NEMO, that has stretched terrain-following coordinates based upon Song and Haidvogel (1994). It is nested into a geopotential coordinate eddy-resolving basin scale model of the North Atlantic, the FOAM NATL12 (Storkey et al., 2010).

Geopotential coordinates (commonly referred to as Z-coordinates) are the most commonly used vertical coordinate system, at least for deep ocean applications. The vertical coordinate is discretized onto fixed levels that are taken as a depth from a reference level. The vertical levels normally have different thicknesses which allows the resolving of surface mixing and upper ocean dynamics

* Corresponding author. Tel.: +44 (0)1392 886824.
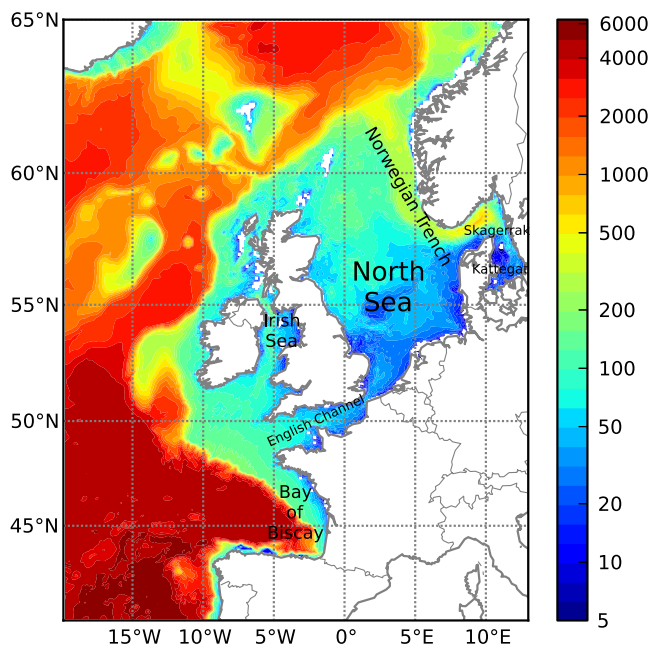 *E-mail address:* john.siddorn@metoffice.gov.uk (J.R. Siddorn).

Fig. 1. The bathymetry of the North–West European Continental Shelf (NWS), as used in the FOAM AMM7 model.

without the computational overhead of a large number of vertical levels. However, this schema does not allow a good representation of varying topography because the bottom slope becomes approximated by a series of steps. This leads to inaccurate representation of the bottom boundary layer through poor representation of kinematic conditions (Gerdes, 1993) and bottom pressure torques (Bell, 1999; Hughes and de Cuevas, 2001; Song and Wright, 1998). This leads to problems when representing the flow between shallow and deep waters (Roberts and Wood, 1997; Beckmann and Döscher, 1997) and hence leads to the poor representation of flows over sills and ultimately deep water formation. This has been partially mitigated through the use of partial or shaved-cell techniques (Adcroft et al., 1997; Pacanowski and Gnanadesikan, 1998).

Terrain-following coordinates, introduced as a concept for meteorological modelling by Phillips (1957), transform real space into a dimensionless computational domain bounded by the sea surface on the one hand and the sea bed on the other. This coordinate type is generally referred to as a σ-coordinate when the domain is equally divided or S-coordinate if some stretching is applied. Terrain-following coordinates are most commonly used in models that are predominantly designed for shelf or coastal applications, for example the Regional Ocean Modelling System (ROMS; Shchepetkin and McWilliams, 2005, 2009) and the Proudman Oceanographic Laboratory Coastal-Ocean Modelling System (POLCOMS; Holt and James, 2001) and have also been implemented in the NEMO model to allow its use for coastal applications. The major advantage of this system is that it follows the topography, and therefore naturally represents the bottom boundary conditions. However, as the coordinate is defined in computational space rather than real space it is not independent of local depth, and thus in applications where the topography being modelled varies significantly then so does the vertical resolution. Another significant downside with σ/S-coordinates is their use results in errors in the calculation of the horizontal pressure gradient, particularly over steep topography (Janjić, 1989; Haney, 1991). Recent advances in the calculation of horizontal pressure gradients (e.g. Shchepetkin and McWilliams, 2003) however have reduced these errors. The horizontal pressure force in σ/S-coordinates consists of two terms, the pressure force along the model coordinate and a correction term that depends on both the tilt of the

coordinate surface relative to the horizontal and the rate of change of the pressure in the vertical. This introduces an error that is a function of the S-coordinate slope and the stratification as well as model resolution, the equation of state, the form of the horizontal pressure gradient calculation and the finite difference scheme (Haney, 1991; Beckmann and Haidvogel, 1993). Other errors are also introduced when using sloping coordinates, due to what is often termed errors in hydrostatic consistency, whereby adjacent grid cells in coordinate space are not well aligned in real space.

A terrain-following coordinate, therefore, that minimises the coordinate slope, especially near regions of high stratification, would be expected to minimise computational errors. Similarly, a coordinate system that allowed enhanced resolution near areas of dynamic variability would allow these dynamic processes to be better resolved. For this reason stretching is applied. Atmosphere models have for many years used terrain-following coordinates, and there are a number of methods for stretching the coordinate. Schär et al. (2002), for example, developed a function that removes high frequency variability in the topography from the coordinate and hence significantly reduces numerical truncation errors. However, the ocean is fundamentally different to the atmosphere in that the range of depths in the ocean are the same as, or at least of the order of, the maximum depth (i.e. the depth of the water goes to zero) whereas in the atmosphere the variability in the orography is only a small proportion of the total modelled depth. This makes the stretching functions used in atmosphere models generally unsuited to use in oceans. Stretching functions have therefore been developed for ocean modelling, such as the commonly used function of Song and Haidvogel (1994) which is presently available within the NEMO framework. Mixed terrain-following and geopotential coordinates have also been used, for example Mellor et al. (2002) and Gerdes (1993), on which the NEMO implementation of mixed terrain-following and geopotential coordinates (Madec et al., 1996) is based. However, these mixed coordinate systems do not have smooth analytical solutions and thus have a tendency to generate large changes in vertical resolution. Treguier et al. (1996) demonstrates the need for smooth coordinate transformations if numerical accuracy is to be maintained. It is also desirable to minimise the rate of change of the coordinate to maintain modelled features and to minimise model errors, as also noted in Treguier et al. (1996). Similar results are found in studies on horizontal resolution, for example Spall and Holland (1991), in a study on horizontal propagation of waves. Therefore, coordinate systems which are not based on a smooth and gradually changing analytical stretching function are to be avoided.

Alternatively, σ/S-coordinates have been adapted to vanish through the sea bed in what Dukhovskoy et al. (2009) refer to as Vanishing Quasi-Sigma (VQS) coordinates. These coordinates, also available within NEMO, allow the σ-coordinate to follow a pseudo-bathymetry below the real bathymetry at times when the bottom slope becomes steep, reducing the coordinate slope and thus the pressure-gradients. This can be helpful, but in effect reverts the model to a stepped bathymetry in some regions and so reduces the benefit of having a terrain-following coordinate with regards to the bottom stress calculations.

Decisions on which coordinate system to use depend upon the application for which the model is intended. Applications on or including shelf waters tend to use S-coordinates to allow the interaction with the relatively shallow bottom to be well resolved. These coordinates give variable resolution at the surface leading to inconsistencies in the simulation of surface processes across the domain. The importance of this is obvious if using the ocean model for providing predictions of surface temperature or currents. It is also important in a coupled ocean–atmosphere system to provide consistent and realistic boundary layer conditions of

temperature and momentum to the atmosphere and to provide well-prescribed air–sea exchange of gases in an Earth System Model. The AMM7 is a shelf-wide model that spans depths from 10 m in coastal areas to 300 m across the shelf-break and into the deep ocean at greater than 5000 m (Fig. 1). The surface grid box depth in this model ranges over three orders of magnitude, resolving diurnal cycles in some parts of the domain and not in others. This means it does not optimally resolve the surface properties, and is not well suited for use as part of a coupled system. It also means that interpretation of the model solutions in the near surface is often difficult.

This is simply resolved by switching to using a Z-coordinate model, where the surface grid box depth is prescribed and, given sufficient numbers of vertical levels to allow a reasonable gradient in the cell thickness, can be set to whatever the modeller deems fit. A sensible surface depth can then be prescribed to explicitly resolve some processes (diurnal layers, wind driven surface flows) and allow for sub-grid scale parameterisation for others (i.e. heat exchange at the viscous scale, surface wave breaking). However, given the disadvantages of using Z-coordinates in the AMM region a better option would be to design a stretching function that allows terrain-following coordinates to emulate the fixed surface of Z-coordinates.

Burchard and Peterson (1997) gives a good description of the benefits of using terrain-following coordinates, and provides useful discussion on, for example, the improvement over geopotential coordinates to the bottom kinematic boundary condition. The benefits of well designed stretching functions are demonstrated in this paper, and their conclusion is that coordinate transformations that suit the specific problem should be designed. The terrain-following coordinates used in Burchard and Peterson (1997) and in some implementations of ROMS (Shchepetkin and McWilliams, 2009) go some way towards providing the surface stretching required to resolve the surface mixed layer, having formulations that in, deep water, allow constant surface grid resolutions. However in both cases the surface grid resolution is the critical depth divided by the number of vertical levels. This constrains either the surface resolution, the number of vertical levels or the critical depth and therefore limits their applicability.

This paper outlines an analytically derived, and thus smooth, vertical coordinate system that is terrain-following and allows a user defined surface and/or bottom grid box depth.

2. Methods

2.1. Defining the vertical coordinate

The vertical coordinate is defined in computational space such that:

$$z = \gamma(H + \zeta) - \zeta \quad \text{with} \quad 0 \leqslant \gamma \leqslant 1 \tag{1}$$

where z is the geopotential depth (positive downwards from the mean sea level), H is the total water depth and ζ is the free surface (positive upwards). γ is a function (derived below) of σ, and σ defines the unstretched coordinate space, indexed in the integer k from 0 to $n - 1$ to give n surfaces:

$$\sigma = \frac{k}{n-1} \quad \text{where} \quad 0 \leqslant k \leqslant n - 1 \tag{2}$$

The function γ is derived so that it meets the following constraints:

- the surface cell thickness (ΔZ_s) and bottom cell thickness (ΔZ_b) are user prescribed as real depths and included in the analytical function,

- the function allows user controlled stretching at the surface and bottom,
- the function is constrained to a monotonically increasing solution,
- the rate of change of cell thickness in both the horizontal and the vertical is minimised.

It is also desirable for the coordinate to converge on σ or Z-coordinates in shallow water.

A number of formulations were explored, for example based upon Song and Haidvogel (1994) and Pietrzak et al. (2002), but were found to be unable to give a reasonable analytical profile when the above constraints were applied over a wide range of depths. A constrained solution based upon the Song and Haidvogel (1994) formulation worked reasonably for a depth range of a few hundred metres, but required a prohibitive number of vertical levels to work for larger depth ranges. A new formulation has therefore been derived that has suitable characteristics. A number of other formulations may well be suitable and could be derived using similar methodologies.

2.2. The analytical solution

The solution for γ is derived by defining the differential of the stretched coordinate system. The function is formed of three parts. One is a function of $(1 - \sigma)$ and controls the stretch towards the surface. Another is a function of σ and controls the stretch towards the bottom. Additionally a function of $\sigma(1 - \sigma)$ and a dependent variable (X) is included to give the function flexibility, enabling it to meet the imposed constraints. This incorporates a user controlled stretching parameter (α) to give some control over the function shape. A number of variants on this functional form were explored, some of which could not be solved, gave overly complicated solutions or did not give adequate control over the function shape. After some trial and error the following form was found to be both mathematically solvable and effective.

$$\frac{d\gamma}{d\sigma} = A(1 - \sigma) + 3B\sigma^2 + X(\alpha + 1)(\alpha + 2)\sigma^\alpha(1 - \sigma) \tag{3}$$

Given the constraints at the surface, $\gamma = 0$ when $\sigma = 0$, and the bottom, $\gamma = 1$ when $\sigma = 1$, this can be integrated and solved for X, giving:

$$\gamma = A\left(\sigma - \frac{1}{2}(\sigma^2 + f(\sigma))\right) + B(\sigma^3 - f(\sigma)) + f(\sigma) \tag{4}$$

where:

$$f(\sigma) = (\alpha + 2)\sigma^{\alpha+1} - (\alpha + 1)\sigma^{\alpha+2}$$

The solution can be constrained to given specified surface (ΔZ_s) and bottom (ΔZ_b) grid cell thicknesses, as σ has known solutions at all values of k, and prescribing the surface and bottom cell thicknesses also therefore constrains γ at $k = 1$ and $k = n - 2$:

$$\gamma|_1 = \frac{\Delta Z_s}{D} \quad \gamma|_{n-2} = 1 - \frac{\Delta Z_b}{D}$$
$$\sigma|_1 = \frac{1}{n-1} \quad \sigma|_{n-2} = 1 - \frac{1}{n-1} \tag{5}$$

where

$$D = \begin{cases} H + \zeta & \text{for time varying } \gamma \\ H & \text{for constant } \gamma \end{cases} \tag{6}$$

Substituting the constraints defined in Eq. (5) into Eq. (4) allows a unique solution to be found for A and B:

$$A = \frac{1 - \frac{\Delta Z_b}{D} - \lambda_3\left(\frac{\Delta Z_s}{D} - \lambda_1\right) - \lambda_2}{n_2 - \frac{1}{2}(n_2^2 + \lambda_2) - \lambda_3\left(n_1 - \frac{1}{2}(n_1^2 + \lambda_1)\right)} \tag{7}$$

$$B = \frac{\frac{\Delta Z_s}{D} - \lambda_1 - A\left(n_1 - \frac{1}{2}\left(n_1^2 + \lambda_1\right)\right)}{n_1^3 - \lambda_1} \tag{8}$$

where:

$$n_1 = \frac{1}{n-1}$$

$$n_2 = 1 - \frac{1}{n-1}$$

$$\lambda_1 = (\alpha + 2)n_1^{\alpha+1} - (\alpha + 1)n_1^{\alpha+2}$$

$$\lambda_2 = (\alpha + 2)n_2^{\alpha+1} - (\alpha + 1)n_2^{\alpha+2}$$

$$\lambda_3 = \frac{n_2^3 - \lambda_2}{n_1^3 - \lambda_1}$$

So that the coordinate stretching does not have to be recalculated at every timestep a time invariant solution for γ can be found if D is taken to be equal to H (see Eq. (6)). In a non-linear free surface model this will result in differences in the surface and bottom depths from the prescribed values of ΔZ_s and ΔZ_b as ζ changes and z is recalculated (see Eq. (1)). The impact is normally small and so for many applications this approximation would be appropriate.

The water depth at the coordinate surface is now fully described with Eqs. (1), (2) and (4) in terms of the user-prescribed parameters, ΔZ_s, ΔZ_b, α and n and the water depth, H.

One of the potential criticisms of any vertical coordinate solution that is heavily constrained would be that the user control of the coordinate is potentially reduced. That would appear at first glance to be the case in the γ stretching. However, the stretching is formulated such that the extent and position of the stretching are a function of α. If α is unity, there is no stretching except that required by the definitions of ΔZ_s and ΔZ_b, if it is less than unity the coordinate gives greater resolution in the surface and less towards the bottom, and vice versa if greater than unity. This allows the user to recreate pure σ-coordinates in the special case where ΔZ_s and ΔZ_b are both equal to $\frac{H}{n-1}$. Fig. 2 shows the impact of changing α in the case where ΔZ_s and ΔZ_b are equal, and in the case where additionally both are equal to $\frac{H}{n-1}$, and shows the stretching towards the surface for $\alpha > 1$ and towards the bottom for $\alpha < 1$.

The γ function described here will work in waters of all depths, although may produce undesirable stretching if not applied carefully. The following section describes how to constrain the coordinate solution so that it can be used in practice.

2.3. Constraining the solution

2.3.1. Shallow water

In shallow water, where the prescribed surface and bottom depths become large relative to $\frac{H}{n}$, the stretching will result in a coordinate that increases in resolution away from the surface/seabed. It is therefore desirable that in water depths shallower than some critical depth H_c the coordinate is treated differently to prevent this. Two options are considered, the coordinate transitioning to σ-coordinates or to Z-coordinates. This is simply done by applying the following transformation at depths less than the critical depth (H_c):

$$z|_{H<H_c} = \begin{cases} \sigma(H + \zeta) & \text{for } \sigma \text{ coordinates} \\ \sigma(H_c + \zeta) & \text{for } Z - \text{coordinates} \end{cases} \tag{9}$$

The Z-coordinate form requires the vertical coordinate system to be able to deal with inactive cells in a stretched coordinate framework. The advantage of this over the σ approach is that it keeps a prescribed surface/bottom resolution, although it has the

problems in resolving the bottom boundary associated with Z-coordinate models discussed previously. Chosing a σ-coordinate in the shallow water will allow improved model solutions at the expense of increasing the resolution at the surface and hence potentially creating inconsistent air–sea exchange.

To ensure a gradual transition from the shallow to deep formulations H_c should be approximately $n\left[\frac{\Delta Z_s + \Delta Z_b}{2}\right]$. To prevent sharp changes in the coordinate smoothing must be applied around H_c, as a function of $H - H_c$. This is achieved by stipulating that for $H \geqslant H_c$:

$$z|_{H \geqslant H_c} = \gamma(H + \zeta)\left[\tanh\left(\frac{H - H_c}{e}\right)\right] + \sigma(H + \zeta)\left[1 - \tanh\left(\frac{H - H_c}{e}\right)\right] \tag{10}$$

where e is a transition length scale. It is worth noting that the vertical coordinate will differ from the prescribed surface and bottom resolutions close to H_c, and the extent to which it does so depends on the length scale e and the change in ΔZ_s and/or ΔZ_b at H_c.

2.3.2. Deep waters

In waters of depth greater than the critical depth, H_c, the analytical solution described in Eqs. (4) and (10) are used. These satisfy many, but not all, of the criteria for the coordinate system. The solution does not give a monotonically increasing value of γ in all cases. Nor does it always give a gradually varying grid cell size in either the vertical or horizontal dimensions.

To ensure a monotonically increasing solution the following must be true.

$$\gamma_{k+1} - \gamma_k > 0 \tag{11}$$

Similarly, for the solution to be gradually increasing in the vertical, to a given tolerance (χ), the following must also be true:

$$\left|\frac{\gamma_{k+1} - \gamma_k}{\gamma_k - \gamma_{k-1}} - 1\right| < \chi \tag{12}$$

A tolerance of approximately 30%, or $\chi = 0.3$ gives vertical changes in grid size of a similar order to those used presently in the Met Office Z-coordinate and S-coordinate models. The smaller the value of χ chosen (strong constraint) the slower the vertical coordinate can change, and hence the more limited the coordinate becomes. The larger χ (weak constraint) the greater the range of thicknesses that can be chosen for the surface and bottom box. However with the increased rate of change in model resolution it is harder to preserve wave like features (Spall and Holland, 1991) and with large variations in resolution between adjacent coordinates comes increased errors (Treguier et al., 1996).

The above criteria are not straightforward to apply analytically, but can be used to define the range of acceptable input values for the user controlled parameters. In practice the value for n will be limited by the computational cost of the solution and for most applications ΔZ_s will be expected to be constant to ensure consistent representation of air–sea exchange processes. Once n and ΔZ_s have been chosen, it is therefore neccessary to explore the acceptable parameter ranges for ΔZ_b and α, given the constraints on monotonicity and rates of change given in Eqs. (11) and (12). Selecting ΔZ_b and α within these ranges leaves all criteria met except the stipulation that the stretching minimises the rate of change of the coordinate for adjacent cells in the horizontal. The variations between heights of adjacent grid cells is determined by a combination of the stretching and the variation in the bathymetry. The shape of the stretching function determines how much of an impact this will have. It is possible to create a coordinate with undesirable oscillations in the horizontal coordinate which are unrelated to changes in the bathymetry. These are caused by changes in the user defined variables and so can
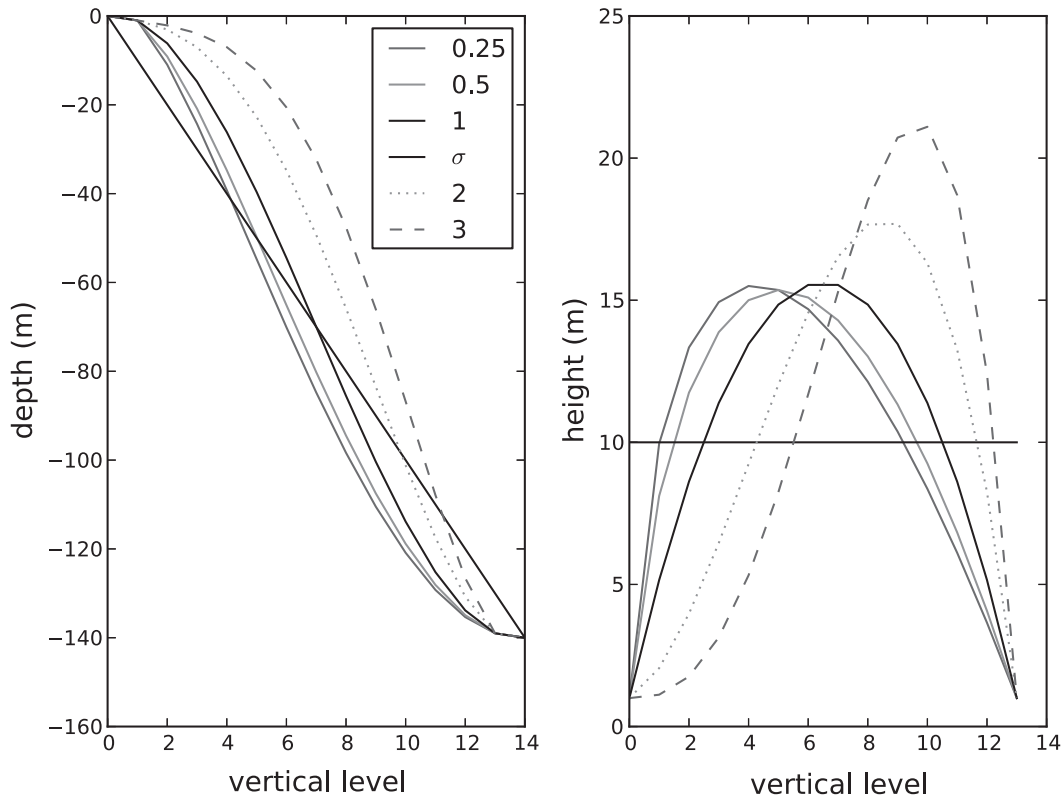
Fig. 2. The change in the vertical coordinate with change in α. Shown on the left is the depth of the coordinate in a 140 m water column where 15 levels are used, and on the right is the corresponding cell height. Surface and bottom cell thicknesses are fixed at 1 m for all cases expect that labelled σ, which has ΔZ_s and ΔZ_b set at 10 m $\left(\frac{1}{n-1}\right)$. The values used for α are shown in the figure legend, except for the σ case where it is 1.0.

be prevented by ensuring that ΔZ_s, ΔZ_b and α either remain constant or vary gradually as a function of bathymetric depth. The fewer variations in the user defined parameters the better, and it is recommended that only one input parameter be allowed to be non-constant. Some experimentation of the sensitivity to these parameters for a new configuration would be needed and the resultant coordinate should be carefully checked.

An example of the sensitivity to the choice of values for α and ΔZ_b has been explored in an idealised case where the bathymetry ranges from 50 m to 5500 m (Fig. 3). The number of vertical cells used is 50 and the surface resolution (ΔZ_s) is 1 m. The figure compares the thickness of the bottom grid cell (ΔZ_b) for three coordinates, a geopotential coordinate used in FOAM for deep ocean modelling that has a 1 m surface resolution and 50 vertical levels (labelled L50), a terrain-following coordinate based upon Song and Haidvogel (1994) stretching as used in the AMM7 model (labelled SH94; for comparability this example uses 50 levels rather than the 34 used by the AMM7) and the γ stretching with three different prescribed values for α. It should be noted that in geopotential-coordinate FOAM applications the partial-cells technique is used so the effective bottom grid depth will be smaller than shown here. The maximum and minimum possible values for ΔZ_b in the γ stretching given $n = 50$, a surface resolution of 1 m ($\Delta Z_s = 1.0$), stipulation of monotonicity (as given in Eq. (11) and a χ of 0.3 (Eq. (12)) are shown (Fig. 3) giving the envelope of acceptable values for ΔZ_b given the prescribed ΔZ_s and α values.

The choice of α determines the range of ΔZ_b which is allowable given the constraints applied and vice versa (Fig. 3). It is notable that in this case no one value of ΔZ_b can be used across all depths, which is not surpising given ΔZ_s is relatively small and fixed, and there is a large range of depths being tested. ΔZ_b would have to therefore vary as a function of water depth; it has already been
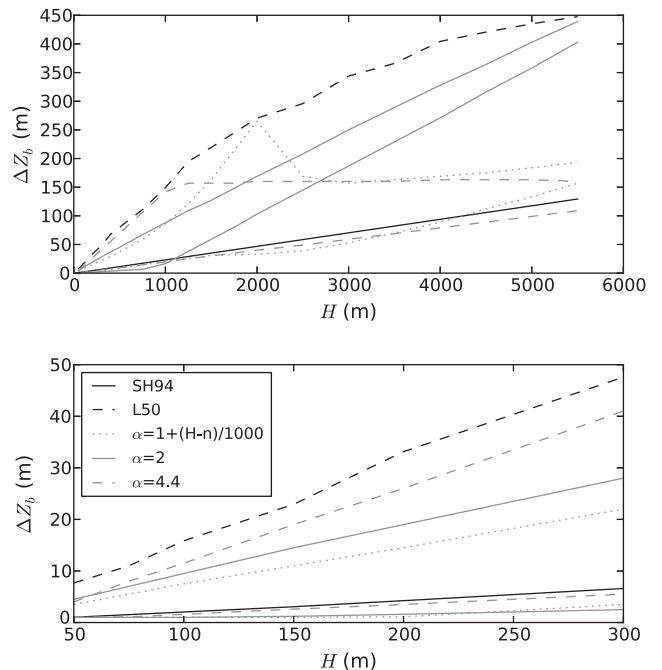

Fig. 3. Thickness of the bottom cell, ΔZ_b, for a given total water depth, H, for a Song and Haidvogel (1994) stretched coordinate (SH94, solid black line), a Z-coordinate (L50, dashed black line) and three different γ stretching setups (grey lines). For the three γ stretches two lines for each are plotted giving the maximum and minimum bounds for ΔZ_b for a χ of 0.3, ΔZ_s of 1.0 m and different values of α (see legend). All coordinates use 50 vertical levels. The plot on the top shows the full range of depths tested, and the bottom plot only shelf-slope depths

noted above that it is desirable to introduce as little heterogeneity into the parameter space as possible. If the use of a constant value for α does not give desirable stretching then one would question whether the number of vertical levels is sufficient, or whether the surface grid resolution should be relaxed. Given the input parameters prescribed above, although the spatially varying α gives some benefits over the other solutions, it is actually rather similar to the $\alpha = 4.4$ solution, and therefore setting a constant α would be sensible in this case.

In Fig. 3 the ranges of the bottom resolution allowable can be described as L50-like with $\alpha = 2$ and SH94-like with $\alpha = 4.4$. They both allow high resolution at the bottom in shallow water and down to the bottom of the shelf slope. The key difference is the SH94-like option keeps the resolution relatively high at the bottom, mimicking the SH94 solution in deep water, whereas the L50-like solution transitions to give a solution similar to the FOAM L50 model in deep water.

3. Results

3.1. Model description

The primary motivator for this work is to improve the vertical coordinate in a tidal model, the AMM7 (O'Dea et al., 2012), that covers a region of the ocean that includes deep water in the North Atlantic and in the Norwegian Trench but is primarily run to produce forecasts for the wide, shallow European North–West Shelf itself. Traditional Z-coordinate systems have inherent weaknesses for this and similar domains, namely that Z-coordinates require a large number of vertical coordinates to adequately resolve all waters, and the bottom boundary condition is poorly represented, and so σ/S-coordinates are generally used. However these are unable to give a consistent and high resolution surface coordinate. The AMM7 uses an S-coordinate following Song and Haidvogel (1994) (SH94):

$$-z = sH_c + C(s)(H + \zeta - H_c) \tag{13}$$

where

$$s = -\frac{k}{n-1} \quad \text{where} \quad 0 \leqslant k \leqslant n-1 \tag{14}$$

$$C(s) = (1-b)\frac{\sinh(\theta s)}{\sinh(\theta)} + b\frac{\tanh\left[\theta\left(s+\frac{1}{2}\right)\right] - \tanh\left(\frac{\theta}{2}\right)}{2\tanh\left(\frac{\theta}{2}\right)} \tag{15}$$

In the AMM7 the parameter settings used are $\theta = 6, H_c = 150m$ and $b = 0.8$. The critical depth of 150 m is chosen to give stretching in the surface mixed layer. To prevent the coordinate going non-monotonic at depths less than H_c the coordinate is forced to pure σ in these regions.

A non-linear free surface using variable volume, and time-splitting with leap-frog time stepping, is used. The baroclinic time step is 150 s and the barotropic sub-cycle time step is 5 s. The momentum advection is both energy and enstrophy conserving and the lateral boundary condition on the momentum is free-slip. Horizontal diffusion of momentum is specified using both laplacian and bilaplacian operators. The laplacian diffusion is applied on geopotential surfaces to prevent spurious mixing in the vertical, and bilaplacian diffusion is applied on model levels to retain stability. The coefficients of laplacian and bilaplacian diffusion are $30.0\ \text{m}^2\ \text{s}^{-1}$ and $1.0 \times 10^{10}\ \text{m}^4\ \text{s}^{-2}$ respectively. The Total Variance Dissipation (TVD) advection scheme is used. The tracer diffusion operator is only laplacian and operates along geopotential levels. The tracer diffusion coefficient is $50\ \text{m}^2\ \text{s}^{-1}$.

A pressure Jacobian method for calculating the horizontal pressure gradient following Shchepetkin and McWilliams (2003) is

used, and is described in detail in O'Dea et al., 2012. Vertical turbulent viscosities/diffusivities are calculated using the Generic Length Scale (GLS) turbulence model (Umlauf and Burchard, 2003). The second-moment algebraic closure model of Canuto et al., 2001 is solved with the two dynamical equations for the turbulence kinetic energy (TKE) and TKE dissipation. Neumann boundary conditions on TKE and TKE dissipation are applied at the surface and sea bed and surface wave mixing is parameterised (Craig and Banner, 1994). The dissipation is limited under stratification using a limit of 0.267 (Galperin et al., 1988). The bottom friction uses a spatially varying log layer based drag coefficient with a minimum drag coefficient set at 0.0025.

The AMM7 uses the North–West Shelf Operational Oceanographic System (NOOS) bathymetry (Fig. 1), which is a combination of GEBCO 1' data and a variety of local data sources from the NOOS partners. The 1 nm resolution source data is gridded onto the AMM7 domain using a volume-conservative box averaging. The bathymetry is not smoothed but the vanishing quasi sigma (VQS) coordinates discussed in the introduction are usually used. This results in the terrain-following coordinates disappearing into the seabed in high slope regions, reducing the slope of the coordinates. In this work the VQS option has not been used to simplify interpretation of the results.

At the open boundaries tidal energy enters the domain via a Flather (1976) radiation boundary condition specified using fifteen tidal constituents for the depth mean velocities and sea surface elevation. The equilibrium tide is also specified. In addition to the tidal boundaries the model is one-way nested to a $\frac{1}{12}^\circ$ deep ocean model for the North Atlantic.

Differences can be seen between SST fields from the AMM7 and those from the geopotential-coordinate FOAM model into which it is nested, which includes both SST and temperature profile data assimilation. Although the model used to provide boundary conditions is different in a number of ways to the AMM7 (for example as it uses a different turbulence scheme and does not include tides) none of these differences is likely to account for the difference in the SST solution, which is thought to be caused by the poor surface resolution.

Another known issue with the AMM7 is that water masses coming from the shallow Skagerrak/Kategatt region are not well resolved where they flow from the shallow regions of the southern Kattegat, into the considerably deeper waters of the Skagerrak and on into the Norwegian Trench. This impacts upon the stratification in the Norwegian Trench and has both a local effect on the quality of temperature and salinity forecasts and an indirect impact on the quality of the simulations in the adjacent North Sea. The γ stretching is therefore in this example primarily proposed to maintain surface and near-surface resolution across a wide range of depths whilst maintaining the terrain-following bottom box.

3.2. The stretched coordinate for a shelf application

The methodology described in Sections 2.2 and 2.3 above has been used to create a γ stretching for use in the AMM7 model described in Section 3.1. The choice of surface resolution is relatively straightforward as 1 m is, after Bernie et al. (2005), considered optimal for resolving diurnal cycles and also matches the Z-coordinate models used in the Met Office and elsewhere. The number of vertical levels required to get a reasonable coordinate given the constraints of having a 1 m surface has been found to be a minimum of approximately 50. The three cases for different values of α shown in Fig. 3 all have potentially useful properties. Simulations (not shown) with the L50-like bottom resolution indicate that the loss of resolution at the bottom is undesirable.

The use of $\alpha = 4.4$, given the potential to have high resolution at the bottom and the surface, has been chosen as optimal for the AMM7. This allows the specification of ΔZ_b to be prescribed within the limits allowable with a χ of 0.3 as a function of the local water depth. The parameters used are $n = 51$, $\Delta Z_s = 1$ and $H_c = 50$, and $\Delta Z_b = 1$ at the critical depth, so that the γ and σ solutions are equal at the critical depth. In this case Eq. (10) is not neccessary, and an efold number (e) of zero is used. In shallow waters ($H < H_c$) it has been chosen to revert to σ-coordinates, rather than the pseudo-Z-coordinate. To maintain the required resolution whilst maintaining a smooth coordinate the following linear function in water depth has been chosen for ΔZ_b:

$$\Delta Z_b = 0.024H - 0.2 \quad \text{for} \quad H > H_c \quad (16)$$

To reduce computational cost the approximation of $D = H$ given in Eq. (6) is used for the remainder of this work, with the stretching function γ calculated only once during model initialisation. The geopotential depth (z) is then calculated at every timestep using Eq. (1) as is currently the case for standard AMM7 simulations using the non-linear free surface option in NEMO. Therefore although the stretching function is not altered throughout the simulation, the coordinate itself is updated at each time step and "breathes" with the free surface. This results in the size of the surface and bottom box varying with ζ, and therefore not remaining the same as the the user defined values ΔZ_s and ΔZ_b, respectively. However in relatively deep waters (where the stretching is applied) ζ can be assumed to be small relative to H and so the impact of not recalculating γ at each timestep upon the grid sizes will also be small. In applications where a strict adherence to the values of ΔZ_s and ΔZ_b is required this can be achieved by taking $D = H + \zeta$ in Eq. (6), and recalculating the stretching function γ at each time step.

This implementation of the coordinate gives bottom resolutions very similar to those found in Song and Haidvogel (1994) (SH94), as used in the present AMM7 configuration (although with 50 levels), and is used for all the following experiments.

The resultant vertical coordinate for the Song and Haidvogel (1994) stretched coordinate (SH94), the Z-coordinate from FOAM (L50) and the γ stretching have been calculated for an idealised bathymetry (Figs. 4 and 5). This shows the γ stretching has achieved the primary aim of maintaining high, and constant, resolution at the surface whilst maintaining the relatively high resolution near the bottom in shallow and intermediate waters. The coordinate gives the same resolution near the surface as the FOAM

L50, which is a significant improvement on the SH94 stretching. The impact on air–sea exchange of using the γ over the SH94 formulation is shown in Section 3.5. It also gives better resolution than the FOAM L50 throughout the watercolumn in shallow and intermediate depth water, and keeps similar bottom resolution to the SH94 throughout the domain. It should also be noted that both the SH94 and the γ stretching give sloped coordinates, and there are noticable changes in the slope at their critical depths (150 m and 50 m, respectively). It is important to understand the potential impact of the sloping surfaces. Section 3.3 investigates this in more detail. An idealised test case is presented in Section 3.4 that investigates the impact of the sloping surfaces upon the horizontal pressure gradient error.

3.3. Quantifying the coordinate slope

Although stretching the coordinate be may desirable to generate increased resolution where it is required, this may come at the expense of increasing the slope of the coordinate and hence impacting upon the model's numerical accuracy. To understand this better a hydrostatic consistency parameter following Haney (1991) has been reformulated to deal with the stretched coordinate:

$$r = \frac{2}{H} \frac{\Delta x}{\Delta z} \frac{\partial_x(SH)}{\partial_z S} \quad (17)$$

where S denotes the coordinate in computational space, and could be the σ or SH94/γ stretched coordinate. The maximum value for the four horizontal directions is taken as the value of r for that point. An r of greater than unity formally violates hydrostatic consistency. It should be noted however that σ/S-coordinate models rarely meet this criteria. The aim is to therefore minimise the value of r, not to prevent the violation of hydrostatic consistency entirely.

A slope parameter, s, following Beckmann and Haidvogel (1993), but adapted for stretched terrain-following coordinates and therefore calculated at each depth level, is an alternative measure.

$$s = \Delta x \left| \frac{\partial_x(SH)}{H} \right| \quad (18)$$

As with the hydrostatic consistency factor, the slope parameter is calculated in all horizontal directions, and the maximum slope used. This slope factor is a measure of the resolution compared to the bathymetric variability and its range is $0 < s < 1$, with
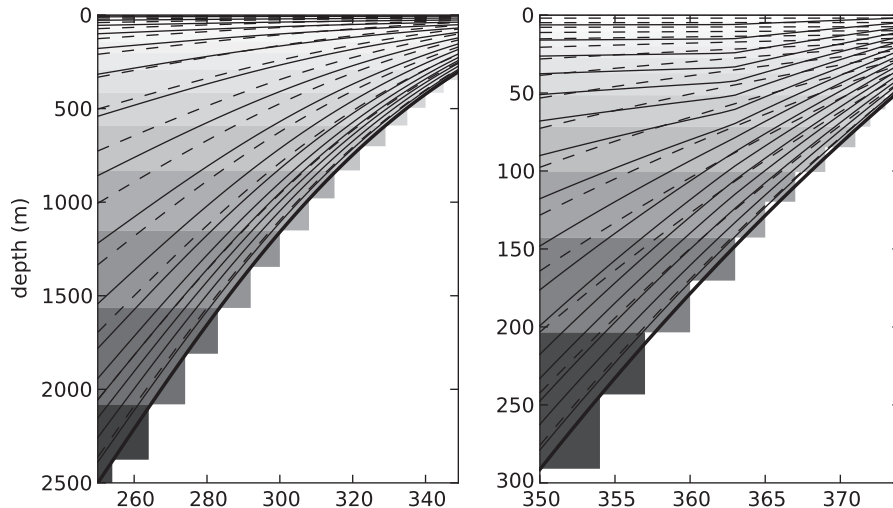

Fig. 4. A comparison of the SH94 stretching (solid lines), the L50 Z-coordinate (contoured surfaces) and the γ stretching (dashed lines) for a idealised bathymetry. For clarity every third coordinate surface is shown. The plot on the left shows waters from 500 m to 2500 m in depth and on the right from 50 m to 300 m.
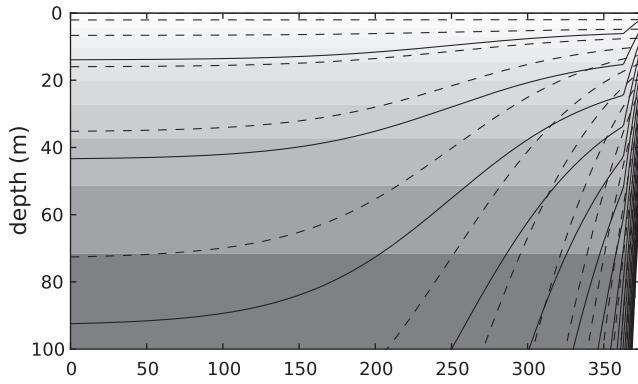
Fig. 5. A comparison of the SH94 *S*-coordinate (solid lines), the L50 *Z*-coordinate (contoured surfaces) and the γ stretching (dashed lines) in the surface 100 m for a idealised bathymetry that goes from 50 m to 5500 m depth. For clarity every third coordinate surface is shown.

values of zero when there is no slope (i.e. the resolution is infinite relative to the bathymetric variability) and is unity when the vertical change in depth for adjacent grid cells is the total water depth.

The γ and SH94 stretching are compared using the slope factor (s) and hydrostatic consistency (r) on the AMM7 domain with 50 levels and on the seamount domain described in 3.4. The γ and SH94 stretching parameters used are described in Section 3.2. As these coordinates are stretched the values of r and s are a function of depth, and so for simplicity of interpretation the maximum and the mean over depth have been calculated. The maxima of both of these properties are generally found at the sea bed, and so in the case where the coordinate is matched at the bottom (as in this case) the maximum is similar and so is not shown. Both the hydrostatic consistency and the slope parameter show qualitatively similar results, with the γ stretching giving considerably smaller values than the Song and Haidvogel (1994) setup. Both the slope factor and hydrostatic consistency increase up the slope of the sides of the seamount, reaching a maximum where the seamount flattens off (Fig. 7). The difference in the coordinates is also clearly evident in the comparison on the AMM domain Fig. 6 with the γ stretching showing significantly smaller values over steep
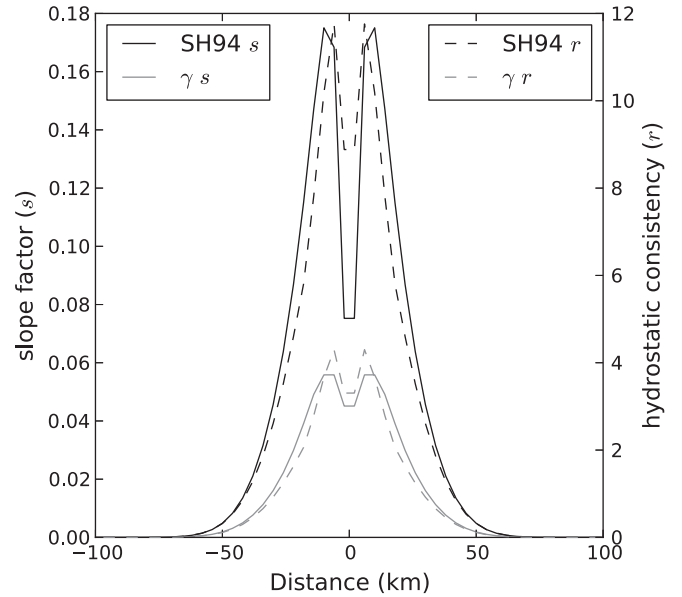
Fig. 7. The depth mean hydrostatic consistency, r, and slope parameter, s, for the γ and SH94 stretching for an idealised seamount with 50 levels.

bathymetry (see Fig. 1) such as along the shelf slope, the Norwegian Trench, the Faroe Isles and the Rockall Bank, where both the coordinate systems have maximum hydrostatic consistency and slope factors. The SH94 stretching also has significant areas onshelf where the values are much higher than the γ stretching, due to its use of σ-coordinates in less than 150 m of water. In shallow waters (less than 50 m, for example in the southern North Sea) both stretching functions give the same (relatively high) values, as would be expected as both use σ-coordinates in these regions.

It is not obvious that the γ stretched coordinate should neccessarily have better slope or hydrostatic consistency parameters than the SH94 stretched coordinate, and one could envisage situations where the reverse might be the case. The reason in this case it does is that (a) the surface resolution is constant and hence the coordinate is flatter near the surface in γ than SH94 stretched coordinates
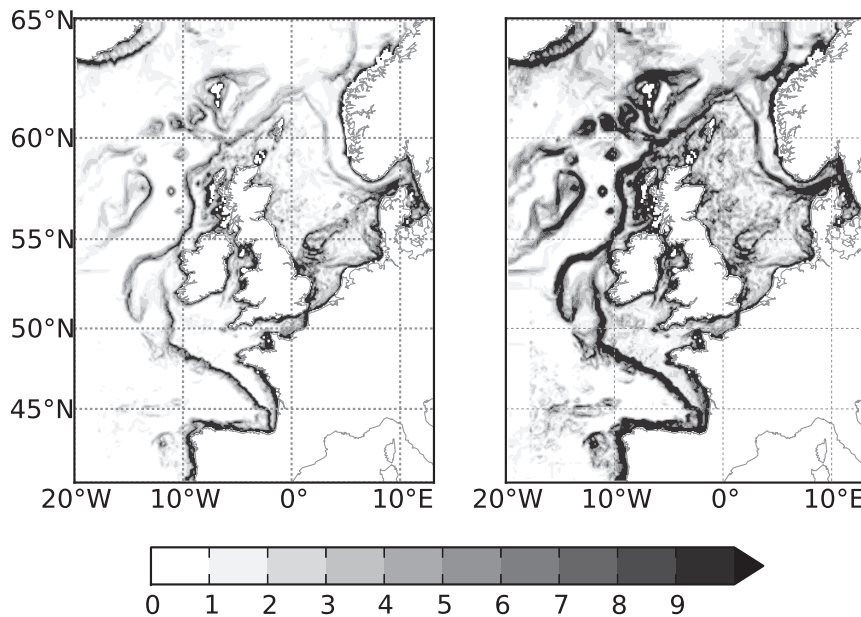
Fig. 6. The depth mean hydrostatic consistency, r for the γ (left) and SH94 (right) stretching for the AMM7 domain with 50 levels.

(b) the bottom resolution is the same in both coordinates and hence they have similar slopes towards the bottom and (c) the maximum vertical rate of change in the γ stretched coordinate has been constrained to be similar to the maximum rate of change in the SH94 stretched coordinate. This combination prevents the maximum slope or hydrostatic consistency being worse than in the SH94 case and, given the small surface slopes, ensures the mean slopes remain smaller.

The smaller slopes, especially in the surface waters where the pressure gradients are large, would be expected to give improvements in the horizontal pressure gradient errors. This is explored in the following section.

3.4. A horizontal pressure gradient error test case

It has been hypothesised above that the γ stretching proposed in this paper, being flatter than the SH94 stretching near the surface and hence in regions of high stratification, should result in reduced horizontal pressure gradient errors. This was tested for in an idealised seamount test case similar to that used by Beckmann and Haidvogel (1993). No external forcing was applied, and lateral boundaries were clamped to the initial condition, for a mid-latitude ($\sim$50°N) seasonally stratified ocean model with horizontal resolution of approximately 7 km. No explicit horizontal or vertical diffusion was applied. Any velocities that occur in the simulations must therefore be as a result (directly or indirectly) of the horizontal pressure gradient errors.

The simulations were started from rest and initialised with a constant salinity profile, and a prescribed temperature profile of:

$$T_z = 5\left(1 - \tanh\left(\frac{z-120}{20}\right)\right) + 10\left(\frac{5500-z}{5500}\right)$$

This gives a mixed layer of around 120 m and similar Burger number to that of Beckmann and Haidvogel (1993). Two simulations were run, one with SH94 and one with γ stretching as described in Section 3.2. The results are not shown here but confirm the hypothesis that at least in this idealised case the γ stretching gives lower mean and maximum velocities. The SH94 solution gives a very similar outcome to those presented in Beckmann and Haidvogel (1993), with domain maximum velocities spinning up quickly to give a domain maximum speed of 1 cm/s. These maxima oscillate over time at the inertial period of just under 16 h, settling down to give a maximum speed of around 0.6 cm/s. The simulations using the γ stretching give quite different results, with the initial error being less than half that for the S-coordinate, and with insufficient velocities generated to sustain the oscillations. The γ simulation reaches a state where no oscillations occur and the maximum velocities were an order of magnitude smaller than for the SH94 simulation. This is a result of both the generally flatter coordinates with the γ stretching and the fact that the coordinate surfaces are most flat towards the surface, where maximum gradients in pressure occur.

The same experiments were then run on the AMM7 domain (Fig. 1) to learn more about how these changes would translate to our operational models. The density profile used was similar to that described above, but with the initial temperature and salinity profiles as used in Section 3.5 to be representative of the AMM7 domain.

The southern Bay of Biscay is a particular problem to model in terrain-following coordinates as the bathymetry goes from depths of order 1000's to 10's of metres in a few grid cells. Normally this is mitigated by using the hybrid, or vanishing (VQS), coordinates, but as these are not used in these simulations the region south of 44°N has been removed from the analysis.
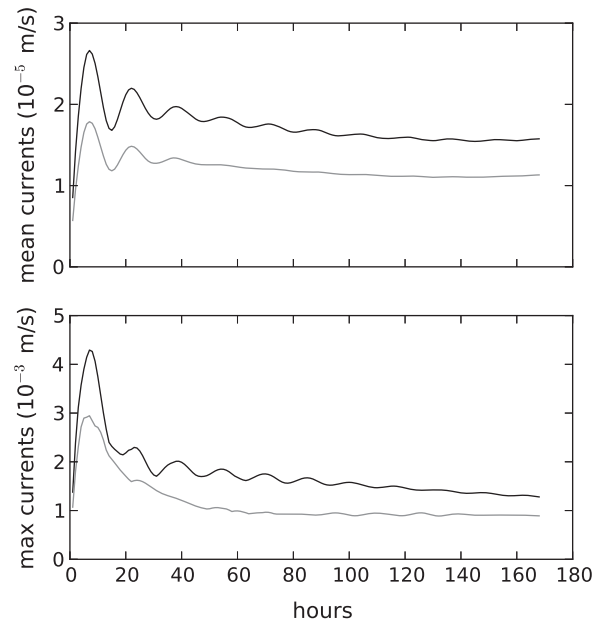

Fig. 8. Domain mean (top) and maximum (bottom) current speeds (m/s) for the AMM7 domain with the SH94 (black) and γ (grey) vertical stretching.

The results on the AMM7 domain show similar time evolution of the domain mean solutions to the seamount test case, with the mean and maximum current speeds spinning up over an inertial period and then slowly being damped to reach a pseudo-steady state solution (Fig. 8). The mean and maximum amplitudes of the currents in the γ experiment are smaller than in the SH94 experiment. The inertial oscillations are also more quickly damped in the γ test case.

Fig. 9 shows the spatial pattern of the depth mean horizontal pressure gradient derived currents after an hour of simulation. The erroneous currents, as expected, closely follow the hydrostatic consistency parameter (Fig. 6) which in turn closely aligns to the gradients in bathymetry.

The system reaches a pseudo equilibrium after a few inertial periods, although it seems that the maximum current speeds are still after 168 h gradually reducing in the SH94 case. Maximum current speeds (Fig. 10) are of an order of magnitude greater than the mean, and reach $\sim$0.1 cm/s in steeply sloping areas, most notably along the continental shelf slope. It should however be noted that these current speeds are still small, and even at their maximum are significantly smaller than the slope current itself, which has maximum current speeds of 10 cm/s or greater (Pingree et al., 1999). Although the domain mean and maximum current speeds (Fig. 8) are significantly higher in the SH94 experiment than in the γ experiment these figures are dominated by the large parts of the domain where the bathymetry is relatively flat and the horizontal pressure gradient derived currents are small. When focusing on steeply slowing areas there is even greater impact of the changed vertical coordinate stretch upon the mean (Fig. 9) and and maximum (Fig. 10) current speeds, with the mean currents speeds in some regions being five times greater in the SH94 simulation than in the γ simulation.

3.5. An idealised air–sea exchange test case

To understand the potential impact of the change in the surface cell thickness on the AMM7 model in going from the SH94 to a γ formulation an idealised air–sea exchange test case has been run. The coordinates were implemented as described in Section 3.2
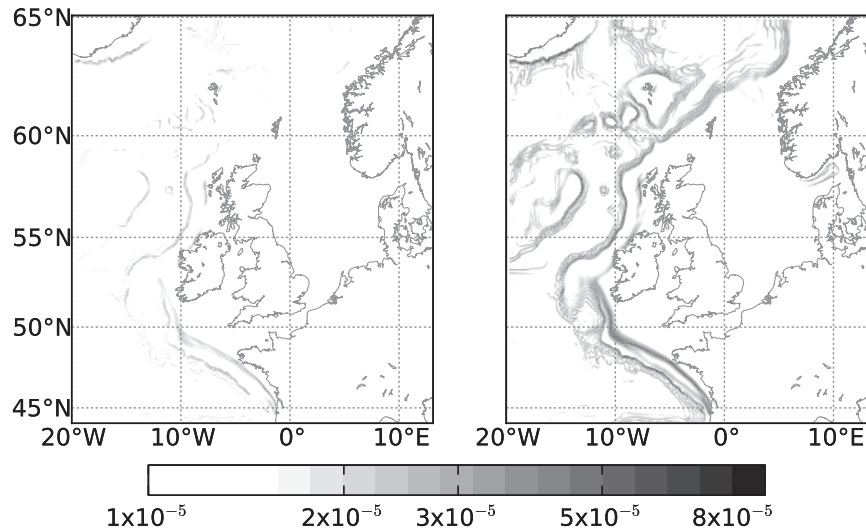
Fig. 9. Depth mean current speeds (m/s) after 1 h for the γ stretching (left) and SH94 stretching (right). Contour intervals are logarithmic.
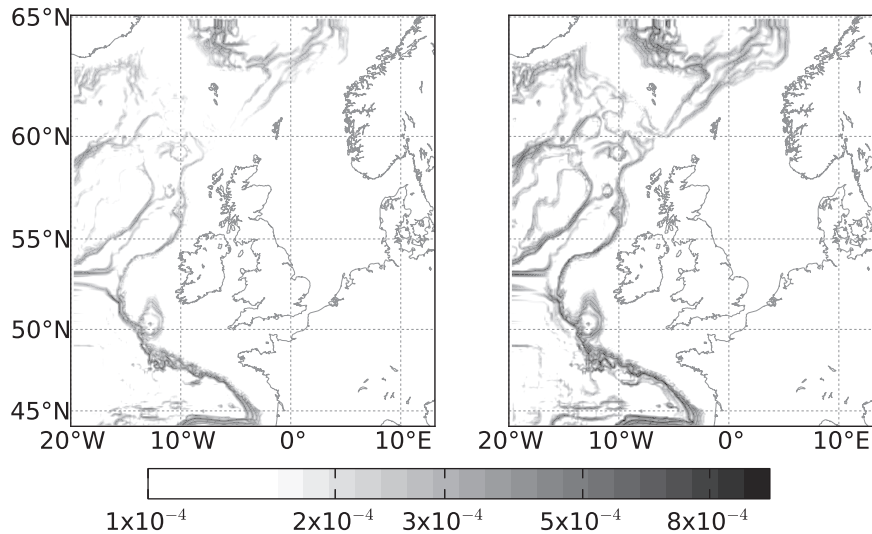

Fig. 10. Column maximum current speeds (m/s) after 48 h for the γ stretching (left) and SH94 stretching (right). Contour intervals are logarithmic.

for the AMM7 model set up as described in Section 3.1. The simulations were initialised with a surface temperature of 12°C and a tanh profile of temperature (below) similar to that used in the seamount testcase and that (given the temperature criterion detailed below) initialises the mixed layer to 120 m.

$$T_z = 3\left(1 - \tanh\left(\frac{z - 120}{20}\right)\right) + 6\left(\frac{5500 - z}{5500}\right)$$

The model was initialised with a constant salinity of 35.5 psu, and the simulations were run without boundaries, rivers or any external forcing other than prescribed heat fluxes to isolate the effects of the air–sea exchange. A daily-averaged shortwave-radiation flux of 300 W m^{-2}, with diurnal cycle, was imposed. A constant 400 W m^{-2} of downward longwave-radiation was also imposed, and the radiative, sensible and evaporative heat fluxes were calculated using the CORE formulation (Large and Yeager, 2004) and a low, constant, background windspeed and a constant air temp of 16°C. This would be typical of warm, high-pressure periods in the early summer in the AMM7 area, and thus gives some indication of the model's response, in terms of forming a diurnal layer and modifying seasonal stratification.

To investigate the impact on stratification the daily maximum and minimum temperatures at each grid point for hourly instantaneous output were calculated. These maxima and minima were used to calculate a diurnal range. The mixed layer depth (MLD) at midnight was calculated using a simple temperature based criterion, where the mixed layer depth is taken to be the depth at which the temperature is 0.2°C less than the SST.

After 14 days (following the initial rapid mixed layer shallowing, Fig. 11) the γ simulation has markedly shallower mixed layers, warmer nighttime temperatures and a greater diurnal range than the SH94 simulation. This is most marked in the deeper waters but is still significant over the shelf slope and continental shelf regions. This is due to an improved representation of the ocean surface boundary layer in the γ stretching and the associated reduced implicit diffusion. This is reflected in the regional mean evolution of the simulations (Fig. 12). The figure shows waters for the on-shelf and shelf slope region (labelled shelf, and defined as waters of depths ranging from 50 m to 300 m) and for the deep waters (labelled off-shelf, and defined as waters of depths greater than 300 m). Waters shallower than 50 m, where both coordinates are the same and significantly smaller differences occur, are not
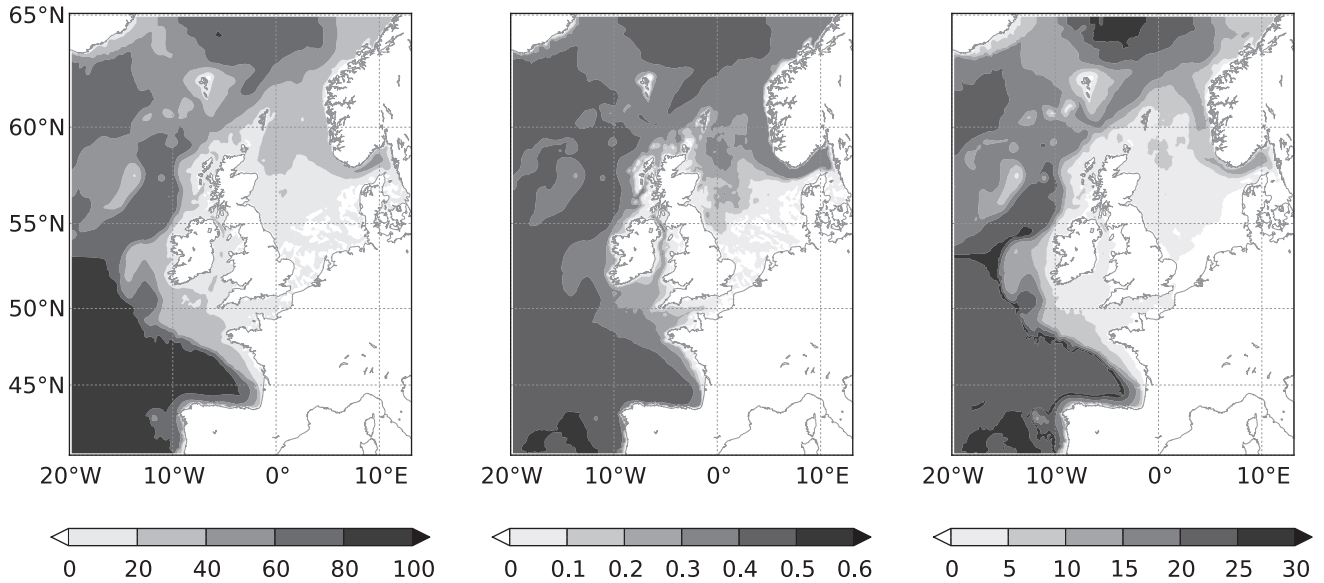
Fig. 11. The difference between γ and SH94 stretching for diurnal range (%, left) midnight temperature (°C, middle) and midnight mixed layer depth (m, right) after 14 days. The difference in diurnal range is calculated as a proportion of the SH94 diurnal range. These are calculated so that a positive mixed layer depth difference means the γ stretching solution is shallower than the SH94, whereas positive diurnal ranges and midnight temperatures mean the γ solution is the larger.
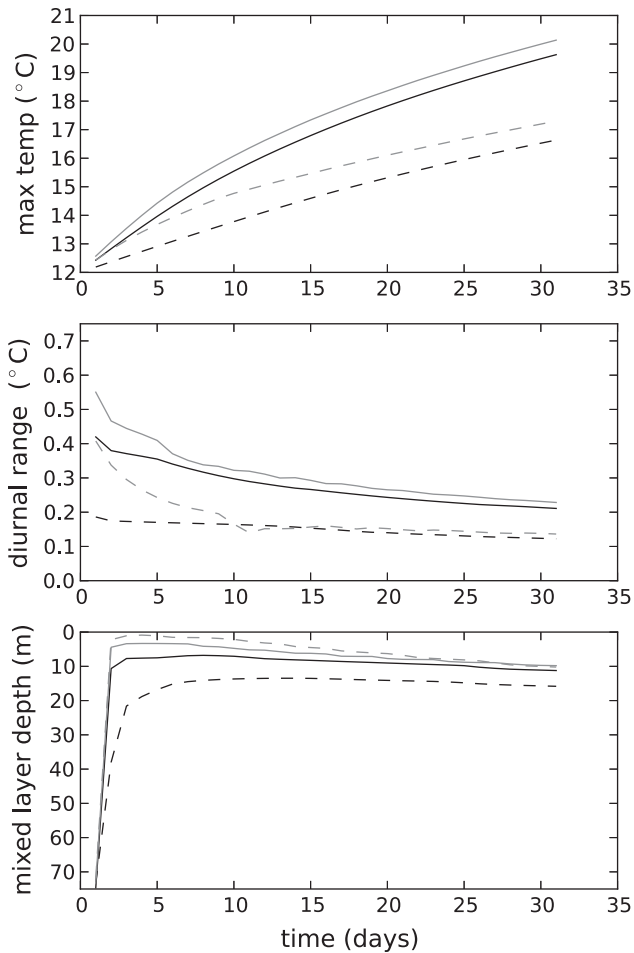

Fig. 12. Comparison of mean daily maximum sea surface temperature (top) mean diurnal range (middle) and mean mixed layer depth (bottom) for shelf (defined as 50 to 300 m depth waters; solid lines) and off-shelf (greater than 300 m depth waters, dashed lines). The SH94 stretching simulation is in black and the γ stretching in grey.

shown. In both simulations the mean diurnal range starts relatively large, decreasing as the mean sea surface temperature increases towards the air temperature. For the shallower waters the surface temperature increases more quickly, the mixed layer becomes more shallow and diurnal cycle is more pronounced than in the deeper waters, although the difference between the deep and shallower waters is less marked in the γ stretching simulation. This implies that vertical resolution is still a limiting factor in the deep waters for the new coordinate, but less so. Although the initial response of the simulations is quite different, they converge to similar solutions for diurnal range once the sea surface temperature approaches the air temperature. The mixed layer depth in the γ solution remains shallower in deep waters throughout the simulations, although the two simulations do appear to be slowly converging.

In summary, the γ stretching is more sensitive to surface heating, with a more rapid increase in surface temperatures, a more rapid and greater reduction in mixed layer depth and larger diurnal ranges. These impacts are to be expected given the change in the coordinate, and confirm the potential for the γ stretching to give better representation of the surface ocean both off-shelf and on the shelf in regions with depths greater then 50 m.

4. Discussion

In this work the emphasis has been upon the use of the γ stretching in the AMM7, a model that presently uses terrain-following coordinates. The intention was to improve the representation of air–sea exchange in this model in deep waters, something that has been seen to be a weakness at present. It has been demonstrated that the γ stretching has the potential to improve the AMM7 in this way. It has also been shown that the hydrostatic consistency and slope factors are in general improved and the associated horizontal pressure gradient errors are reduced. Although it has not been demonstrated it is to be expected that, given the improved hydrostatic consistency and slope factor, other numerical artefacts will also be reduced.

Initially on commencing this work, the authors had envisaged running simulations of the AMM7 using realistic conditions and validating the results against observations. However, it became

clear that the use of the γ stretching would not improve the AMM7 simulations immediately for two reasons. Firstly, the AMM7 is tuned to have realistic shelf slope current and thus a realistic input of heat to the North Sea. It is clear that by reducing the horizontal pressure gradient errors, and therefore improving process representation, the simulations would no longer provide sufficient heat transport along the shelf slope current. Secondly, the AMM7 is known to have a tendency to be slightly warm at the surface, something that is thought to be due to a combination of the air–sea flux used and the downwelling radiation schemes. By improving the representation of heat-exchange at the surface the model would become warmer still, further increasing its bias.

It is intended that now the coordinate is well tested it will be implemented within the AMM7 as part of a suite of changes designed to improve the model.

Although the focus in this work has been upon the shelf seas models, where there is the need to model a wide range of water depths effectively, it has always been the intention of the authors that this coordinate should bridge the gap between deep ocean Z-coordinate and shelf seas σ-coordinate systems. As global ocean models become higher resolution there is an increasing potential for representing shallow water dynamics in deep ocean models. There is also a known problem in simulating flows over sills in global models. These flows are important in driving overturning circulations, and thus in determining global climate. It is therefore worth considering the potential for a terrain-following coordinate that gives a consistent representation of the surface and bottom boundaries in coupled ocean–atmosphere models of the climate.

Simulated Nordic Sea overflow entering into the deep North Atlantic through the Greenland–Iceland–Scotland (GIS) ridge is generally too weak in climate models with, for example, Met Office climate models giving GIS overflows of the order 3–4 Sv (Graham, pers comm), compared to the observed value of about 5–6 Sv from Dickson et al., 1990. This bias is thought to be caused by excessive convective entrainment of the overflow over staircase bathymetry in the model, leading to much lighter and shallower overflow waters (Winton et al., 1998). Danabasoglu et al. (2010) and other authors have attempted to correct these weak overflows with parameterisations that increase the overflows, with some partial success. Griffies et al. (2000) conclude that the ability to resolve these overflows is dependent upon the model vertical coordinate scheme, and that even with partial/shaved cells, Z-coordinate models do not capture these flows well. Ezer and Mellor (2004) compared the use of terrain-following and geopotential coordinate systems in modelling dense water overflows, and concluded that terrain-following coordinates could, at least in an idealised case, provide realistic plume formation. It should also be noted that due to the smooth topography in terrain-following ocean models, they have the advantage of being stable with lower diffusivities than equivalent geopotential models (Mellor et al., 2002). This would suggest that climate modellers should be considering global model domains using terrain-following coordinates if the disadvantages of poor representation of the surface exchange and high horizontal pressure gradient errors in terrain-following systems can be overcome.

A secondary benefit, therefore of this work, is expected to be the potential for improved water mass formation in climate prediction models. Historically, climate models have not used terrain-following coordinates, but recent work Lemarié et al. (2012) suggests that this should be reconsidered given improved numerical solutions for terrain-following coordinates. Lemarié et al. (2012) describes an implementation of ROMS that uses the Shchepetkin and McWilliams (2009) terrain-following stretching to do basin scale simulations. The numerical choices required for global climate simulations and how they differ from the traditional choices made within ROMS, which is predominantly designed for shallow tidal

seas simulations, are discussed and it is concluded that a terrain-following coordinate global climate model is viable and presents no greater numerical difficulties than any other coordinate. It should be noted, though, that the Lemarié et al. (2012) implementation uses a critical depth of 400 m and 50 vertical levels, giving a surface resolution of a little under 10 m. This is not considered sufficient to resolve diurnal cycles (Bernie et al., 2005) and would therefore limit the ability of this model to adequately represent air–sea exchange. A terrain-following coordinate that allows improved consistency in the surface grid resolutions over a range of water depths would further improve the potential for their use in climate simulations.

The aim of this work has been to provide a coordinate stretching that optimises the placement of the vertical resolution and follows the low frequency changes in sea-level but does not adapt to local changes in density at high frequency. The Arbitrary Lagrangian Eulerian (ALE) method (Hirt et al., 1974) has been implemented in NEMO (Leclair and Madec, 2011) to allow the coordinate to adapt to high frequency fluctuations in the density field, such as those due to internal waves. An ALE coordinate such as that given in Leclair and Madec (2011) superimposed upon a terrain-following coordinate such as the one presented here would be a powerful approach to resolving internal waves, flows over steep slopes, the non-linear free surface and surface exchange processes.

The Met Office Hadley Centre uses the NEMO model in its coupled ocean–atmosphere climate modelling system (HadGEM3 Hewitt et al. (2011)). The intention is to firstly look at the impact of the coordinate upon flows over sills and if it provides an improvement upon the present coordinates then to test it more generally within the coupled system.

5. Conclusions

The paper has defined a coordinate that can be shown, in theoretical cases at least, to be able to combine the representation of the ocean surface boundary layer in deep water associated with geopotential (Z) coordinate model frameworks with the ability of terrain-following (σ/S) coordinates to represent bottom boundary layers. It is also shown that the horizontal pressure gradient error associated with terrain-following coordinates is reduced using this coordinate as the mean slopes, and particularly the mean slopes in regions of high vertical density gradients, are less than a commonly used stretched coordinate.

This results in simulations that have fewer spurious currents due to numerical artefacts, and better representation of air–sea exchange, than the coordinate used presently for a stretched terrain-following coordinate model, the FOAM AMM7.

The potential for this coordinate to be used for global ocean models has not been explored here. It is expected that given advances in the numerics of terrain-following models, and the benefits they give for modelling flows over sills, that this work can be extended to coupled ocean applications with potential benefits for modelling overturning circulations.

References

Adcroft, A., Hill, C., Marshall, J., 1997. Representation of topography by shaved cells in a height coordinate ocean model. Monthly Weather Review 125, 2293–2315.

Beckmann, A., Döscher, R., 1997. A method for improved representation of dense water spreading over topography in geopotential-coordinate models. Journal of Physical Oceanography 27, 581–591.

Beckmann, A., Haidvogel, D.B., 1993. Numerical simulation of flow around a tall isolated seamount. Part I: Problem formulation and model accuracy. Journal of Physical Oceanography 23, 1736–1753.

Bell, M.J., 1999. Vortex stretching and bottom torques in the Bryan–Cox ocean circulation model. Journal of Geophysical Research 104, 23545–23563.

Bernie, D.J., Woolnough, S.J., Slingo, J.M., Guilyardi, E., 2005. Modeling diurnal and intraseasonal variability of the ocean mixed layer. Journal of Climate 18, 1190–1202.

Burchard, H., Peterson, O., 1997. Simulating the wave-enhanced layer under breaking surface waves with two-equation turbulence models. International Journal for Numerical Methods in Fluid 25, 1003–1023.

Canuto, V., Howard, A., Cheng, Y., Dubovikov, M., 2001. One-point closure model-momentum and heat vertical diffusivities. Journal of Physical Oceanography 31, 1413–1426.

Chassignet, E.P., Arango, H., Dietrich, D., Ezer, T., Ghil, M., Haidvogel, D.B., Ma, C.C., Mehra, A., Paiva, A.M., Sirkes, Z., 2000. DAMÉE-NAB: the base experiments. Dynamics of Atmospheres and Oceans 32, 155–183.

Craig, P., Banner, M., 1994. Modelling wave-enhanced turbulence in the ocean surface layer. Journal of Physical Oceanography 24, 2546–2559.

Danabasoglu, G., Large, W.G., Briegleb, B.P., 2010. Climate impacts of parameterized Nordic Sea overflows. Journal of Geophysical Research 115, C11005.

Dickson, R.R., Gmitrowicz, E.M., Watson, A.J., 1990. Deep-water renewal in the northern North Atlantic. Nature 344, 848–850.

Dukhovskoy, D.S., Morey, S.L., Martin, P.J., O'Brien, J.J., Cooper, C., 2009. Application of a vanishing, quasi-sigma, vertical coordinate for simulation of high-speed, deep currents over the Sigsbee Escarpment in the Gulf of Mexico. Ocean Modelling 28, 250–265.

Ezer, T., Mellor, G.L., 2004. A generalized coordinate ocean model and a comparison of the bottom boundary layer dynamics in terrain-following and in z-level grids. Ocean Modelling 6, 379–403.

Flather, R., 1976. A tidal model of the northwest European continental shelf. Mémoires de la Société Royale des Sciences Liége 10, 141–164.

Galperin, B., Kantha, L., Hassid, S., Rosati, A., 1988. A quasi-equilibrium turbulent energy model for geophysical flows. Journal of the Atmospheric Sciences 45, 55–62.

Gerdes, R., 1993. A primitive equation ocean circulation model using a general vertical coordinate transformation. 1. Description and testing of the model. Journal of Geophysical Research 98, 14683–14701.

Griffies, S.M., Böning, C., Bryan, F.O., Chassignet, E.P., Gerdes, R., Hasumi, H., Hirst, A., Treguier, A.M., Webb, D., 2000. Developments in ocean climate modelling. Ocean Modelling 2, 123–192.

Haidvogel, D.B., Beckmann, A., 1999. Numerical Ocean Circulation Modeling. Imperial College Press.

Haney, R.L., 1991. On the pressure gradient force over steep topography in sigma coordinate ocean models. Journal of Physical Oceanography 21, 610–619.

Hewitt, H.T., Copsey, D., Culverwell, I.D., Harris, C.M., Hill, R.S.R., Keen, A.B., McLaren, A.J., Hunke, E.C., 2011. Design and implementation of the infrastructure of HadGEM3: the next-generation Met Office climate modelling system. Geoscientific Model Development 4, 223–253.

Hirt, C.W., Amsden, A.A., Cook, J.L., 1974. An arbitrary Lagrangian–Eulerian computing method for all flow speeds. Journal of Computational Physics 14, 227–253.

Holt, J.T., James, I.D., 2001. An S coordinate density evolving model of the northwest European continental shelf 1, model description and density structure. Journal of Geophysical Research 106, 14015–14034.

Hughes, C.W., de Cuevas, B.A., 2001. Why western boundary currents in realistic oceans are inviscid: a link between form stress and bottom pressure torques. Journal of Physical Oceanography 31, 2871–2885.

Janjić, Z.I., 1989. On the pressure gradient force error in – coordinate spectral models. Monthly Weather Review 117, 2285–2292.

Large, W., Yeager, S., 2004. Diurnal to decadal global forcing for ocean and sea-ice models: the data sets and flux climatologies. Technical Report NCAR/TN-460+STR. National Center for Atmospheric Research.

Leclair, M., Madec, G., 2011. z-Coordinate, an arbitrary Lagrangian–Eulerian coordinate separating high and low frequency motions. Ocean Modelling 37, 139–152.

Lemarié, F., Kurian, J., Shchepetkin, A.F., Jeroen Molemaker, M., Colas, F., McWilliams, J.C., 2012. Are there inescapable issues prohibiting the use of terrain-following coordinates in climate models? Ocean Modelling 42, 57–79.

Madec, G., 2008. NEMO ocean engine. Technical Report 27. Institut Pierre-Simon Laplace (IPSL).

Madec, G., Delecluse, P., Crépon, M., Lott, F., 1996. Large-scale preconditioning of deep-water formation in the northwestern Mediterranean sea. Journal of Physical Oceanography 26, 1393–1408.

Mellor, G.L., Hakkinen, S., Ezer, T., Patchen, R., 2002. A generalization of a sigma coordinate ocean model and an intercomparison of model vertical grids. In: Pinardi, N., Woods, J.D. (Eds.), Ocean Forecasting: Conceptual Basis and Applications. Springer, New York, pp. 55–72.

O'Dea, E.J., Arnold, A.K., Edwards, K.P., Furner, R., Hyder, P., Martin, M.J., Siddorn, J.R., Storkey, D., While, J., Holt, J.T., Liu, H., 2012. An operational ocean forecast system incorporating NEMO and SST data assimilation for the tidally driven European North–West shelf. Journal of Operational Oceanography, 3–17.

Pacanowski, R.C., Gnanadesikan, A., 1998. Transient response in a Z-level ocean model that resolves topography with partial cells. Monthly Weather Review 126, 3248–3270.

Phillips, N.A., 1957. A coordinate system having some special advantages for numerical forecasting. Journal of Meteorology 14, 184–185.

Pietrzak, J., Jakobson, J.B., Burchard, H., Jacob Vested, H., Petersen, O., 2002. A three-dimensional hydrostatic model for coastal and ocean modelling using a generalised topography following co-ordinate system. Ocean Modelling 4, 173–205.

Pingree, R.D., Sinha, B., Griffiths, C.R., 1999. Seasonality of the European slope current (Goban Spur) and ocean margin exchange. Continental Shelf Research, 929–975.

Roberts, M.J., Wood, R.A., 1997. Topographic Sensitivity Studies with a BryanGCox-type ocean model. Journal of Physical Oceanography 27, 823–836.

Schär, C., Leuenberger, D., Fuhrer, O., Lüthi, D., Girard, C., 2002. A new vertical coordinate formulation for atmospheric prediction models. Monthly Weather Review 130, 2459–2480.

Shchepetkin, A., McWilliams, J., 2005. The regional oceanic modeling system (ROMS): a split-explicit, free-surface, topography-following-coordinate oceanic model. Ocean Modelling 9, 347–404.

Shchepetkin, A., McWilliams, J., 2009. Correction and commentary for ocean forecasting in terrain-following coordinates: formulation and skill assessment of the regional ocean modeling system by Haidvogel et al.. Journal of Computational Physics 227 (7), 3595–3624, Journal of Computational Physics 228, 8985–9000.

Shchepetkin, A.F., McWilliams, J.C., 2003. A method for computing horizontal pressure-gradient force in an oceanic model with a nonaligned vertical coordinate. Journal of Geophysical Research 108, 3024–3090.

Song, Y., Haidvogel, D.B., 1994. A semi-implicit ocean circulation model using a generalized topography-following coordinate system. Journal of Computational Physics 115, 228–244.

Song, Y.T., Hou, T.Y., 2006. Parametric vertical coordinate formulation for multiscale, Boussinesq, and non-Boussinesq ocean modeling. Ocean Modelling 11, 298–332.

Song, Y.T., Wright, D.G., 1998. A general pressure gradient formulation for ocean models. Part II: Energy, momentum, and bottom torque consistency. Monthly Weather Review 126, 3231–3247.

Spall, M.A., Holland, W.R., 1991. A nested primitive equation model for oceanic applications. Journal of Physical Oceanography 21, 205–220.

Storkey, D., Blockley, E.W., Furner, R., Guiavarc'h, C., Lea, D., Martin, M.J., Barciela, R.M., Hines, A., Hyder, P., Siddorn, J.R., 2010. Forecasting the ocean state using NEMO: the new FOAM system. Journal of Operational Oceanography 3, 3–15.

Treguier, A., Dukowicz, J., Bryan, K., 1996. Properties of nonuniform grids used in ocean general circulation models. Journal of Geophysical Research 101, 20877–20881.

Umlauf, L., Burchard, H., 2003. A generic length-scale equation for geophysical turbulence models. Journal of Marine Research 61, 235–265.

Winton, M., Hallberg, R., Gnanadesikan, A., 1998. Simulation of density-driven frictional downslope flow in Z-coordinate ocean models. Journal of Physical Oceanography 28, 2163–2174.

Surface heat fluxes and ecosystem function in the Cretan Sea (eastern Mediterranean): a modelling study

J. R. Siddorn and J. I. Allen

Plymouth Marine Laboratory, Prospect Place, West Hoe, Plymouth PL1 3DH, UK

Abstract. As a component of the Mediterranean Forecast System Pilot Project, a data buoy was deployed in the Cretan Sea. A 1-D ecosystem model of the site has been used to investigate the role of surface heat fluxes in determining modelled ecosystem behaviour. The method of calculation of these fluxes, the quality of the data used, and the temporal resolution of the data all had an impact upon the modelled ecosystem function. The effects of the changes in heat flux formulation were substantial, with both annually averaged properties of the system and the seasonal evolution of the biology being affected. It was also found that the ecosystem model was extremely sensitive to the accuracy of the meteorological forcing data used, with substantial changes in biology found when offsets in the forcing data were imposed. The frequency of forcing data was relatively unimportant in determining the biological function, although lower frequency forcing damped high frequency variability in the biology. During periods of mixing the biology showed an amplified response to changes in physical dynamics, but during periods of stratification the variations in the physics were found to be less important. Zooplankton showed more sensitivity to physical variability than either phytoplankton or bacteria. The consequences for ecosystem modelling are discussed.

Key words. Oceanography: physical (air-sea interactions; turbulence, diffusion, and mixing processes) – Oceanography: biological and chemical (plankton)

1 Introduction

The effective modelling of ecosystems requires a suitable knowledge of both the governing biogeochemical equations and physical processes. The ecosystem function is influenced by physical processes, through changes in the temperature, light and mixing regimes (Huisman et al., 1999; Margalef, 1997; Sharples and Tett, 1994; Pingree et al., 1978). There-

Correspondence to: J. I. Allen (jia@pml.ac.uk)

fore, the physical parameterisation of the model may have an important effect upon the biological function (Chen and Annan, 2000). Additionally, the choice of forcing at the air-sea interface can strongly influence modelled ecosystem behaviour (Lacroix and Nival, 1998).

This work has been undertaken as part of the Mediterranean Forecasting System Pilot Project (MFSPP), which aims to predict the marine ecosystem variability in coastal areas of the Mediterranean Sea. A forecasting system requires two parts, an observing system and a numerical modelling component. The M3A buoy, in the Cretan Sea, has been installed to supply the observational data. The forecast capability of the modelling system is dependent upon the ecosystem model's responses to variability in physical forcing, and temporal and spatial resolution of forcing functions.

The aim of this work is to investigate the role of surface heat flux, as determined by the frequency of meteorological data and the choice of heat flux formulations, in determining the biological function of a one-dimensional ecosystem model of the Cretan Sea. The primary productivity of a system is determined by both nutrient availability and the residence time of plankton in the euphotic zone, which, in turn, are both dependent upon the stability of the water column (Huisman et al., 1999). In a 1-D model this is dependent upon surface fluxes of heat and momentum.

The Cretan Sea, in the eastern basin of the Mediterranean, is a seasonally stratified oligotrophic system, and in the winter months the water column frequently overturns, mixing up bottom waters (Tselepides et al., 2000). Phosphorus is generally considered to be the limiting nutrient in this region. These overturning events are important to the ecosystem function of the Cretan Sea, since they sporadically mix up nutrients to the surface waters. Air-sea transfers of momentum and heat, which determine the timing and extent of these overturning events, are, therefore, an important factor in controlling the local biogeochemistry. The extent to which modelled ecosystem behaviour is affected by the method of modelling surface fluxes of heat and momentum is, therefore, a pertinent question. Castellari et al. (1998) have shown, us-
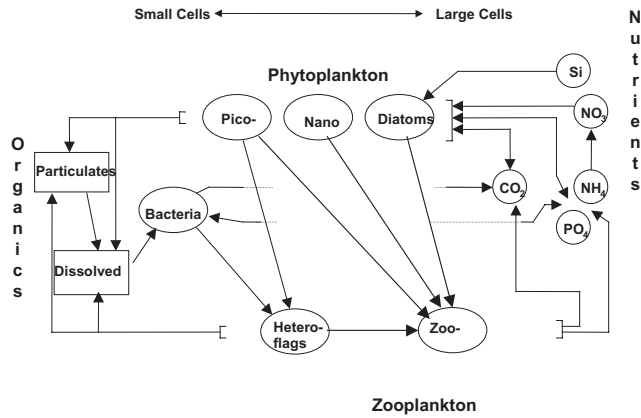
Pelagic Food Web - Trophic Model

Fig. 1. Diagram showing the trophic links in ERSEM.

Table 1. The model code and the descriptive names for the ERSEM functional groups

Phytoplankton		Zooplankton		Bacteria	
P1	Diatoms, (Silicate dependence)	Z5	Zooplankton (20–300 μm)	B1	Bacteria
P2	Flagellates ($>2\,\mu$m)	Z6	Heterotrophic Flagellates ($<20\,\mu$m)		
P3	Picoplankton ($<2\,\mu$m)				

ing an OGCM of the Mediterranean Sea, that the hydrodynamics are sensitive to the heat flux formulation and meteorological data used. Lacroix and Nival (1998) have also shown that in the western Mediterranean the frequency of forcing has a strong effect upon the biological function.

2 Methods

2.1 Models

2.1.1 ERSEM

The European Seas Ecosystem Model (ERSEM) is a generic ecosystem model, with a proven record of use in the Mediterranean Sea (Allen et al., 2002a; Zavatarelli et al., 2000; Allen et al., 1998; Vichi et al., 1998). ERSEM is a modelling framework in which an ecosystem is represented as a network of physical, chemical and biological processes that display coherent system behaviour (Baretta et al., 1995). A "functional group" approach is used to describe the biota. The ecosystem is subdivided into three functional types: producers (phytoplankton), decomposers (bacteria) and consumers (zooplankton), and subdivided on the basis of trophic links and/or size (Table 1 and Fig. 1).

Physiological (ingestion, respiration, excretion and egestion) and population (growth, migration and mortality) processes are included in the descriptions of functional group dynamics. Physiological processes and population dynamics are described by fluxes of carbon or nutrients between functional groups. Each functional group, therefore, has a number of components, each of which is explicitly modelled. These include carbon, nitrogen, and phosphorus for all functional groups and, in the case of diatoms (P1), silicon. Detailed descriptions of ERSEM and its sub-models can be found in Baretta et al. (1995), Baretta-Bekker et al. (1995; 1998) and Ebenhöh et al. (1997). Sensitivity analyses of parameterisations of ERSEM have been undertaken by Ebenhöh et al. (1997) and Varela et al. (1995).

The model used in this study is a version of ERSEM as described above, with the main adaptation being the inclusion of dynamically varying carbon to chlorophyll ratios in the primary producers, following methods described in Geider et al. (1996) (Allen, 2002b).

2.1.2 POM

The ERSEM code is coupled with a 1-D version of the Princetown Ocean Model (POM) (Blumberg and Mellor, 1987). The POM code calculates Richardson number dependent eddy diffusion coefficients for momentum (K_M) and scalar variables (K_H), using the Mellor-Yamada 2.5 turbulence closure model (Mellor and Yamada, 1982), modified after Galperin et al. (1988) and using a prescribed turbulence length scale following Bakhmetev (1932). These coefficients are used to transport variables in both the physical and ecosystem sub-models. The physics is driven at the air-sea interface by surface fluxes of heat and momentum, calculated from meteorological boundary data, with salinity held at the surface to climatological values (Psarra et al., 2000). Horizontal velocity is derived from surface and bottom stresses, and transported in the same way as other parameters. These velocity gradients are used to determine the shear production.

The vertical resolution of the model is a metre at the surface, increasing a metre at a time to five metres. The resolution stays at five metres for the rest of the 250 m deep water column.

2.2 Surface heat flux formulations

The net flux of heat (Q_T) across the air-sea interface is given by:

$$Q_T = Q_S + Q_E + Q_H + Q_B, \tag{1}$$

where Q_S is the solar radiation flux, Q_E is the latent heat of evaporation flux, Q_H is the sensible heat flux and Q_B is the long-wave radiation flux. Q_S is calculated at every time step

Table 2. Long-wave radiation formulations; (a) Rosati and Miyakoda (1998) and (b) Budyko (1974)

	Formulation
Brunt-Berliand[a]	$Q_B = \varepsilon \sigma T_S^4 \left(0.39 - 0.005\sqrt{e_A}\right)\left(1 - 0.8C\right) + 4\varepsilon \sigma T_S^4 \left(T_S - T_A\right)$
May[b]	$Q_B = \left\lfloor \sigma T_S^4 \left(0.4 - 0.005\sqrt{e_A}\right) + 4\sigma T_S^3 \left(T_S - T_A\right)\right\rfloor \left(1 - 0.75C^{3,4}\right)$
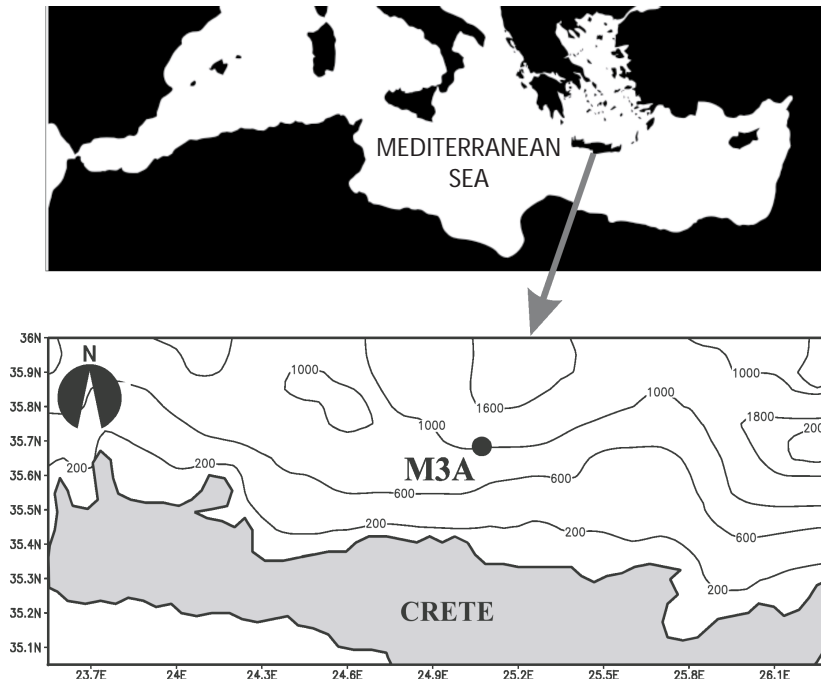
Fig. 2. The location of the M3A buoy site.

using astronomical calculations of solar radiation, modified by cloud cover (Dobson and Smith, 1988).

The sensible (Q_H) and latent heat (Q_E) fluxes are calculated using standard formulae; the net flux of heat (Q_T) across the air-sea interface is given by:

$$Q_H = p_A C_P C_H |V|(T_S - T_A) \tag{2}$$

$$Q_E = p_A L_E C_E |V|(q_S - q_A), \tag{3}$$

where p_A is the air density, q_A is the specific humidity of air, q_S is the saturation specific humidity of air, C_p is the specific heat capacity of water, L_E is the latent heat of vaporisation, T_S and T_A are the surface and air temperatures, respectively, and C_E and C_H are the exchange coefficients for latent and sensible heat, respectively.

The calculations for the latent and sensible heat are dependent upon the calculations of the coefficients C_E and C_H. Two formulations taken from Castellari et al. (1998) are used; the "neutral" formulation (Rosati and Miyakoda, 1988), which sets both coefficients equal to 1.1×10^{-3}, and the Kondo formulation (Kondo, 1975), where the coefficients are a function of air-sea temperature difference, wind speed and a stability criterion for the surface waters.

Two formulations for the long-wave radiation flux (Q_B) are used (Table 2). The formulations for the exchange coefficients and longwave radiation are combined to give three heat flux models (Table 3). These were found by Castellari et al. (1998) to model the hydrodynamics of the Mediterranean most successfully, although it should be noted that the model used in the Castellari et al. (1998) work is different from that used here and, therefore, direct comparisons cannot be made.

European Centre for Medium-range Weather Forecasts (ECMWF) 6-hourly data, at a 2.5° horizontal resolution, was extracted for a position close to the M3A buoy site to provide the meteorological forcing for the model. Air temperature at 2 m (T_A), 10 m winds, and cloud cover were available. Dew point temperature (T_D) and mean sea level pressure (P_A) data were also available and were used in the calculation of the relative humidity (RH) based on a formulation in Wallace and Hobbs (1977), and a calculation for the saturation vapour pressure (E_S) (Tetens, 1930):

$$RH = 100 \times \frac{E_S(T_D)}{P_A - E_S(T_D)} \times \frac{P_A - E_S(T_A)}{E_S(T_A)} \tag{4}$$

Table 3. The combinations of heat flux formulations used; (a) Rosati and Miyakoda (1998), (b) Kondo (1975) and (c) Budyko (1974)

Method	Turbulent Exchange Coefficient (C_E/C_H) Method	Long-wave Radiation Method
PA1	Neutral[a]	Brunt-Berliand[a]
PA2	Kondo[b]	Brunt-Berliand[a]
PA3	Kondo[b]	May[c]

Table 4. Production and biomass data in the Cretan Sea:
(a) Psarra et al. (2000); integrated over the surface 100 m for station D4, at 35°30′ N, 25°06′ E
(b) Ignatiades (1998); for station 59 (36°0′ N, 25°30′ E); integrated over the surface 50 m
(c) Gotsis-Skretas et al. (1999); for station 59 (36°0′ N, 25°30′ E); integrated over the surface 50 m
(d) Antoine et al. (1995); estimates made by CZCS for the Cretan Sea
(e) Turley et al. (2000); estimates for the Cretan Sea

	Phytoplankton	Bacteria
Biomass (mg-C m^{-2})	1240[d]	1372±274[e]
	296–1400[c]	
Production (mg-C m^{-2} d^{-1})	220±64.3[a]	48.5±39.2[e]
	65.2[b]	
	114–169[c]	
	151.0±91.6[e]	

$$E_S(T) = 0.611 \exp\left(\frac{17.27T}{T + 237.3}\right). \tag{5}$$

Temperatures are in degrees Celsius and pressures in Pascals.

2.3 Site

The Mediterranean Multisensor Moored Array (M3A) buoy is located 30 nm north of Heraklion in the Cretan Sea (35°40′ N, 25°00′ E), in 1030 m of water (Fig. 2).

The buoy was deployed to collect three-hourly data for a number of physical and biological variables, including temperature and chlorophyll, at various depths. In situ meteorological information was also collected. Further details of the instrumentation used and calibration of data sets can be found in Nittis et al. (2003). Other data sets are also available for the Cretan Sea, and some relevant data are summarised in Tables 4 and 5.

Table 5. Nutrient data in the Cretan Sea, and annually averaged nutrient concentrations (depths 0–250 m) for the model simulations PA1, PA2 and PA3:
(a) Tselepides et al. (2000); for stations in the Cretan Sea in depths of more than 500 m; annual averages of samples taken from depths 0–200 m
(b) Gotsis-Skretas et al. (1999); for station 59 (36°0′ N, 25°30′ E); annual average of samples from depths 0–100 m

	Phosphate (mmol m^{-3})	Nitrate (mmol m^{-3})	Silicate (mmol m^{-3})
Tselepides[a]	0.08±0.06	1.37±1.14	1.49±0.69
Gotskis-Skretas[b]	0.03	1.03	2.65
PA1	0.030	1.32	3.14
PA2	0.036	1.36	3.08
PA3	0.035	1.36	3.09

3 Results

3.1 Sensitivity to variations in heat flux formulation

The model was run using the three heat flux formulations, labelled PA1, PA2 and PA3 (Table 3), forced using six-hourly ECMWF meteorological data for the year 2000. A repeating-year forcing was applied for five years to spin the models up to a quasi-steady state for each formulation. The simulations presented here were initialised for both biological and physical variables using the results from these spin-up runs.

3.1.1 Temperature

A comparison of these simulations with the M3A data shows that the surface temperature was underestimated by up to 3° by all three formulations. The PA1 and PA2 runs were most seriously affected, with PA3, although still significantly underestimating the surface temperature, showing the closest fit to the data (Fig. 3). Simulated temperatures at lower depths (not shown) pick up the correct seasonal trends, but not the high-frequency variability shown by the M3A data.

The inability of the model to reproduce the surface temperature could be related to horizontal advection of heat to the site. It is well documented that the Mediterranean has a negative heat budget (Castellari et al., 1998), compensated for by transport of heat across the Gibralter Sill, and, therefore, a 1-D model with no compensation for this would be expected to underestimate the temperature. An underestimation of the solar inputs to the system may also have an effect, although this has been discounted, since the modelled solar heat flux was substantially higher than literature estimates for the Mediterranean; Garrett et al. (1993) gives the long-term mean solar heat flux as 202 W m^{-2}, compared to 219 W m^{-2} for this model.

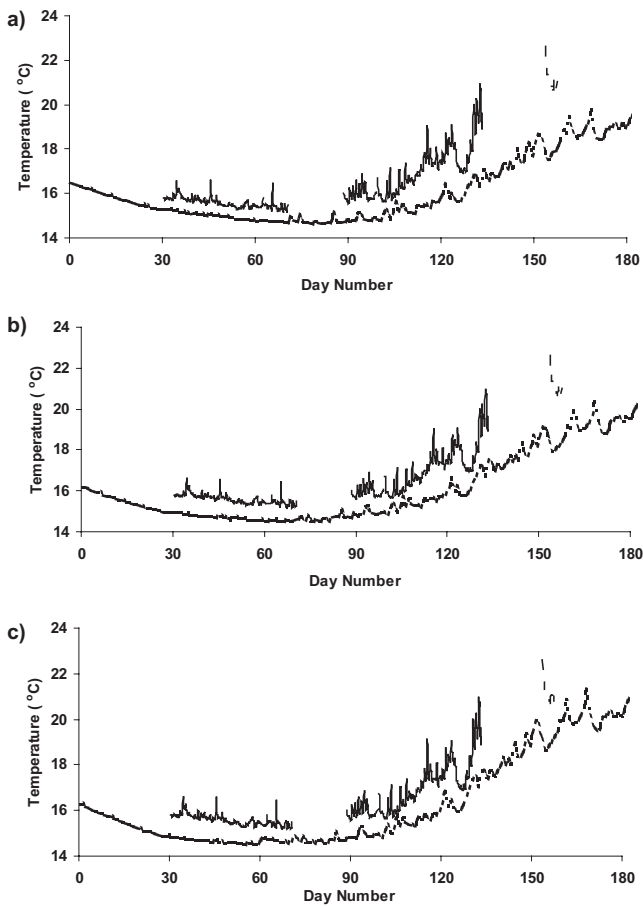Other potential causes of this temperature underestimation were also investigated. The ECMWF forcing data used was

Fig. 3. Surface temperature for **(a)** PA1, **(b)** PA2 and **(c)** PA3 runs. Dashed line indicates model, solid line indicates data.
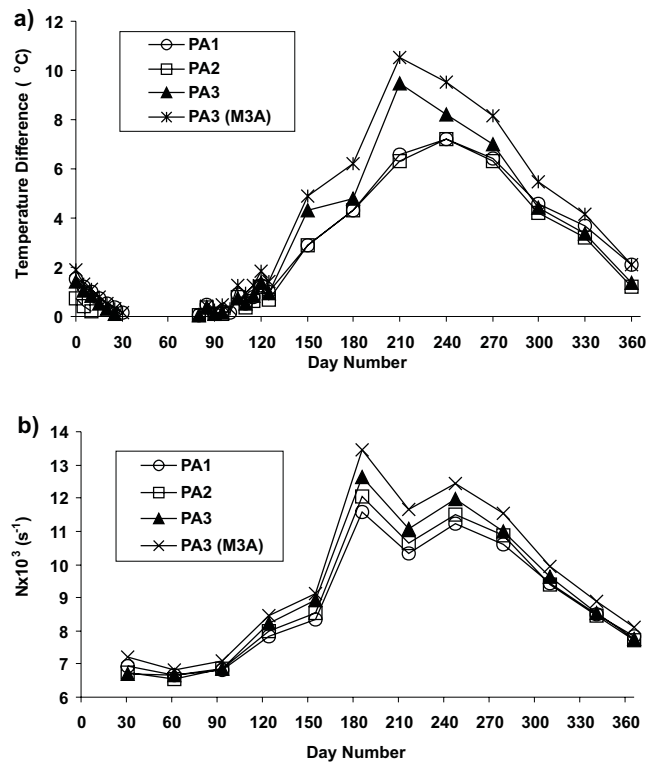

Fig. 4. Stratification strength as given by **(a)** temperature difference across the thermocline and **(b)** the monthly running-mean of the depth-averaged Brunt-Väisälä frequency, for runs PA1, PA2, PA3 and PA3 with M3A humidity.

checked against the meteorological data taken from the M3A buoy (Nittis et al., 2003), and the two data sets showed good agreement for most variables. However, the humidity, as calculated from the ECMWF data, showed substantial differences to the measured M3A data. The importance of the accuracy of the forcing data is investigated further in Sect. 3.3.

The three runs, as mentioned above, showed substantial differences in their calculations of the hydrodynamic properties of the M3A site. As an indicator of the physical behaviour of each model run, strength of stratification, as given by the maximum Brunt-Vaisala frequency and temperature difference across the thermocline, was calculated (Fig. 4).

The onset of stratification occurred around day 80 for all three runs, with the strongest stratification not occurring until after day 100. Differences between the runs were evident, with PA1 giving a deeper thermocline in the initial stages and stronger stratification in the latter parts of the year. PA1 also appeared to give a more diffuse thermocline. The PA3 simulation resulted in the shallowest thermocline depth, and subsequently the extent of the stratification was the greatest.

3.1.2 Comparison of biological time-series data

The physical differences between the modelled water columns have an effect upon the biological function of the model, through the timing of stratification, the water temperature and the extent of mixing. The timing and magnitudes of the spring blooms were quite different for the three simulations. The PA1 simulation bloomed the latest and with the smallest peak (87 days and 0.51 mg–Chl m^{-3}). PA2 gave a rather diffuse bloom, with substantial secondary blooms at most depths; these peaks occurred earlier than for the PA1 run (at days 62 and 71), and with a similar magnitude (0.54 and 0.53 mg–Chl m^{-3}). The PA3 simulation resulted in an early bloom (day 61) which was of a greater magnitude (0.68 mg–Chl m^{-3}) than either the PA1 or PA2 blooms.

The comparisons of simulated chlorophyll concentrations with data show that they are of the right order of magnitude (Fig. 5). However, the relatively large peaks in chlorophyll in the model runs are not consistent with the apparent lack of any significant spring bloom in the measured data. There is unfortunately little data available for the period up until day 65, and none between day 40 and 65, so it is possible that some elevated chlorophyll concentrations were present in this period.

The three runs showed remarkable similarity in the summer and autumn, and substantial differences in the winter and
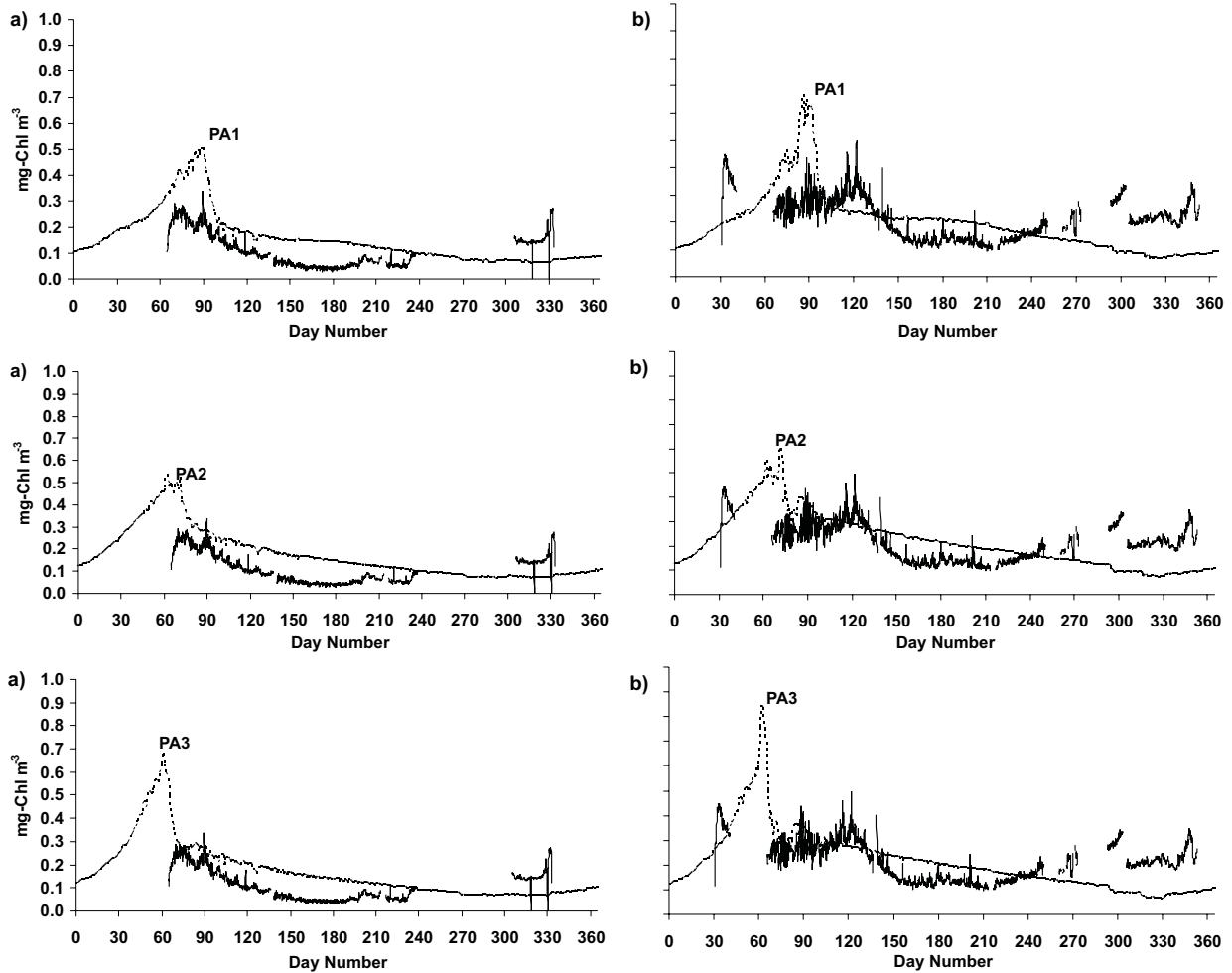
Fig. 5. Comparison of chlorophyll from the model runs PA1 , PA2 and PA3 for **(a)** 40 m depth, **(b)** 65 m depth.

spring (Fig. 6). The winter and spring periods coincide with overturning events, and hence, the nutrient supply to, and residence times of, phytoplankton in the euphotic zone are controlled by the physical properties of the water column. In the summer and autumn stratification disconnects the surface waters from the nutrient rich bottom waters. Hence, the limit to primary production is the in situ recycling of nutrients in the surface layers, and the ecosystem comes under biological control.

Turley et al. (2000) found a highly significant relationship between bacterial and primary production in the Cretan Sea, and this relationship is well replicated in the simulations (Fig. 7). No obvious differences were evident between model runs, with all showing relative bacterial and primary production of the same order as the Turley data.

3.1.3 Annually averaged biology

The comparison of the three runs with data for phytoplankton production show good agreement (Table 4 and Fig. 8), although the scatter in the data does not allow a judgement to be made on the relative merits of them. The phytoplankton

biomass also agrees well with published data for the region, although possibly slightly on the high side in all cases. Both bacterial biomass and production lie within the range of published data. Similarly, modelled nutrient levels show good agreement with observations (Table 5).

The annual average production and biomass of the three runs showed some significant differences (Fig. 8). The main differences between the three runs lie in the production data, with the zooplankton being particularly affected (the difference between the PA1 and PA2 annually averaged production is greater than 300%). The biomass varied by less than 10% for both the phytoplankton and bacteria, although the zooplankton showed a much more marked variation (a 60% difference between the PA1 and PA2 runs).

3.2 Sensitivity to the frequency of meteorological forcing

To investigate the role of surface forcing frequency, the three simulations were each rerun with the meteorological data read in at 12-hourly, daily, weekly and monthly intervals. Annually-averaged simulated zooplankton were more sensitive than either the bacteria or the phytoplankton to changes
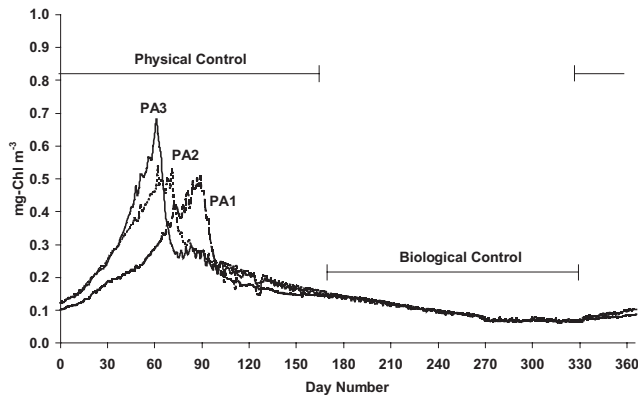
Fig. 6. Chlorophyll concentrations for the runs PA1, PA2 and PA3 showing the periods under physical and biological control.
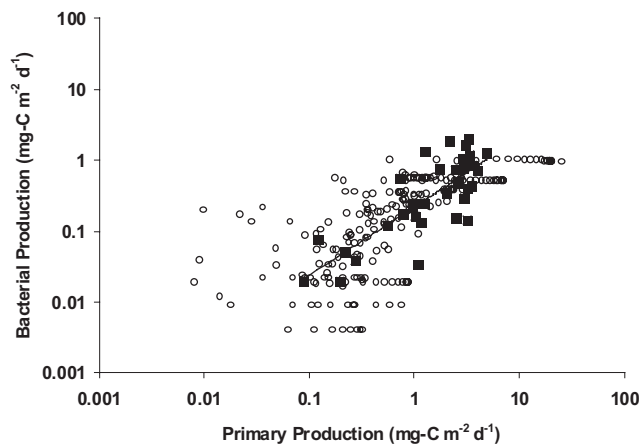
Fig. 7. Logged bacterial against primary production rates. Data taken in the eastern Mediterranean (Turley, 2000) (closed squares) and model output for the standard PA3 run (open circles). Model output taken every 30 days from the surface 100 m. The line shows the best fit for the Turley data.

Fig. 8. Annually averaged **(a)** production and **(b)** biomass for total phytoplankton, zooplankton and bacteria.

3.3 Sensitivity to variations in the forcing data

Inaccuracy in the forcing data could well be a cause of the consistent shortfall in sea surface temperatures (Fig. 3). Comparison of measured (M3A) data and the ECMWF forcing data shows that the ECMWF gives good estimates of air temperature, wind speed and mean sea level pressure, but a poor estimate of humidity. The average relative humidity for days one to 160 was 51% for the ECMWF and 65% for the M3A measured data. To investigate the significance of this difference, a simulation (spun up for a year from the PA3 standard initialisation), forced with the M3A humidity, rather than ECMWF data, was run. The accuracy of the M3A humidity sensor is ±3% (Nittis, pers. comm.). In the second half of the year, and at other times where no M3A data was available, an average value of 65% was used. This run resulted in a marked increase in modelled temperatures, and a much better fit with the chlorophyll data (Fig. 10). It also showed markedly stronger stratification than the previous run using the PA3 formulation (Fig. 4).

The chlorophyll peak that was being produced at between 40 and 70 days no longer appeared and a far lower, broader peak at around day 90 was found. It is apparent from this that the ecosystem function of the model is extremely sensitive to the quality of the humidity data used. Even when using rather patchy data, with average values used in periods of no data, a far better result is obtained than if using high resolution, but inaccurate, data.

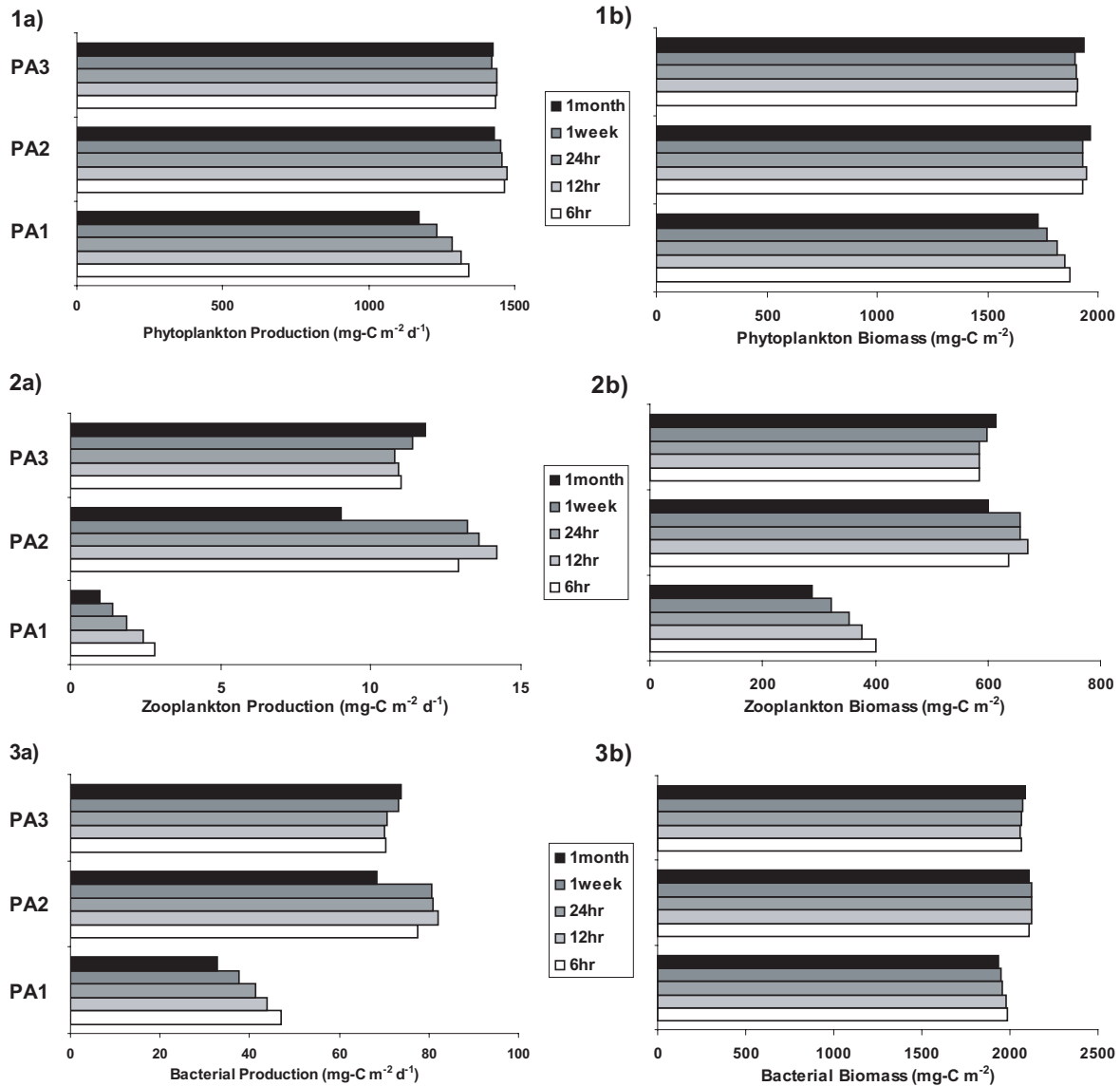The quality of the humidity data influences the behaviour

in forcing frequency (Fig. 9); the bacteria and phytoplankton biomass values were surprisingly unaffected by the use of extremely low temporal resolution surface forcing data. The PA3 run was particularly insensitive to changes in frequency of forcing, with little change in any of the annually averaged production values for the 6-, 12- or 24-hourly forced simulations, and relatively small changes when using weekly or monthly forcing. The production was more sensitive to frequency of forcing than the biomass, with the PA1 run showing by far the most sensitivity.

The chlorophyll concentrations showed little dependence upon the frequency of forcing. The differences were mainly in the fine scale detail, with the simulations that used lower frequency forcing showing damping of the short-term fluctuations in chlorophyll concentrations, but the main chlorophyll peak remaining of largely the same amplitude and timing.

Fig. 9. Comparison of the annually averaged **(a)** production and **(b)** biomass for (1) phytoplankton, (2) zooplankton and (3) bacteria for PA1, PA2 and PA3 runs using different forcing frequencies.

of the model, which indicates that the accuracy of other meteorological forcing data should be considered. Therefore, perturbations of the forcing variables were performed to compare the influence that these data have on the surface heat flux. These were run from the standard PA3 initialisation, and the differences in model behaviour over 160 days (the period of M3A data availability) analysed.

An increase in air temperature led to increases in sea surface temperature and stronger, earlier stratification, and vice versa. Similarly, increasing the humidity also acted to raise sea surface temperature (and give more pronounced stratification). The wind also had an effect upon stratification, with increased winds giving less stratification as would be expected.

The simulations that gave earlier stratification also had earlier phytoplankton blooms. These earlier blooms were more intense but shorter lived. When the onset of stratification was delayed the bloom became delayed and far less intense. The overall net effect upon the biomass and production is a balance between the longevity and intensity of the bloom, and hence there was no strict pattern as to how a change in air temperature or wind speed affected the net production or biomass (see Table 6). However, it is apparent that even relatively small offsets in the forcing data may have major effects upon the ecosystem function of the model. A comparison between a standard run and runs using perturbed forcing data show that substantial changes in heat flux can be induced (Fig. 11). Large, but realistic, perturbations over a period of a month give changes of the order of ± 50–$150\,\mathrm{W\,m^{-2}}$ differences in the total heat flux (compared with a heat flux of the order of -200–$200\,\mathrm{W\,m^{-2}}$). The strength of influence of the perturbation does not appear to be dependent upon its sign,

Table 6. Percent change in 160 day mean biomass (ΔB) and production (ΔP) for depth-integrated phytoplankton, zooplankton and bacteria with changes in forcing variables. Note the increase in relative humidity is scalar – a 20% increase in a humidity value of 50% gives 70%, not 60%

		Phytoplankton		Zooplankton		Bacteria	
		ΔP (%)	ΔB (%)	ΔP (%)	ΔB (%)	ΔP (%)	ΔB (%)
Humidity							
	+20%	−29.5	−12.1	−58.2	−32.2	−31.5	−2.8
	+10%	−7.0	−3.5	−15.5	−3.1	−1.8	2.4
	−10%	−5.3	−1.0	−0.4	1.7	3.1	0.4
	−20%	−2.4	1.6	6.7	5.9	7.0	1.6
Wind							
	+2 m/s	11.4	6.5	39.3	22.1	29.0	4.9
	+1 m/s	9.1	6.4	17.6	11.1	10.5	2.7
	−1 m/s	14.5	2.4	19.2	9.8	13.6	3.8
	−2 m/s	−9.9	−5.6	−33.9	−13.2	−15.6	−0.3
Air Temperature							
	+2°C	−7.9	−4.5	−31.4	−10.8	−13.5	0.2
	+1°C	10.1	2.4	17.6	10.5	13.5	3.6
	−1°C	3.4	3.7	10.5	7.3	7.4	1.7
	−2°C	17.4	6.9	50.6	23.7	32.5	6.2

and is significant for all three parameters investigated.

4 Discussion and conclusion

The behaviour of the biological model was shown to be sensitive to variations in the heat flux formulations used. It is difficult to judge the relative merits of these formulations, since they all produced broadly acceptable ecosystem responses. However, the combination of the Kondo and May formulations (simulation PA3) gave the best temperature validation, which is in agreement with Castellari et al. (1998). Annual average biomass and production estimates from the three simulations showed distinct differences, although all showed agreement with literature data. Changes in production were far greater than the changes in biomass, and zooplankton seemed to be particularly sensitive. The timing and amplitude of the spring bloom showed quite substantial differences for the different simulations. All three simulations had peaks of chlorophyll in the period between 60 and 90 days, yet stratification did not occur in any of the simulations until about day 80, with significant levels of stratification not occurring before day 100. In addition, the stratification occurred at similar times in the three runs, although with some difference in intensity, and yet the phytoplankton blooms occurred at quite different times. This does not fit with the classic theory of phytoplankton bloom development, which requires stratification to take place before blooming occurs

(e.g. Mann and Lazier, 1996). Huisman et al. (1999) developed a model where blooming may occur without stratification if the turbulence is below a critical level and the light penetration is sufficient for growth to occur. They suggest that in clear waters the critical turbulence theory would become important. The results of these simulations support this; the clear waters of the oligotrophic Cretan Sea allow the turbulence to dictate the onset of phytoplankton blooming, and hence, the timing of the spring bloom is sensitive to changes in turbulence induced by small changes in surface heat flux. This is illustrated in Fig. 12, which shows the temporal evolution of scalar eddy diffusion coefficients, primary productivity and phosphate concentration for the first 90 days of the simulation. In addition, this shows that in the PA2 and PA3 simulations strong mixing events ($K_H > 0.3 \, \text{m}^2 \, \text{s}^{-1}$) coincide with net respiration. The reduced exposure to light and poor adaptation to ambient light conditions due to the mixing of phytoplankton out of the euphotic zone is likely to be the cause. The same is not true for the PA1 simulation, where the mixing is less intense. Similarly, there appears to be a threshold of phosphate concentrations below which there is little primary production, as can be seen by the late winter lack of primary productivity in the PA1 simulation, in contrast to the PA2 and PA3 simulations. The PA2 and PA3 simulations have higher average vertical mixing constants than PA1, resulting in enhanced mixing of phosphate into the euphotic zone. A simple rule of thumb for this system seems
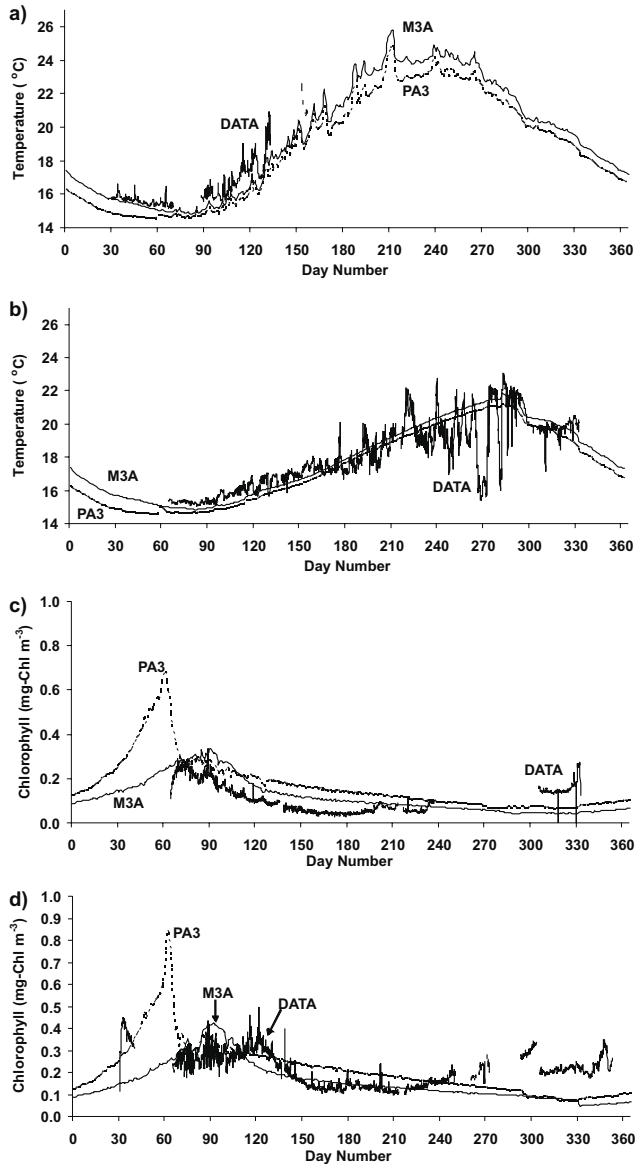
Fig. 10. Temperature at **(a)** the surface and **(b)** 40 m and chlorophyll at **(c)** 40 m and **(d)** 65 m for the standard PA3 run (solid line) and the PA3 run with M3A derived humidity (dashed line).
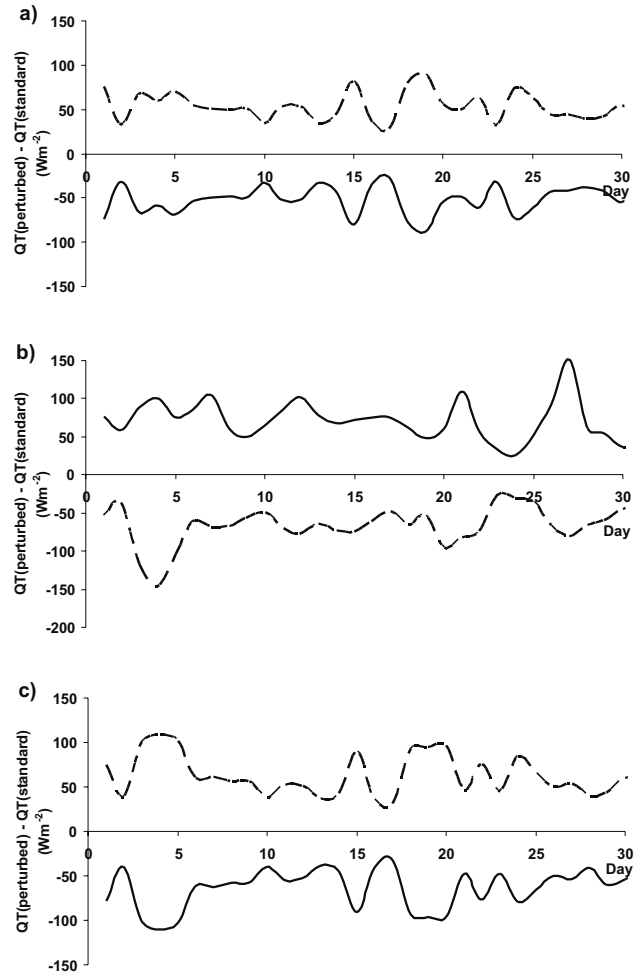

Fig. 11. The change in QT (net heat flux from the ocean to the atmosphere) in Wm^{-2} for **(a)** an increase of 20% (solid line) and a decrease of 20% (dashed line) of humidity, **(b)** an increase of $2\,ms^{-1}$ (solid line) and a decrease of $2\,ms^{-1}$ (dashed line) of wind speed and **(c)** an increase of $2°C$ (solid line) and a decrease of $2°C$ (dashed line) of air temperature.

to be that threshold values of phosphate of approximately $0.004\,mmol\,m^{-3}$ must be exceeded and eddy diffusion values of approximately $0.3\,m^2\,s^{-1}$ must not be exceeded for primary productivity greater than $100\,mg$–$C\,m^{-2}\,d^{-1}$ to occur. The surface heat flux, which, to a large extent, determines the turbulence of the surface waters, can, therefore, be seen to heavily influence biological behaviour through, first, determining the transport of phosphate up from deeper waters and second in determining the residence time of phytoplankton in the surface, euphotic waters.

The influence of the forcing frequency upon the biology was investigated. The main differences with changes in frequency forcing were found in the high-frequency phenomenon, which were reduced when using lower frequency

forcing data. The annual mean biological properties showed relatively little dependence upon the frequency of forcing data used, although the level of dependence varied for the different flux formulations. As with other simulations the major changes in the annual mean values were generally found in the production values, and the zooplankton data were most affected. This is consistent with the observation of Colebrook (1985) that the interannual variability in zooplankton in the North Sea is dependent upon phytoplankton abundance early in the year. It is felt that the model behaves similarly; Figure 8 shows the zooplankton biomass and production to be substantially higher in the simulations where the bloom occurs the earliest (PA3) or persists (PA2).

Even though changing the heat flux formulation had significant impacts upon the model function, it still did not significantly alter the fact that all three formulations significantly underestimated the surface heating. The model sim-

ulates the M3A site in the Cretan Sea, which is close to two gyres, to the east cyclonic and to the west anticyclonic (Georgopoulos et al., 2000). One-dimensional water column models are incapable of simulating the horizontal processes associated with these gyres. However, the sporadic advection to the gyres is thought unlikely to be responsible for the consistent underestimation of temperature. It is more likely that it is due to the well documented continuous input of heat to Mediterranean waters across the Gibralter Sill.

Other possible sources of error in the model were investigated, and the hydrodynamic properties of the simulations were found to be greatly improved when using humidity forcing based upon M3A data, even though the data set was incomplete and averages had to be used throughout much of the year. Improving the physical performance of the model was matched with a better simulation of the chlorophyll; the chlorophyll maximum was delayed significantly, and reduced in amplitude, to give a dramatically improved validation. Accurate meteorological forcing data, therefore, seems to be extremely important in ecosystem modelling.

In summary, the accuracy of meteorological data is of paramount importance in determining ecosystem behaviour in the 1-D ERSEM/POM model of a Cretan Sea site. The frequency of the forcing data is of only relatively minor importance, and has very little effect on any of the seasonal properties of the system. The heat flux formulation has a significant effect upon the biological function of the system. In the winter and early spring, when the system is overturning and hence, mesotrophic, the biomass is sensitive to changes in heat flux. The system is said to be under physical control, with nutrient availability being primarily dependent upon the strength and depth of mixing; small variations in the physical regime are amplified by the modelled biological system. Later in the year, when the water column stratifies and the system becomes oligotrophic, the variations in heat flux have little effect on the biomass estimates, and the system is under biological control; old production dominates, and the system becomes dependent upon bacterially mediated cycling of nutrients.

Therefore, in systems where this physical control is likely, great care must be taken to effectively model the physics if there is to be any chance of effectively predicting biological behaviour. During times of biological control, the physics becomes less important, and emphasis must be placed on paramaterizing the biogeochemical model. This has implications for data assimilation systems; ideally, both biological and physical parameters would be assimilated, but knowledge of the properties of the system would allow for judgement to be made on the relative importance of biological or physical parameters to the ecosystem function of the model.
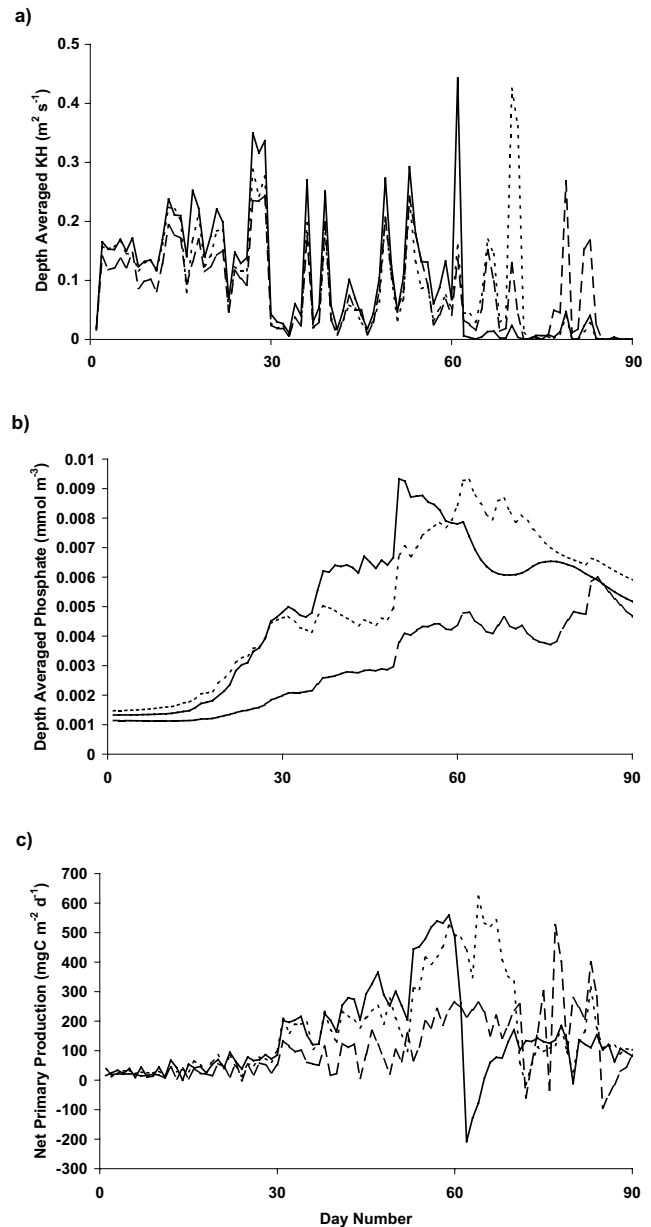
Fig. 12. Comparison of **(a)** vertical diffusion coefficient, depth averaged over whole water column (250 m), **(b)** phosphate concentration, depth averaged over the euphotic zone (surface 120 m) and **(c)** the depth integrated primary production over the whole water column, for the PA1 (large dashes), PA2 (small dashes) and PA3 (solid line) runs.

maps of the Mediterranean and Cretan Seas.

References

Allen. J. I., Somerfield, P. J., and Siddorn, J. R.: Primary and bacterial production in the Mediterranean Sea: a modelling study, J. Marine Sys., 33–34, 473–495, 2002a.

Allen J. I.: Simulating the spring phytoplankton bloom in the Humber Plume (UK) with a variable phytoplankton Carbon:Chlorophyll-a model. Proceedings of the Rome Euro-GOOS conference March 1999, (Ed) Flemming, N., Elsevier, Amsterdam, in press, 2002b.

Allen, J. I., Blackford, J. C., and Radford, P. J.: A 1-D vertically resolved modeling study if the ecosystem dynamics of the middle and southern Adriatic Sea, J. Mar. Sys., 18, 265–286, 1998.

Antoine, D., Morel, A., and Andre, J. M.: Algal pigment distribution and primary production in the Eastern Mediterranean as derived from Coastal Zone Color Scanner observations, J. Geophys. Res. Oceans., 100 (C8), 16 193–16 209, 1995.

Baretta, J. W., Ebenhöh, W., and Ruardij, P.: The European Regional Seas Ecosystem Model, a complex marine ecosystem model, Neth. J. Sea Res., 33, 233–246, 1995.

Baretta-Bekker, J. G., Baretta, J. W., Hansen, A. S., and Riemann, B.: An improved model of carbon and nutrient dynamics in the microbial food web in marine enclosures, Aquat. Microb. Ecol., 14, 91–108, 1998.

Bakhmetev, B. A.: Hydraulics of open channels, Eng. Soc. Monograph, McGrawhill, 1932.

Baretta-Bekker, J. G., Baretta, J. W., and Rasmussen, E. K.: The microbial food web in the European Regional Seas Ecosystem Model, Neth. J. Sea Res., 33, 363–379, 1995.

Blumberg, A. F. and Mellor, G. L.: A description of a three-dimensional coastal ocean circulation model, Three-Dimensional Coastal Ocean Models, (Ed) Heaps, N., AGU, Washington, D.C., 1987.

Budyko, M. I.: Climate and life, Academic Press, New York, 1974.

Castellari, S., Pinardi, N., and Leaman, K.: A model of air-sea interactions in the Mediterranean Sea, J. Marine Syst., 18, 89–114, 1998.

Chen, F. and Annan, J. D.: The influence of different turbulence schemes on modelling primary production in a 1-D coupled physical-biological model, J. Marine Syst., 26, 259–288, 2000.

Colebrook, J. M.: Continuous plankton records: overwintering and annual fluctuations in the abundance of zooplankton, Mar. Biol., 84, 261–265, 1985.

Dobson, F. W. and Smith, S. D.: Bulk models of solar-radiation at sea, Q. J. Roy. Meteor. Soc., 114 (479), 165–182, 1988.

Ebenhöh, W., Baretta, J. W., and Baretta-Bekker, J. G.: The primary production module in a marine ecosystem model ERSEM II, J. Sea Res., 38, 173–194, 1997.

Galperin, B., Kantha, L. H., Hassid, S., and Rossati, A.: A quasi-equilibrium turbulent energy model for geophysical flows, J. Atmos. Sci., 45, 55–62, 1988.

Garrett, C., Outerbridge, R., and Thompson, K.: Interannual variability in Mediterranean heat and buoyancy fluxes, J. Climate, 6, 900–910, 1993.

Geider, R. J., MacIntyre, H. L., and Kana, T. M.: A dynamic model of photoadaptation in phytoplankton, Limnol. Oceanogr., 41 (1), 1–15, 1996.

Georgopoulos, D., Chronis, G., Zervakis, V., Lykousis, V., Poulos, S., and Iona, A.: Hydrolgy and circulation in the Southern Cretan Sea during te CINCS experiment (May 1994–September 1995), Prog. Ocean., 46, 89–112, 2000.

Gotsis-Skretas, O., Kalliopi, P., Moraitou-Apostolopoulou, M., and Ignatiades, L.: Seasonal horizontal and vertical variability in primary production and standing stocks of phytoplankton and zooplankton in the Cretan Sea and the Straits and the Cretan Arc (March 1994–January 1995), Prog. Ocean., 44, 625–649, 1999.

Huisman, J., van Oostveen, P., and Weissing, F. J.: Critical depth and critical turbulence: two different mechanisms for the development of phytoplankton blooms, Limnol. Oceangr., 44(7), 1781–1787, 1999.

Ignatiades, L.: The productive and optical status of the oligotrophic waters of the Southern Aegean Sea (Cretan Sea), Eastern Mediterranean, J. Plank. Res., 20(5), 985–995, 1998.

Kondo, J.: Air-sea bulk transfer coefficients in diabatic conditions, Boundary-Layer Meteorol., 9, 91–112, 1975.

Lacroix, G. and Nival, P.: Influence of meteorological variability on primary production dynamics in the Ligurian Sea (NW Mediterranean Sea) with a 1-D hydrodynamic/biological model, J. Marine Syst., 16(1–2), 23–50, 1998.

Mann, K. H. and Lazier, J. R. N.: Dynamics of marine ecosystems: Biological-physical interactions in the oceans, 2nd Ed., Blackwell, Oxford, 1996.

Margalef, R.: Turbulence and marine life, Sci. Mar., 61, 109–123 (Suppl. 1), 1997.

Mellor, G. L. and Yamada, T.: Development of a turbulence closure-model for geophysical fluid problems, Rev. Geophys., 20 (4), 851–875, 1982.

Nittis, K., Tziavos, C., Thanos, I., Drakopoulos, P., Cardin, V., Gacic, M., Petihakis, G., and Basana, R.: The Mediterranean Moored Multi-sensor Array (M3A): System Development and Initial Results, Ann. Geophysicae, this issue, 2003.

Pingree, R. D., Holligan, P. M., and Mardell, G. T.: The effects of vertical stability on phytoplankton distributions in the summer on the northwest European Shelf, Deep-Sea Res., 25, 1011–1128, 1978.

Psarra, S., Tselepides, A., and Ignatiades, L.: Primary productivity in the oligotrophic Cretan Sea (NE Mediterranean): seasonal and interannual variability, Prog. Ocean., 46, 187–204, 2000.

Rosati, A. and Miyakoda, K.: A general circulation model for upper ocean simulation. J. Phys. Oceanogr., 18(11), 1601–1626, 1988.

Sharples, J. and Tett, P.: Modelling of the effect of physical variability on the midwater chlorophyll maximum, J. Mar. Res., 52(2), 219–238, 1994.

Tetens, O.: Uber einige meteorologische Begriffe, z. Geophys, 6, 297–309, 1930.

Tselepides, A., Zervakis, V., Polychronki, T., Danovaro, R., and Chronis, G.: Distribution of nutrients and particulate organic matter in relation to the prevailing hydrographic features of the Cretan Sea (NE Mediterranean), Prog. Ocean., 46 (2–4), 113–142, 2000.

Turley C. M., Bianchi M., Christaki U., Conan P., Harris J. R. W., Psarra, S., Ruddy G., Stutt, E. D., Tselepides, A., and Van Wambeke, F.: Relationship between primary producers and bacteria in an oligotrophic sea – the Mediterranean and biogeochemical implications, Mar. Ecol. Prog. Ser., 193, 11–18, 2000.

Varela, R. A., Cruzado, A., and Gabaldón, J. E.: Modelling primary in the North Sea using the European Regional Seas Ecosystem Model, Neth. J. Sea Res., 33, 337–361, 1995.

Vichi, M., Zavatarelli, M., and Pinardi, N.: Seasonal modulation of microbially mediated carbon fluxes in the northern Adriatic Sea – a model study, Fish. Oceanogr., 7 (3–4), 182–190, 1998.

Wallace, J. M. A. and Hobbs, P. V.: Atmospheric Science: An Introductory Survey, Academic Press, San Diego, 1977.

Zavatarelli, M., Baretta, J. W., Baretta-Bekker, J. G, and Pinardi, N.: The dynamics of the Adriatic Sea ecosystem. An idealized model study, Deep-Sea Res. (Oceans), 47(5), 937–970, 2000.

Turbulence as a control on the microbial loop in a temperate seasonally stratified marine systems model

J. Icarus Allen*, John R. Siddorn[1], Jerry C. Blackford, Francis J. Gilbert

Plymouth Marine Laboratory, Prospect Place, West Hoe, Plymouth, PL1, 3DH, UK

Abstract

The European Regional Seas Ecosystem Model (ERSEM) has been coupled with the General Ocean Turbulence Model (GOTM) to create a 1-D representation of a seasonally stratified site in the North Sea. This model has been validated and shown to reproduce biomass and production measurements successfully. The model was then used to investigate the role of turbulence in transporting nutrients across the thermocline. It was found that the turbulence characteristics control the pumping of nutrients into the mixed layer and the export of carbon into the deeper layers. Hence primary production in the thermocline is driven by the import of nutrients and inhibited by the export of carbon. Furthermore it is demonstrated that the temporal variability of production is strongly influenced by fluctuations in solar irradiance. The effect of tidal mixing upon nutrient transport leads to a 23% increase in primary production compared to a simulation without tidal mixing. On a spring tide, nutrient pumping enhances phytoplankton growth. As the tide moves from springs towards neaps, the phytoplankton above the thermocline become nutrient stressed and undergoes lysis. The resultant release of dissolved organic carbon drives bacterial production in this region. The optimal position for grazers is found to lie where the peaks of bacterial and phytoplankton biomass overlap. External physical forcing is found to indirectly drive both the microbial loop and secondary production, thus demonstrating that changes in the stratification of the water-column influences the development of the microbial loop. Zooplankton biomass and grazing is substantially enhanced in the tidally forced model leading to an increase in the production of fast sinking POM which in turn impacts substantially on the flux of carbon to the seabed. Hence the degree of stratification ultimately influences the benthic pelagic coupling. Additionally, we present a simple scheme to classify both the physical and biological properties of the system.
© 2004 Published by Elsevier B.V.

* Corresponding author. Tel.: +44-1752-633-468; fax: +44-1752-633-101.

E-mail address: jia@pml.ac.uk (J.I. Allen).

[1] Present address. UK Meteorological Office, The Hadley Centre, London Road, Bracknell RG12 2SY, UK.

1. Introduction

It is well known that turbulent processes and stratification are often important in determining physical and biological processes (e.g. Zakardjian and Prieur, 1994; Mann and Lazier, 1996; Huisman et al., 1999; Luyten et al., 2002). Tidal and surface currents interact with turbulence via the vertical

shear, generated by surface stress, tidal bottom friction and waves. In shelf seas the seasonal thermocline is an important physical barrier between the surface mixed layer and deeper water. Key biological processes, such as primary production and the generation and supply of nutrients, are highly sensitive to not only the precise depth of the thermocline but also the amount of turbulence and turbulent diffusion within the thermocline. The temperature (and hence density) gradient associated with the thermocline acts to restrict the diapycnal transfer of the systems properties (e.g. heat, momentum, oxygen, nutrients, algal biomass). This region is the transition zone between a light-rich, nutrien-poor surface layer and darker nutrient-rich deeper waters and is often characterised by a subsurface maximum (SSM) of chlorophyll and a sharp nutricline. Two main processes dominate the production and maintenance of these features, the supply of nutrients from deeper waters into the subsurface chlorophyll maxima, stimulating growth and the removal of carbon by mixing cells from the bottom of the maxima into deeper waters.

In shelf seas the tide often exerts a significant influence upon turbulent production. Sharples et al. (2001) suggest that the vertical flux of nitrate across the thermocline is associated with the depth-integrated tidal energy dissipation, with increased tidal energy leading to increased nitrate transfer. They also demonstrated that up to 25% of the gross annual production in shelf seas could be exported into the bottom mixed layer. Horne et al. (1996) showed that on the Georges Bank, the flux of nitrate up the water column varied with tidal strength and stratification. The transfer of nutrients across the thermocline varies significantly in different stratified systems. For example nitrogen transport of $0.8-3.2$ mmol N m^{-2} d^{-1} has been estimated for a station in the western English Channel (Sharples et al., 2001), whilst values of $3-11$ mmol N m^{-2} d^{-1} have been calculated for the Georges Bank (Horne et al., 1996). This compares with measured oceanic nitrogen transfer in an oligotrophic stratified system of ~ 0.14 mmol N m^{-2} d^{-1} (Lewis et al., 1986) and $0.05-0.5$ mmol N m^{-2} d^{-1} (Planas et al., 1999). The understanding of the physical controls on the supply of nutrients across the thermocline has implications for the understanding of global carbon budgets, with many of the productive coastal regions of the world being stratified for significant periods of time.

The aim of this work is to investigate how turbulence and related processes influence biological behaviour in a seasonally stratified system. Particularly to explore the hypothesis that stratified water columns induce development of a microbial loop dominated system with little vertical export of particulate material.

To achieve this we implement (to investigate the suitability of such a modelling system) a coupled 1-D physical ecosystem model of a seasonally stratified site at high vertical resolution. The site chosen for this work was sampled during the North Sea Project (Simpson, 1993) from August 1988 to October 1989 for physical and biological parameters (Joint and Pomroy, 1993; Prandle et al., 1997). The seasonal properties of the southern North Sea are well documented for this period (Lowry et al., 1992; Howarth et al., 1993). Furthermore, the site is relatively unaffected by direct terrigenous inputs of nutrients, with the regeneration of nutrients through biological processes dominating the nutrient inputs (Howarth et al., 1993). The site CS, is situated at $55°30'$N $0°55'$E (Fig. 1) in

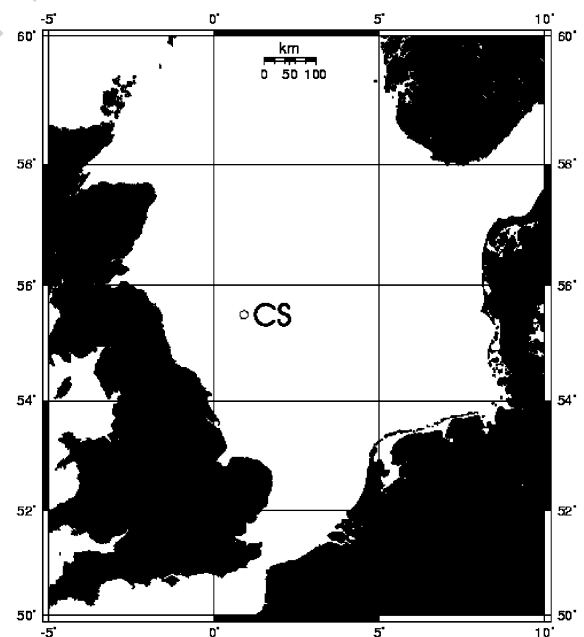

Fig. 1. The location of the site CS, in the North Sea at $55°30'$ N, $1°00'$ E.

approximately 85 m of water. CS has been the focus of several previous modelling studies. Tett and Walne (1995) used a simple NPZ model which did not include the microbial loop combined with a Krause-Turner mixed layer model. This provided a satisfactory simulation of the spring phytoplankton bloom and nitrate concentrations. Sharples and Tett (1994) combined the same NPZ model with a 1-D vertically resolved turbulence closure model (Mellor and Yamada, 1974) and demonstrated that variations in surface wind stress episodically weaken the thermocline, allowing nutrient transport and helping to maintain the SSM. In this paper we aim to take this work further by investigating the roles of turbulence and light in controlling phytoplankton, bacteria and zooplankton growth during the thermally stratified summer period.

2. Methods

A version of the European Regional Seas Ecosystem Model (ERSEM) (Baretta et al., 1995; Baretta-Bekker et al., 1995, 1998; Ebenhöh et al., 1997), has been coupled with the General Ocean Turbulence Model (GOTM) (Burchard et al., 1999) to produce a state-of-the-art marine systems model.

2.1. Physical model

GOTM is a 1-D physical model designed as a generic system for marine modelling. For this work we have used the k-ε model, where k is the turbulent kinetic energy (m^2 s^{-2}) and is calculated from:

$$\frac{\partial k}{\partial t} = \frac{\partial}{\partial z}\left(v_k \frac{\partial k}{\partial z}\right) + P + B - \varepsilon \tag{1}$$

where v_k is the eddy viscosity, P the shear production and B the buoyancy production and ε is the turbulent dissipation rate. The shear production (P) is given by:

$$P = v_k M^2 \tag{2}$$

where M is the shear frequency (s^{-1}) and is a measure of the rate of change of the vertical velocity gradient:

$$M = \sqrt{\left(\frac{\partial^2 u}{\partial z^2} + \frac{\partial^2 v}{\partial z^2}\right)} \tag{3}$$

Similarly, the buoyancy production (B) is given by:

$$B = v_z N^2 \tag{4}$$

where v_z is the eddy diffusivity, used to transport the scalar properties in both the physical and biological submodels, and N (the Brunt-Väisälä frequency, s^{-1}) is a function of the buoyancy gradient:

$$N = \sqrt{\frac{\partial b}{\partial z}} \tag{5}$$

The dissipation rate, ε, i.e. the rate at which turbulent kinetic energy is dissipated into heat by means of viscous friction is calculated from:

$$\frac{\partial \varepsilon}{\partial t} = \frac{\varepsilon}{k}(c_{\varepsilon 1} P + c_{\varepsilon 3} B - c_{\varepsilon 2} \varepsilon) \tag{6}$$

where $c_{\varepsilon 1} = 1.44$, $c_{\varepsilon 2} = 1.92$ (Rodi, 1987), and $c_{\varepsilon 3} = 1.0$ for stable stratification and -0.8 for unstable stratification (Burchard, pers. comm., 2002). The turbulent length scale (L) is calculated as in Blanke and Delecleuse (1993), with the Galperin et al. (1988) limitation applied. Eddy viscosity and diffusivity are calculated using equations of the form:

$$v_k = c_\mu \sqrt{k} L \tag{7}$$

where c_μ is the stability function, calculated as in Schumann and Gerz (1995). The dissipation rate is related to the length scale by:

$$\varepsilon = (c_\mu^0)^3 \frac{k^{3/2}}{L} \tag{8}$$

where c_μ^0 is a constant with the value 0.5562. These methods have been demonstrated to give good simulations of observed turbulent dissipation data in the stratified waters of the northern North Sea (Burchard et al., 2002).

At the sea surface, fluxes of heat and momentum are calculated. The net flux of heat (Q_T) across the air-sea interface is given by

$$Q_T = Q_E + Q_H + Q_B \tag{9}$$

where Q_E is the latent heat of evaporation flux, Q_H is the sensible heat flux and Q_B is the longwave radia-

tion flux. Additionally the solar radiation flux (Q_s) down the water is modelled as:

$$Q_s = \frac{1}{C_p \rho_0} \frac{\partial I_z}{\partial z} \tag{10}$$

where I_z is the energy flux into the cell (described in the light model), ρ_0 is the water density (approximated to 1027 kg m^{-3})and C_p is the specific heat capacity of seawater (3980 J kg^{-1}K^{-1}).

The sensible (Q_H) and latent heat (Q_E) fluxes are calculated using standard formulae (Casterllari et al., 1998). The calculations for the latent and sensible heat are dependent upon the calculations of their coefficients, which are a function of air-sea temperature difference, wind speed and a stability criterion for the surface waters (Kondo, 1975). The longwave (back) radiation (Q_B) is calculated using the May formulation (Budyko, 1974). The surface stress is calculated from the wind stress.

Temperature and salinity profiles from the North Sea Project (Lowry et al., 1992), at approximately monthly resolution, were used to constrain the model temperature and salinity using a simple relaxation assimilation method (Burchard et al., 1999). The reasons for applying this technique are discussed later.

2.2. The light model

The daily mean solar radiation at the surface ($\overline{I_0}$) used to drive the primary production modules is calculated from astronomical values:

$$\overline{I_0} = -\left(\frac{\sin(d) \cdot \sin(\varphi) \cdot D}{2} + \cos(d) \cdot \cos(\varphi) \right. $$
$$\left. \cdot \sin\left(\frac{D}{2}\right) \right) \cdot \frac{S}{\pi} \cdot (1 - 0.72C) \tag{11}$$

where S is the solar radiation constant (1368 Wm^{-2}), d is the solar declination (°), D is the daylength (in days), φ is the latitude (°) and C is the cloud cover. The instantaneous radiation (I_z) used in the physical model is calculated from the daily mean value using:

$$I_z = \overline{I_z} \cdot \left(\cos\left(\frac{T}{2D}\right) + 0.5\left(1 + \cos\left(\frac{T}{D}\right)\right) \right) $$
$$\cdot 2 \cdot \frac{\pi}{4 + \pi} \tag{12}$$

where T is the time in the day (with 0 as midnight and 0.5 as midday).

Light is attenuated as it is transmitted down the water column to give light at depth Z ($\overline{I_z}$):

$$\overline{I_z} = \overline{I_0}\exp(-K_d Z) \tag{13}$$

where K_d is an extinction coefficient. K_d is dependent upon a background extinction coefficient, and variable components of extinction due to shading by phytoplankton, detritus and silt. Thus the physical model influences the biological model through shading by phytoplankton.

2.3. The ecosystem model

ERSEM is a generic ecosystem model which was originally developed and applied in the context of the North Sea (e.g. Baretta et al., 1995; Radach and Lenhart, 1995; Pätsch and Radach, 1997; Allen et al., 2001). It has also been successfully applied in the Mediterranean Sea (Allen et al., 2002; Siddorn and Allen, 2003), the Adriatic Sea (Allen et al., 1998; Vichi et al., 1998; Zavatarelli et al., 2000) and the Arabian Sea (Blackford and Burkill, 2002).

ERSEM is a modelling framework in which the ecosystem is represented as a network of physical, chemical and biological processes. A schematic of the pelagic trophic links is given in Fig. 2. A 'functional group' approach is used to describe the biota. The ecosystem is subdivided into three functional types: primary producers, consumers and decomposers, and subdivided on the basis of trophic links and/or size. It should be noted that individual species may straddle more that one functional group, and that the functional groups describe particular types of behaviour rather than species lists.

Physiological (ingestion, respiration, excretion and egestion) and population (growth, and mortality) processes are included in the descriptions of functional group dynamics. These dynamics are described by fluxes of carbon and nutrients between functional groups. Each functional group is defined by a number of components, namely carbon, nitrogen, and phosphorus and, in the case of diatoms silicon, each of which is explicitly modelled.

Detailed descriptions of ERSEM and its pelagic sub-models can be found in Baretta et al. (1995),
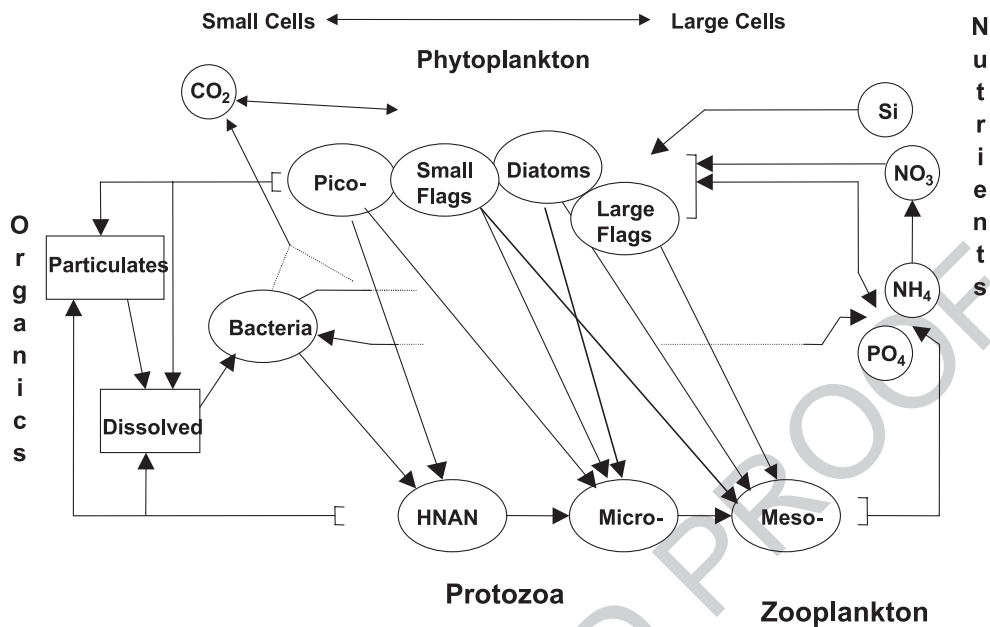
Pelagic Food Web - Trophic Model

Fig. 2. Diagram showing the trophic links in the ERSEM pelagic ecosystem.

Baretta-Bekker et al. (1995, 1998) and Ebenhöh et al. (1997). Although the simulations include the benthic processes, in the analysis that follows we do not consider them in any detail and the modules are not described. Detailed descriptions can be found in Blackford (1997) and Ebenhöh et al. (1995).

The phytoplankton community is described by four functional types; picophytoplankton (0.2–2 μm), small autothrophic flagellates (2–20 μm), large autotrophic flagellates (20–200 μm) and diatoms (20–200 μm). The phytoplankton populations' adaptation to ambient light is described by an optimal light parameter, which is transported along with the biomass terms and relaxes towards the ambient light levels. Light in the water column is modelled from astronomical values, corrected by cloud cover, to give PAR at the sea surface. Photosynthetic production is a function of temperature, availability of and adaptation to light and phytoplankton biomass. In the case of diatoms silicon availability is also considered. Nutrient limitation is a function of the internal C:N and C:P ratios of the phytoplankton.

Nutrient stress lysis (partitioned between particulate and dissolved detritus), excretion (activity excretion and nutrient stress excretion) to the dissolved phase and respiration (activity respiration and basal metabolism, related to ambient temperature) are the loss processes for the phytoplankton groups. Sedimentation of phytoplankton is assumed to occur if they are nutrient stressed.

Three zooplankton functional groups are described: mesozooplankton, microzooplankton and heterotrophic nanoflagellates. Grazing uptake is a function of a maximal assimilation rate, temperature, food availability and the zooplankton biomass. The trophic pathways are shown in Fig. 2. Respiration loss consists of two terms, a temperature dependent rest respiration and an activity respiration. Excretion is a function of assimilation efficiency and excreted fraction of uptake and is split between particulate detritus and dissolved organic carbon. Mortality loss consists of two terms, one triggered by low oxygen conditions and a constant term. As with excretion, mortality loss is split between the dissolved and particulate fraction. The zooplankton itself may also be preyed upon. An over-wintering function has been applied to the mesozooplankton description in order to compensate

340
341

309 for the omission of life cycle processes. The mes-
310 ozooplankton is assumed to become sedentary when
311 (depth-integrated) food supply falls below a given
312 threshold. In this 'over-wintering state' biomass is
313 only affected by a minimal mortality and respiration
314 rate. An increase in food availability over the
315 threshold in spring provides the cue for the meso-
316 zooplankton to resume its normal physiological and
317 ecological role.
318 There is one pelagic decomposer functional group,
319 bacteria. Bacterial uptake is a function of potential
320 assimilation rate, temperature, oxygen availability and
321 the concentration and nutrient quality of the food
322 source (dissolved organic matter). Respiration loss
323 consists of two terms, a temperature-dependent rest
324 respiration and an activity respiration which contains
325 a variable component dependent on the ambient
326 oxygen saturation. Mortality is given by a tempera-
327 ture-dependent rate. Additionally bacteria are consid-
328 ered to mediate the breakdown of particulate organic
329 matter to dissolved organic matter according to the
330 nutritional content of the particulate fraction.
331 The particulate carbon model has been subdivided
332 into three classes with differing sink rates whose
333 sources are related to the size of functional groups
334 as follows: 200 μ faecal material from mesozooplank-
335 ton, sink rate 10 m d^{-1}; >20 μ faecal material and
336 grazing by microzooplankton, diatoms, dinoflagel-
337 lates, sink rate 1.0 m d^{-1}; <20 μ picoplankton,
338 autotrophic flagellates, excretion and grazing by het-
339 erotrophic nanoflagellates, sink rate 0.1 m d^{-1}.

2.4. Model set-up

342 Depth profiles of temperature, salinity and sedi-
343 ment along with surface meteorological data and tidal
344 constituents were used to force the model. The mete-
345 orological forcing data (six hourly air temperature at 2
346 m (T_A), 10 m winds, and cloud cover, dew point
347 temperature (T_D) and mean sea level pressure (P_A))
348 were supplied by the European Centre for Medium-
349 range Weather Forecasts. T_D and P_A data were used to
350 calculate relative humidity (RH) based on the formu-
351 lation in Wallace and Hobbs (1977), using the calcu-
352 lation of the saturation vapour pressure (E_S) of Tetens
353 (1930). Evaporation and precipitation are not consid-
354 ered. The tidal constituents for M2 and S2 tides used
355 to force the model were taken from the simulations
356 described in Sinha and Pingree (1997).
357 The model was run using a three year repeating
358 cycle of forcing data for 1987 as a 'spin-up' period to
359 allow the model to reach a quasi-equilibrium state and
360 provide initial conditions. The simulations presented
361 here are from August 1988 to September 1999, the
362 period of the North Sea project.

3. Results and discussion

3.1. Seasonal cycles and validation

366 The simulation of the North Sea site CS (Fig. 1)
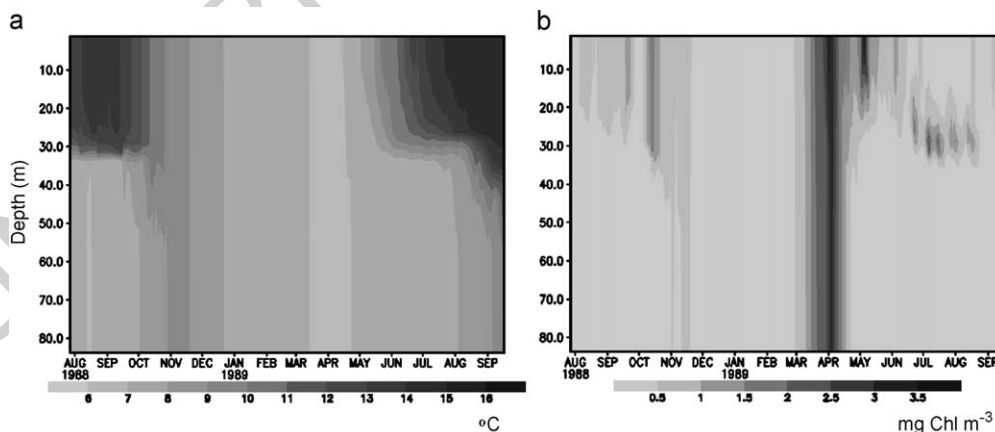367 gives the temporal evolution of temperature and

Fig. 3. The model output for the North Sea Project period for (a) temperature (°C), and (b) chlorophyll (mg C m^{-3}).
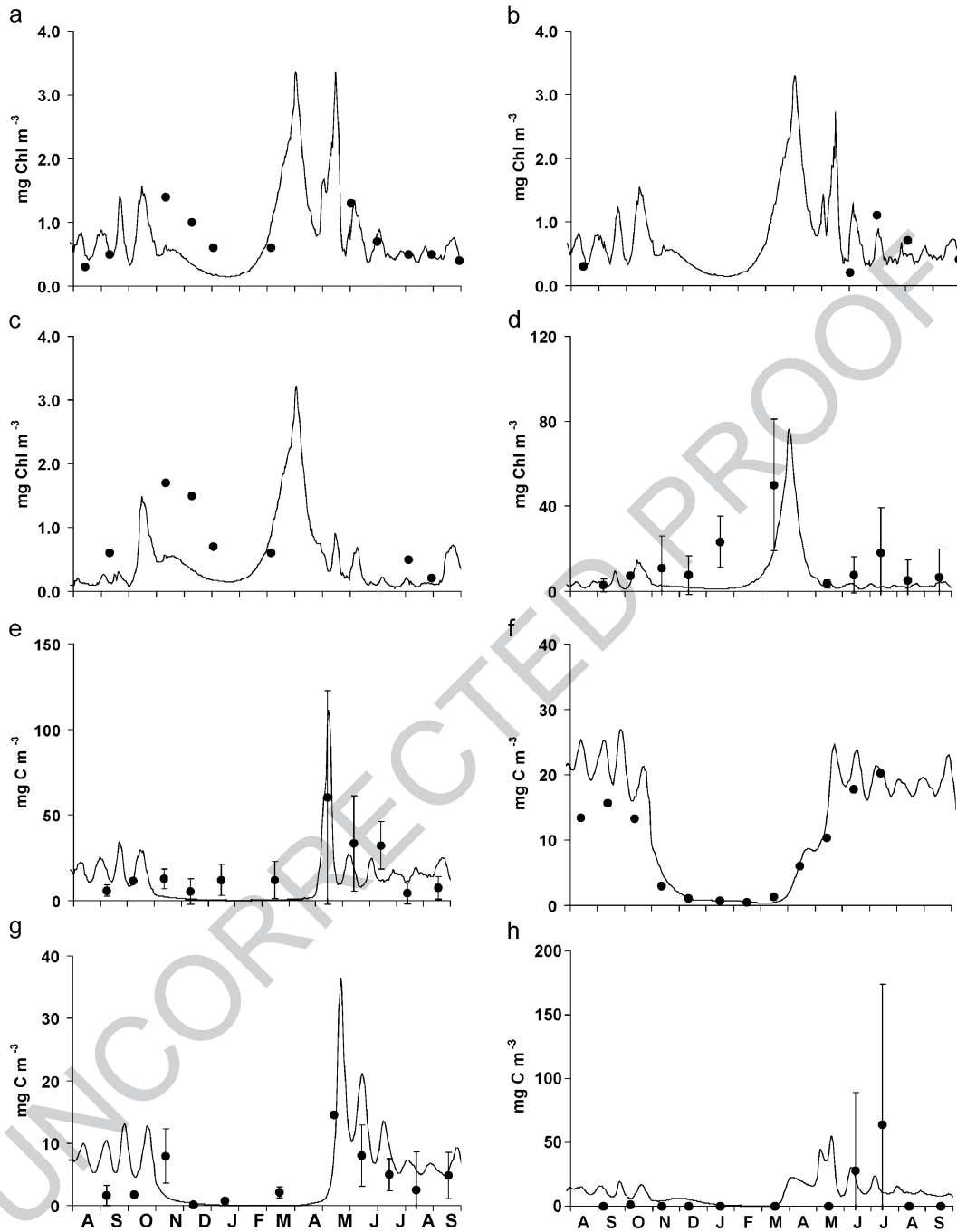
Fig. 4. Seasonal succession graph for August 1989–September 1999 of modelled (line) and measured (circles) chlorophyll (mg C m^{-3}) for (a) NSP data, depths 0–10 m, model data at 5 m, (b) NSP data, depths 15–25 m, model data at 20 m, (c) NSP data, depths 35 m–40 m, model data at 40 m and ERBAS biomass (mg C m^{-3}) for (d) diatoms, (e) flagellates, (f) mesozooplankton, (g) microzooplankton, (h) heterotrophic flagellates.

368 chlorophyll as shown in Fig. 3 for the period of the
369 North Sea Project. The system is stratified to a depth
370 of 30 m in late summer 1988, the stratification deep-
371 ens during the autumn and is finally mixed out by mid
372 November. In the spring of 1989, the onset of strat-
373 ification occurs in mid May, with a thermocline
374 forming at 30 m, which persists at this depth during
375 the summer before starting to deepen in September. In
376 order to correctly reproduce the observed thermocline
377 a simple assimilation scheme using the relaxation
378 method described in Burchard et al. (1999) was
379 applied to take account of horizontal advective pro-
380 cesses. Without this the mixed layer is found to be too
381 shallow (lying at 20 m rather than 30 m). Sharples and
382 Tett (1994) have previously noted the underestimation
383 of the depth of the mixed layer at this site when using
384 1-D turbulence models.
385   In the summer of 1988, the chlorophyll is mainly
386 found in the surface 30 m, with values ranging from
387 0.3 to 1.5 mg C m^{-3}. As the summer progresses and
388 the pycnocline deepens and weakens, the chlorophyll
389 maximum also deepens until stratification disappears
390 in November and the production is mixed throughout
391 the water column. Over the winter period chlorophyll
392 stays below 0.5 mg C m^{-3}, and is well mixed
393 throughout the water column. Chlorophyll concentra-
394 tions begin increasing again by the middle of Febru-
395 ary, with the maximum of 3.3 mg C m^{-3} being found
396 at the beginning of April. The chlorophyll is still well
397 mixed down the water column until the onset of a
398 second, less intense, bloom in early May, which is
399 triggered by the onset of stratification and then tracks
400 the depth of the pycnocline at around 30 m for the
401 remainder of the summer.

402 Modelled chlorophyll concentrations agree well
403 with the data (Fig. 4a, b, c), although it should be
404 noted that the model uses fixed carbon to chlorophyll
405 ratios and therefore the carbon biomass is a better test
406 of the models efficacy. The ERBAS data set (Baretta-
407 Bekker et al., 1995) gives values of carbon biomass
408 for diatoms, autotrophic flagellates, microzooplankton
409 and heterotrophic flagellates and data from the Con-
410 tinuous Plankton Recorder give mesozooplankton
411 values (Broekhuizen et al., 1995), which are com-
412 pared in Fig. 4d–h with the model data. These show
413 excellent agreement, indicating that the ERSEM mod-
414 el represents the biomass at different trophic levels
415 effectively. In Fig. 5 the simulations are compared to
416 measured North Sea Project surface primary produc-
417 tion data (I. Joint, pers. comm., 2002) and estimated
418 bacterial production rates from a comparable season-
419 ally stratified Celtic Sea site (Joint et al., 2001). These
420 both show good agreement.

421 Modelled and observed nitrate, phosphate and
422 silicate concentrations start to deplete in the euphotic
423 zone in March and reach a minimum in the spring.
424 Nutrients remain depleted in the euphotic zone,
425 which is bounded by a distinct nutricline during
426 the summer, and are replenished by vertical mixing
427 when the thermal stratification breaks down in the
428 autumn. The comparison of observed and modelled
429 nutrient data shows good agreement (Fig. 6a–h).
430 This suggests that the nutrient cycling may be
431 dominated by in-situ recycling mechanisms, and that
432 advective transport of nutrients may be of secondary
433 importance.

434 To investigate how light and turbulence influence
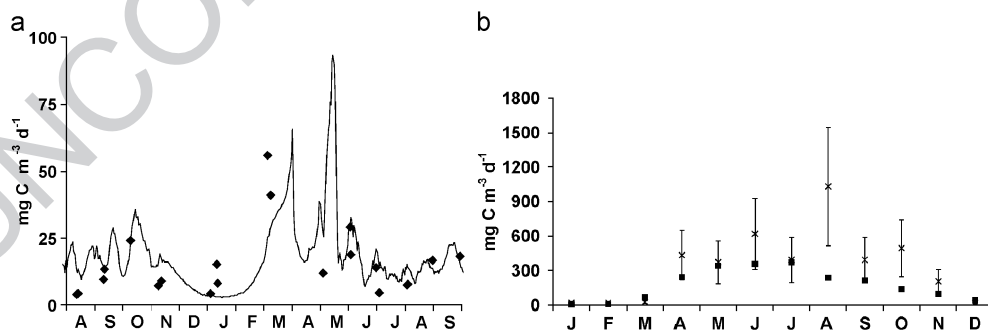435 the biological function of the system, four simulations

Fig. 5. (a) Seasonal succession graph for August 1989–September 1999 of modelled and North Sea Project primary production (mg C m^{-3} d^{-1}), (b) and the estimated annual cycle of bacterial production for the Celtic Sea (mg C m^{-3} d^{-1}).
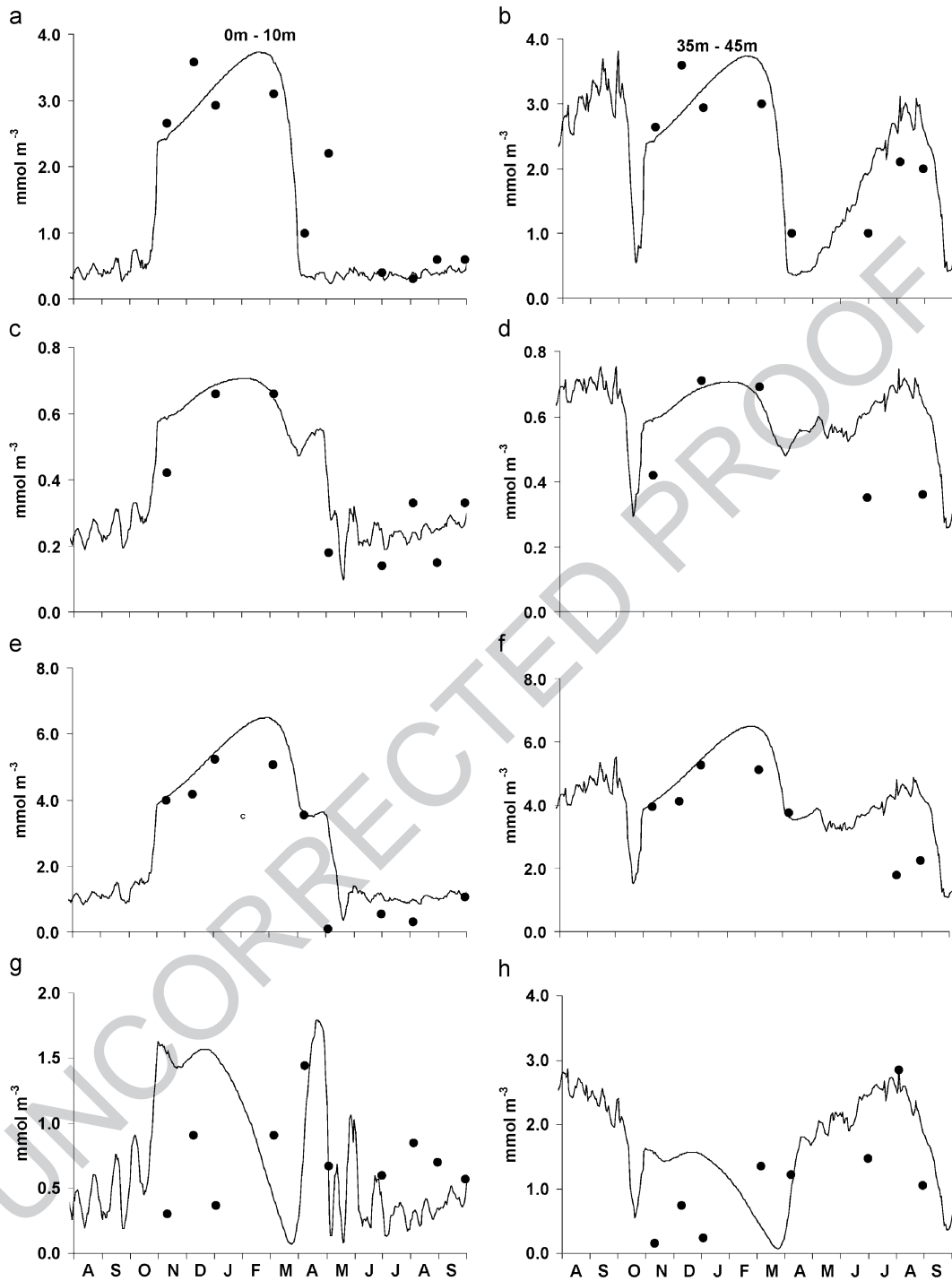
Fig. 6. Seasonal succession graphs for August 1989–September 1999 of modelled and NSP nutrient concentration (mmol m^{-3}) at depths 0–10 m (left) and 35–45 m (right) for (a, b) silicate, (c, d) phosphate, (e, f) nitrate and (g, h) ammonia.
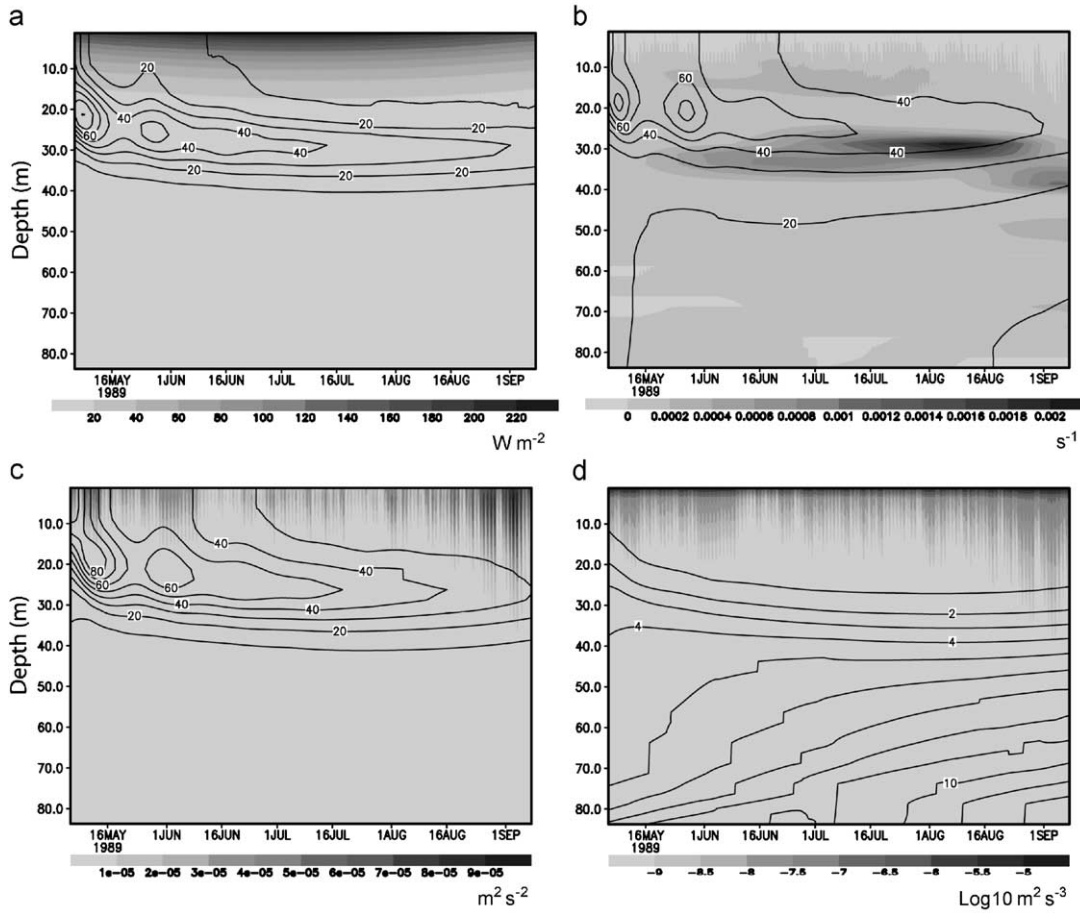
Fig. 7. Scenario A. No tide, constant cloud cover, 6 hourly meteorological forcing for days late spring and summer 1989 (Julian days 125–250 inclusive): (a) irradiance (W m^{-2}) and phytoplankton biomass (mg C m^{-3}), (b) Brunt Väsiälä frequency (s^{-1}) and bacterial biomass (mg C m^{-3}), (c) turbulent kinetic energy (m^2 s^{-2}) and zooplankton biomass (mg C m^{-3}), (d) log10 (turbulent dissipation) (m^2 s^{-3}) and nitrate (mmol m^{-3}).

were run with hourly output for the period mid May to early September 1989 to investigate the controlling factors on the development and maintenance of the sub surface production over the summer period.

3.2. Sensitivity analysis

We start with the simplest situation, where the model is forced with constant cloud cover and no tidal mixing (run A). This is illustrated in Fig. 7. Under these circumstances, a SSM of phytoplankton biomass forms at about 25 m and its position appears to be controlled by the region of maximum buoyancy gradient. The bacterial biomass lies above the SSM and the peak zooplankton biomass forms a layer between the two. Some predator-prey interaction occurs in late May/early June, which is then damped out by mid summer. This is confirmed by the biomass

Fig. 8. Evolution of the simulation autotrophic and heterotrophic community structure during the summer period (scenario A (a, b), scenario B (c, d), scenario C (e, f) and scenario D (g, h)). P1c = diatoms, P2c = autotrophic flagellates (2–20μ), P3c = picoplankton (<2μ), P4c = autotrophic flagellates (>20μ), Z4c = mesozooplankton (>200 m), Z5c = microzooplankton (20–200μ), Z6c = heterotrophic flagellates (<20μ), B1c = heterotrophic bacteria.

Legend: □P1c ■P2c □P3c ■P4c

Legend: □Z4c ■Z5c □Z6c ■B1c
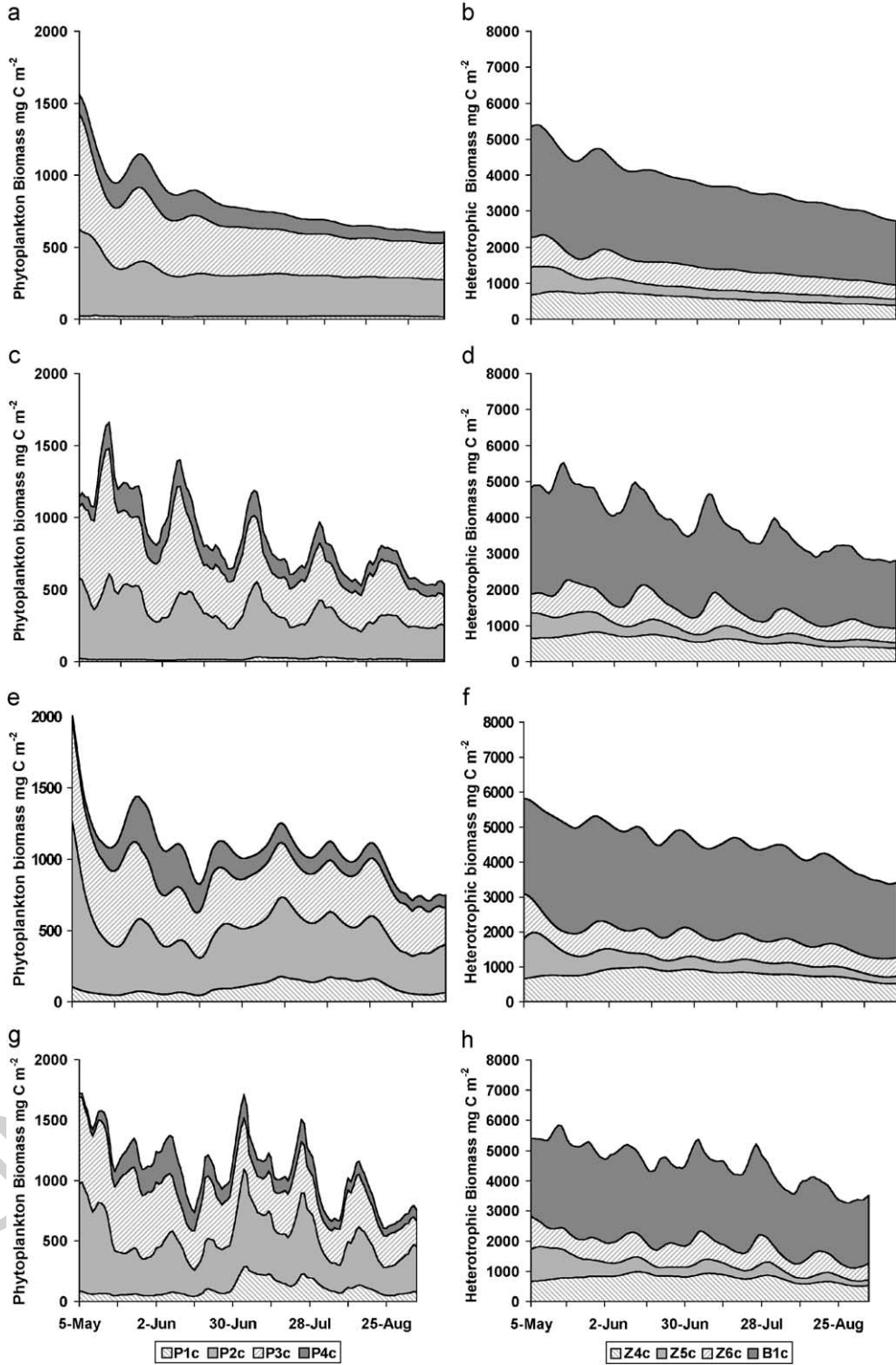
distributions shown in Fig. 8a, b and by phase diagram of both biomass and production (not shown). It should be noted that the diatoms are not a significant part of the phytoplankton community in this run.

When the simulation is re-run forced with variable cloud cover and no tide (run B) the SSM growth spots occur at approximately 20–24 d intervals (Fig. 9). The high biomass peaks of bacteria lie directly above the phytoplankton and the zooplankton maximum occurs in between the two lagged by a few days. Fig. 10a shows the relationship between the surface irradiance and the net primary production after the seasonal trends have been removed. Light explains 65% (R = 0.81) of the variability in the de-trended primary production suggesting that light is the dominant source of variability. The biomass pulses that

occur at 20–24 d intervals appear to be due to predator-prey interactions, suggesting that the variability in the light forcing is being amplified by the biological system. This behaviour can be replicated by running the model with a randomly generated cloud forcing confirming this assertion.

In run C (Fig. 11) the simulation is forced with the observed tidal signal and constant cloud cover. The addition of tidal forcing causes the SSM to form a month later and the nutrient pumping to occur. A significant consequence of this is a general increase in biomass and the presence of diatoms (Fig. 8e). Additionally the proportion of heterotrophic biomass contributed by bacteria decreases (Fig. 8f), indicating a shift in ecosystem behaviour away from the microbial loop. In May and June when significant phytoplank-
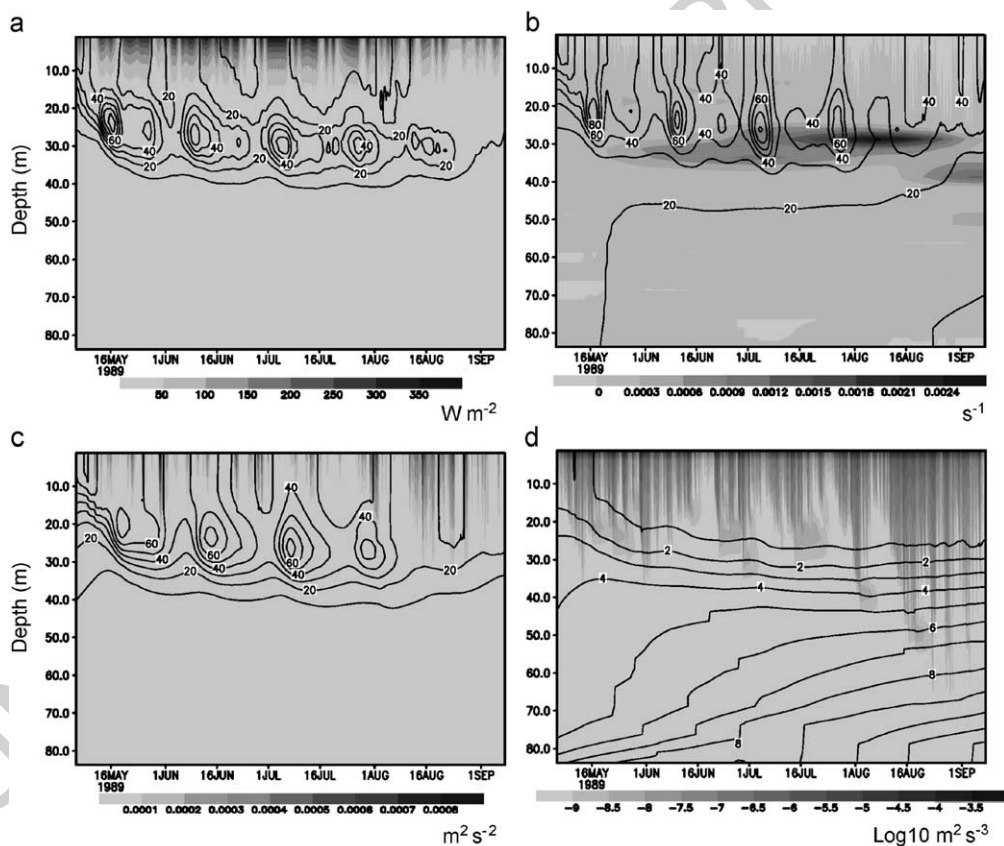

Fig. 9. Scenario B. No tide, 6 hourly meteorological forcing for days late spring and summer 1989 (Julian days 125–250 inclusive): (a) irradiance (W m^{-2}) and phytoplankton biomass (mg C m^{-3}), (b) Brunt Väsiälä frequency (s^{-1}) and bacterial biomass (mg C m^{-3}), (c) turbulent kinetic energy (m^2 s^{-2}) and zooplankton biomass (mg C m^{-3}), (d) log10 (turbulent dissipation) (m^2 s^{-3}) and nitrate (mmol m^{-3}).

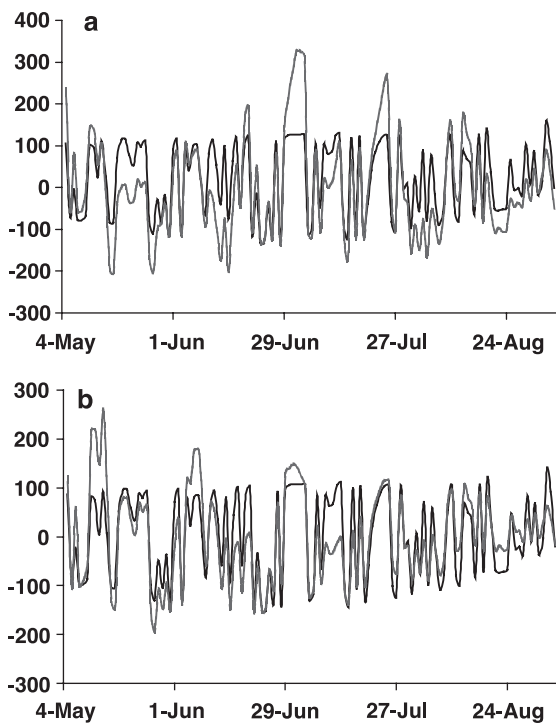Fig. 10. Net primary production, light line (mg C m^{-2} d^{-1}) and surface irradiance, solid line (W m^{-2}) after the seasonal trends have been removed for (a) scenario B, (b) scenario C.

485 ton growth is taking place in the surface layer, peaks
486 in production occur just after the spring tide turbu-
487 lence maxima, indicating that nutrient supply is driv-
488 ing these pulses. From July onwards the bulk of the
489 production takes place in the SSM, and the biomass
490 peaks occur on the neap tide turbulence minima,
491 indicating that the balance between nutrient pumping
492 and carbon sequestration during these mixing events
493 is a significant control.

494 In the standard run (D) as described previously, the
495 tidal forcing and variability in cloud cover are fully
496 resolved. A sub surface plankton biomass maxima
497 forms at about 30 m in late June, which lies in the
498 region of maximum buoyancy gradient (Fig. 12). The
499 SSM exhibits patches of growth and decay, which are
500 not in phase with spring neap cycle of TKE and
501 turbulent dissipation, but shows some indication of
502 being driven by light. This is confirmed by the
503 correlation between net production and light (R =
504 0.78) after the seasonal trends have been removed
505 suggesting that light is responsible for 61% of the

506 variability (Fig. 10b). Temporally coincident with the
507 SSM but 5–10 m higher up the water column, the
508 bulk of bacterial biomass occurs. Peaks in zooplank-
509 ton biomass with a 3–4 d lag follow these peaks of
510 phytoplankton and bacterial biomass suggestive of
511 predator prey dynamics. Simulated turbulent dissipa-
512 tion rates (Fig. 12d) are of the correct magnitude and
513 show a similar vertical distribution to observed meas-
514 urements in North West European Shelf seas (e.g.
515 Sharples et al., 2001; Burchard et al., 2002; Luyten et
516 al., 2002). The pumping of nutrients into the euphotic
517 zone is illustrated by the raising of the nutricline after
518 the dissipation maxima on a spring tide (Fig. 12d).
519 Comparison of Fig. 8c and d with Fig. 8g and
520 h indicates that the biomass peaks for both phyto-
521 plankton and heterotrophs are roughly in phase once
522 the spring bloom is over, thus suggesting that the
523 predator-prey interactions found in B are also found in
524 the standard run (D).

525 Further sensitivity analysis (not shown) reinforces
526 these basic properties of the system. For example,
527 unsurprisingly, doubling the tidal mixing leads to a
528 26% increasing in primary production, while remov-
529 ing the tidal mixing reduces it by 23%. When the
530 spring neap cycle is removed from the standard run
531 (D), the simulation exhibits temporally similar bio-
532 mass pulses (20–24 d) to run B (no tide). However,
533 the magnitude of these pulses in terms of both
534 production and biomass is considerably enhanced.

535 When the model is forced with, for example, no
536 tide and sinusoidally varying cloud, production and
537 biomass peaks occur at the same frequency as the
538 peaks in available solar radiation during the stratified
539 period, thus indicating that the biology may resonate
540 with periodic forcing. Similarly, changing constant
541 cloud cover from the observed 60% to 0% results in a
542 slightly earlier spring bloom, no significant change in
543 the timing of the ecosystem response but a significant
544 increase in the magnitude of the response. Again the
545 model is clearly amplifying hidden predator prey
546 oscillations.

547
548 *3.3. Discussion*

549 The effects of buoyancy production and shear upon
550 the microbial loop in the reference run are illustrated
551 in Fig. 13. Nutrient pumping into the mixed layer
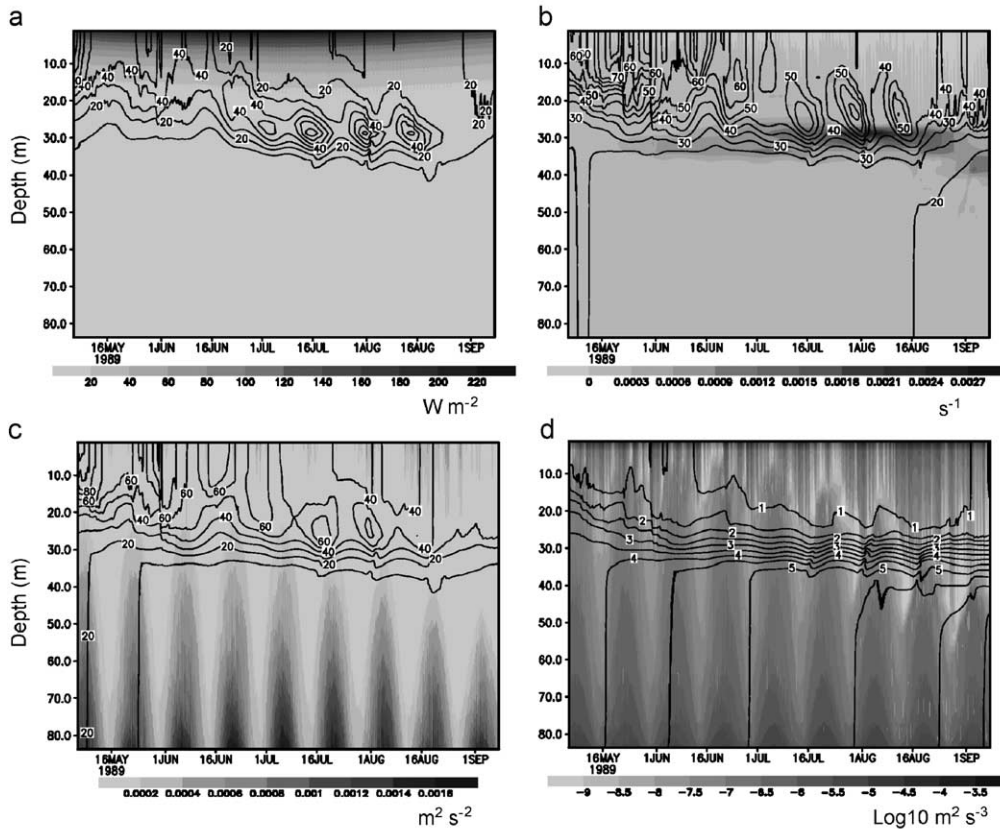552 relieves the nutrient limitation on phytoplankton en-

Fig. 11. Scenario C. Tide, constant cloud, 6 hourly meteorological forcing for days late spring and summer 1989 (Julian days 125–250 inclusive): (a) irradiance (W m^{-2}) and phytoplankton biomass (mg C m^{-3}), (b) Brunt Väsiälä frequency (s^{-1}) and bacterial biomass (mg C m^{-3}), (c) turbulent kinetic energy (m^2 s^{-2}) and zooplankton biomass (mg C m^{-3}), (d) log10 (turbulent dissipation) (m^2 s^{-3}) and nitrate (mmol m^{-3}).

553 couraging growth if the light conditions are favour-
554 able. When the phytoplankton becomes nutrient
555 stressed it undergoes leakage and lysis, releasing
556 DOC in to the mixed layer. This in turn drives
557 bacterial production, indicating that bacteria are pri-
558 marily carbon limited in this system.
559   In scenario C (Fig. 13a), bacterial production is
560 found to be enhanced above the thermocline as the
561 system moves from springs to neaps. Nutrient pump-
562 ing on a spring tide enhances phytoplankton growth.
563 As the system moves to neaps, the phytoplankton
564 above the thermocline becomes nutrient stressed and
565 undergoes lysis. The resultant release of DOC drives
566 bacterial production in this region. The optimal place
567 for growth for protozoan grazers is found to lie
568 between the peaks of bacterial and phytoplankton

569 biomass where they overlap both food sources. In
570 scenario B (Fig. 13b), periods of low irradiance and
571 hence low primary production allow nutrients to
572 diffuse across the thermocline. When this is fol-
573 lowed by high irradiance, primary production
574 occurs. Simultaneously bacterial production occurs
575 above the phytoplankton maxima. This is because
576 the plankton on the upper side of the thermocline is
577 nutrient stressed and undergoes lysis. Once again the
578 optimal place for zooplankon growth lies in the
579 region where the phytoplankon and bacterial bio-
580 mass peaks overlap. This scenario is analogous to
581 that found in the stratified north western Mediterra-
582 nean Sea and there is some evidence from observed
583 profiles of chlorophyll, bacterial biomass and prima-
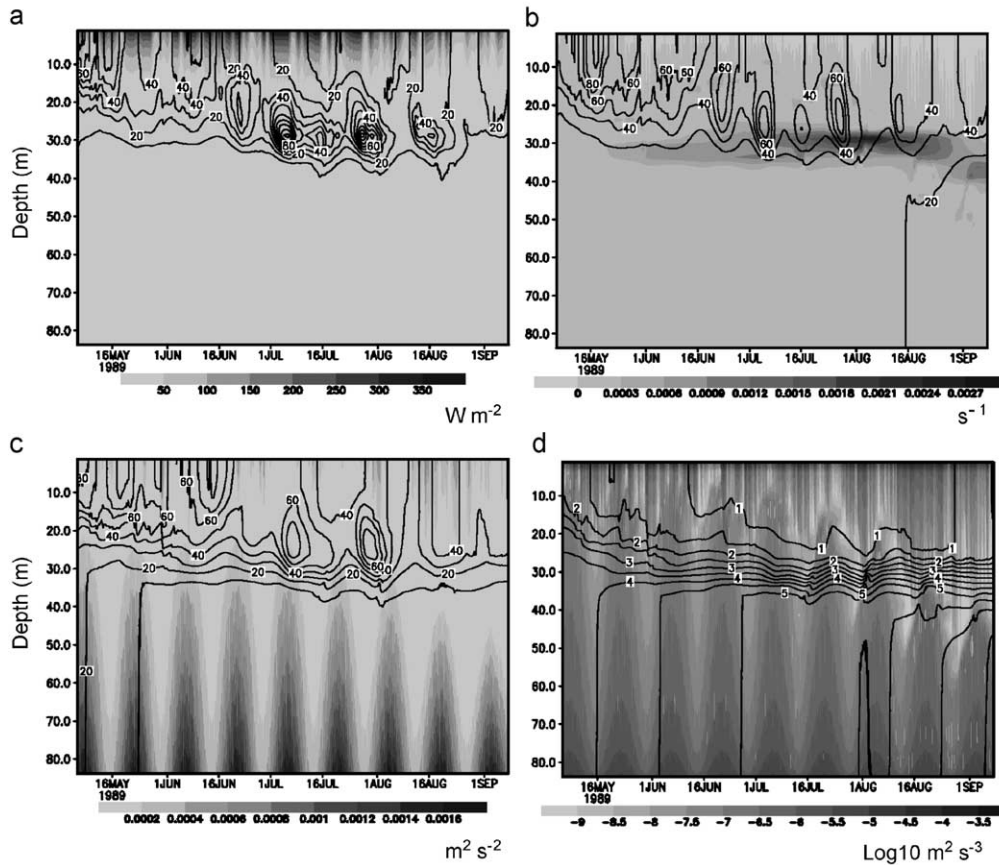584 ry and bacterial production to suggest that this

Fig. 12. Scenario D. Tide, 6 hourly meteorological forcing for days late spring and summer 1989 (Julian days 125–250 inclusive): (a) irradiance (W m^{-2}) and phytoplankton biomass (mg C m^{-3}), (b) Brunt Väsiälä frequency (s^{-1}) and bacterial biomass (mg C m^{-3}), (c) turbulent kinetic energy (m^2 s^{-2}) and zooplankton biomass (mg C m^{-3}), (d) log10 (turbulent dissipation) (m^2 s^{-3}) and nitrate (mmol m^{-3}).

585 occurs in reality (Conan et al., 1999; Van Wambeke
586 et al., 2002).

587　The rate of transport of nitrate across the nutricline
588 during the stratified period for scenario A is shown in
589 Fig. 14. Nitrate transport is a function of the vertical
590 nitrate concentration gradient and the vertical eddy
591 diffusivity and consequently shows strong tidal de-
592 pendence. The magnitude of the nitrate transport in
593 the bottom waters, below the pycnocline, is dependent
594 upon the semi-diurnal tide. There is also a spring-neap
595 cycle in the signal, with the transport maxima occur-
596 ring further up the water column at spring tides than at
597 neaps. The height to which the tidal transport of
598 nitrate occurs (not shown) closely follows the peaks
599 in shear frequency within the water column. In the
600 early summer the base of the thermocline is eroded by

601 TKE leading to enhanced mixing of nitrate into this
602 region. As tidal currents increase from neap to spring
603 tides, the amount of TKE at the base of the thermo-
604 cline and hence the rate of turbulent dissipation will
605 increase. This leads to erosion of stratification. By
606 August the increased stability of the mixed layer has
607 forced the regions of maximum shear deeper and they
608 coincide with the regions of maximum buoyancy
609 gradient. As the tidal cycle approaches springs the
610 increased shear breaks through the thermocline lead-
611 ing to enhanced nutrient transport events. This can
612 clearly be seen in Fig. 14, which shows the transport
613 of nitrate across the nutricline as defined by the region
614 of maximum nitrate gradient. The mean and range of
615 the magnitude of nitrate flux over the stratified sum-
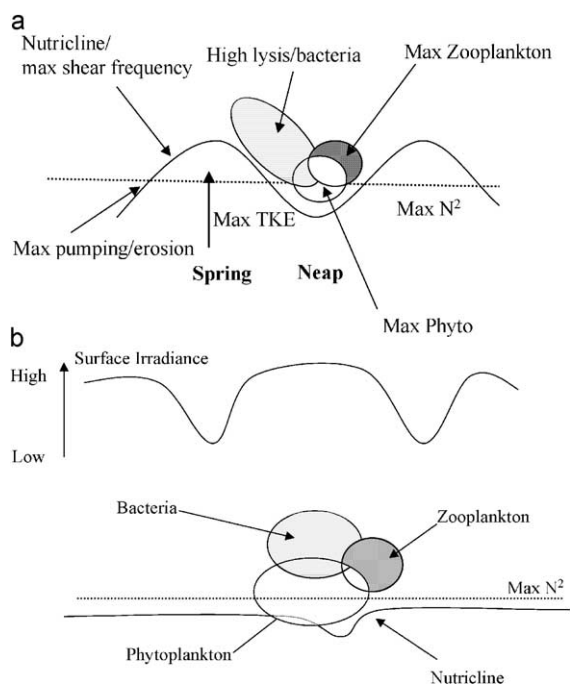616 mer months was calculated as 1.05 (0.32–51.7) mmol

Fig. 13. Schematic diagram of the interaction between, turbulence light and ecosystem processes in (a) constant light tidal scenario, and (b) variable light non-tidal scenario.

617 N m^{-2} d^{-1}, which compares with the 2.0 (0.8–3.2)
618 mmol N m^{-2} d^{-1} estimated for a similar seasonally
619 stratified station in the western English Channel
620 (Sharples et al., 2001). The observations were made
621 halfway through the transition from neaps to springs
622 and consequently do not display the same degree of
623 variability as displayed by the model.
624   The uptake and recycling of dissolved inorganic
625 nitrogen (both nitrate and ammonia) for the euphotic
626 zone (0–34 m) is shown in Fig. 15a. The phytoplank-
627 ton (62%) and bacterial (38%) nitrogen demands are
628 balanced by vertical transport (15%) and in-situ recy-
629 cling via heterotrophs (85%). The influence of the
630 tidal pumping on uptake can clearly be seen (Figs. 7
631 and 8). When the tide is removed (Fig. 15b) the
632 transport term is effectively zero and phytoplankton/
633 bacterial nitrogen demand is met entirely by hetero-
634 trophic recycling. The bacterial nitrogen requirement
635 is now 44% and that for phytoplankton is 56%,
636 indicating a shift towards a more microbially domi-
637 nant system as the stratification becomes stronger.

638   Fig. 14 also shows the transport of carbon across
639 the nutricline from the mixed layer to the deeper
640 waters during late spring and summer. The spring
641 neap cycle can be clearly seen as suggested by
642 Sharples et al. (2001). Once the phytoplankton is
643 mixed into the deeper water regions they are lost
644 from productive regions and this process acts as a one-
645 way removal of carbon from the euphotic zone. The
646 mean and range of the modelled export of carbon was
647 11.01 (7–347) mg C m^{-2} d^{-1}, compared with the
648 290 (120–480) mg C m^{-2} d^{-1} observed by Sharples
649 et al. (2001). The measurements of Sharples et al.
650 (2001) were made in the western English channel,
651 where the SSM was found to have extremely high
652 chlorophyll concentrations (>40 mg Chl m^{-3} com-
653 pared with 1–2 mg Chl m^{-3}), which explains the
654 order of magnitude discrepancies between the two
655 situations. It should be noted that the highest modelled
656 values of C sequestration (over 0.35 g C m^{-2} d^{-1})
657 occur when the thermocline temporally breaks down,
658 and that such substantial removal of carbon inhibits
659 the production in the thermocline inspite of the
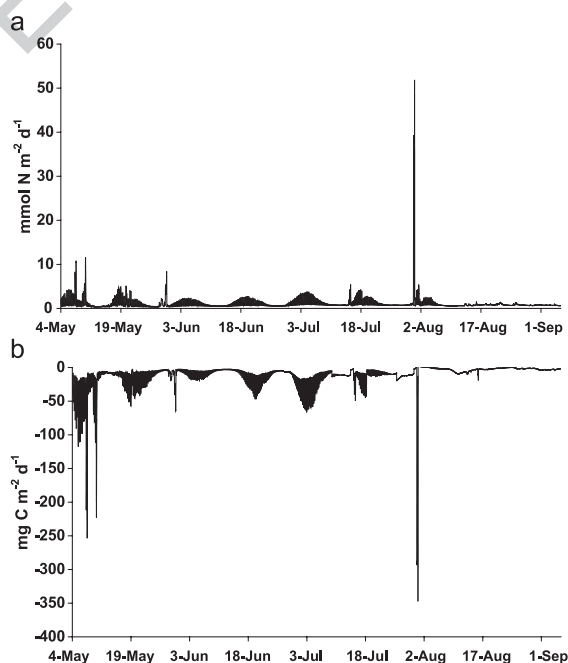660 increased nutrient availability. This can be seen by

Fig. 14. Daily flux of (a) nitrate, and (b) phytoplankton carbon across the nutricline during the summer period. Fluxes are calculated at the point of the sharpest gradient in the nitrate profile.
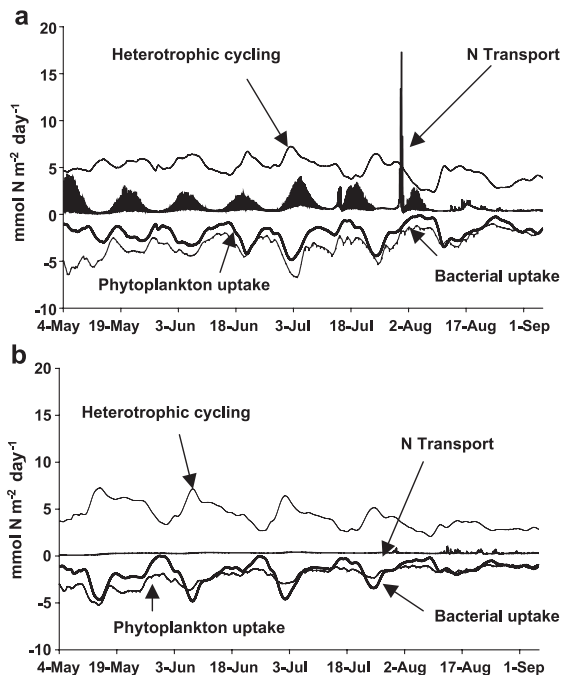
Fig. 15. Dissolved inorganic nitrogen demand and supply in the euphotic zone (0–34 m), (a) tidal scenario, (b) non-tidal scenario (mmol m^{-2} d^{-1}).

comparing Figs. 12 and 14b. A consequence of this is that the degree of stratification influences the carbon flux to the benthos (Fig. 16). Increased inputs are in phase with the spring neap cycle when the export flux is dominated by fast sinking zooplankton faecal pellets in midsummer. At other times of year, the inputs are lagged according to the sinking velocities of the dominant flux of particulate organic matter. Essentially a decrease in the strength of stratification leads to higher turbulence and a shift towards a phytoplankton/grazer dominated ecosystem and consequently an enhanced export flux of carbon from the surface mixed layer to the seabed.

3.4. Ecosystem classification

Finally we present a classification of the system in terms of its physical mixing and its ecosystem properties. We define the physical properties in terms of the stability of the water column using a Richardson number (Ri) with critical value for stability of 0.25. Ri is defined as the ratio buoyancy frequency (N) to shear frequency (M). In winter the water column is well mixed, while in summer the water column exists as a three-layer system, a surface mixed layer (approximately 0–15 m Ri < 0.25), a stable mid water layer (20–40 m, Ri > 10) and a mixed bottom layer. Ecosystem properties are defined in terms the ratio of bacterial to primary production. Three classes are defined: (1) the bacteria dominate (BP/PP > 150), (2) A mixed system (50 < BP/PP < 150) and (3) phytoplankton dominated (BP/PP < 50). This gives six classes and a seventh class is defined for regions with negative primary production, this region being approximately bounded by the 1% light contour. Fig. 17 shows the results of this classification plotted in space and time. Essentially there is a photosynthetically active surface mixed layer all year round and a stable mid water layer, which forms in April and persists till mid September. In the surface mixed layer in winter phytoplankton dominates the ecosystem except in a thin layer at the bottom of the euphotic zone where bacteria dominate. As the water column stabilises in spring, the patterns become more complex. Increasingly bacteria rather than phytoplankton dominate in the unstable nutrient-depleted surface mixed layer and the system shifts from phytoplankton dominated to mixed in the spring and then to a bacterially dominated system in summer. Within the thermocline, a bacterially dominated ecosystem lies in the regions immediately above and below the region of maximum buoyancy gradient because the phytoplankton is nutrient (above) and light limited
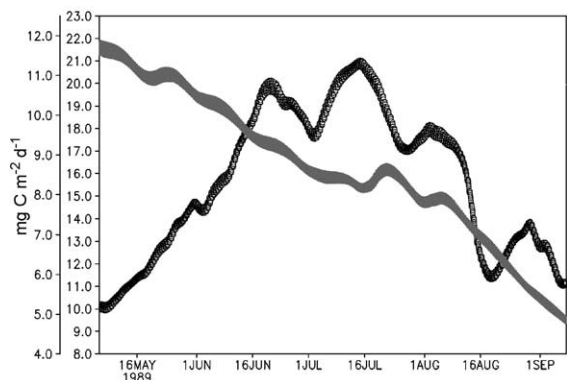

Fig. 16. Flux of carbon into the benthos (mg C m^{-2} d^{-1}), light grey = POC with sink rate 1 m s^{-1}, dark grey = POC with sink rate 10 m s^{-1}.

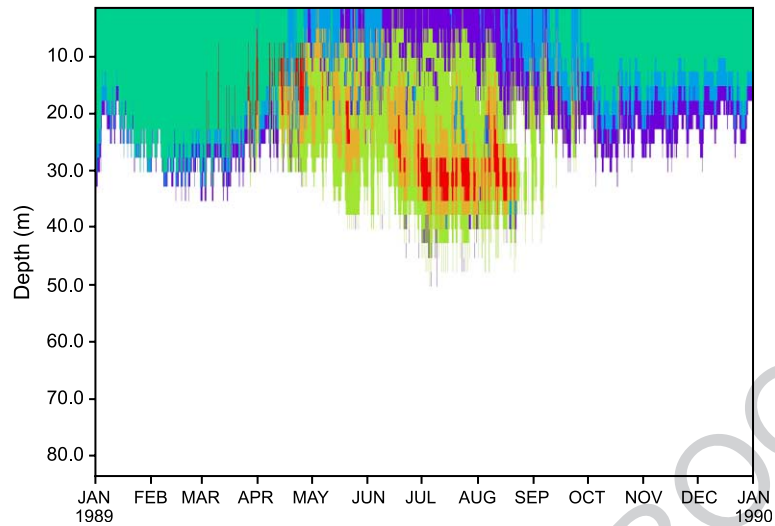Fig. 17. Classification scheme for system behaviour: dark green = unstable BP/PP < 50, light blue = unstable 50 < BP/PP < 150, dark blue = unstable BP/PP > 150, light green = stable BP/PP > 150, orange = stable 50 < BP/PP < 150, red = stable BP/PP < 50, white = negative primary production.

(below), respectively. Phytoplankton dominates in the regions of very high stability where the nutricline lies. Within these general patterns, some quite subtle high-resolution changes can be seen as the ecosystem dynamics respond to changes in the physical environment. Along the region of maximum buoyancy gradient the ecosystem changes from mixed to phytoplankton dominated in response to the changes in light availability and tidally induced nutrient pumping discussed previously. Analysis of the index for runs B, C and D (not shown) indicates that the tidal forcing is the dominant factor in inducing a phytoplanktonic foodweb in this region of the water column. In simulation D (no tide, constant cloud) this region is characterised by a mixed function for the stratified period once the spring bloom is finished. The shift towards a phytoplankton-dominated system also manifests itself as an increase in the inputs of mesozooplankton faecal material into the benthos (Fig. 16). By September, the water column becomes increasingly unstable, the surface mixed layer becomes increasingly more nutrient rich and primary production once again dominates in the surface waters (0–20 m) of this region. However the bottom of the euphotic zone is now characterised by a band of mixed function, with a bacterially dominated layer below (20–30 m).

4. Conclusions

The coupling of GOTM with ERSEM enables the examination of the impact of high frequency changes in the turbulence characteristics of the water column upon the behaviour of the pelagic ecosystem, at a high resolution in both time and space. A 1-D model of a site in the North Sea has been shown to effectively reproduce the known seasonal patterns of biomass and production. The biomass distribution between the functional groups shows excellent agreement with the data. This allows us to have confidence that the biological model, if supplied with realistic physical forcing, can adequately reproduce the biomass and growth rates.

The model was used to investigate the impact of turbulence and light upon the pelagic ecosystem. In terms of short-term variability, the dominant qualitative link between driving forces and system behaviour is between light and primary production. These are very strongly coupled and light variability explains approximately two thirds of the variability in primary production seen in the model. Qualitatively vertical mixing determines the overall bulk seasonal bulk properties of biomass and production. The control is the strength of stratification (the difference between surface and bottom temperature), which is essentially

a measure of the seasonal variation in nutrient availability. Competition between turbulence production by shear and turbulence suppression by density stratification governs the turbulence profile. In turn this regulates the pumping of nutrients into the surface mixed layer and the export of carbon into the deeper mixed layer. Primary production in the thermocline is driven by the import of nutrients and inhibited by the export of carbon. Tidally driven nutrient transport leads to a significant increase in production (23%) over a simulation without tidal mixing. A consequence of these processes is that zooplankton biomass and grazing are substantially enhanced in the tidally forced model. Enhanced mesozooplankton grazing leads to an increase in the production of fast-sinking POM, which in turn impacts substantially on the flux of carbon to the seabed. Hence the degree of stratification ultimately influences the benthic pelagic coupling. The strength of vertical mixing due to either tide and/or wind determines the fine-scale transport across the thermocline and these are amplified by the biological system. The ability of ERSEM to amplify subtle changes in meteorological forcing has previously been reported in Taylor et al. (2002).

In conclusion, these external physical drivers are found to indirectly drive both the microbial loop and secondary production, thus demonstrating that changes in the turbulent properties of the water column influence the development of the microbial loop.

Acknowledgements

References

Allen, J.I., Blackford, J.C., Radford, P.J., 1998. A 1-D vertically resolved modelling study of the ecosystem dynamics of the middle and southern Adriatic Sea. J. Mar. Sys. 18, 265–286.

Allen, J.I., Blackford, J.C., Holt, J., Proctor, R., Ashworth, M., Siddorn, J., 2001. A highly spatially resolved ecosystem model for the North West European Continental Shelf. Sarsia 86, 423–440.

Allen, J.I., Somerfield, P.J., Siddorn, J.R., 2002. Primary and bacterial production in the Mediterranean Sea: a modelling study. J. Mar. Sys. 33–34, 473–495.

Baretta, J.W., Ebenhöh, W., Ruardij, P., 1995. The European Regional Seas Ecosystem Model, a complex marine ecosystem model. Neth. J. Sea Res. 33, 233–246.

Baretta-Bekker, J.G., Baretta, J.W., Rasmussen, E.K., 1995. The microbial food web in the European Regional Seas Ecosystem Model. Neth. J. Sea Res. 33, 363–379.

Baretta-Bekker, J.G., Baretta, J.W., Hansen, A.S., Riemann, B., 1998. An improved model of carbon and nutrient dynamics in the microbial food web in marine enclosures. Aquat. Microb. Ecol. 14, 91–108.

Blackford, J.C., 1997. An analysis of benthic biological dynamics in a North Sea ecosystem model. J. Sea Res. 38, 213–230.

Blackford, J.C., Burkill, P.H., 2002. Planktonic community structure and carbon cycling in the Arabian Sea as a result of monsoonal forcing: the application of a generic model. J. Mar. Sys. 36, 239–267.

Blanke, B., Delecleuse, P., 1993. Variability of the tropical Atlantic Ocean simulated by a general circulation model with two different mixed-layer physics. J. Phys. Oceanogr. 23, 1363–1388.

Broekhuizen, N., Heath, M.R., Hay, S.J., Gurney, W.S.C., 1995. Modelling the dynamics of the North Seas mesozooplankton. Neth. J. Sea Res. 33, 381–406.

Budyko, M.I., 1974. Climate and Life Academic Press, New York.

Burchard, H., Bolding, K., Ruiz Villarreal, M., 1999. GOTM—a general ocean turbulence model. Theory, applications and test cases. Tech. Rep. EUR 18745 EN, European Commission.

Burchard, H., Bolding, K., Rippeth, T.P., Stips, A., Simpson, J.H., Sundermann, J., 2002. Microstructure of turbulence in the Northern North Sea: a comparative study of observations and model simulations. J. Sea Res. 47, 223–238.

Casterllari, S., Pinardi, N., Leaman, K., 1998. A model study of air sea interactions in the Mediterranean Sea. J. Mar. Sys. 18, 89–114.

Conan, P., Turley, C., Stutt, E., Pujo-Pay, M., Van Wambeke, F., 1999. Relationship between phytoplankton efficiency and the proportion of bacterial production to primary production in the Mediterranean Sea. Aquat. Microb. Ecol. 17, 131–144.

Ebenhöh, W., Kohlmeier, C., Radford, P.J., 1995. The benthic biological model in the European Regional Seas Ecosystem Model. Neth. J. Sea Res. 33, 423–452.

Ebenhöh, W., Baretta, J.W., Baretta-Bekker, J.G., 1997. The primary production module in a marine ecosystem model ERSEM II. J. Sea Res. 38, 173–194.

Galperin, B., Kantha, L.H., Hassid, S., Rosati, A., 1988. A quasi-equilibrium turbulent energy-model for geophysical flows. J. Atmosph. Sci. 45, 55–62.

Horne, E.P., Loder, J.W., Naimie, C.E., Oakey, N.S., 1996. Turbulence dissipation rates and nitrate supply in the upper water column on Georges Bank. Deep-Sea Res. 43, 1683–1712.

Howarth, M.J., Dyer, K.R., Joint, I.R., Hydes, D.J., Purdie, D.A.,

Prieur, L., Jones, J.E., Lowry, R.K., Moffat, T.J., Pomroy, A.J., Proctor, R., 1993. Seasonal cycles and their spatial variability. Phil. Trans. R. Soc. London Ser. A-Math. Phys. Eng. Sci. 343, 383–403.

Huisman, J., Van Oostveen, P., Weissing, F.J., 1999. Critical depth and critical turbulence: two different mechanisms for the development of phytoplankton blooms. Limnol. Oceangr. 44, 1781–1787.

Joint, I, Pomroy, A., 1993. Phytoplankton biomass and production in the southern North Sea. Mar. Ecol. Prog. Series. 99, 169–182.

Joint, I., Wollast, R., Chou, L., Batten, S., Elskens, M., Edwards, E., Hirst, A., Burkill, P., Groom, S., Gibb, S., Miller, A., Hydes, D., Dehairs, F., Antia, A., Barlow, R., Rees, A., Pomroy, A., Brockmann, U., Cummings, D., Lampitt, R., Loijens, M., Mantoura, F., Miller, P., Raabe, T., Alvarez-Salgado, X., Stelfox, C., Woolfenden, J., 2001. Pelagic production at the Celtic Sea shelf break. Deep Sea Res. II 48, 3049–3081.

Kondo, J., 1975. Air-sea bulk transfer coefficients in diabatic conditions. Boundary-Layer Meteorol. 9, 91–112.

Lewis, M.R., Harrison, W.G., Oakey, N.S., Herbert, D., Platt, T., 1986. Vertical nitrate fluxes in the oligotrophic ocean. Science 234, 870–873.

Lowry, R., Cranmer, K., Rickards, L., 1992. North Sea Project CD ROM and users guide British Oceanographic Data Centre, Natural Environment Research Council, Swindon, UK.

Luyten, P.J., Carniel, S., Umgiesser, G., 2002. Validation of turbulence closure parameterisation for stably stratified flows using the PROVESS turbulence measurements in the North Sea. J. Sea Res. 47, 239–267.

Mann, K.H., Lazier, J.R.N., 1996. Dynamics of Marine Ecosystems: Biological-Physical Interactions in the Oceans, 2nd ed. Blackwell, Oxford.

Mellor, G.L., Yamada, T., 1974. A hierarchy of turbulence closure models for planetary boundary layers. J. Atmos. Sci. 31, 1791–1806.

Pätsch, J., Radach, G., 1997. Long-term simulation of the eutrophication of the North Sea: temporal development of nutrients, chlorophyll and primary production in comparison to observations. Neth. J. Sea Res. 38, 275–310.

Planas, D., Agusti, S., Duarte, C.M., Granata, T.C., Merino, M., 1999. Nitrate uptake and diffusive nitrate supply in the Central Atlantic. Limnol. Oceanogr. 44, 116–126.

Prandle, D., Hydes, D.J., McManus, J., 1997. The seasonal cycles of temperature, salinity, nutrients and suspended sediment in the southern North Sea in 1988 and 1989. Estuar. Coast. Shelf Sci. 45, 669–680.

Radach, G., Lenhart, H.J., 1995. Nutrient dynamics in the North Sea: fluxes and budgets in the water column derived from ERSEM. Neth. J. Sea Res. 33, 301–335.

Rodi, W., 1987. Examples of calculation methods for flow and mixing in stratified flows. J. Geophs. Res. 92, 5305–5328.

Schumann, U., Gerz, T., 1995. Turbulent mixing in stably stratified shear flows. J. Appl. Meteorol. 34, 33–48.

Sharples, J., Tett, P., 1994. Modelling of the effect of physical variability on the midwater chlorophyll maximum. J. Mar. Res. 52, 219–238.

Sharples, J., Moore, C.M., Rippeth, T.P., Holligan, P.M., Hydes, D.J., Fisher, N.R., Simpson, J.H., 2001. Phytoplanton distribution and survival in the thermocline. Limnol. Oceanogr. 46, 486–496.

Siddorn, J.R., Allen, J.I., 2003. A 1-D ecosystem model: dependence upon surface heat fluxes. Ann. Geophys. 21, 377–388.

Simpson, J.H., 1993. The North Sea project; An overview and the way forward. Phil. Trans. R. Soc. A 343 (1669), 585–596.

Sinha, B., Pingree, R.D., 1997. The principal lunar semidiurnal tide and its harmonics: baseline solutions for M-2 And M-4 constituents on the North-West European continental shelf. Cont. Shelf Res. 17, 1321–1365.

Taylor, A.H., Allen, J.I., Clarke, P., 2002. Extraction of a weak climatic signal by an ecosystem. Nature 416, 629–632.

Tetens, O., 1930. Über einige meteorologische Begriffe. Z. Geophys. 6, 297–309.

Tett, P.B., Walne, A.W., 1995. Observation and simulations of hydrography, nutrients and plankton in the southern North Sea. Ophelia 42, 371–416.

Van Wambeke, F., Heussner, S., Diaz, F., Raimbault, P., Vonan, P., 2002. Same scale variability in the coupling/uncoupling of bacteria, phytoplankton and organcic carbon fluxes along the continental margin of the Gulf of Lions, Northwestern Mediterranean Sea. J. Mar. Syst. 33–34, 411–430.

Vichi, M., Zavatarelli, M., Pinardi, N., 1998. Seasonal modulation of microbially mediated carbon fluxes in the northern Adriatic Sea—a model study. Fish. Oceanogr. 7, 182–190.

Wallace, J.M.A., Hobbs, P.V., 1977. Atmospheric Science: An Introductory Survey. Academic Press, San Diego.

Zavatarelli, M., Baretta, J.W., Baretta-Bekker, J.G., Pinardi, N., 2000. The dynamics of the Adriatic Sea ecosystem. An idealised model study. Deep-Sea Res. 47, 937–970.

Zakardjian, B., Prieur, L., 1994. A numerical study of primary production related to vertical turbulent diffusion with special reference to vertical motions of the phytoplankton cells in nutrient and light fields. J. Mar. Syst. 5, 267–295.

Modelling the hydrodynamics and ecosystem of the North-West European continental shelf for operational oceanography

John R. Siddorn [a,*], J. Icarus Allen [b], Jerry C. Blackford [b], Francis J. Gilbert [b],
Jason T. Holt [c], Martin W. Holt [a], Jeff P. Osborne [a], Roger Proctor [c], David K. Mills [d]

[a] Met Office, FitzRoy Road, Exeter, Devon, EX1 3PB, United Kingdom
[b] Plymouth Marine Laboratory, Prospect Place, The Hoe, Plymouth, PL1 3DH, United Kingdom
[c] Proudman Oceanographic Laboratory, Bidston Observatory, Birkenhead, CH43 7RA, United Kingdom
[d] The Centre for Environment, Fisheries and Aquaculture Science, Pakefield Road, Lowestoft, Suffolk, NR33 0HT, United Kingdom

Abstract

This paper outlines an approach to complex spatio-temporal marine ecosystem modelling as applied to the North Western European Continental Shelf. The model presented here combines an eddy-permitting (approximately 6 km horizontal resolution) baroclinic model, the Proudman Oceanographic Laboratory Coastal Ocean Modelling System (POLCOMS), with the European Regional Seas Ecosystem Model (ERSEM). This has been run within an operational framework using operationally available high resolution atmospheric and lateral boundary forcing, allowing hindcast and near-real time nowcast simulations to be performed. The modelled surface temperature and chlorophyll distributions are presented, and interannual variations discussed. Validation of both the physical and ecosystem submodels show the system to be effective, whilst highlighting areas where improvements in the system can be made. Distinct regional differences in predictive skill are shown. The system presented is ready for operational implementation to provide products and services for use both scientifically and in coastal zone and shelf seas management activities. A programme of work to update the system is already in place.

1. Introduction

Shelf seas have high biological and hydrodynamic variability and are the regions of the ocean where most human contact with the marine systems occurs. Human activity and changes induced by natural climatic variability have a significant impact upon their physical and biogeochemical properties which, in turn, impact upon those industries and individuals that rely on shelf-seas regions. It is thus of great importance to the marine community to understand the processes that determine the state of our seas, and to use this understanding to inform decision making. Consequently there is a need for a robust source of hydrodynamic, ecological and water quality data upon timescales useful for decision making. The hydrodynamic properties of shelf-seas have been simulated operationally for a number of years, with users including

* Corresponding author. Tel.: +44 1392 886824; fax: +44 1392 885681.
  E-mail address: john.siddorn@metoffice.gov.uk (J.R. Siddorn).

the fisheries, oil industry, ports and harbours and scientific communities. However, there is a growing realisation that the biogeochemical state of our seas cannot be inferred from their physical properties alone (e.g. Blackford et al., 2004), and there is a requirement for explicit operational modelling of the combined physical, chemical and biological systems. The increased interest in the assessment of our marine systems using an "ecosystem approach" implies an increased need for timely, accurate modelled information to provide the detailed and spatially complete dataset required. There is also increasing demand for near-real time and forecast products such as diver visibility and harmful algal bloom likelihood. It is intended that these operational systems provide the infrastructure to support marine decision making in these and other areas. The forecasts have also already been used to good effect in support of a scientific research cruise (Fernand, pers. comm.).

Ecosystems have dynamics that are extremely nonlinear and their modelling requires adequate representation of both physical and biological processes. Much work has been done in recent decades to improve the underlying scientific knowledge of European coastal waters and our understanding of both the hydrodynamic properties of the region and the ecosystem behaviour is continually improving. This knowledge has been used to inform the development of modelling systems, and there are now a number of studies which have successfully coupled lower-trophic level ecosystem models with three-dimensional hydrodynamic models. A review of ecosystem models of the North Sea (Moll and Radach, 2003) shows that there are several that robustly replicate the regional ecology, one of which (POL3dERSEM) is the basis for the modelling system used here.

Up until now complex ecosystem models have been used primarily as scientific tools studying specific processes, regions or temporal scales. The aim in this work is to show that both technically and scientifically we have reached the stage where nowcasting and short-period forecasting of the marine ecosystem of the North-West European Continental shelf is feasible in an operational framework.

This paper details a pilot study with a model of the North-West European continental shelf, the Medium-Resolution Continental Shelf model coupled with the European Regional Seas Ecosystem Model (MRCS-ERSEM2004). This has been implemented within an operational framework giving the capability for near-real time and forecast simulations. As a test of the system the model has been run for the years 2002 to 2004, with validation presented for 2002 and 2003.

Several years experience in using the coupled version of the codes in European waters (e.g. Allen et al., 2001; Proctor et al., 2003; Holt et al., 2005) is of great benefit in providing a stable, robust environment in which to implement operational code. A systematic verification of the coupled model system in this domain, particularly using data from the North Sea Community Project (Charnock et al., 1993), is currently being carried out (Allen et al., unpublished results and Holt et al., 2005).

The horizontal grid size of the MRCS modelling system, although eddy permitting, is insufficient to resolve the on shelf mesoscale eddy processes, where a characteristic Rossby radius of ∼3 km can be expected. However, the MRCS is planned as part of a suite of models which cascade down to high resolution (∼1.8 km) applications of the model where needed, for example the Southern North Sea (Proctor and James, 1996) and Irish Sea (Holt and Proctor, 2003).

2. Methods

Detailed descriptions of the MRCS implementation of the Proudman Oceanographic Coastal Ocean Modelling System (POLCOMS) are given in Holt and James (2001) and Holt et al. (2005). It is a 3D baroclinic finite difference model which uses an Arakawa-B grid (Arakawa, 1972) in the horizontal and sigma coordinates in the vertical. This choice of grid, the decision not to model explicitly the horizontal diffusion and the use of a sophisticated horizontal advection scheme – the Piecewise Parabolic Method (James, 1996) – combine to give the model good fronts conserving properties. The MRCS is thus ideally formulated for high resolution shelf-seas work, where gradients in both topography and scalar properties can be large. The PPM advection scheme also transports the biological variables, which often demonstrate high spatial variability, so providing a sound modelling framework from the ecosystem perspective.

POLCOMS has been shown to successfully simulate the region of interest; descriptions of the POLCOMS modelling system as applied within the North-East Atlantic region can be found in the literature (Proctor and James, 1996; Holt and James, 1999a,b; Holt et al., 2001; Holt and James, 2001).

ERSEM (Baretta et al., 1995) was conceived as a generic model, and is one of the most complex lower trophic-level marine ecosystem models currently in use. Its philosophy is to include all those processes which significantly influence ecosystem dynamics, and to resolve the ecosystem into sufficient functional groups so that those processes can be sensibly defined. It thus has one bacteria, four phytoplankton and three zooplankton functional groups, and has a fully resolved diurnal cycle, variable carbon to chlorophyll ratios (after Geider et al.,

1997) and independent nutrient pools for carbon, nitrogen, phosphorous and silicate (Baretta-Bekker et al., 1997). The decoupling of the nutrient pools gives a superior approximation of nutrient limitation (and the associated changes in plankton regimes), and also allows the production of significant pools of Dissolved Organic Matter (DOM), thereby allowing the model to represent the continuum of trophic pathways from the classic large-cell based to the DOM recycling based microbial-loop systems. The inclusion of an "over-wintering" physiology for the mesozooplankton (Calanus-like) functional group has been included to act as a proxy for the egg and early nauplii stages, overcoming some of the problems associated with using the functional group based approach for the more complex and behavioural life-stages of these plankton. Coupled with this pelagic complexity is a benthic model, designed to give not only detailed process information of the benthic ecosystem (Ebenhöh et al., 1995; Blackford, 1997), but also a well defined nutrient coupling between the benthic and pelagic systems (Ruardij and van Raaphorst, 1995). Many coastal regions, including sites in the North Sea (Proctor et al., 2003), have nutrient cycling dominated by benthic inputs and so a simple re-suspension and advection model of detritus is not considered adequate. Blackford et al. (2004) gives a full description of the ERSEM2004 model and para-meterisations used.

ERSEM was initially developed for use in the North Sea, and has since been used for a number of North Sea and North-West European continental shelf studies (e.g. Pätsch and Radach, 1997; Ruardij et al., 1997). Due to the generic nature of the functional group approach the use of ERSEM has not been limited to the North Sea; it has been used in a number of studies within the Mediterranean (Allen et al., 2002; Triantafyllou et al., 2003a) and Arabian (Blackford and Burkill, 2002) Seas, showing that it can be successfully applied in eutrophic, mesotrophic and oligotrophic systems. A recent study (Blackford et al., 2004) shows that the ERSEM2004 model can, without any re-parameterisation, be applied to the North Sea, Mediterranean Sea and Arabian Sea sites, all with very different hydrodynamic and ecosystem characteristics. This makes it an ideal model for use within operational structures, as it allows for the relocation of the modelling system to other regions with minimal modification. This also suggests that the model will respond correctly to in situ changes in climate and hydrodynamic forcing that may arise from climate variation. The modular nature of ERSEM means that it may be used in conjunction with other complementary codes, and has for example been coupled with a fish population model (Bryant et al., 1995; Heath et al., 1997), allowing the possibility for an expansion to the operational capabilities of the system in the future.

Robinson and Frid (2003) review the potential of a number of ecosystem models for providing useful information to fisheries scientists and decision makers, and conclude that the ERSEM group of models seem well designed for fisheries uses. Similarly a review of ecosystem models of the North Sea (Moll and Radach, 2003) concludes that POL3dERSEM, the precursor to the Medium Resolution Continental Shelf (MRCS)-ERSEM2004 implementation used in this work, "sets new standards in the three-dimensional ecosystem modelling of the North Sea".

2.1. Model setup

Results presented here have been derived from the MRCS-ERSEM2004 model, setup in the NW European shelf region at an approximately 6 km resolution, with 20 sigma levels in the vertical. The open boundary of the model has been defined to follow the 200 m bathymetry contour around the continental shelf edge, with lateral boundary conditions being provided by the Met Office Atlantic Margin Model (AMM) operational implementation of a 12 km resolution POLCOMS (Holt et al., 2003). The AMM is one-way nested within the Met Office operational FOAM 1/3 degree resolution deep ocean model (Bell et al., 2003). Temperature, salinity, barotropic velocity and sea-surface height (six-hourly fields in the case of FOAM, daily temperature and salinity fields and hourly velocity and elevation fields in the case of AMM) are used in the nesting process. Surface forcing is provided from the Met Office's Mesoscale Numerical Weather Prediction model (also at approximately 12 km resolution) via three-hourly average fields of penetrating and non-penetrating heat fluxes (corrected for intra-model SST differences by a flux correction term, after Haney, 1971), moisture fluxes, and hourly instantaneous fields of windspeed and surface pressure. The FOAM and Mesoscale NWP models include state of the art operational data assimilation systems that allow the full model hierarchy to benefit from the best set of near-real time observations possible.

The operational numerical weather prediction and ocean models provide both nowcast and forecast information (which are archived for future hindcast studies) allowing a forecast period of 48 h for the MRCS-ERSEM2004 model. Atmospheric data is also routinely produced by the Met Office's Global model at lower resolution but increased forecast lead time allowing a T+120 forecast period to be employed in future implementations if required. The forcing models are run

to a fixed daily schedule, with operator supervision, in the suite of forecast models at the Met Office and output products are available by a specified time each day. The safeguards built into this system ensure that the data is produced in a fully robust and timely manner, allowing the model to be run in hindcast, near-real time, or forecast mode as appropriate. To ensure reliability there is a careful change control procedure applied to the models run in the operational suite.

The model is currently been run in semi-operational mode automatically every week, with a 7 day hindcast of the previous week and a 48 h forecast. Results are disseminated (again automatically) to the internet, where the near-real time data is made freely available at http://www.metoffice.gov.uk/research/ncof/mrcs/browser.html. The system receives near-real time and forecast data as described above from the Met Office's operational system. The forecast is being assessed and will in time be extended to five days. The aim is to make the forecasts available alongside the near-real time data. The MRCS-ERSEM2004 model is scheduled to enter the operational suite shortly.

3. Results

The model has been run from January 2002 to the present day in hindcast mode using the archived datasets described above. Interpolated data for the 1st January 2002 from the AMM POLCOMS model were used to initialize the physical variables, with biological data taken from a 1988/89 MRCS POLCOMS-ERSEM simulation (Allen et al., unpublished results and Holt et al., 2005). Although the use of 1989 data for the biological restart fields is not ideal it is likely to be an improvement on the spatially constant initial field used in previous applications of the model. The impact on the model run due to errors in the restart fields is presumed to be small because the bio-chemical variables, with the exception of the nutrient and detrital pools, are at background levels during the winter; examination of timeseries of a number of variables indicate that the model quickly spins up to match the data. Surface temperature and chlorophyll fields are presented as examples of the spatio-temporal evolution of the model physics and ecology, followed by the results of validation intended to provide a more rigorous test of the models performance.

3.1. A brief description of model behaviour

3.1.1. Temperature

The modelled surface temperature for 2002 is described. It starts cool in the winter with a strong east to west gradient, waters in the Skagerrak having temperatures of close to 0 °C and those in the Celtic Sea of around 10 °C. The structure of the English Channel can be seen clearly, with warmer waters in the central water mass, and cooler coastal waters near to the UK and French landmasses. Similarly the central Irish Sea is significantly warmer than the surrounding coastal waters. There is a great deal of variability in the North Sea waters, where Baltic and Atlantic waters mix. For the first few months of the year the North Sea and Irish Sea waters gradually cool until the end of spring when surface heating and warming river waters start having an impact. By the beginning of June temperatures throughout the domain are between 10 and 14 °C, with the exception of the Norwegian Trench and Skagerrak where the warming being distributed through a deeper water column means the temperatures stay relatively low. By July shallow regions such as the German Bight reach 18 °C. Throughout the summer surface temperatures continue to increase, especially in the seasonally stratified regions of the southern North Sea. Temperatures peak in late September, after which they return to their winter state.

3.1.2. Chlorophyll

Modelled surface chlorophyll starts low in the winter of 2002 (Fig. 1), with particularly low values in the northern North Sea and Celtic Sea. Levels of chlorophyll start increasing in late February near to the coasts, especially in regions of river inputs such as the German Bight and near the Thames. These areas of elevated chlorophyll levels expand with time and by the beginning of March cover patches in the shallower parts of the southern North Sea, such as the Dogger Bank, as well as the heavily river influenced coastal regions. At this time chlorophyll concentrations of up to 10 mg-Chl/m^3 are found in the Southern North Sea, whereas in the central and northern North Sea and the Celtic Sea biological activity is still minimal. Towards the end of March the Celtic Sea shows signs of the onset of biological activity, with a bloom occurring in the first two weeks of April. During this same period the northern North Sea also starts to show some chlorophyll growth and by mid-April levels of above 1 mg-Chl/m^3 can be found throughout the domain. During April the bloom over the Dogger Bank intensifies and shifts northwards so that by the beginning of May the highest concentrations of chlorophyll are to be found in the central North Sea and the Skagerrak, whilst the southern North Sea shows patchy blooms. Towards the end of May and beginning of June the stratified areas of the North Sea become nutrient depleted, the spring bloom dies back and a clear frontal pattern demarcating the transition between the well mixed southern and the
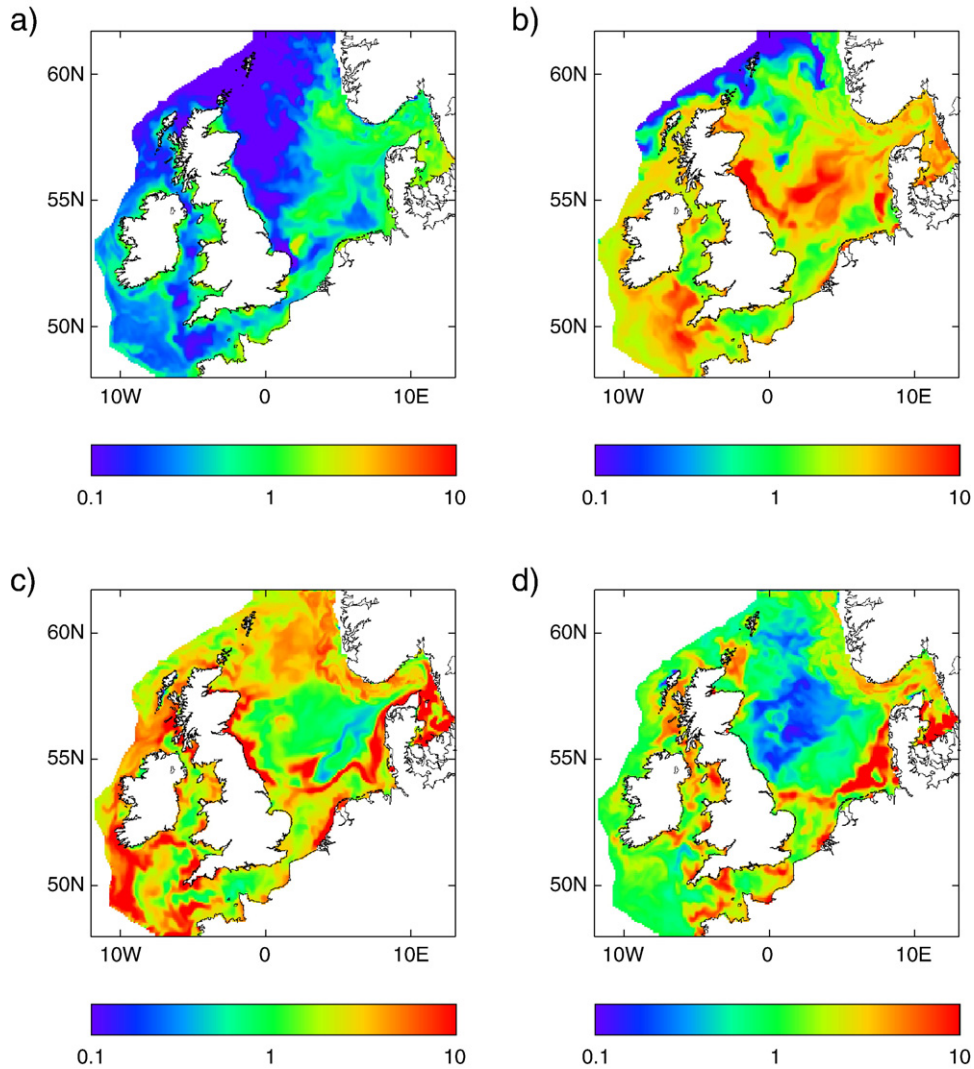
Fig. 1. Modelled surface chlorophyll (in mg-Chl/m^3) for a) 1st January 2002, b) 1st April 2002, c) 1st June 2002 and d) 1st October 2002. A logarithmic scale is used.

stratified northern waters can be seen. During May biological activity in the Irish Sea also increases, with peak chlorophyll levels being found in the last week of May, when there is an extensive bloom covering the majority of the southern North Sea and the Irish Sea. Chlorophyll levels at this time can be found of above 20 mg-Chl/m^3 in the German Bight (consistent with results for this region shown in Reid et al., 1990) and the Skagerrak, and, more sporadically, throughout the southern North Sea. Throughout June, July and August the chlorophyll concentrations become patchier and high levels (of the order 10 mg-Chl/m^3) appear to be predominantly around frontal areas or off headlands. By the beginning of August the levels of nutrients in the

stratified areas become too low to support much growth and the central North Sea shows decreased levels of chlorophyll. No clear autumn bloom is evident in the model data, although the end of August and beginning of September shows some increased growth in the German Bight and Dutch coastal areas, and by the beginning of October the central North Sea recovers to show increased, but still, low levels of chlorophyll. By the end of the year the distribution of chlorophyll is uniformly low, with less than 1 mg-Chl/m^3 across the whole domain.

These results are consistent with the chlorophyll climatology presented in Moll (1998), where data from a range of sources has been composited into regional bins for the North Sea.

3.2. Model validation

Efforts have been made to validate both physical and ecosystem properties. Surface temperature data have been obtained from the Marine Automated Weather Station (MAWS, the Met Office's near real time network). Data have also been supplied by the UK's Centre for the Environment, Fisheries and Aquaculture Science (CEFAS) from their sampling buoys (Smart-Buoys) situated in the Thames outflow region (stations Warp Anchorage and Gabbard, Fig. 2). These buoys sample for both physical variables (temperature and salinity) as well as biological variables (nutrients and chlorophyll). In the English Channel the L4 station, off Plymouth Sound, has also been used to validate both the physical and ecosystem submodels.

3.2.1. Moored Automatic Weather Stations surface temperature

Comparisons between modelled surface temperature and observations from the MAWS buoys, taken at depths of 1.5 m, are shown in Fig. 3. These sites show varying degrees of stratification, with the near-shore sites at Turbot Bank and Greenwich LV remaining well mixed throughout most of the year, whilst M1 and K16 show significant seasonal stratification. In both stratified and unstratified regions the model replicates the measured sea surface temperature and the timing and amplitude of the stochastic features are, in the main, well reproduced. This highlights the quality of the surface heat and momentum forcing.

The M1, and to a lesser extent M2 and Greenwich LV, sites show some underestimation of the winter sea
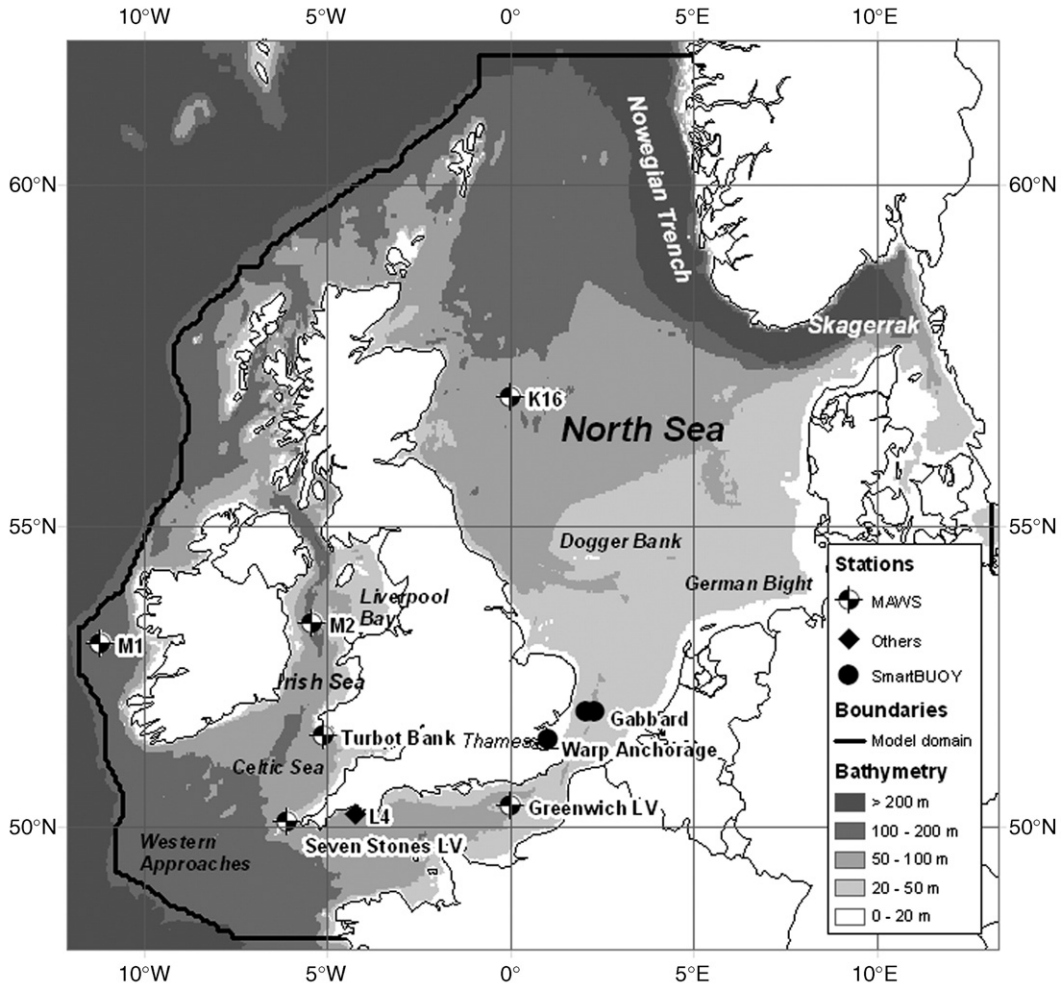

Fig. 2. Map of the North-West European Continental Shelf, showing the MRCS model domain, and the sites of the sampling stations and buoys used for validating the model.
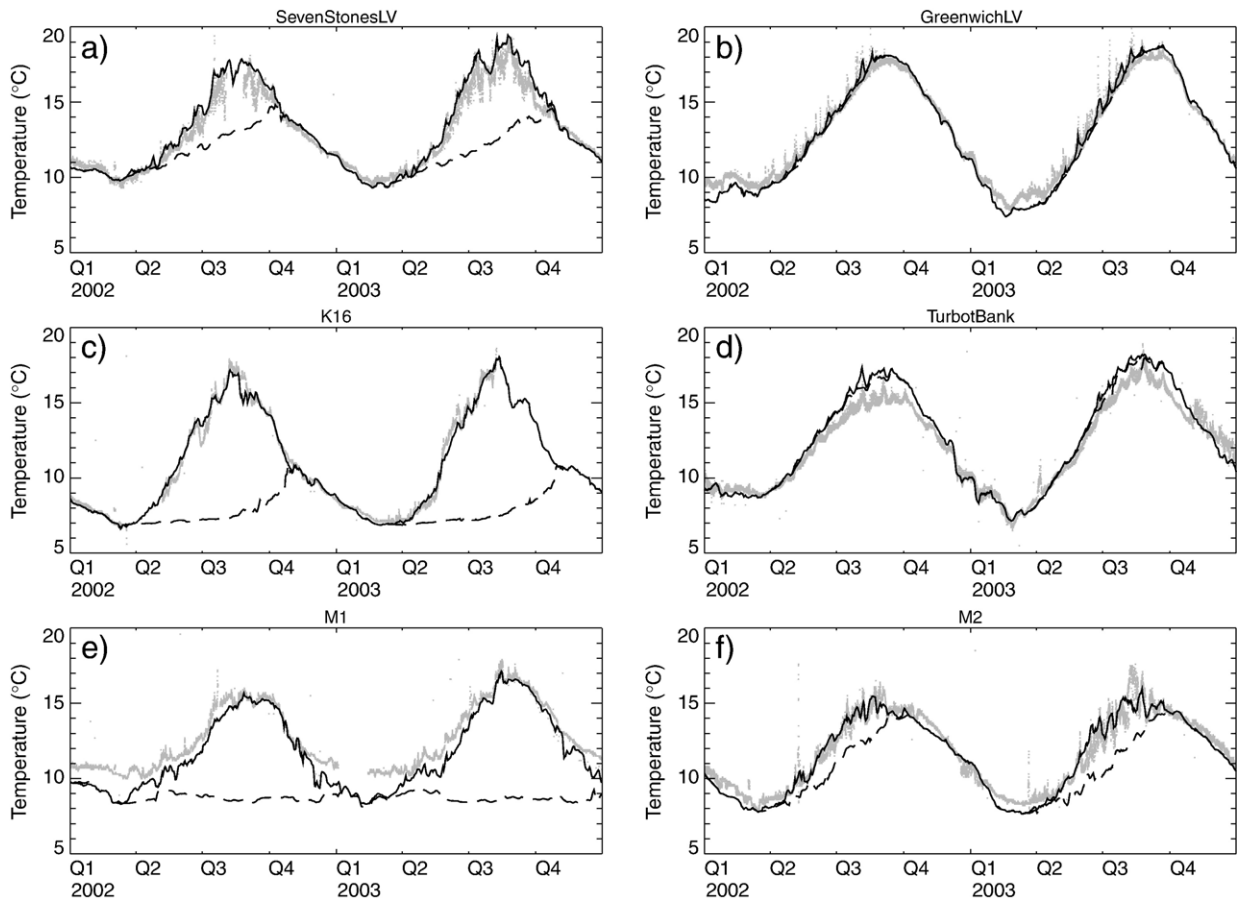
Fig. 3. Measured and modelled sea surface temperatures for a) Seven Stones Light Vessel, b) Greenwich Light Vessel, c) K16 buoy, d) Turbot Bank buoy, e) M1 buoy and f) M2 buoy. The solid line is the modelled data, the broken line the measured data. Modelled bottom temperatures are also shown (dashed lines).

surface temperatures. This discrepancy at M1 may be due to its proximity to the open boundaries, where temperature and salinity are prescribed using data taken from the Atlantic Margin Model (AMM). A comparison of AMM data against the MAWS sites (not shown) indicates a tendency to underestimate winter sea surface temperatures, and it follows that the relatively large errors at the M1 site are a direct result of the inputs at the boundaries. Turbot Bank, on the other hand, has a slight overestimation of the sea surface temperatures in the summer months. The precise cause of this is unclear, but the site is close to land and in a region influenced by both Celtic Sea and Bristol Channel waters.

3.2.2. CEFAS SmartBuoy surface temperature, nutrient and chlorophyll

Modelled temperature, salinity, silicate, nitrate and chlorophyll are compared with CEFAS 'SmartBuoys' at two sites in the Thames ROFI, Warp Anchorage (at 51°31.5′ N, 1°01.9′ E in approximately 15 m water) and

Gabbard (at 52°00′ N, 2°20′ E in 45 m water). The Gabbard SmartBuoy was moved in August 2002 to the West Gabbard site in the southern North Sea, about 9 nm closer to shore and in slightly shallower water (at 1°59′ N, 2°05′ E in approximately 32 m water depth). The data shown is therefore labelled Gabbard but includes model and measured data from the West Gabbard site from this date onwards.

The temperature comparisons for both Gabbard (Fig. 4) and Warp Anchorage (Fig. 5) are good, with the model quickly spinning up to match the data. The longer period seasonal variability and the shorter timescale stochastic events show excellent correspondence, with all the main mixing events evident in the measurements also evident in the model data. Both the buoy locations are close to the Thames outflow and modelling these sites needs the surface forcing, the dynamics of the model, and to a lesser extent river inputs, to be well represented.

Salinity is a more stringent test of the river inputs. The modelled salinity shows mean values of the same
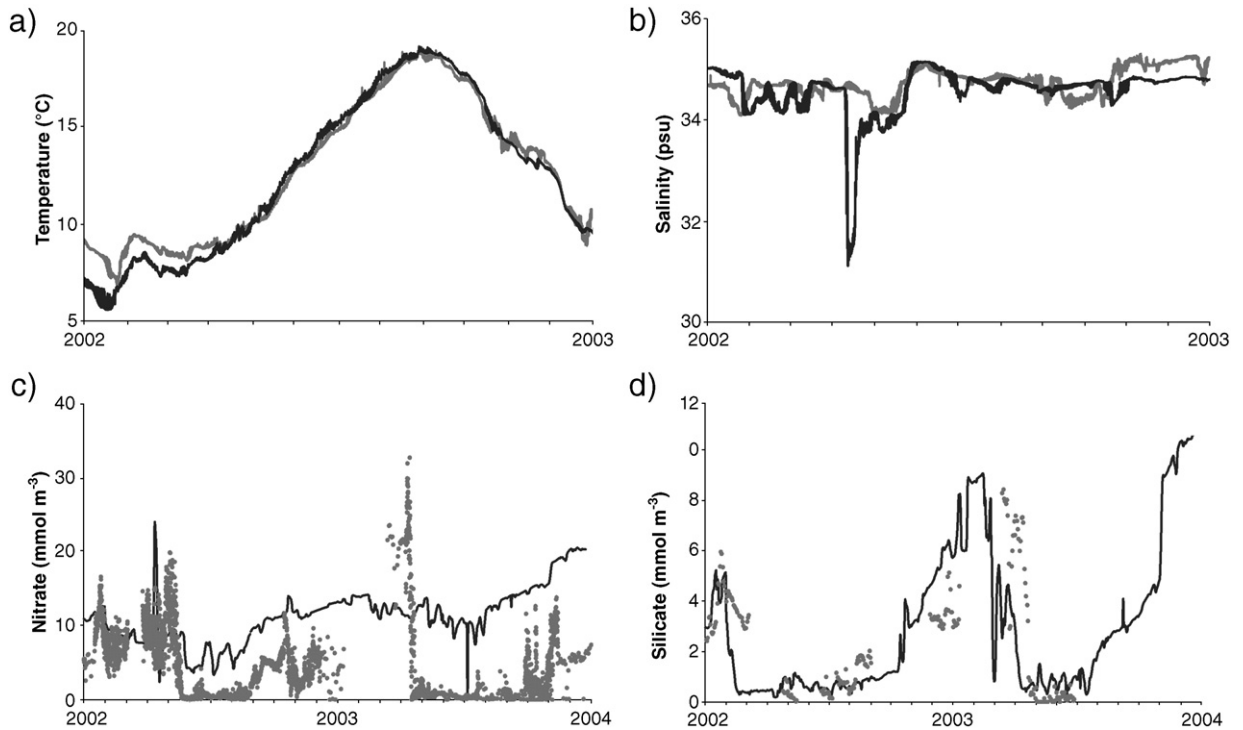
Fig. 4. Model comparisons with data from the CEFAS Gabbard SmartBuoy for a) sea surface temperature, b) surface salinity, c) surface nitrate and d) surface silicate. This includes data for Gabbard and, after 28th August 2002, West Gabbard. Modelled data are the black solid lines and SmartBuoy data the grey solid lines or points. Temperature and salinity data are not available for 2003.

order as the measured data, and has similar amplitude and frequency of the stochastic perturbations (Figs. 4 and 5). However, the use of climatological inputs means that there are events in the model not seen in the measured data, and vice versa. Improvements in river source data would clearly improve the salinity distribution within the model, and ways of obtaining such data are being investigated.

The observed nutrients show a seasonal variability, with maxima in the winter and depletion in surface waters in the spring and summer, as would be expected in an area that is seasonally stratified and biologically active. This seasonality is well replicated in the modelled silicate, especially at the Gabbard site where the winter levels of around 6 mmol/m^3 and summer depletion can be seen in both the model and the measurements. The Warp site shows good replication of measured silicate values, especially in summer and winter 2003 (Fig. 5). However, the winter 2002/3 peaks of silicate are significantly underestimated in the model. This may be due to an underestimation of inputs from the Thames. Overall, the modelled silicate values indicate the diatom functional group, which is dependent upon silicate, is being modelled adequately. The comparison between modelled and observed nitrate is

good, although there appears to be an underestimation of nitrate depletion in summer months. This lack of draw-down of modelled nitrate is thought to be a consequence of underestimation of primary production as a result of difficulties in prescribing the light field in these optically complex waters. There is also some suggestion that the phytoplankton functional group parameterisation needs adjusting and/or supplemental detrital groups need to be included to improve modelled nutrient cycling (Vichi et al., 2004). The winter nitrate, conversely, shows lower levels than those indicated by the data, again suggesting the inputs from the Thames are being underestimated.

3.2.3. L4 monitoring station chlorophyll and plankton biomass

The L4 station lies approximately 20 km off Plymouth in the English Channel in around 50 m of water, and is sampled weekly for biological and physical data. Comparisons with the measured temperature profiles (not shown) indicate that the model performs well in obtaining the temperature structure at this site with intermittent stratification occurring to depths of approximately 20 m in both the modelled and measured data. The measured data shows periods of low salinity,
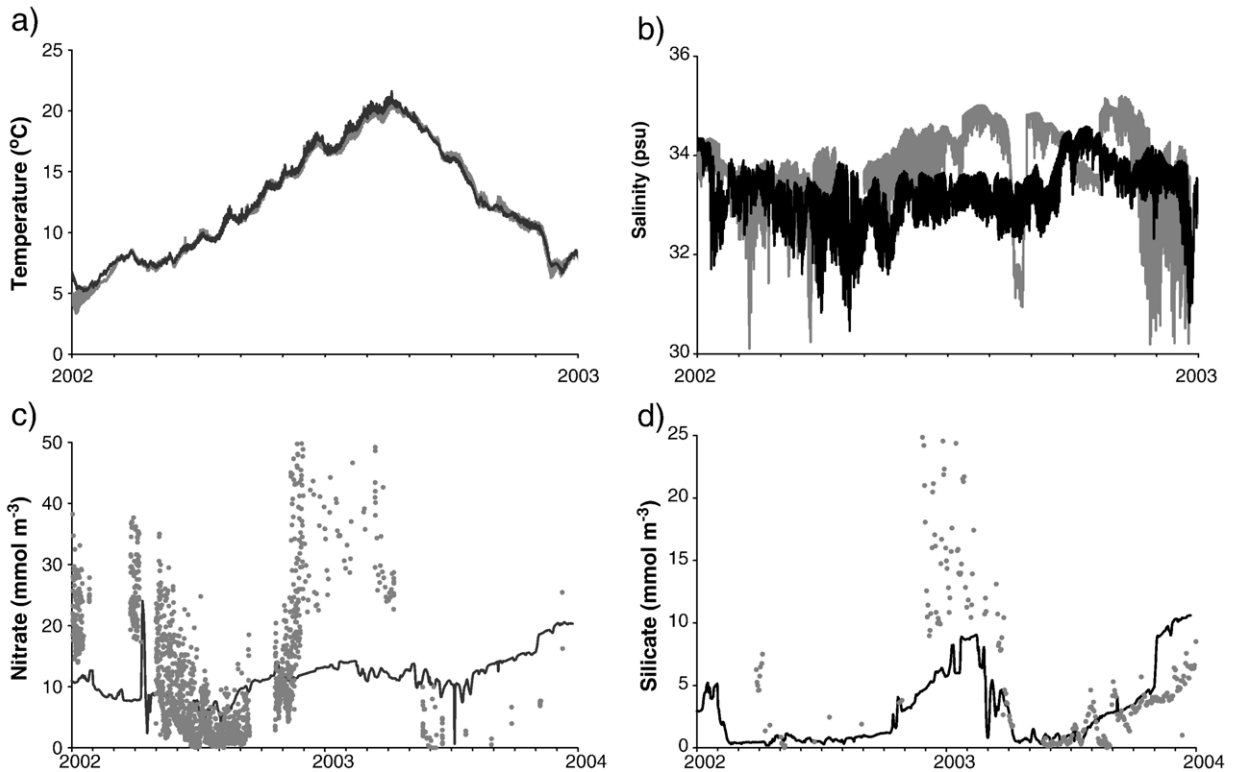
Fig. 5. Model comparisons with data from the CEFAS Warp Anchorage SmartBuoy for a) sea surface temperature, b) surface salinity, c) surface nitrate and d) surface silicate. Modelled data are the black solid lines and SmartBuoy data the grey solid lines or points. Temperature and salinity data are not available for 2003.

due to the intermit influence of freshwater from Plymouth Sound (Siddorn et al., 2003), not evident in the model. This is because the spatial resolution of the model is insufficient to reproduce the fine-scale features which determine the plume position, possibly combined with an underestimation of river inputs due to the use of climatological values.

Fig. 6a shows the measured values and the MRCS predicted surface chlorophyll. Both data and model show chlorophyll levels of between 0.5 and 5 mg-Chl/m^3 throughout the year, with some peaks of above 10 mg-Chl/m^3. The model simulates a spring bloom too early in 2002. The measured data indicates there is more intense biological activity in the autumn months than the model predicts. In 2003 the modelled spring bloom is far closer in timing to that shown in the measured data and again the summer and winter values match well, although with more variability evident in the measurements than have been predicted.

The model predicts a spring bloom of diatoms followed by a summer dominance of flagellates in both 2002 and 2003 (Fig. 6), which matches the normal pattern at L4 (Rodríguez et al., 2000). This isn't, however, shown in the

measured data for 2002, when the diatom peak actually follows the flagellate bloom suggesting that some unusual events occurred in 2002 that were not picked up by the model. Fig. 6d shows the picoplankton biomass, which show large discrepancies between the model and data. However, other data taken from L4 for the same period (unpublished results, Archer, pers. comm.) show levels of picoplankton an order of magnitude higher than that in Fig. 6, indicating the discrepancy is lower than indicated by Fig. 6d. Even given the picoplankton data underestimates the biomass the model still appears to be overestimating it, suggesting that the parameterisation of the phytoplankton functional groups shows a bias in favour of small plankton growth during nutrient limited periods.

3.2.4. Comparison with satellite chlorophyll

SeaWIFS chlorophyll data, provided by the SeaWiFS Project, NASA/Goddard Space Flight Center and ORB-IMAGE, was obtained for 2002. Eight day satellite composites (regridded from the original 9 km grid to the same spatial dimensions as the MRCS) were compared with eight day averages of MRCS surface chlorophyll (which were masked with the satellite cloud mask to
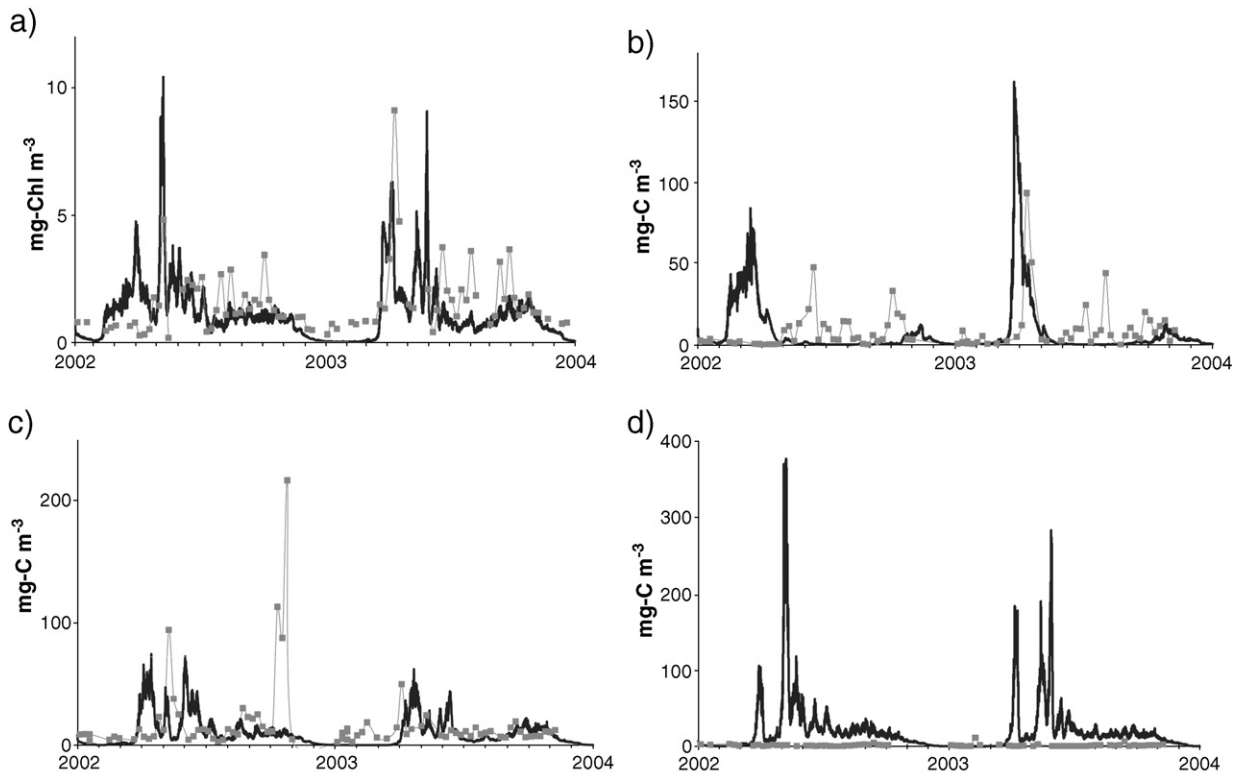
Fig. 6. Station L4 surface data for a) chlorophyll, b) diatoms, c) flagellates and d) picoplankton. Measurements are shown in grey, modelled data in black.

ensure true comparability). In total 44 composites were compared, giving a total of nearly half a million datapoints collocated in space and time, an average of 22 data values per cell. The annual mean spatially averaged chlorophyll for 2002 from SeaWIFS and MRCS was 1.72 and 2.05 mg-Chl/m^3 respectively, a 16% difference between the satellite and MRCS values, well within the error of the satellite measurements (which lie in the order 30 to 65%, Gregg and Casey, 2004; Garcia et al., 2005). However, a significant proportion of the domain lies within Case II waters, where the satellite is to be expected to significantly overestimate the chlorophyll concentrations. The model bias (Fig. 7a) shows significantly lower estimates than the satellite in the Irish Sea, eastern English Channel and German Bight — all case II waters. However, in other regions the tendency for the model is to overestimate relative to satellite chlorophyll values. Over a significant proportion of the domain this overestimation lies within the accepted range of error for satellite data, but some clear regions exist where the model is significantly in error. A skill map has been produced in which the proportions of data which lie within limits of satellite error (taken to be 50%) are shown (Fig. 7b).

This shows there is significant skill a significant proportion of time across the domain. However, the Dogger Bank, the slopes of the Norwegian Trench and the South West Approaches rarely have model chlorophyll values that fit the data. In all these regions the chlorophyll values are significantly overestimated by the model. On the Dogger Bank the model appears to be underestimating the suspended sediment load; this is a known issue with this version of the model. Similarly, the high chlorophyll values on the western slopes of the Norwegian Trench are likely to be related to high mixing found in this region, a known issue that will be dealt with in future model configurations. The high chlorophyll values found in the South West Approaches are not as easily explained; one may speculate that it is in an issue with boundary values of sediments or nutrients, or related to strength of stratification or maybe an artefact of the biological model behaviour. Further investigation into the model behaviour in this region needs to be undertaken.

Several sub-regions were assessed to gauge the models variability in seasonal response. The regions chosen where restricted to those with mainly case I waters, and included the northern North Sea (defined as the region bound by the
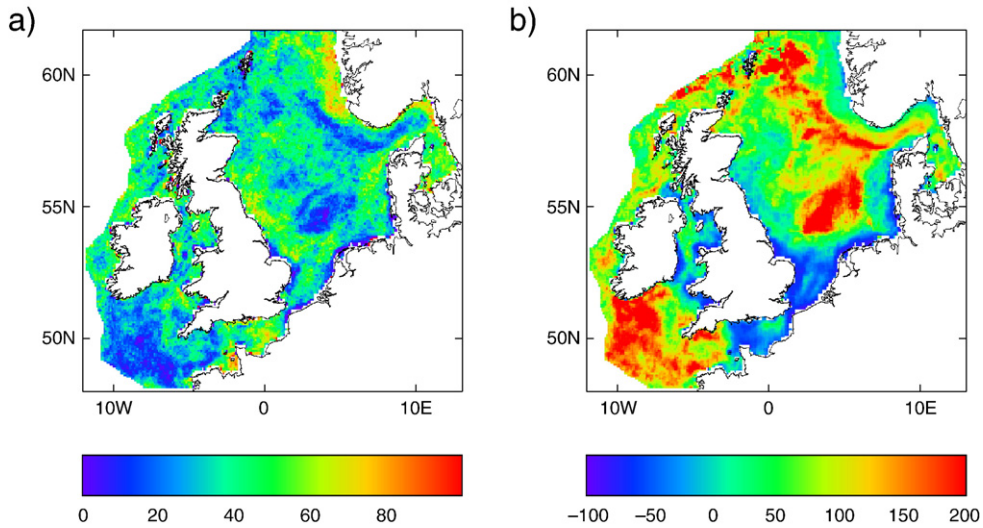
Fig. 7. a) a Chlorophyll skill map. A skill of 100% is assigned for every model value that lies within 50% of the SeaWIFS value, and the average skill score for each grid point calculated and b) the model vs. SeaWIFS chlorophyll data as an annual average bias in %.

box 5°W to 2°E, 53° N to 60° N in which the water depth is greater than 50 m), the Celtic Sea (defined as the region bound by the box 8° W to 2° W, 50.7° N to 52° N), and the West of Scotland (defined as the region bound by the box 10° W to 4° W, 55° N to 60° N in which the water depth is less than 200 m). Only those data with a reasonable coverage for the region where used in this analysis.

The annual mean chlorophyll data obtained from satellite and model averaged over the MRCS domain show good agreement (Table 1). However, there are marked differences in the correspondence between annual mean satellite and modelled chlorophyll in a number of the sub-regions. The model has a tendency to overestimate the size of the spring chlorophyll values, which is particularly evident in the West of Scotland. In the Celtic Sea, on the other hand, the model tends to consistently underestimate chlorophyll. The weekly evolution of chlorophyll values (not shown) however are well replicated, even if the amplitudes are not.

4. Conclusions and further discussion

This paper presents a modelling framework in which the hydrodynamics and ecosystem function of the North-West European continental shelf are simulated using the MRCS-ERSEM2004 model forced by data available in both near-real time and as forecasts. The capability to run the models with operationally available forcing gives the potential to include this system within the Met Office operational suite, and hence to model both the hydrodynamics and ecosystem function of the region with the level of robustness associated with operational numerical weather prediction models. This is a substantial step towards a community model resource with significant potential as a data source and management tool.

The results presented show that the system adequately represents aspects of both the hydrodynamics and ecosystem behaviour of the region in those areas where data is available. It would have been desirable to have

Table 1
Area weighted averages of surface chlorophyll for SeaWIFS satellite and the MRCS for the whole MRCS region and sub-regions

	MRCS Domain		NNS		Celtic Sea		W Scotland	
	SeaWIFS	MRCS	SeaWIFS	MRCS	SeaWIFS	MRCS	SeaWIFS	MRCS
Annual Mean (mg-Chl/m^3)	1.72	2.05	1.21	1.72	1.93	1.57	1.65	2.20
Winter	–	–	0.92	0.28	0.39	1.59	–	–
Spring	2.19	3.41	1.69	2.70	2.89	2.42	1.51	2.97
Summer	1.64	2.18	0.92	1.44	2.28	1.23	1.95	2.36
Autumn	1.48	1.50	1.01	1.18	1.36	1.21	1.50	1.59

Winter is taken as the middle of November through to the middle of February and the subsequent seasons are taken as three months each. Boxes with no data indicates no composites with sufficient data coverage (as a proportion of the area) exist in that period.

conducted the validation at a wider range of sites, especially given the complexity and diversity of the study region. However there is a continuing problem with attempting validation exercises such as this in that the availability of data is poor, especially for biological and chemical parameters, and where data exists it is often hard to obtain data within reasonable timeframes. The bulk of the validation undertaken for this paper was in near-shore areas. However, other work using this model (Holt and James, 1999a and Allen et al., unpublished results) show that offshore regions validate better than near-shore ones. This is also supported by the validation against satellite data.

The predicted sea surface temperature compares extremely well with measurements, emphasising the strength of the hydrodynamic model coupled with the use of the high resolution surface forcing and good lateral boundary data. The validation of ecosystem parameters is generally good, although this work highlights areas of model design already identified for improvement. The data at the L4 site indicates that although the general characteristics of the ecosystem are effectively reproduced by the model, the distribution of biomass between functional groups does not validate well. The SmartBuoy data show that the model underestimates the drawdown of nitrate in the summer and autumn in near coast regions, which may be related to plankton functional group parameterisations and/or detrital cycling. The plankton succession problems raised by the L4 comparisons may similarly be related to errors in nutrient modelling or plankton functional group parameterisations.

Improvements to the model are being investigated, including the impacts of an improved light submodel, to include assimilation of satellite colour information and improved determination of the light extinction due to suspended particulate matter. Additionally, further resolving the sediment components to improve sinking rates will improve the modelled nutrient cycling. The nutrient cycling in the model is dependent upon the effective modelling of sediment transport, deposition and resuspension and research is in place to improve this component of the model. Furthermore, the use of climatological river sources of salinity, detritus and nutrients is not optimal and efforts to improve the quality of the river data available to the model are underway. Work is also being done to improve the ecosystem model further by including data assimilation (the assimilation of incoming solar radiation and chlorophyll are being investigated Allen et al., 2003; Triantafyllou et al., 2003b), which will, once tested and published, be used in the next generation of ERSEM

models. The comparison with satellite data show that the model has variable skill across the domain, and the causes of this are being investigated and will inform any future developments of the model.

Whilst acknowledging the potential for improvement identified above, the MRCS-ERSEM2004 has been shown to be an effective modelling tool. The structures are now in place for this to be used in an operational environment where products and services can be provided on request, either for the present day, as short-term forecasts or for past events. It is envisaged that these products will range from model variables such as sea surface temperature, sea surface height and currents and chlorophyll, to derived products like annual or seasonal mean primary productivity, OSPAR like eutrophication indices and Harmful Algal Bloom event predictions. All these, when validated against available observations, could provide input to a climate status assessment of the North Sea, as well as forming a component of an integrated model and observation-based monitoring system.
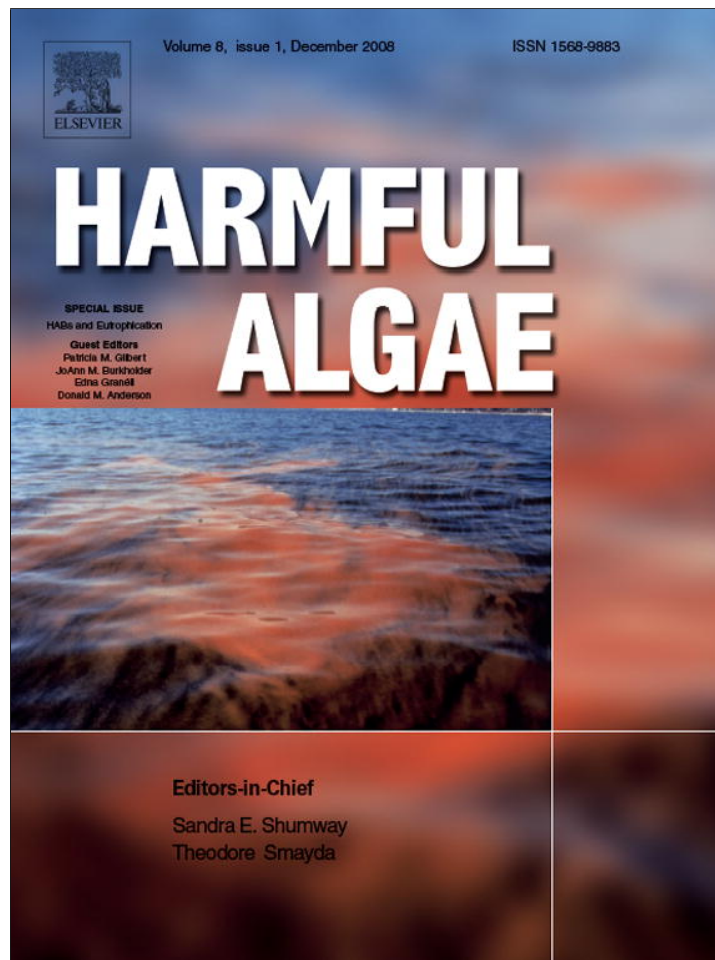
Acknowledgements

References

Arakawa, A., 1972. Design of the UCLA general circulation model. Tech. Rep., vol. 7. Univ. of California, Los Angeles. 116 pp.

Allen, J.I., Blackford, J., Holt, J.T., Proctor, R., Ashworth, M., Siddorn, J.R., 2001. A highly spatially resolved ecosystem model for the North West European continental shelf. Sarsia 86, 423–440.

Allen, J.I., Somerfield, P.J., Siddorn, J., 2002. Primary and bacterial production in the Mediterranean Sea: a modelling study. Journal of Marine Systems 33, 473–495.

Allen, J.I., Eknes, M., Evensen, G., 2003. An Ensemble Kalman Filter with a complex marine ecosystem model: hindcasting phytoplankton in the Cretan Sea. Annales Geophysicae 21, 399–411.

Baretta, J.W., Ebenhöh, W., Ruardij, P., 1995. The European regional Seas Ecosystem Model, a complex marine ecosystem model. Netherlands Journal of Sea Research 33, 233–246.

Baretta-Bekker, J., Baretta, J.W., Ebenhöh, W., 1997. Microbial dynamics in the marine ecosystem model ERSEM II with decoupled carbon assimilation and nutrient uptake. Journal of Sea Research 38, 195–212.

Bell, M.J., Barciela, R., Hines, A., Martin, M.J., McCulloch, M.E., Storkey, D., 2003. The Forecasting Ocean Assimilation Model

(FOAM) system. In: Dahlin, H., Flemming, N.C., Nittis, K., Petersson, S.E. (Eds.), Building the European Capacity in Operational Oceanography. Proceedings of the Third International Conference on EuroGOOS. Elsevier Oceanography Series, vol. 69, pp. 196–202.

Blackford, J.C., 1997. An analysis of benthic biological dynamics in a North Sea ecosystem model. Journal of Sea Research 38, 213–230.

Blackford, J.C., Burkill, P.H., 2002. Planktonic community structure and carbon cycling in the Arabian Sea as a result of monsoonal forcing: the application of a generic model. Journal of Marine Systems 36, 239–267.

Blackford, J.C., Allen, J.I., Gilbert, F.J., 2004. Ecosystem dynamics at six contrasting sites: a generic modelling study. Journal of Marine Systems 52, 191–215.

Bryant, A.D., Heath, M.R., Broekhuizen, N., Ollason, J.G., Gurney, W.S.C., Greenstreet, S.P.R., 1995. Modeling the predation, growth and population-dynamics of fish within a spatially-resolved shelf-sea ecosystem model. Netherlands Journal of Sea Research 33, 407–421.

Charnock, H., Dyer, K.R., Huthnance, J.M., Liss, P.S., Simpson, J.H., Tett, P.B., 1993. Understanding the North Sea system. Philosophical Transactions of the Royal Society of London. A 343, 377–605.

Ebenhöh, W., Kohlmeier, C., Radford, P.J., 1995. The benthic biological model in the European Regional Seas Ecosystem Model. Netherlands Journal of Sea Research 38, 169–172.

Garcia, C.A.E., Garcia, V.M.T., McClain, C.R., 2005. Evaluation of SeaWiFS chlorophyll algorithms in the Southwestern Atlantic and Southern Oceans. Remote Sensing of Environment 95, 125–137.

Geider, R.J., MacIntyre, H.L., Kana, T.M., 1997. Dynamic model of phytoplankton growth and acclimation: Responses of the balanced growth rate and the chlorophyll a: carbon ratio to light, nutrient-limitation and temperature. Marine Ecology. Progress Series 148, 187–200.

Gregg, W.W., Casey, N.W., 2004. Global and regional evaluation of the SeaWiFS chlorophyll data set. Remote Sensing of Environment 93, 463–479.

Haney, R.L., 1971. Surface thermal boundary condition for ocean circulation models. Journal of Physical Oceanography 1, 241–248.

Heath, M., Scott, B., Bryant, A.D., 1997. Modelling the growth of herring from four different stocks in the North Sea. Journal of Sea Research 38, 413–436.

Holt, J.T., James, I.D., 1999a. A simulation of the southern North Sea in comparison with measurements from the North Sea project, part 1, Temperature. Continental Shelf Research 19, 1087–1112.

Holt, J.T., James, I.D., 1999b. A simulation of the southern North Sea in comparison with measurements from the North Sea project, part 2, Suspended particulate matter. Continental Shelf Research 19, 1617–1642.

Holt, J.T., James, I.D., 2001. An s-coordinate density evolving model of the northwest European continental shelf Part 1 model description and density structure. Journal of Geophysical Research 106, 14015–14034.

Holt, J.T., Proctor, R., 2003. The role of advection in determining the temperature structure of the Irish Sea. Journal of Physical Oceanography 33, 2288–2306.

Holt, J.T., James, I.D., Jones, J.E., 2001. An s-coordinate density evolving model of the northwest European continental shelf- 2, Seasonal currents and tides. Journal of Geophysical Research 106, 14035–14053.

Holt, M., Li, Z., Osborne, J., 2003. Real time forecast modeling for the NW European Shelf Seas. In: Dahlin, H., Flemming, N.C., Nittis, K., Petersson, S.E. (Eds.), Building the European Capacity in Operational Oceanography. Proceedings of the Third International Conference on EuroGOOS. Elsevier Oceanography Series, vol. 69, pp. 484–489.

Holt, J.T., Allen, J.I., Proctor, R., Gilbert, J., 2005. Error quantification of a high-resolution coupled hydrodynamic-ecosystem coastal-ocean model: Part 1 model overview and assessment of the hydrodynamics. Journal of Marine Systems 57, 167–188.

James, I.D., 1996. Advection schemes for shelf sea models. Journal of Marine Systems 8, 237–254.

Moll, A., 1998. Regional distribution of primary production in the North Sea simulated by a three dimensional model. Journal of Marine Systems 16, 151–170.

Moll, A., Radach, G., 2003. Review of three-dimensional ecological modelling related to the North Sea shelf system — Part 1: models and their results. Progress in Oceanography 57, 175–217.

Pätsch, J., Radach, G., 1997. Long-term simulation of the eutrophication of the North Sea: temporal development of nutrients, chlorophyll and primary production in comparison to observations. Netherlands Journal of Sea Research 38, 275–310.

Proctor, R., James, I.D., 1996. A fine-resolution 3D model of the southern North Sea. Journal of Marine Systems 8, 285–295.

Proctor, R., Holt, J.T., Allen, J.I., Blackford, J., 2003. Nutrient fluxes and budgets for the North West European Shelf from a three-dimensional model. Science of the Total Environment 314, 769–785.

Reid, P.C., Lancelot, C., Gieskes, W.W.C., Hagmeir, E., Weichart, G., 1990. Phytoplankton of the North Sea and its dynamics: a review. Netherlands Journal of Sea Research 26, 295–331.

Robinson, L.A., Frid, C.L.J., 2003. Dynamic ecosystem models and the evaluation of ecosystem effects of fishing: can we make meaningful predictions? Aquatic Conservation-Marine And Freshwater Ecosystems 13, 5–20.

Rodríguez, F., Fernández, E., Head, R.N., Harbour, D.S., Bratbak, G., Heldal, M., Harris, R.P., 2000. Temporal variability of viruses, bacteria, phytoplankton and zooplankton in the western English Channel off Plymouth. Journal of the Marine Biological Association of the UK 80, 575–586.

Ruardij, P., van Raaphorst, W., 1995. Benthic nutrient regeneration in the ERSEM ecosystem model of the North Sea. Netherlands Journal of Sea Research 33, 453–483.

Ruardij, P., van Haren, H., Ridderinkhof, H., 1997. The impact of thermal stratification on phytoplankton and nutrient dynamics in shelf seas: a model study. Journal of Sea Research 38, 311–332.

Siddorn, J.R., Allen, J.I., Uncles, R.J., 2003. Heat, salt and tracer transport in the Plymouth Sound coastal region: A 3D modelling study. Journal of the Marine Biological Association of the UK 83, 673–682.

Triantafyllou, G., Petihakis, G., Allen, J.I., 2003a. Assessing the performance of the Cretan Sea ecosystem model with the use of high frequency M3A buoy data set. Annales Geophysicae 21, 365–375.

Triantafyllou, G., Hoteit, I., Petihakis, G., 2003b. A singular evolutive interpolated Kalman filter for efficient data assimilation in a 3-D complex physical–biogeochemical model of the Cretan Sea. Journal of Marine Systems 40, 213–231.

Vichi, M., Ruardij, P., Baretta, J.W., 2004. Link or sink: a modelling interpretation of the open Baltic biogeochemistry. Biogeosciences Discussions 1, 219–274.

How well can we forecast high biomass algal bloom events in a eutrophic coastal sea?

J. Icarus Allen [a,*], Timothy J. Smyth [a], John R. Siddorn [b], Martin Holt [b]

[a] Plymouth Marine Laboratory, Prospect Place, West Hoe, Plymouth PL1 3DH, UK
[b] Met Office, Fitzroy Road, Exeter, Devon EX1 3PB, UK

ARTICLE INFO

ABSTRACT

High biomass algal bloom events are a characteristic of eutrophic coastal waters; these may result both in ecosystem degradation and economic loss. We present a skill evaluation of a coupled hydrodynamic ecosystem model of the NW European shelf for predicting bloom events based on a comparison with satellite chlorophyll estimates. By setting thresholds to define bloom events we use a binary classification system to generate maps showing the probability a model bloom prediction is correct. Model and satellite data limitations are discussed along with the application of this method to forecasting specific harmful algal species.

© 2008 Elsevier B.V. All rights reserved.

1. Introduction

A common characteristic of eutrophic aquatic ecosystems is nutrient enrichment of the water column, with subsequent enhanced growth of phytoplankton, leading to distortion of foodwebs and degradation of water quality (e.g. OSPAR, 1998). These increases in total algal biomass can lead to undesirable effects such as oxygen depletion from the decay of biomass, suffocation of fish, deleterious effects on benthic biomass and enhanced biomass of toxic algal species. The result is poor energy transfer to higher trophic levels. An extensive literature exists on these subjects and details of the influence of enhanced nutrients on harmful algae can be found in for example GEOHAB (2006), Anderson et al. (2002) and references within. Clearly there is a strategic imperative to be able to forecast algal bloom occurrence.

The NW European shelf, can be divided into two regions (Fig. 1), the north and west of the region is characterised by seasonally stratified, optically clear mesotrophic water and the south and east is characterised by tidally well mixed, optically complex eutrophic waters, in particular the southern North Sea, Irish Sea and English Channel. The UK National Centre for Ocean Forecasting (NCOF) has established a pre-operational ecosystem model of this region, based on POLCOMS-ERSEM. This model is run every week in a 7-day rolling hindcast (http://www.met-office.gov.uk/research/ncof/mrcs/browser.html). While ERSEM is a relatively complex ecosystem model, describing four phytoplankton functional types it does not resolve individual species.

There are a number of HAB species found regularly in northern European waters. They are a disparate group, with examples coming from all of the major phytoplankton classes. Their effects are wide ranging from nuisance blooms (which produce foam and are aesthetically unappealing but have no major direct impacts) to high biomass blooms, which lead to anoxia and related effects, to ichthytoxic blooms which kill fish, and may have large direct economic impacts, to blooms which produce toxins which are subsequently bio-accumulated in shellfish and thus have health and economic impacts. Shellfish poisoning in European waters comes in three major types, defined by their impacts upon human consumers; Paralytic Shellfish Poisoning (PSP), Diarrhetic Shellfish Poisoning (DSP) and Amnesic Shellfish Poisoning (ASP). Some major genera implicated in harmful events in European waters are shown in Table 1. This list is not exhaustive and other genera exist that are potentially problematic. For instance the LIFEHAB workshop report (LIFEHAB 2001) lists more than 25 diatom species found in European waters that are, or have the potential to be, toxic, of which nine are species of Pseudo-nitzschia.

Currently there are few heuristic models capable of simulating aspects of the processes controlling specific harmful algal species,

* Corresponding author at: PML, Prospect Place, West Hoe, Plymouth PL1 5LT, UK. Tel.: +44 1752 633100.
E-mail address: jia@pml.ac.uk (J.I. Allen).
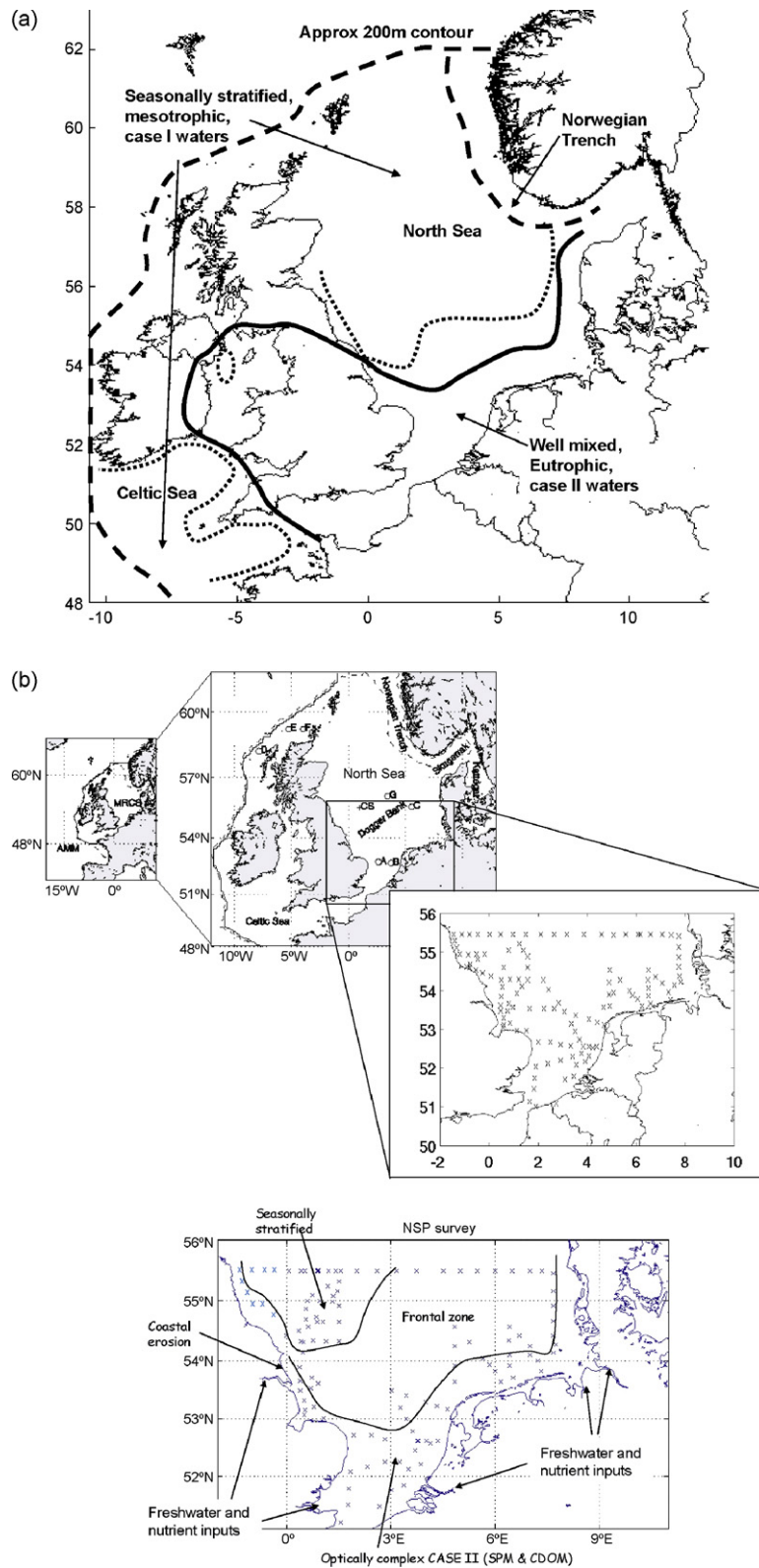
Fig. 1. (a) Map of the study region. The thick dashed line denotes the 200 m contour on the shelf break and the model boundary. The thin dotted lines indicate the approximate position of the seasonally stratified tidal mixing fronts in the region. (b) A schematic diagram of the functional groups and linkages in the pelagic components of the ERSEM model.

for example, *Phaeocystis* (Lancelot et al., 2007; Ruardij et al., 2005), *Pfiesteria* (Hood et al., 2006) and *Pyrodinium* (Villanoy et al., 2006). The forecast modelling of harmful algal blooms is in its infancy and the starting point in evaluating the usefulness or otherwise of

models such as POLCOMS-ERSEM for HAB prediction is to quantify the ability of the model to simulate high biomass algal blooms.

Satellite observations of ocean colour provide extensive spatio-temporal data coverage of the distribution of chlorophyll, which in

Table 1
Some important plankton genera that cause problems in European coastal waters.

Organism	Effect	Areas with major HAB problems
Dinoflagellates		
Alexandrium	PSP, high biomass	All European coasts, except Bay of Biscay, southern North Sea and Baltic Sea
Dinophysis	DSP	Europe wide
Karenia	Ichthyotoxic	Skagerrak, Kattegat, Celtic Sea, western English Channel, central and northern North Sea, Bay of Biscay
Diatoms		
Pseudo-nitzschia	ASP	Europe wide
Flagellates		
Phaeocystis	High biomass, foam production	North Sea, English Channel, northern Norwegian fjords
Chattonella	Ichthyotoxic, high biomass	Skagerrak, North Sea coasts of Denmark, Germany and the Netherlands

Adapted from the LIFEHAB workshop report.

turn indicate the presence of large algal blooms. The aim of this paper is to assess the models ability to predict large algal blooms. We present a technique for determining the probability that the model correctly predicts a bloom event, along with a brief discussion of the sources of model errors and the generic application of the method to bloom prediction.

2. Methods

2.1. Model

The Medium Resolution Continental Shelf (MRCS) model is a hindcasting/forecasting system (Siddorn et al., 2007). It is based on a coupled 3D hydrodynamic and ecosystem model (the Proudman Oceanographic Laboratory Coastal Ocean Modelling System coupled with the European Regional Seas Ecosystem Model POLCOMS-ERSEM; Allen et al., 2001; Holt et al., 2004), set up on a $1/10°$ longitude by $1/15°$ latitude horizontal grid ($\sim$7 km) and 20 s-levels (Song and Haidvogel, 1994) in the vertical with boundaries following the North-West European Continental Shelf break (approximate along the 200 m isobath, except for the Norwegian Trench; Fig. 1a). Boundary forcing for temperature, salinity, currents and sea surface elevation is obtained from a $1/6°$ longitude by $1/9°$ latitude ($\sim$12 km) Atlantic Margin Model, which is nested in the Met Office's FOAM system (Bell et al., 2000). An averaged annual cycle is used for boundary conditions since the operational system has not simulated the period of interest here. The model includes the density evolving physics of POLCOMS (Holt and James, 2001) and a size-fractionated SPM sub-model (Holt and James, 1999), coupled with the biogeochemical processes of ERSEM (Blackford et al., 2004; Baretta et al., 1995); Fig. 1b, is a schematic of the pelagic model. ERSEM is a functional group model and has one bacteria, four phytoplankton and three zooplankton pelagic functional groups. It has a fully resolved diurnal cycle, variable carbon to chlorophyll ratios and independent nutrient pools for carbon, nitrogen, phosphorous and silicate. Coupled with the pelagic model is a benthic model to give not only detailed process information of the benthic ecosystem but also a well defined nutrient coupling between the benthic and pelagic systems. Full details of the model experiment are given in Siddorn et al. (2007).

2.2. Satellite data

Satellite data was acquired from the NASA Moderate Resolution Imaging Spectroradiometer (MODIS) Aqua ocean colour sensor as pre-processed level 2 chlorophyll-a (O'Reilly et al., 1998) individual 1 km resolution passes within the model domain. These were then projected (Mercator), mapped and weekly chlorophyll composites produced. The weekly satellite composites were then re-sampled onto the same grid as the MRCS model domain using a 14 pixel moving window median filter.

2.3. Statistical methods

We can assess model skill by using the predictive power of a binary classification system as a discrimination threshold is varied. Brown and Davis (2006) provide a detailed and accessible tutorial of these methods. The basis is a simple "yes" or "no" decision, based on the comparison of two independent information sets (in our case satellite retrievals and model) with respect to a threshold value. The aim is to assess how well a test (model) can discriminate between two discrete observed outcomes (e.g. harmful algal bloom). The perfect model is one where all the points in a scatter diagram of model vs. data lie on the $x = y$ line. The threshold criteria (t) set divides the data into two parts; by then comparing it with the model using the same threshold we can assess model data similarity at that threshold. This effectively assesses the model ability to discriminate that threshold. The decision process has four possible outcomes for each trial, either correctly positive (CP), correctly negative (CN), incorrectly positive (IP) or incorrectly negative (IN). The perfect model will only give CP and CN outcomes; the more scatter there is in the model–data relationship the more IP and IN conditions will occur and the worse the model performance is judged to be. By varying the threshold across the full range of observations, we obtain a non-parametric measure of the models ability to simulate a given variable, which can be then compared directly with other simulated variables. The classification rate for n samples is defined as

$$CR = \frac{CP + CN}{n} \tag{1}$$

The decision process can be further assessed by calculating the correct negative fraction (CNF) and the correct positive fraction (CPF).

$$CNF = \frac{CN}{CN + IP}, \quad CPF = \frac{CP}{CP + IN} \tag{2}$$

CNF and CPF express the fraction of negative and positive events, which were correctly determined. These values are independent of the actual numbers of positive and negative events in the trials. Decisions based on CPF and CPN are estimators of probabilities of decisions conditioned on events: i.e., if a positive event (a bloom) has occurred what is the probability the correct decision has been made? While these probabilities are useful they do not address the fundamental question, if a positive decision is made what is the probability that the decision is correct. The
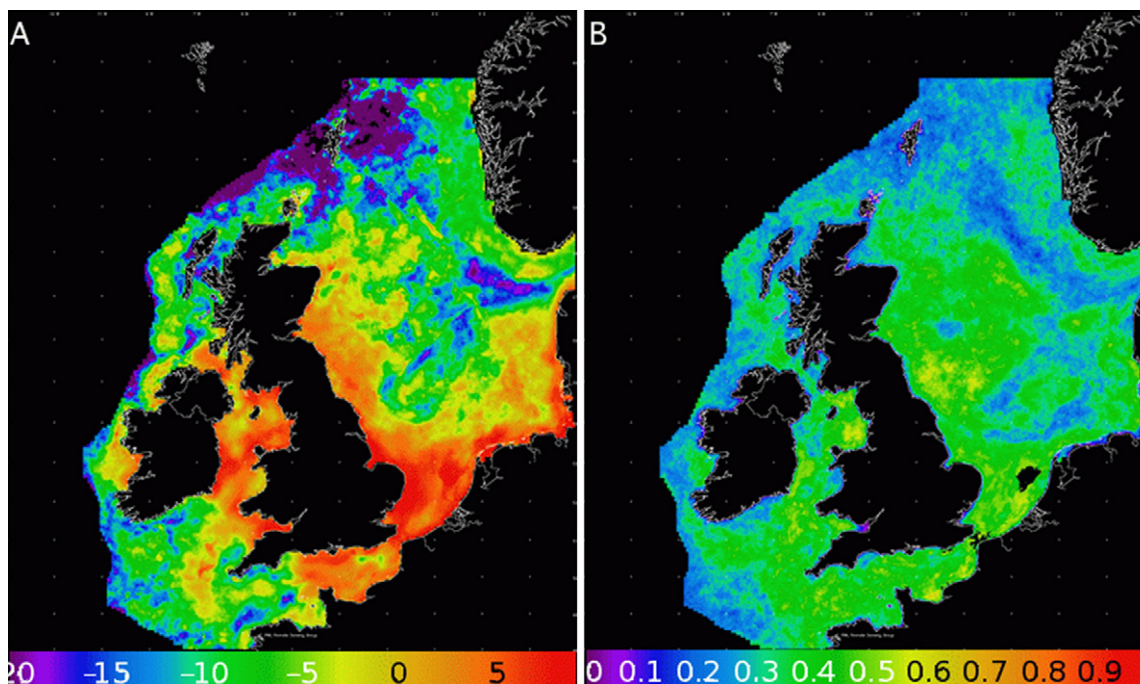
Fig. 2. (a) Percentage bias (the sum of model error normalized by the data) and (b) the classification rate for each pixel; computed from the comparison of weekly composites of MODIS Aqua chlorophyll and simulated chlorophyll for 2005. Negative bias indicates model overestimates chlorophyll. Pbias $= \sum_{n=1}^{N}(D^n - M^n)/\sum_{n=1}^{N} D^n \times 100$ D = data value, M = model value.

positive predictive value (PPV) and negative predictive value (NPV) can be expressed as (see Brown and Davis (2006) for the theoretical background and derivation).

$$PPV = \frac{CP}{CP + IP}, \quad NPV = \frac{CN}{CN + IN} \tag{3}$$

Values of PPV and NPV can range between 0 and 1, reflecting the intrinsic power of the decision; high values indicating a decision can be trusted, low values suggesting the decision should be regarded with scepticism.

To establish thresholds we have calculated the mean chlorophyll concentration for each pixel over the period 2004–2005 from the satellite weekly composites. The thresholds for a bloom are set as (i) the mean chlorophyll concentration and (ii) the mean plus 50%, for each individual pixel, to discriminate small and large bloom events, respectively.

3. Results

The distribution of the percentage bias in the model and the classification rate when compared with MODIS Aqua chlorophyll is illustrated in Fig. 2. The bias map (Fig. 2a) shows some clear trends, the model systematically overestimates chlorophyll concentrations along the ocean boundaries and in the stratified regions and systematically underestimates biomass in the highly eutrophic waters of the Irish Sea and the southern North Sea. The classification rate map (Fig. 2b) is quite similar in structure to the bias map; regions of poor performance (CR < 0.3) corresponding with regions of high negative bias (model overestimation) resulting in large numbers of false positive predictions. In terms of classification rate the model skill is best in the eutrophic waters, and the stratified central North Sea and western English Channel, achieving rates of 40–60%.

Basic error statistics have been calculated for model data misfit of the weekly composites for chlorophyll in 2005 (2004 shows similar behaviour). We illustrate the temporal evolution of model

errors made by plotting the square of the correlation coefficient against the root mean square error (RMSE, Fig. 3) which gives a crude estimation of model skill. In winter there is limited forecast skill ($r^2 \sim 0.3$), but as we move into spring it decreases markedly. In April the r^2 is almost zero implying very little skill; this is probably a consequence of errors in the timing of the spring bloom. During the summer the model explains up to 50% of the variability in the data ($r^2 \sim 0.5$ in August), then the skill steadily deteriorates until by November it is close to zero. This deterioration in skill may be in part due to prolonged thermal stratification (Holt et al., 2005).

Fig. 4 shows maps of the spatial probability distribution for PPV and NPV being correct for the two thresholds of the annual mean chlorophyll (panel A and C) and 50% above the pixel mean chlorophyll (panel B and D) for each pixel. These maps indicate on a pixel by pixel basis the ability of the model to discriminate thresholds of chlorophyll concentration. When the threshold is set to the mean, 40–50% of the model bloom predictions are correct over most of the domain (Fig. 4a). There are patches where the skill
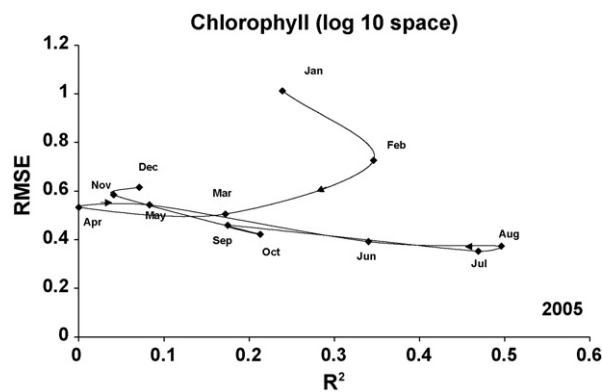
Fig. 3. Phase space plots of the monthly variation in errors in chlorophyll in 2005.
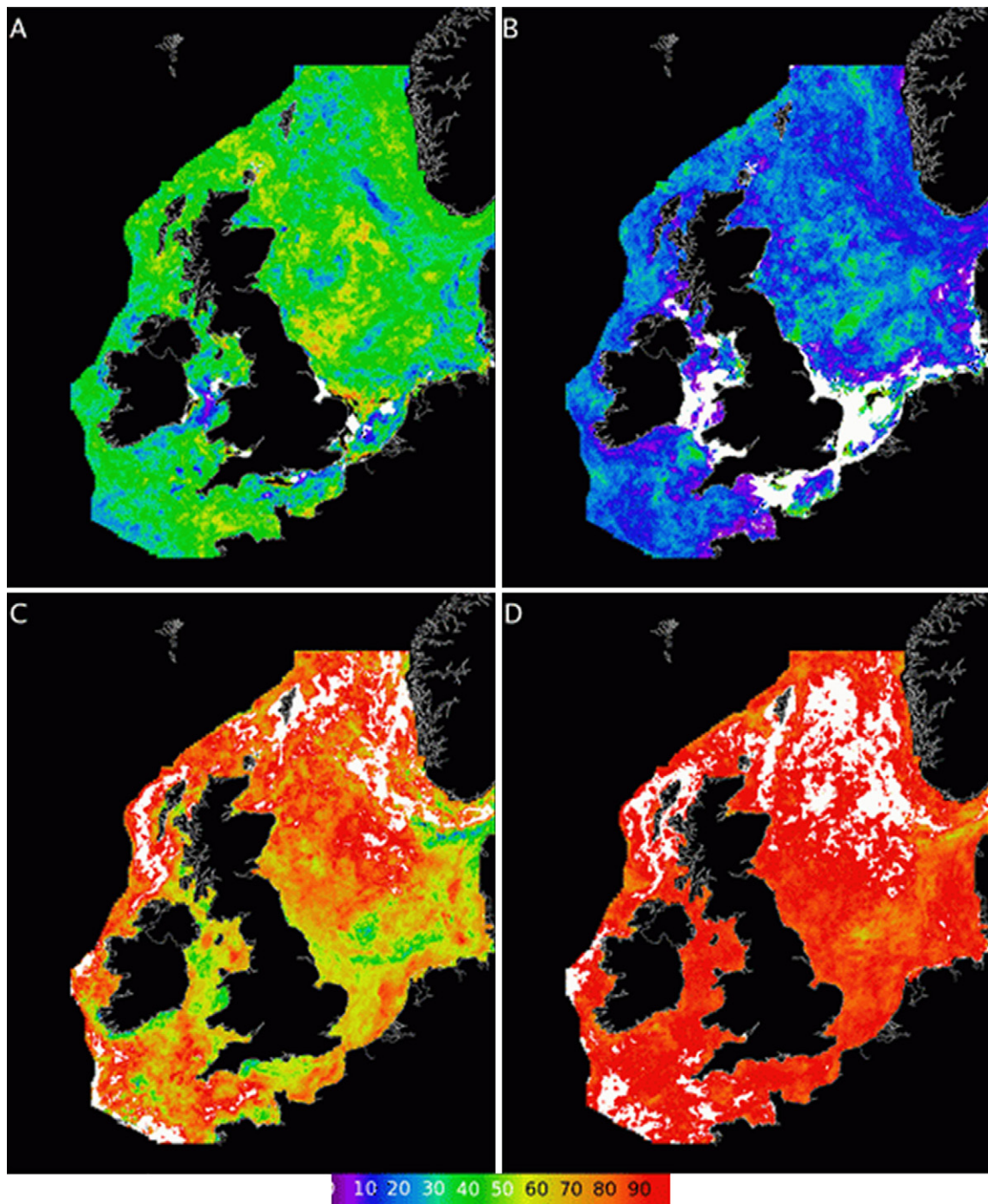
Fig. 4. PPV and NPV estimator fields (units are %). (A) PPV for threshold > mean chlorophyll concentration for that pixel, (B) PPV for threshold > 1.5 mean chlorophyll concentration for that pixel, (C) NPV for threshold > mean chlorophyll concentration for that pixel, (D) NPV for threshold > 1.5 mean chlorophyll concentration for that pixel. The data used as input were the weekly composite chlorophyll fields of both MRCS and Aqua (generated from the daily passes) for 2004 and 2005. Black indicates zero probability, White indicates no data; a pixel where the model bias is such it never exceeds the threshold (PPV maps) for falls below it (NPV maps).

is much higher (>70%) mostly either in the middle of stratified regions or in near shore regions. The regions of very low skill (<20%) occur in the turbid well-mixed waters (however see discussion for caveats concerning the satellite data) and in frontal regions particularly along the boundary of the Norwegian coastal current. When the threshold for a bloom is raised to 50% above the mean chlorophyll concentration the model skill is much lower (Fig. 4b); PPV < 30% for most of the domain, with the lowest values occurring in frontal regions. In the eutrophic regions the model is biased towards underestimation. Consequently there are sub-stantial areas where the model does not predict values above the threshold and has no skill (indicated in white). The corresponding skill maps for negative events are shown in Fig. 4c and d. At the lower threshold the model gets 90% of non-bloom events correct in the stratified regions and the skill is much lower in the (<70%) in the eutrophic regions. At the higher threshold the model correctly predicts no bloom occurrence over 90% of the time. In both cases over estimation of chlorophyll concentration in the Northern and Western parts of the domain indicates that the model never predicts values below the threshold.

4. Discussion and conclusions

It is apparent that the model has some aspect of skill for predicting blooms at the mean, but not at the higher (>50% mean) threshold. Also if the model indicates no bloom it is usually correct. However it is also apparent that there are many discrepancies between the model and satellite data, the most notable being, errors in the timing of the spring bloom (e.g. Fig. 3; Lewis et al., 2006) and high bias in frontal regions (Fig. 1; Siddorn et al., 2007). The discrepancies in the timing of the spring bloom can be attributable to under estimation of turbulent mixing in the stratified regions and poor model representation of the in-water optics in the well-mixed regions. Further evidence and the potential mechanisms are discussed in more detail in Holt et al. (2005), Allen et al. (2007a,b), and Lewis et al. (2006). The errors associated with physical structures (fronts) are attributed to enhanced mixing in these regions (Siddorn et al., 2007).

Discrimination analysis allows us to assess model performance in a way which is potentially highly relevant for environmental management. Many decisions are based on thresholds. For example OSPAR criteria for enhanced eutrophic status, has a series of assessment criteria (e.g. winter dissolved nitrate or phosphate concentrations, increased winter N:P ratio and elevated maximum and mean chlorophyll concentrations). Elevated levels are defined as 50% above the regional specific background concentration. Once these thresholds are defined we can use the discrimination analysis to determine the probability that a predicted elevated level in the model is correct.

A basic assumption of the method outlined in this paper is that the satellite data represents the 'truth'. Inevitably our ability to interpret this information is limited by the quality of the satellite chlorophyll estimates used. The highly eutrophic regions where high biomass blooms occur are optically complex (classified as case II), being characterised by high sediment loads and both land derived and marine dissolved coloured organic matter (Prieur and Sathyendranath, 1981). Such waters present a major challenge to satellite algorithms (Doerffer and Fischer, 1994; Ruddick et al., 2001) and the current operational band ratio algorithms are unable to accurately retrieve chlorophyll concentrations (Blondeau-Patissier et al., 2004; Harding et al., 2005) in case II waters. It is imperative that there is a significant improvement in accuracy of chlorophyll estimates from satellite in case II regions so we can better assess model predictive skill. A possible pragmatic solution to this problem, with relevance to our particular application, is to introduce a statistical data error model with appropriately higher variance in case II waters. This would result in a map of "correct classification probability" relevant throughout the domain. However it is likely that even if a "perfect" chlorophyll product from space were developed in case II waters, this problem is only a second order effect when compared with the complexity of developing models to forecast/nowcast/hindcast the occurrence and magnitude of algal blooms and their possible toxicity.

In the more oceanic waters where the variable optical signature is dominated by phytoplankton (classified as case I waters) the accepted accuracy goal from satellite is chlorophyll to within 30%.

An important aspect of modelled data is that it allows an expert user to infer from it aspects of the system that the model is not able to simulate directly. In the same way that a weather forecaster takes information about pressure and moisture fields from a numerical weather prediction model to infer what the weather will be, a marine environmental forecaster may be able to take information from a numerical ecosystem prediction model to predict aspects of the ecosystem not directly simulated. For example, we know that HAB events often coincide with distorted nitrate: phosphate ratios (e.g. Burkholder et al., 2001; Radach et al.,

1990) and low turbulence (e.g. Dahl and Tangen, 1993), and that toxin production often occurs when the phytoplankton is nutrient stressed (e.g. Johansson and Graneli, 1999; Anderson et al., 1990). Currently we cannot make species-specific forecasts of HABs but we can simulate the aforementioned indicators. If suitably large data sets are available, we can assign thresholds for these indicators and determine the probability the model predicts an event correctly in much the same way as we have outlined here for satellite data. Therefore in principle, we can combine information from hydrodynamic and ecosystem models to provide probability-based risk maps of HAB occurrence in a manner similar to that suggested by Brown et al. (2002) and Decker et al. (2007).

Acknowledgements

References

Allen, J.I., Blackford, J.C., Holt, J.T., Proctor, R., Ashworth, M., Siddorn, J.R., 2001. A highly spatially resolved ecosystem model for the North West European Continental Shelf. Sarsia 86, 423–440.

Allen, J.I., Somerfield, P.J., Gilbert, F.J., 2007a. Quantifying uncertainty in high-resolution coupled hydrodynamic-ecosystem models. J. Mar. Syst. 64, 3–14.

Allen, J.I., Holt, J.T., Blackford, J.C., Proctor, R., 2007b. Error quantification of a high-resolution coupled hydrodynamic-ecosystem coastal-ocean model: Part 2. Chlorophyll-a, nutrients and SPM. J. Mar. Syst. 68 (3-4) 381–404.

Anderson, D.M., Glibert, P.M., Burkholder, J.M., 2002. Harmful algal blooms and eutrophication: nutrient sources, composition and consequences. Estuaries 25, 702–726.

Anderson, D.M., Kulis, D.M., Sullivan, J.J., Hall, S., 1990. Toxin composition variations in one isolate of the dinoflagellate *Alexandrium-Fundyense*. Toxicon 28, 885–893.

Baretta, J.W., Ebenhoh, W., Ruardij, P., 1995. The European Regional Seas Ecosystem Model, a complex marine ecosystem model. Neth. J. Sea Res. 33, 233–246.

Bell, M.J., Forbes, R.M., Hines, A., 2000. Assessment of the FOAM global data assimilation system for real time operational forecasting. J. Mar. Syst. 25, 1–22.

Blackford, J.C., Allen, J.I., Gilbert, F.J., 2004. Ecosystem dynamics at six contrasting sites: a generic model study. J. Mar. Syst. 52, 191–215.

Blondeau-Patissier, D., Tilstone, G.H., Martinez-Vicente, V., Moore, G.F., 2004. Comparison of bio-physical marine products from SeaWiFS, MODIS and a bio-optical model with in situ measurements from Northern European waters. J. Opt. A: Pure Appl. Opt. 6, 875–889.

Brown, C.D., Davis, H.T., 2006. Receiver operating characteristics curves and related decision measures: a tutorial. Chemometrics Intell. Lab. Syst. 80, 24–38.

Brown, C.W., Hood, R.R., Li, Z., Decker, M.B., Gross, T., Purcell, J., Wang, H., 2002. Forecasting system predicts presence of sea nettles in Chesapeake Bay. EOS 83 (321), 325–326.

Burkholder, J.M., Glasgow, H.B., Deamer-Melia, N.J., et al., 2001. Species of the toxic *Pfiesteria* complex, and the importance of functional type in data interpretation. Env. Health Persp. 109, 667–679.

Dahl, E., Tangen, K., 1993. 25 years experience with *Gyrodynium aureolum* in Norwegian waters. In: Smayda, T.J., Shimizu, Y. (Eds.), Toxic Phytoplankton Blooms in the Sea. Elsevier, New York, pp. 15–21.

Decker, M.B., Brown, C.W., Hood, R.R., Purcell, J.E., Gross, T.F., Matanoski, J.C., Owens, R.L., Setzler-Hamilton, E.M., 2007. Predicting the distribution of the scypho-medusa, *Chrysaora quinquecirrha*, in Chesapeake Bay. Mar. Ecol. Prog. Ser. 329, 99–113.

Doerffer, R., Fischer, J., 1994. Concentrations of chlorophyll, suspended matter and gelbstoff in case-II waters derived from satellite Coastal Zone Colour Scanner data with inverse modelling methods. J. Geophys. Res. 99 (C4), 7457–7466.

GEOHAB, 2006. In: Glibert, P. (Ed.), Global Ecology and Oceanography of Harmful Algal Blooms, Harmful Algal Blooms in Eutrophic Systems. IOC and SCOR, Paris and Baltimore, 74 pp.

Harding, L.W., Magnuson, A., Mallonee, M.E., 2005. SeaWiFS retrievals of chlorophyll in Chesapeake Bay and the mid-Atlantic bight. Estuarine Coastal Shelf Sci. 62, 75–94.

Holt, J.T., James, I.D., 1999. A simulation of the Southern North Sea in comparison with measurements from the North Sea Project. Part 1. Temperature. Cont. Shelf Res. 19, 1087–1112.

Holt, J.T., James, I.D., 2001. An s-coordinate model of the NorthWest European Continental Shelf. Part 1. Model description and density structure. J. Geophys. Res. 106 (C7), 14015–14034.

Holt, J.T., Proctor, R., Blackford, J.C., Allen, J.I., 2004. Advective controls on primary production in the stratified western Irish Sea: an eddy resolving model study. J. Geophys. Res. 1009, C05024, doi:10.1029/2003JC001951.

Holt, J.T., Allen, J.I., Proctor, R., Gilbert, F., 2005. Error quantification of a coupled high-resolution coupled hydrodynamic-ecosystem coastal ocean model. Part 1. Model overview and assessment of the hydrodynamics. J. Mar. Syst. 57, 167–188.

Hood, R.R., Zhang, X., Patricia, M., Glibert, P.M., Roman, M.R., Diane, K., Stoecker, D.K., 2006. Modeling the influence of nutrients, turbulence and grazing on *Pfiesteria* population dynamics. Harmful Algae 5, 459–479.

Johansson, N., Graneli, E., 1999. Cell density, chemical composition and toxicity of *Chrysochromulina polylepis* (haptophyta) in relation to different N:P supply ratios. Mar. Biol. 135, 209–217.

Lancelot, C., Gypens, N., Billen, G., Garnier, J., Roubeix, V., 2007. Testing an integrated river-ocean mathematical tool for linking marine eutrophication to land use: the Phaeocystis-dominated Belgina coastal zone (Southern North Sea) over the last 50 years. J. Mar. Syst. 64, 216–228.

Lewis, K., Allen, J.I., Holt, J.T., Richardson, A.J., 2006. Error quantification of a high resolution coupled hydrodynamic-ecosystem coastal-ocean model. Part 3. Validation with continuous plankton recorder data. J. Mar. Syst. 63, 209–224.

OSPAR Commission, 1998. Report of the Modelling Workshop on Eutrophication Issues. 5–8 November 1996, Den Haag, The Netherlands, OSPAR Report, 86 pp.

O'Reilly, J.E., Maritorena, S., Mitchell, B.G., Siegel, D.A., Carder, K.L., Garver, S.A., Kahru, M., McClain, C., 1998. Ocean colour algorithms for SeaWiFS. J. Geophys. Res. 103, 24937–24953.

Prieur, L., Sathyendranath, S., 1981. An optical classification of coastal and oceanic waters based on the specific spectral absorption curves of phytoplankton pigments dissolved organic-matter, and other particulate materials. Limnol. Oceanog. 26, 671–689.

Radach, G., Berg, J., Hagmeier, E., 1990. Long-term changes of the annual cycles of meteorological, hydrographic, nutrient and phytoplankton time series at Helgoland and at LV ELBE 1 in the German Bight. Cont. Shelf Res. 10, 305–328.

Ruardij, P., Veldhuis, M.J.W., Brussaard, C.P.D., 2005. Modeling the bloom dynamics of the polymorphic phytoplankter *Phaeocystis globosa*: impact of grazers and viruses. Harmful Algae 5, 941–963.

Ruddick, K.G., Gons, H.J., Rijkeboer, M., Tilstone, G., 2001. Optical remote sensing of chlorophyll a in case 2 waters by use of an adaptive two-band algorithm with optimal error properties. Appl. Opt. 40, 3575–3585.

Siddorn, J.R., Allen, J.I., Blackford, J.C., Gilbert, F.J., Holt, J.T., Holt, M.W., Osbourne, J.P., Proctor, R., Mills, D.K., 2007. Modelling the hydrodynamics and ecosystem of the North-West European continental shelf for operational oceanography. J. Mar. Syst. 65, 417–429.

Song, Y., Haidvogel, D., 1994. A semi-implicit ocean circulation model using a generalized topography-following coordinate system. J. Comp. Phys. 115, 228–244.

Villanoy, C.L., Azanza, R.V., Altemerano, A., Casil, A.L., 2006. Attempts to model the bloom dynamics of *Pyrodinium*, a tropical toxic dinoflagellate. Harmful Algae 5, 156–183.

An operational ocean forecast system incorporating NEMO and SST data assimilation for the tidally driven European North-West shelf

EJ O'Dea, AK Arnold, KP Edwards, R Furner, P Hyder, MJ Martin, JR Siddorn, D Storkey and J While, Met Office, Exeter, UK
JT Holt and H Liu, National Oceanography Centre, Liverpool, UK

A new operational ocean forecast system, the Atlantic Margin Model implementation of the Forecast Ocean Assimilation Model (FOAM-AMM), has been developed for the European North West Shelf (NWS). An overview of the system is presented including shelf specific developments of the physical model, the Nucleus for European Modelling of the Ocean (NEMO), and the Sea Surface Temperature (SST) data assimilation scheme. Initial validation is presented of the tides and model SST. The SST skill of the system is significantly improved by the data assimilation scheme. Finally, an analysis of the seasonal tidal mixing fronts shows that these, in general, agree well with observation, but data assimilation does not significantly alter their positions.

LEAD AUTHOR'S BIOGRAPHY

Enda O'Dea joined the Met Office in 2004 to work in ocean modelling after completing a PhD in computational fluid dynamics. He now develops ocean forecast models in the Ocean Forecasting Research and Development (OFRD) group. Recently, the group has overseen the transition from a POLCOMS based forecast system to a NEMO based forecast system for the shelf seas around the UK. His principal research area is in shelf seas forecasting and interests include the dynamics of tides, seasonal stratification, shelf slope currents and regions of fresh water influence.

INTRODUCTION

The North-West European shelf seas have been the subject of numerous hydrodynamic models of increasing complexity and sophistication.[1,2] 3D baroclinic hydrodynamic models have evolved from research tools into operational forecast systems at operational centres.[3,4] Recently, in addition to operational forecasts for hydrodynamic variables, ecosystem models have been implemented operationally.[5] Such ecosystem models provide model estimates of biogeochemical variables such as chlorophyll in complement to remote Earth observations.[6]

In global ocean and basin scale modelling, data assimilation has proved an invaluable component for operational forecasting.[7] For the shelf seas however,[8] the necessary inclusion of shorter temporal and spatial scale processes, in particular in relation to the interaction of the tides and the shelf, has discouraged the widespread use of data assimilation in operational systems. In this paper the authors outline the development of an operational modelling system for both physical and biogeochemical parameters in the North-West European continental Shelf (NWS) that includes assimilation of Sea Surface Temperature (SST) data.

In the Met Office's Forecasting Ocean Assimilation Model (FOAM)[9] system, the core dynamical model has recently[10] migrated to the Nucleus for European Modelling of the Ocean (NEMO).[11] Using NEMO allows short-term operational ocean forecasting systems to employ the

same fundamental ocean model code as in the global and basin scale seasonal and climate prediction systems at the Met Office. Adopting NEMO is also beneficial to the group by becoming part of a large and active cross-institutional developer base. Like the open ocean, the strategy for the assimilative shelf seas forecasting system described here is to apply NEMO as the physics engine. Assimilation of SST adapts the existing open ocean FOAM system in a manner suitable for application in the shelf seas. Whilst NEMO is also coupled with the European Regional Seas Ecosystem Model (ERSEM)[12,13] for ecosystem modelling, this paper details only the physics and assimilation. The coupled physics-ecosystem will be the subject of a following paper.[13]

Previously, operational modelling of the NWS at the Met Office utilised the Proudman Oceanographic Laboratory (now National Oceanography Centre) Coastal-Ocean Model System (POLCOMS),[14,15] NEMO was developed as an open ocean model and therefore lacked many of the shelf-specific features found in models such as POLCOMS. It was therefore necessary to incorporate significant modifications to NEMO to make it suitable to replace POLCOMS as the operational model for shelf applications. It should be noted that the POLCOMS system is a well established and validated system[16] and provides a reliable reference system from which to compare forecast skill in any new modelling system.

The operational shelf seas forecasting system is run in the Met Office operational suite on a daily cycle and forms part of the Europe-wide operational oceanography contribution to Global Monitoring for Environment and Security (GMES). The NEMO forecasting system documented in this work is now providing operational forecasts. Analyses and five day forecast products for the NWS are provided as part of the MyOcean project, the EC FP7 project that currently delivers the GMES Marine Core Service.[17]

The remainder of this paper firstly describes the model domain and configuration, and then gives an overview of the model in general, and specific enhancements that have been developed to tackle the shelf seas dynamics, in particular. The developments required for assimilation of SST on the shelf are then described, followed by a preliminary validation of the system. Finally, conclusions and future developments are discussed.

SYSTEM DESCRIPTION

Physical context: The North-West European shelf

The Atlantic Margin Model (AMM) region, shown in Fig 1, covers the North-West European shelf and part of the North-East Atlantic ocean. A key feature dividing the shelf from the deep ocean is the shelf slope, running from Portugal to Norway. Associated with the shelf slope is the important Joint Effect of Baroclinity and Bottom Relief (JEBAR)[18] process, which drives a poleward shelf slope current common to many eastern margins. Examples of other poleward eastern boundary currents in other regions include the coastal undercurrents of Chile and California, the Alaskan slope current and the bottom layer shelf break current of southwest Africa.[19] The shelf slope itself varies in width and steepness. It is particularly steep along the Iberian slope to the west of Portugal and the Cantabrian slope to the north of Spain. The combination of step bathymetry and terrain following (sigma) coordinates requires special treatment for the modelling of Horizontal Pressure Gradients (HPG). The slope current is also variable and along the Iberian and Cantabrian slopes it is seasonal. It manifests itself as the Iberian Slope current during autumn and winter.[20,21]

Further north the shelf widens from the Aquitaine slope to the Armorican and Celtic shelf slopes with France to the east. The Celtic shelf slope is a major source of internal tides[22] and enhanced mixing.[23] Travelling northwards, the shelf slope encompasses the Celtic Seas[24] of the English Channel, Irish Sea, and the Celtic, Irish, Malin and Hebrides shelves. Thereafter the shelf slope turns more eastward at the Faroes-Shetland ridge towards Norway with the North Sea to the south and the Faroese channels to the north. Finally, crossing the Norwegian trench to the south, the shelf slope travels parallel to the Norwegian coast towards the northern boundary of the domain.

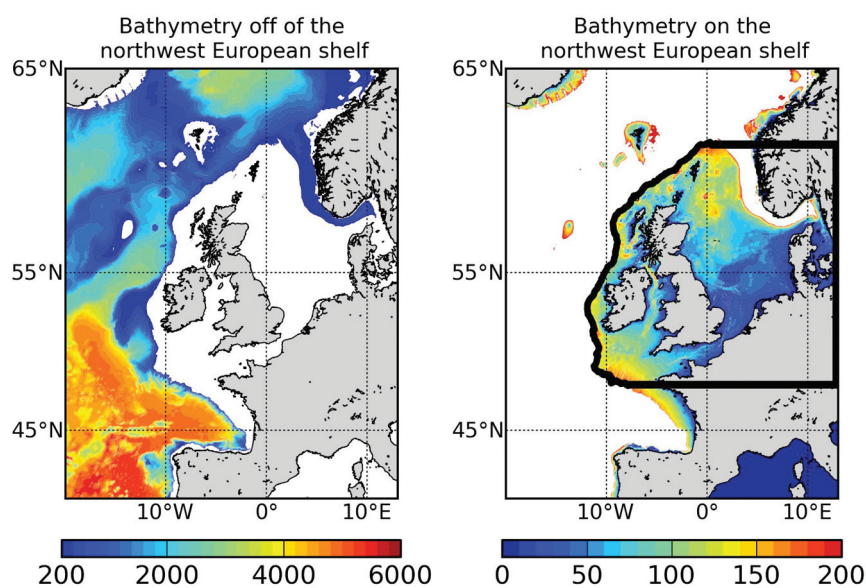The Faroese channels and the Wyville-Thomson Ridge are important areas for the return of the cold dense outflow

Fig 1: AMM domain. Left panel: Off shelf NOOS bathymetry >200m. Right panel: On shelf NOOS bathymetry <200m, with the MRCS domain boundary indicted in thick black

Bathymetry off of the northwest European shelf

Bathymetry on the northwest European shelf

from the Nordic seas.[25,26] Accurate modelling of the overflow requires higher resolution models than is currently computationally possible for operational coupled physical-ecosystem models of the entire region. Careful attention is required at such overflows particularly in relation to the limitations of terrain following coordinates and steep bathymetry.

Although the main aim of the shelf model is in simulating the on-shelf properties, the off-shelf dynamics and the shelf slope current are also important as they impact cross-slope transport. Approximately 12.5% of the global tidal energy is transmitted into the Celtic Seas from the North Atlantic, with large tidal responses in the English Channel, Bristol channel and Irish Sea.[24] The large tidal response results in large dissipation of tidal energy and an input of turbulent kinetic energy into the water column. The seasonal variation in both wind, which further adds to the production of turbulence, and heating, which adds buoyancy, leads to seasonally stratified and mixed regions. The balance between mixing created by wind and tide, and stratification by thermal heating, leads to tidal mixing fronts at the boundary between well mixed and stratified water columns.[27] Thus accurate representation of tidal dynamics, turbulence production and dissipation, and the air-sea flux of momentum and heat are critical for modelling the regional dynamics. The effects of winds are not limited to turbulence production but also drive currents, which along with the buoyancy field provide the residual circulation.[28] Furthermore, wind forcing in combination with atmospheric pressure can produce large and potentially dangerous storm surges in the North Sea.[29] As such, a regional model must include the atmospheric pressure gradient forcing, and the interaction of tides and surges.

Sources of freshwater influence the baroclinic flow with inputs from rivers, such as the Rhine, leading to dynamically complex Regions Of Freshwater Influence (ROFI)[30] and coastal currents. Sources of low saline water are not restricted to local riverine sources alone. Low saline water of Baltic origin, which may be considered as a large estuarine source, exchanges with relatively high saline North Sea water flowing into the Baltic in a dynamically complex transition area. The connection with the Baltic consists of the shallow sills and narrow straits of the Kattegat, the Sound, the Great Belt and the Little Belt. To resolve the flow through these channels requires relatively high resolution models;[31] where the resolution of the shelf model is not adequate to resolve them, fluxes between the Baltic and Kattegat must be specified as a special form of boundary condition. The dynamics are further complicated by the intrusion of the relatively deep Norwegian trench as far as the Skagerrak. This guides North Atlantic water along its slope into the Skagerrak, where it upwells and re-circulates.[32] The outgoing current flowing along the Norwegian coast consists of both low saline Baltic and coastal water, and mixed North Sea and North Atlantic water. Thus any model of the region must be able to represent the complex combination of haline, bathymetric, heating, tidal and surge effects that all interplay in this region.

Physical model

The model is designed to provide simulations of the on-shelf hydrodynamics, biogeochemistry and light environments of the NWS. The high socioeconomic interest in the area has led to an intensive modelling effort, with a variety of high-resolution models exploring specific dynamical regimes in detail. However, in the context of an operational forecast system that is coupled to sediment and ecosystem models, a regional approach that interconnects the variety of dynamical regimes is required.[15] The existing coupled POLCOMS-ERSEM Medium Resolution Continental Shelf (MRCS)[5] system is nested into the physics only 12km POLCOMS-AMM model and has a resolution of approximately 7 km. The new FOAM-AMM system extends the coupling of ERSEM outwards from the MRCS domain to cover the entire AMM region from 40°S, 20°W to 65°N, 13°E. Thus FOAM-AMM replaces both the existing POLCOMS operational models, POLCOMS-AMM[33] and MRCS with a single domain.

Fig 1 depicts the North-West Shelf Operational Oceanographic System (NOOS) bathymetry covering the AMM region, which is a combination of GEBCO 1' data and a variety of local data sources from the NOOS partners. The shelf break in Fig 1 has been highlighted by the 200m isobath. Also depicted is the perimeter of the existing MRCS[16] domain. In order to ensure that the cross-slope exchanges of momentum and tracers are well represented a hybrid s-σ[34] terrain following coordinate system is employed in those models in order to retain vertical resolution on the shelf, while allowing a reasonable representation of deep water processes.

The resolution of FOAM-AMM is 1/15° latitude by 1/9° longitude. The horizontal resolution of ~7km lies between typical shelf wide resolution (~12km) and high-resolution limited-area models (1.8km) sufficient to resolve the dominant fine scale physics on the shelf.[28] It is not sufficient to resolve the internal Rossby radius on the shelf, which is of the order 4km, but well resolves the external Radius (~200km). Ideally the model would be of sufficient resolution to resolve both the internal and external radii, ie, a resolution of the order <2km. At present the computational cost of such a system make this impractical for coupled hydrodynamic-ecosystem operational forecasts.

The model bathymetry of POLCOMS is derived from the NOOS bathymetry. Some smoothing was applied to steep bathymetry, such as the shelf break in the derivation of the existing 12km AMM domain. This was to reduce HPG errors and improve the shelf slope current.[33] The 12km POLCOMS-AMM bathymetry has been interpolated onto the replacement 7km FOAM-AMM grid for inter-comparisons of the two systems. This ensures that the new physics does not gain advantage simply by having more bathymetric information in initial hindcast comparisons. In the initial validation stages NEMO-AMM was also run on the 12km AMM grid for complete like for like comparisons at equivalent grid resolution.

The version of NEMO used in FOAM-AMM is v3.2. As it is necessary to model tides and surges, a non-linear free surface is implemented using a variable volume[35] and time splitting methodology, using 'leap-frog' time stepping. The corresponding baroclinic time step is 150 seconds and the barotropic sub-cycle time step is 5 seconds. The momentum advection is both energy and enstrophy conserving.[36] The lateral boundary condition on the momentum is free-slip. Horizontal diffusion of momentum is specified using both Laplacian and bilaplacian operators. Because FOAM-AMM utilises terrain following coordinates, it is necessary for

the specification of Laplacian diffusion to be applied on geopotential surfaces to prevent spurious mixing in the vertical, and bilaplacian diffusion to be done on model levels to retain stability. The coefficients of Laplacian and bilaplacian diffusion are 30.0 m^2s^{-1} and $1.0x10^{10}$ m^4s^{-1}, respectively. The total variation diminishing (TVD) scheme is used for tracer advection.[37] The tracer diffusion operator is only Laplacian and operates along geopotential levels. The tracer diffusion coefficient is 50 m^2s^{-1}.

There are 32 terrain following coordinates in the vertical. The terrain following coordinate system is modified in two important ways. Firstly, as in[34] and[3], coordinates transition from a stretched S-coordinate system in the deep to a uniform σ-coordinate system on the shelf. Following[33] the critical depth h_c is defined at 150m and the stretching parameters are defined as θ = 6 and B = 0.8. Focused resolution in deep water at the surface is important for air sea fluxes of heat, freshwater and momentum, and the bottom in relation to the bottom boundary layer and bed friction. On the shelf uniform coordinates are preferred, as in shallow regions very small vertical cells will tend to result in violations of the vertical Courant-Friedrichs-Lewy (CFL)[38] condition.

An additional modification to the coordinate system is based upon a z*-σ approach.[39] A major constraint on terrain following coordinates occurs when adjacent ocean depths differ significantly leading to errors in the calculation of the HPG term.[40] To reduce the error the initial S-σ-system is created using a smoothed envelope bathymetry rather than the input bathymetry itself. The motivation of the smoothing is to limit the steepness of the model levels to a given threshold. The threshold in FOAM-NEMO is chosen as 0.3. Thus, for any two adjacent depths, $h_{i,j}^{env}$, $h_{i,j+1}^{env}$ in the envelope bathymetry, the relative difference is:

$$rn = \frac{h_{i,j}^{env} - h_{i+1,j}^{env}}{h_{i,j}^{env} + h_{i+1,j}^{env}} < 0.3 \qquad (1)$$

The smoother only deepens, it does not shallow, the envelope bathymetry relative to the source bathymetry. The S-σ-coordinate system is then created based on the envelope

bathymetry. However, h is then masked for any grid cell that is lower than the input bathymetry. Hence, the coordinate slopes are never more than a desired threshold, at the expense of some vertical levels near steep bathymetry. At such points the levels intersect the bed and levels are lost. Fig 2 depicts a z*-σ-coordinate system with its underlying smoothed envelope bathymetry. A hybrid z*-S-σ system provides one way of reducing HPG errors, that has the distinct advantage that the shape of the topography is not overly distorted by bathymetric smoothing. However, the underlying HPG scheme must also be suitably posed to minimise spurious velocities and cross-pycnocline mixing. Such errors result from inclined model surfaces relative to both geopotential surfaces and isopycnal surfaces. Furthermore, the z*-S-σ system does not resolve the issue of having a non-uniform surface box, which has implications for surface fluxes.

The standard HPG schemes in NEMO were found to give unacceptably large errors with the non-linear free surface, generating large erroneous velocities over steep topography, such as the shelf break. Furthermore, these schemes were not able to deal with the hybrid vertical coordinate. To address this, a new HPG scheme was developed employing a pressure Jacobian method rather than the widely used density Jacobian method. This can be illustrated with the following formula:

$$\left.\frac{\partial P}{\partial x}\right|_z = \left.\frac{\partial P}{\partial x}\right|_S - \left.\frac{\partial P}{\partial z}\frac{\partial z}{\partial x}\right|_S \qquad (2)$$

were, P is the pressure, z is the non-transformed physical vertical coordinate and s is the transformed vertical coordinate used in the model. $\partial/\partial x|_z$ refers to the partial derivative in the horizontal defined on geopotential surfaces and $\partial/\partial x|_S$ is the horizontal partial derivative defined on coordinate surfaces of the model coordinate system.

A constrained cubic spline (CCS) method has been employed here to reconstruct the vertical density profile. The CCS reconstruction has the property of monotonicity. The vertical pressure profile can be calculated analytically, so the density Jacobian method is not needed. By splitting the second term of the two-term pressure gradient formula into left and right hand side parts, the pressure gradient can be
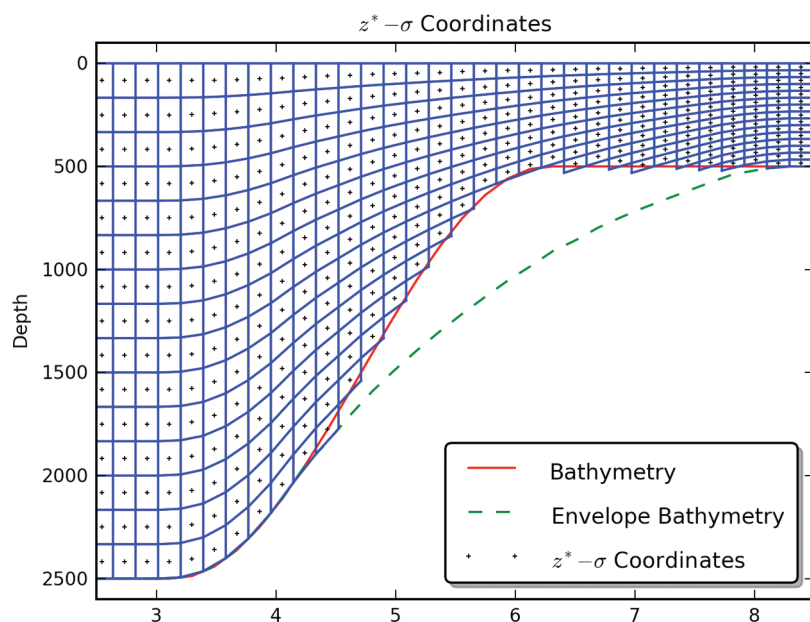

Fig 2: z*-σ coordinates with envelope bathymetry dashed. This generic figure is conceptual and thus the units for the lateral direction (x-axis) and vertical direction (y-axis) are non-dimensional

calculated on the velocity cells without any weight parameter. In this formula, there is no hydrostatic consistency constraint. This pressure Jacobian HPG method can be applied to any hybrid vertical coordinate. For details about this HPG method, refer to[41]. The combination of the new HPG scheme and the vertical coordinate scheme give good results in proximity to steep topography.

The non-linear free surface allows for the accurate representation of tides and surges. At the open boundaries tidal energy enters the domain via a Flather[42] radiation boundary condition. Fifteen tidal constituents, calculated from a tidal model of the North-East Atlantic,[43] are specified for the depth mean velocities and sea surface elevation. As the AMM region covers a significant area, the equilibrium tide is also specified. In addition to the tidal boundaries, FOAM-AMM is one-way nested within the Met Office operational FOAM 1/12° deep ocean model for the North Atlantic.[10] Temperature and salinity are relaxed to the values specified by FOAM 1/12° model over a ten point relaxation zone on the open boundaries using the flow relaxation scheme.[44] Sea surface elevation and barotropic currents from the FOAM 1/12° North Atlantic model are added to the tidal constituents via the Flather boundary condition.

Vertical turbulent viscosities/diffusivities are calculated using the Generic Length Scale (GLS) turbulence model.[45] This allows for a choice from a range of closure schemes. In FOAM-AMM, the second-moment algebraic closure model of Canuto[46] is solved with the two dynamical equations[47] for the turbulence kinetic energy (TKE), k, and TKE dissipation, σ.[48] The choice of this scheme is based upon results in the North-West European shelf with POLCOMS.[49] Neumann boundary conditions on k and ε are applied at the surface and sea bed. The Craig and Banner[50] surface wave mixing parameterisation is also applied. The dissipation is limited under stratification using a Galperin[51] limit of 0.267. The bottom friction uses a spatially varying log layer based drag coefficient with a minimum drag coefficient set at 0.0025.

River flow is specified for 320 European rivers.[52] The river scheme in NEMO has been updated so temperature and salinity boundary conditions at river inflow points can be specified flexibly to better represent the vertical structure of different river outflows. Although this could be used for all rivers in the domain if data were available, in this work it is used for the Baltic flows through the Belt region, which are treated as rivers with specified temperature, salinity, and volume fluxes. The data for the flux between the Kattegat and the Baltic is derived from the Danish Hydrographic Institutes' Dynamics of Connected Seas (DYNOCS) experiment.[3] In this configuration for other 'rivers' the temperature of the river water is specified as the SST of the model box at the river point and the river flow is specified by the river flow climatology. However, the river input is assumed to be of zero salinity.

The model is forced at the surface by fluxes from the global Met Office Numerical Weather Prediction (NWP) model. The NWP model has a horizontal resolution of approximately 25km and incorporates 4-Dimensional Variational Data Assimilation (4DVAR). Three hourly mean fluxes of penetrating and non-penetrating heat fluxes (corrected for intra-model SST differences by a Haney flux correction term[53]), moisture fluxes, and hourly instantaneous fields of wind speed and surface pressure are applied. An atmospheric pressure gradient force is applied at the surface, which is important for surge modelling. The light attenuation coefficient varies in the horizontal depending on the undisturbed water depth following POLCOMS. This is a simple way of partially accounting for more turbid and thus less clear waters in shallow coastal waters.

Data assimilation system

Data assimilation within FOAM-AMM is carried out using a modified version of the Analysis Correction scheme used in global FOAM. This system, described in[10] and[54], consists of three stages. In the first stage a one-day model run is compared to observations using a First Guess at Appropriate Time (FGAT) scheme. In the second stage, observation-minus-model differences (the innovations) are converted to model increments using an iterative[55] method to solve the Best Linear Unbiased Estimator (BLUE) equations. Finally, the model is rerun for the same day with an Incremental Analysis Update (IAU) scheme[56] to update the model state using the pre-calculated increments. This three stage process is repeated for subsequent model analysis days.

Considerable modifications have been made to the global FOAM data assimilation methodology[10] to enable it to be applied to shelf seas. The resulting algorithm is similar to the scheme described in[57] and also the optimal interpolation part of the method of[58]. However, unlike these two methods this scheme does not assume a zero correlation length for forecast error. The most significant difference between data assimilation in the FOAM-AMM and global FOAM systems is that only SST data are assimilated. Temperature and salinity profile assimilation along with sea surface height assimilation are technically more challenging in the shelf environment and will be implemented as future developments to the system. As in[10], data assimilated into FOAM-AMM are comprised of *in-situ* data and level 2 satellite SST data provided by the Global High-Resolution Sea Surface Temperature project (GHRSST[59]). *In-situ* data are obtained from a variety of sources and include measurements taken by ships, moored buoys, and drifters. Satellite observations are obtained from the Advanced Microwave Scanning Radiometer-Earth observing system (AMSRE), the Advanced Along-Track Scanning Radiometer (AATSR), and the Advanced Very High Resolution Radiometer (AVHRR) instruments on board the NOAA and MetOp satellites. Also assimilated are data from the geostationary Spinning Enhanced Visible and Infrared Imager (SEVIRI), a dataset not included in global FOAM. All data are quality controlled using the Bayesian procedure of[60].

Furthermore a bias correction scheme, based on comparisons to *in-situ* and AATSR data, is applied to the AMSRE, AVHRR, and SEVIRI observations. A full description of the satellite data types and the scheme used to bias correct them can be found in[61]. To highlight the data coverage available, Fig 3 shows maps of the data coverage for a 10 day period of August 2008. It is worth noting from this figure the lack of AMSRE data near the coast and also that SEVIRI data is only available south of 60°N. Data availability for satellites is reduced in the winter, not shown, due to increased cloud cover and rain, this is especially true for the infrared satellites (AATSR, the two AVHRR instruments, and SEVIRI).
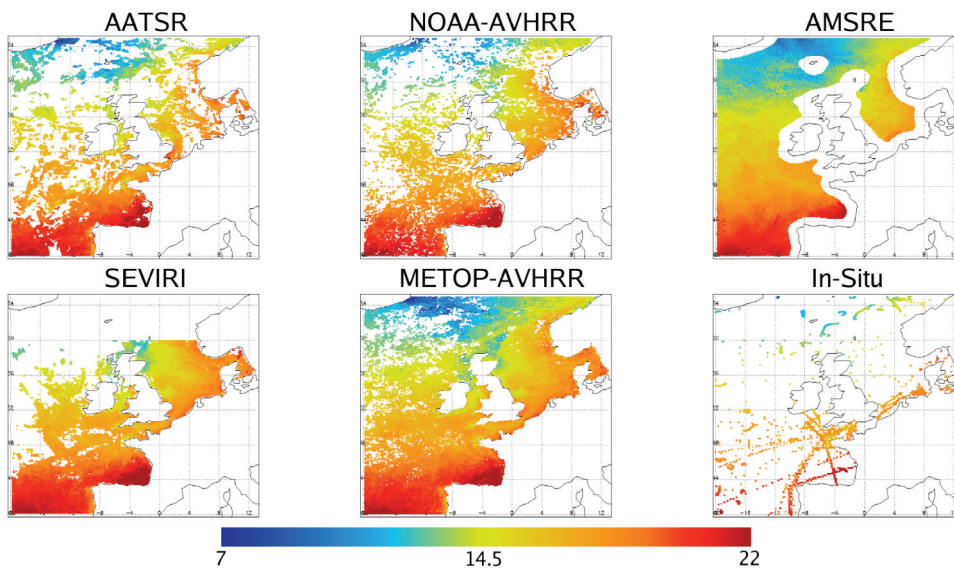
Fig 3: Composites of the data available from each satellite and *in-situ* sources for assimilation over 10 days between 1–10 August 2008. Colours indicate temperature in °C

Fig 4: Variance fields used by the NEMO Shelf data assimilation scheme. The top row shows the mesoscale variance, while the bottom row shows the synoptic-scale variance. The columns represent the seasons: December-January-February (DJF), March-April-May (MAM), June-July-August (JJA), and September-October-November (SON). Units are K^2
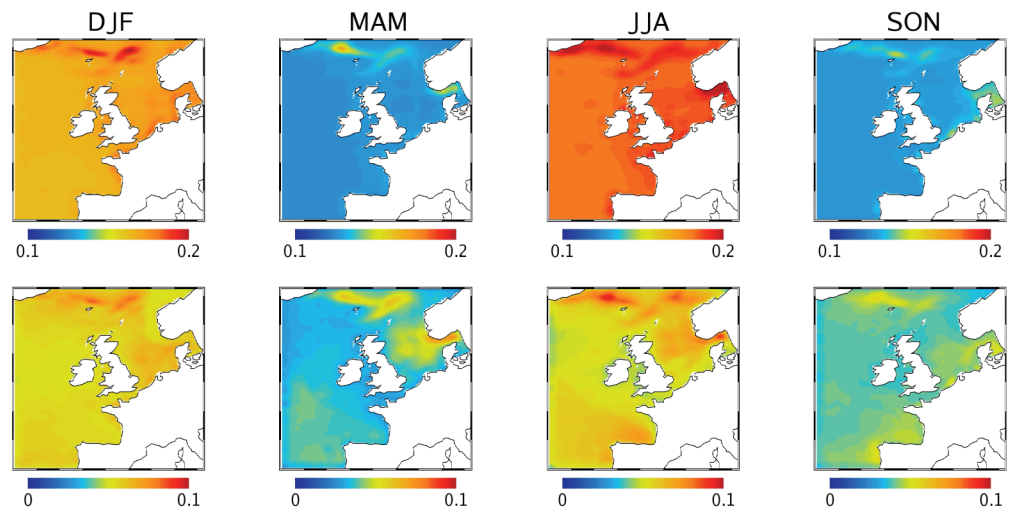
The other major changes to the data assimilation system, as compared to global FOAM, apply to the specification of the forecast error covariance matrix. In the vertical, information is simply applied down to the base of the instantaneous (time-step by time-step) mixed layer, with the mixed layer defined as the 0.2°C change in temperature from the surface (this is the same definition as used in[62]). The horizontal forecast error covariances, as in[10], are specified by two Second Order Auto Regressive (SOAR) functions: a function describing synoptic-scale, atmospherically driven, error correlations and a function for shorter length scale, ocean driven, error correlations. Constant length scales – 450km for the synoptic-scale and 30km for the shorter length scale – are used in these functions. The magnitudes (the variances) of the two terms are allowed to vary both spatially and temporally. Specifically, spatial maps of the variances were calculated for December-January-February, March-April-May, June-July-August, and September-October-November, with linear interpolation used to form a continuous annual cycle. To find the variances, the National Meteorological Center (NMC) method of[63] was used determine the spatial structure, with the method of[64] used to determine the amplitude. The seasonal synoptic and mesos-cale variances used by FOAM-AMM are shown in Fig 4 and reveal that mesoscale variability is dominant throughout the

year. Also evident are the substantial temporal changes that occur on the shelf, particularly in the Norwegian trench and the large magnitude of the synoptic and mesoscale variances near the Faroes and Shetland Islands, which is an area of large SST gradients.

SYSTEM VALIDATION
Hindcasts
Any new modelling system requires systematic validation before being considered for integration into the operational suites. The existing POLCOMS-AMM system provides a baseline target from which to compare FOAM-AMM. A series of hindcasts are performed to assess the skill and reliability of the new system. The barotropic tidal dynamics are assessed first. An assessment is then made of the baroclinic dynamics using a full two-year hindcast integration. The FOAM-AMM hindcast is compared against observations and the operational POLOMS-AMM system for the hindcast period.

Tides
Harmonic analysis of the FOAM-AMM and POLCOMS-AMM systems show greater skill for FOAM-AMM in terms of root mean square (RMS) error of Sea Surface Height (SSH)

	RMS				Mean			
	Amplitude (cm)		Phase (deg)		Amplitude (cm)		Phase (deg)	
	POLC	FOAM	POLC	FOAM	POLC	FOAM	POLC	FOAM
O1	2.2	1.9	17.2	15.7	−1.5	−1.3	−3.8	−2.2
K1	1.9	1.8	20.6	17.1	−0.2	−0.2	−11.9	−8.4
N2	3.1	2.9	19.1	21.6	0.6	0.4	1.2	2.7
M2	12.0	10.3	21.1	14.7	−0.2	−4.7	−0.1	−0.2
S2	6.1	3.7	14.3	12.8	1.6	−0.4	1.0	0.5

Table 1: Elevation amplitude and phase RMS and mean errors (model-observations) for tidal constituents O1, K1, N2, M2, S2 for both POLCOMS (POLC) and FOAM-AMM
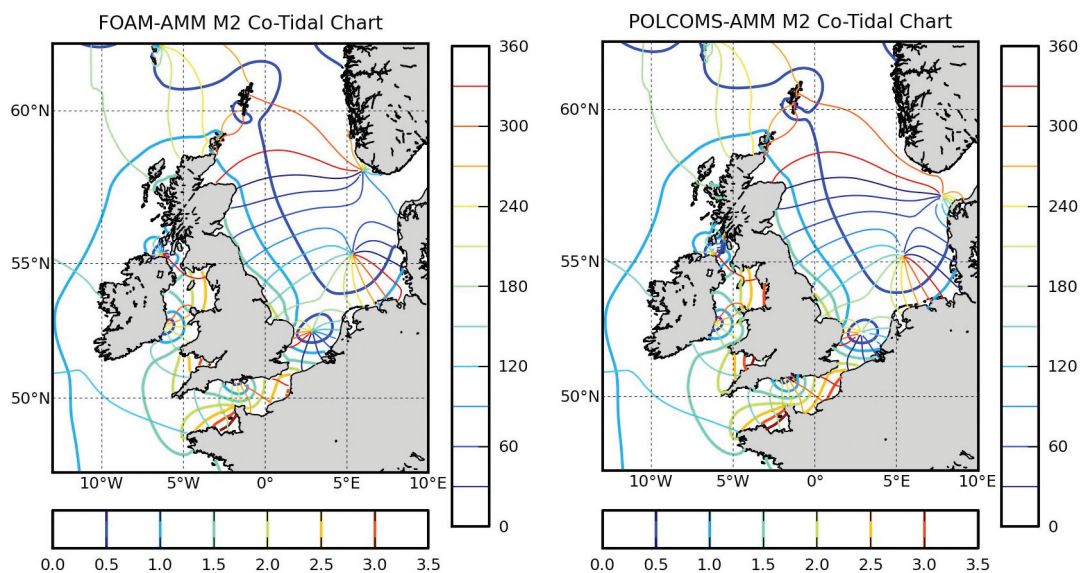

Fig 5: M2 Co-tidal chart for FOAM-AMM (left) and POLCOMS (right). Co-range lines are thick and values are given on the horizontal colourbars. Co-phase lines are thin and values are given on the vertical colourbars

amplitude and phase versus tide gauge data gathered from the British Oceanographic Data Centre (BODC). An analysis of tidal SSH amplitude and phase is presented in Table 1 for a selection of the most significant tidal constituents. The SSH RMS error is about 10% better in FOAM-AMM than POLCOMS-AMM whereas the mean error is similar in both systems with the exception of the M2 tidal constituent. The majority of the mean amplitude error for M2 in FOAM-AMM is due to an underestimation of the M2 amplitude in the Irish sea. The modelled positions of the amphidromes for M2 are shown in the co-tidal chart of Fig 5, which may be compared to observations as depicted in[65]. The positioning of the degenerate amphidrome in southern Norway is better placed in FOAM-AMM. The incorrect position of the degenerate Norwegian amphidrome partially explains the large improvement in terms of RMS phase error for the M2 constituent in FOAM-AMM.

Spatial comparison between the two systems and observations of tidal constituents M2 and S2 is made in Fig 6, in which the absolute error between POLCOMS-AMM and observations is subtracted from the absolute error between FOAM-AMM and observations. From Fig 6 regions of relative

strengths and weakness in each system can be identified. Blue indicates improved skill in FOAM-AMM over POLCOMS-AMM. For the M2 SSH amplitude, the eastern Irish Sea is an area of weakness for FOAM-AMM. In the eastern Irish Sea FOAM-AMM tends to underestimate the SSH amplitude. In contrast for the S2 constituent, FOAM-AMM performs well for most of the Irish Sea. More generally, as may be seen in Fig 7, the SSH amplitude in FOAM-AMM tends to be slightly smaller than POLCOMS-AMM. POLCOMS-AMM tends to have amplitudes that are too large in areas of large tidal amplitude such as the Bristol Channel. Although the harmonic analysis statistics show a general improvement in FOAM-AMM over POLCOMS-AMM, particular regions require further refinement in the FOAM-AMM system particularly in relation to underestimating the amplitude.

Baroclinic hindcasts

Free and SST assimilating hindcasts of FOAM-AMM are integrated for the two-year period of 2007–2008. This period facilitates the inter-comparison of FOAM-AMM against archived operational POLCOMS-AMM data. Initial temperature and salinity fields are interpolated from the analysis
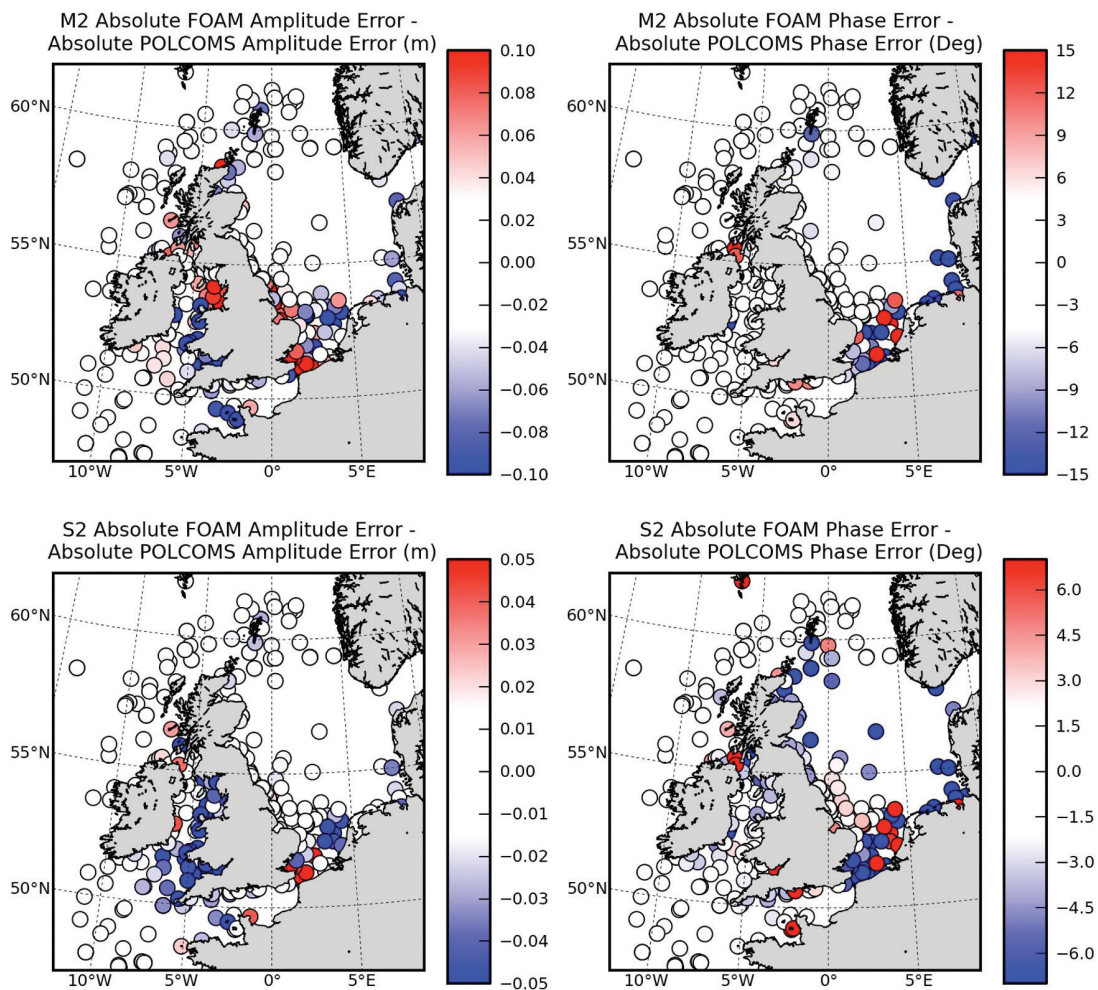
Fig 6: Difference (FOAM-AMM minus POLCOMS-AMM) of absolute SSH error from observations in amplitude (left) and phase (right) for tidal constituents M2 (top) and S2 (bottom)

fields of the assimilative FOAM 1/12° North Atlantic system for November 2006. All other fields are taken at rest for the initial condition. The FOAM 1/12° North Atlantic system assimilates data through the water column and thus provides a good deep-water initial condition off the shelf. However, as profile data are limited on the shelf and the fact that the FOAM North Atlantic system does not include dynamical features of the shelf, such as tides, a number of spin up years are required for the on shelf physics. The system is run without any assimilation for a period of one year until November 2007 as an initial spin-up year. The system is restarted and run for a further spin-up year starting again from November 2006 using the restart from the end of the first spin-up year. Finally, both a free run and an assimilative run are started from November 2006, running until the end of 2008 using the restart produced at the end of the 2nd spin-up year. For the free run, the temperature and salinity statistics between the 2nd spin-up year and the final two-year hindcast are very similar. Thus the adjustment to the initial condition from the assimilative FOAM 1/12° North Atlantic analysis fields is largely attained over the first spin up year and any model drift thereafter is small between subsequent model years.

One of the key objectives of the new FOAM-AMM system is to improve the representation of SST. Thus the daily averaged surface temperature fields from the free and

assimilative two year hindcast runs of FOAM-AMM and the existing POLCOMS-AMM operational archive are compared to the Operational Sea Surface Temperature and Sea Ice Analysis (OSTIA)[66] SST fields for the hindcast period. It must be noted that OSTIA is not an independent data source, both because the NWP derived fluxes use OSTIA data as a reference SST and because the data assimilation uses data common to OSTIA. However, both the POLCOMS-AMM and FOAM-AMM systems use the same Haney correction scheme when applying the NWP fluxes and thus OSTIA is a useful data source for comparing the two non-assimilative systems. Comparisons to independent data in the form of salinity and temperature profiles are presented in Table 2. Here we show comparisons to OSTIA in order to provide a broad overview of the spatial distribution of the SST errors that is not so easily discernable with the data sparse profiles.

The 2008 time series of the daily mean and RMS differences between the model runs and OSTIA for both the entire AMM domain and the on-shelf MRCS domain are compared in Fig 8. The free run of FOAM-AMM has an annual mean warm bias relative to OSTIA of 0.33°C. This warm bias is most marked during winter, which is in contrast to POLCOMS-AMM, which has its largest bias in summer. The POLCOMS-AMM summer SST warm bias is a result of the model over stratifying. The annual mean SST bias in the
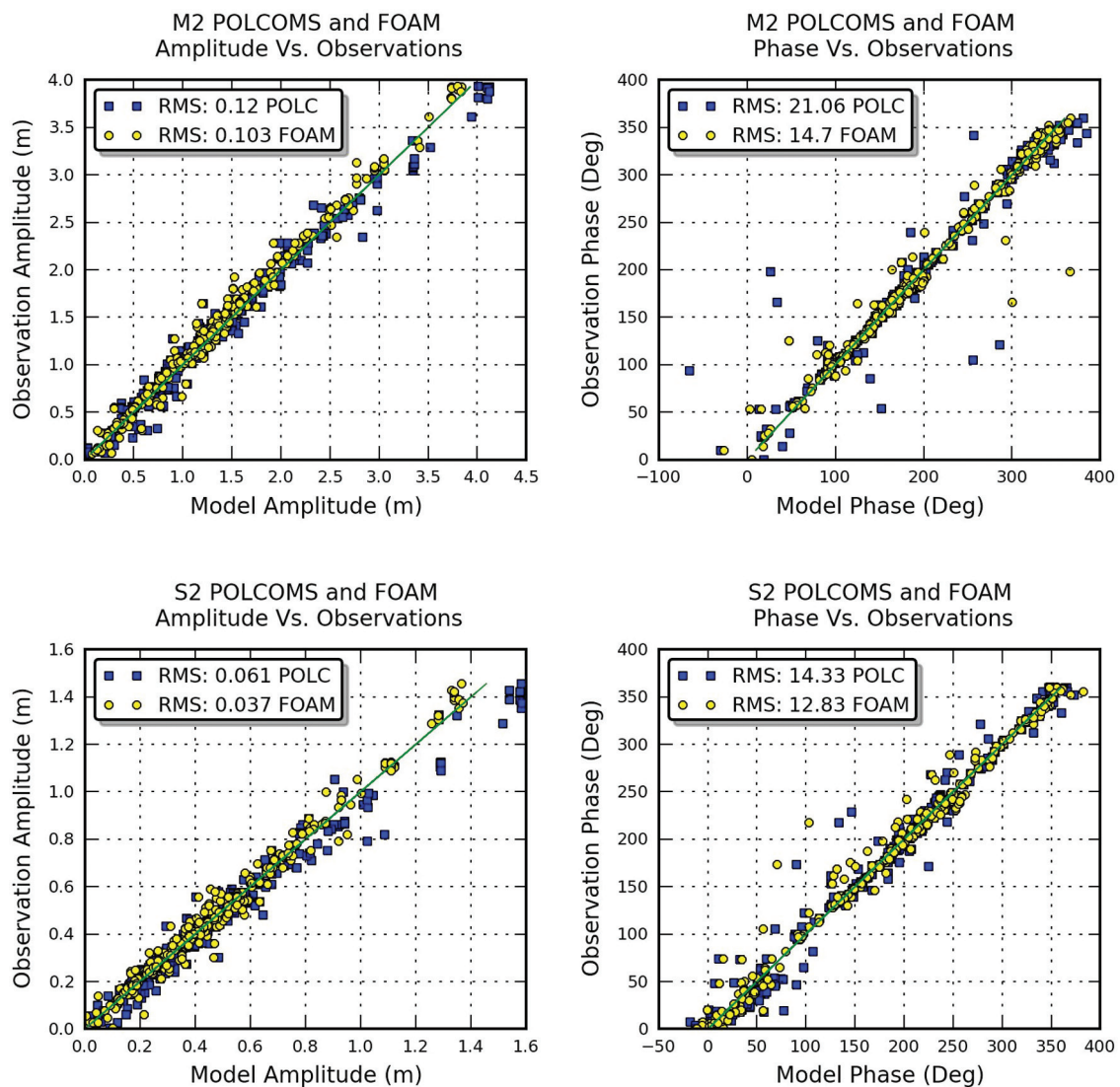
Fig 7: SSH amplitude (left) and phase (right) of POLCOMS (blue square) and FOAM-AMM (yellow circle) against observations for tidal constituents M2 (top) and S2 (bottom)

	RMS		Mean	
	Temperature (°C)	Salinity	Temperature (°C)	Salinity
Assimilative	0.824	1.791	−0.230	0.866
Free	1.062	1.800	−0.673	0.870

Table 2: RMS and mean differences between profile data and the assimilative and non-assimilative hindcasts of NEMO-AMM for August 2008 over the MRCS domain

FOAM-AMM system may be related to a combination of the turbulence scheme, the simple light attenuation scheme and the prescribed fluxes. The surface mixed layer in FOAM-AMM is deeper than that of POLCOMS-AMM. Thus any surface cooling by the Haney correction is reduced and the depth integrated heat content gained over the summer may be overestimated and thus leading to the warm SST bias in winter.

The assimilative FOAM-AMM hindcast has a mean discrepancy with OSTIA of 0.12°C and a similarly much reduced RMS difference with OSTIA of 0.39°C compared to 0.71°C for the free run. The SST data assimilation results in a much improved model analysis field of SST throughout the

year. The mean and RMS errors for all models are slightly larger in the on shelf MRCS region than over the entire AMM domain. Fig 9 shows the 2008 annual and monthly mean difference for February and August between OSTIA and the three model runs for the entire AMM domain. Clearly visible are the summertime warm bias in POLCOMS-AMM and the winter warm bias in FOAM-AMM, which are also visible in the time series of Fig 8. There are two distinct areas of error for both POLCOMS-AMM and FOAM-AMM in the annual mean. The first is the on shelf region and the second is between the northern boundary of the domain and the Faroes. It is found in the case of FOAM-AMM that the
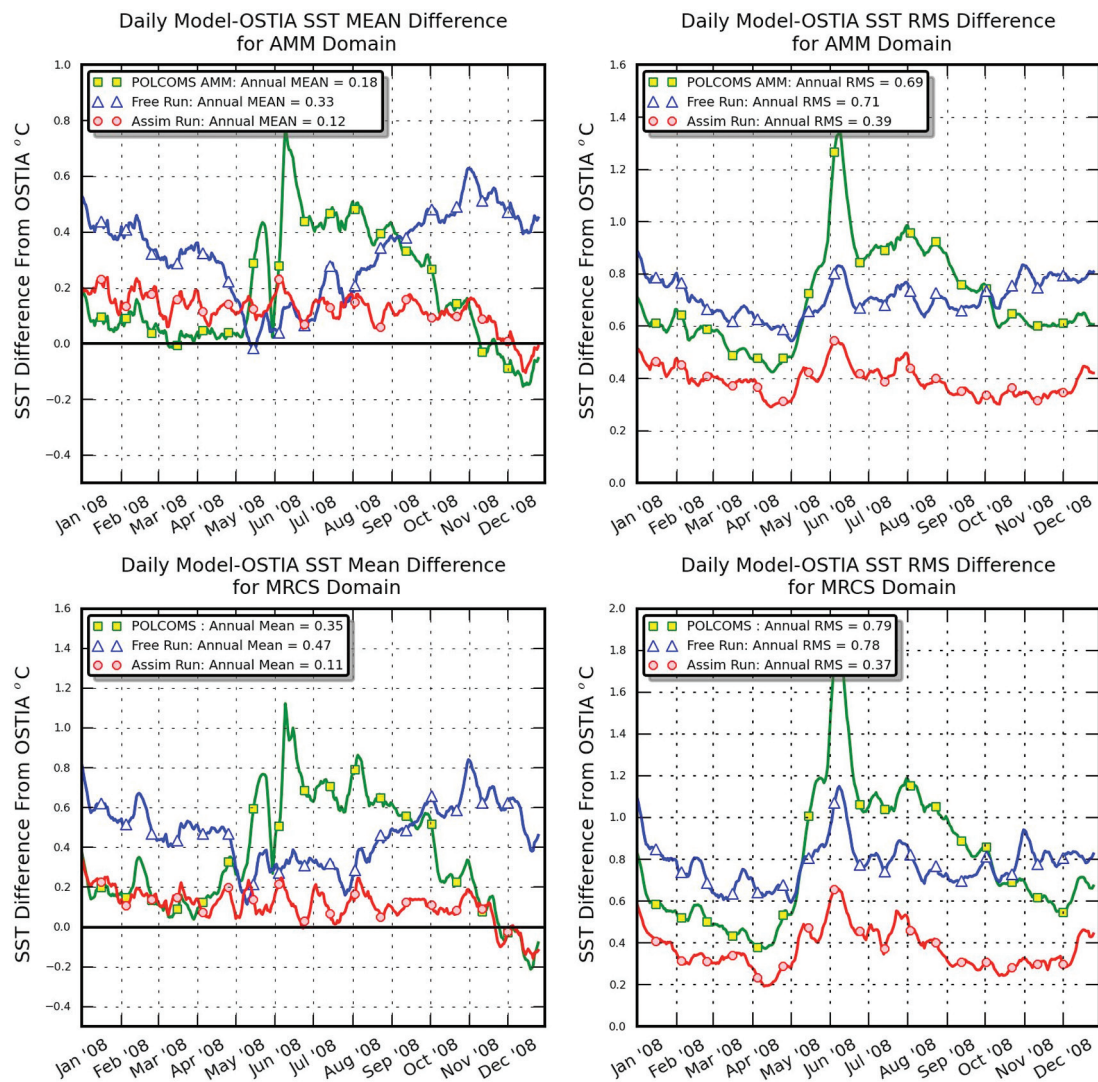
Fig 8: Top panels are the 10 day running mean of RMS (left) and mean (right) differences from OSTIA SST over the AMM domain between POLCOMS-AMM, FOAM-AMM free run and FOAM-AMM assimilative run daily for 2008. Bottom panels are the 10 day running mean of RMS (left) and mean (right) differences from OSTIA SST over the MRCS domain for POLCOMS-AMM, FOAM-AMM free run and FOAM-AMM assimilative run

coarse and smoothed bathymetry inherited from POLCOMS-AMM leads to a shelf break current that is too strong due to the improved HPG scheme in FOAM-AMM. The strong shelf slope current leads to too much advection of relatively warm water along the shelf break. Using bathymetry derived directly from the 1nm NOOS bathymetric dataset reduces the shelf slope error significantly. However, further refinement of the shelf slope bathymetry may be required to simulate the shelf slope current with greater skill.

With regards to the SST error near the northern boundary, sensitivity tests reveal that both POLCOMS-AMM and FOAM-AMM are very sensitive to the prescription of SSH on the lateral boundaries. The boundary SSH affects both surface and the bottom water flows over the Iceland-Shetland Ridge through channels such as the Faroe Bank Channel and small changes of SSH can lead to large changes in the currents in this region. The overflows in each system are potentially too weak, resulting in high temperature waters east of Iceland. Modelling the overflow of cold dense Arctic water through the narrow straits is particularly difficult. The resolution required both in the vertical to capture

bottom water cascades over the sills and the horizontal to capture the geometry of the narrow channels is currently prohibitive to implement across the entire AMM domain in an operational forecast system.

Whilst it is clear that the SST data assimilation improves the system's representation of SST, it is also important to consider whether the data assimilation has a negative impact on sub-surface water structure and the tidal mixing fronts. One of the key features of the NWS is the seasonal tidal mixing fronts between seasonally stratified water such as in the central North Sea and tidal mixed waters such as those of the southern bight. As the assimilation applies constant increments to SST through each day, there is a risk that it may smooth out the fronts and consequently adversely affect the 3D structure.

To assess the tidal frontal locations and summer stratification comparisons of the surface minus bed temperatures of the model runs is made against gridded ICES data[67] following[49]. Fig 10 shows the summer surface – bed temperature difference for the ICES climatology and the models. The frontal location is indicated by the $0.5°C$

contour in surface-bed temperature difference. The location of the front in NEMO-AMM is more close to the ICES dataset than POLCOMS-AMM overall but it appears to over estimate mixing in the German Bight. The difference in the stratification between ICES and FOAM-AMM and POLCOMS-AMM is also shown in the bottom panels of Fig 10. POLCOMS-AMM has much more stratification than either ICES or FOAM-AMM. As noted by[49] this arises from the turbulence model used in POLCOMS-AMM.

The locations of the tidal mixing fronts for the assimilative and free runs of FOAM-AMM do not differ significantly. Thus the SST assimilation does not degrade the frontal positions. However, the level of stratification, particularly in the Norwegian trench is different, with the free run closer to ICES than the assimilative run. One source of the discrepancy is simply that the SST is significantly corrected in the assimilative model run, particularly for the Norwegian

trench area. However, the bottom water temperature in the trench is also cooler in the assimilative run than the free run. The origins of this discrepancy occur in winter months when the North Sea is mixed and the assimilation cools the water along the lip of the trench, which then feeds into the trench proper. Table 2 shows a comparison between the free and assimilative runs of FOAM-AMM and 558 profiles from profiling buoys and ships that are available over the Global Telecommunications System (GTS) on the shelf during August 2008, mostly in the North Sea. These data are not assimilated and thus constitutes a completely independent dataset. The assimilative run does not significantly alter the salinity profile comparisons and improves the temperature profiles. Thus whilst the change in the stratification in the Norwegian trench due to the SST assimilation requires further investigation, the overall effect on the shelf of the assimilation is to improve the SST without degrading salin-
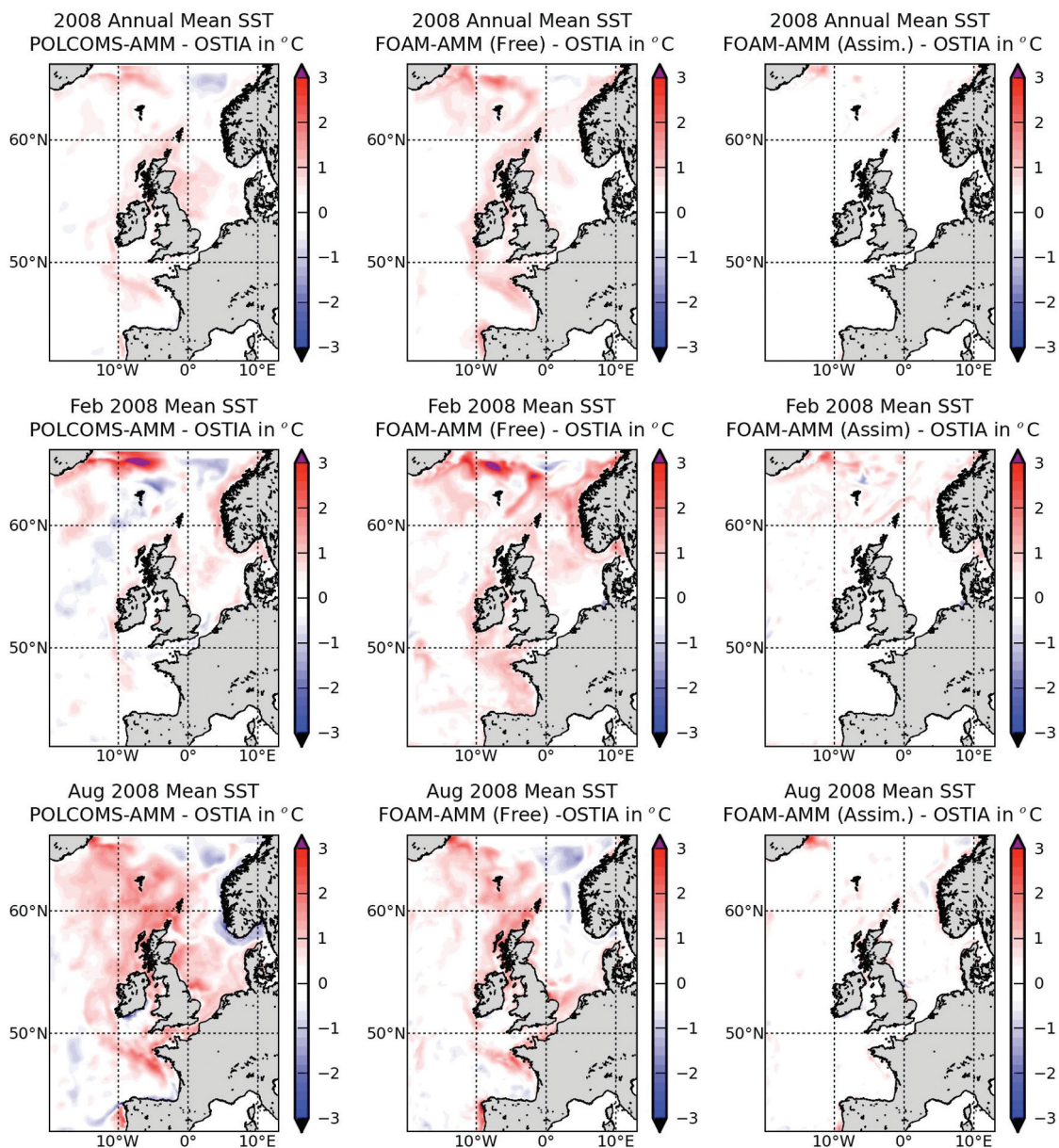
Fig 9: Top row is the 2008 annual mean difference between POLCOMS-AMM (left), FOAM-AMM free (centre), FOAM-AMM assimilative (right) and OSTIA in °C. Middle row is the February 2008 monthly mean difference. Bottom row is the August 2008 monthly mean difference
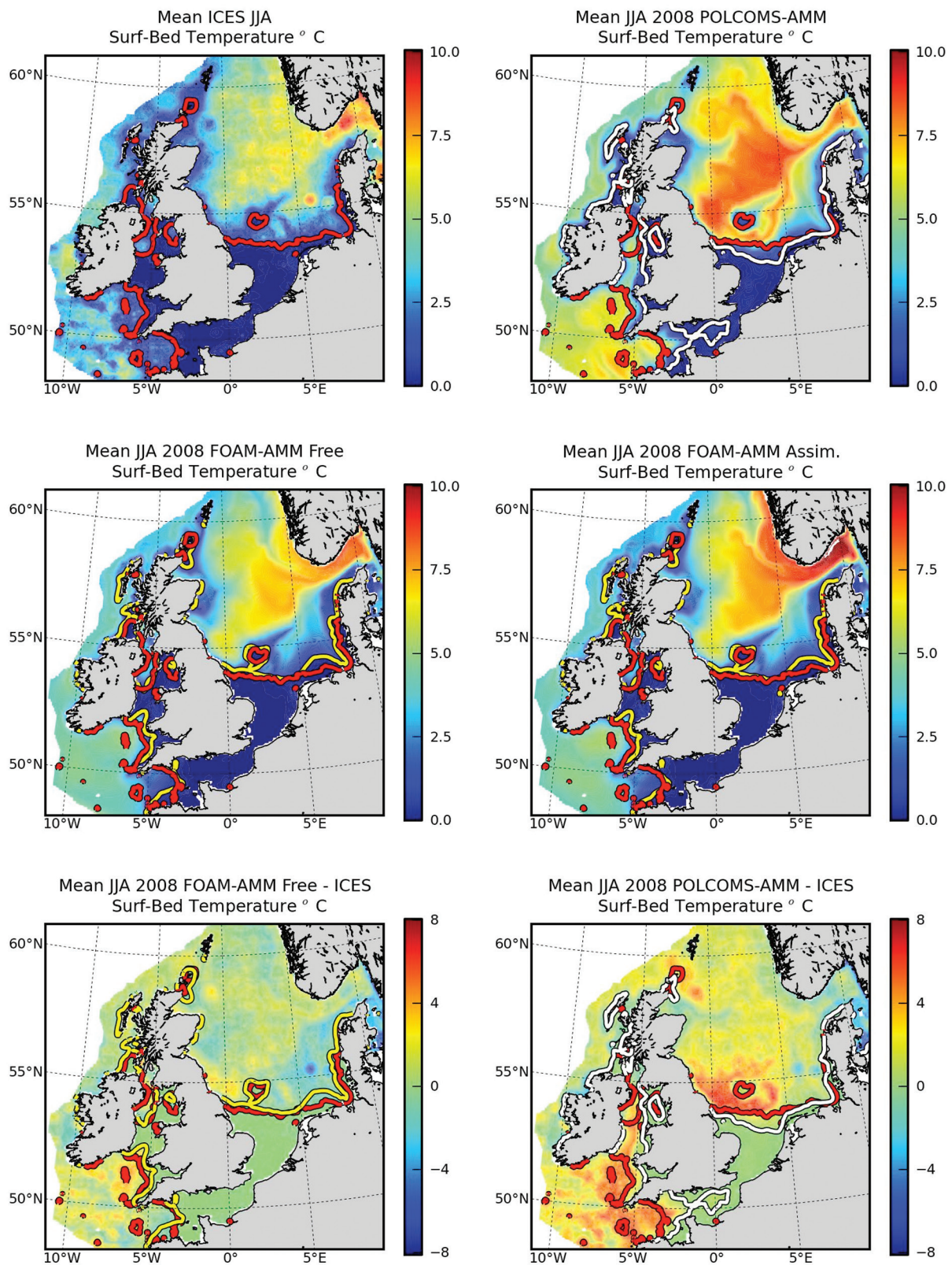
Fig 10: Top left panel is the mean ICES surface–bed temperature for summer (JJA). Top right panel is the mean POLCOMS-AMM surface-bed temperature for JJA 2008. Centre left is the mean FOAM-AMM non-assimilative surface-bed for JJA 2008. Centre right is the same for FOAM-AMM assimilative. Bottom left is the JJA mean difference sf surface-bed temperature between ICES and FOAM-AMM (free). Bottom right is the JJA mean difference between ICES and POLCOMS-AMM. Thick contours indicate mean frontal locations using the 0.5°C surface–bed contour for the ICES data (red), POLCOMS-AMM data (white) and FOAM-AMM data (yellow)

	RMS		Mean	
	Temperature (°C)	Salinity (PSU)	Temperature (°C)	Salinity (PSU)
Assimilative	0.338	0.738	0.088	0.254
Free	0.436	0.762	0.176	0.202

Table 3: RMS and mean differences between profile data and the assimilative and non-assimilative hindcasts of NEMO-AMM for January and February 2008 over the MRCS domain

ity profiles or tidal mixing frontal positions. Table 3 is an equivalent comparison for winter months. However, the number of profiles available during winter is significantly less than summer. For the combined months of January and February there were only 348 observations available from the GTS across the entire MRCS domain.

CONCLUSIONS AND FUTURE DEVELOPMENTS

A new operational forecasting system, FOAM-AMM, has been developed for the European NWS. The system uses NEMO as its core physics engine and includes SST data assimilation. An outline of some of the major dynamical features of the NWS is reviewed, for which several key enhancements required for NEMO have been developed. Details of these key developments and a description of the system in general are outlined including the adaption of the FOAM assimilation scheme for SST data assimilation in a tidally driven shelf seas forecast system.

Initial verification of the system includes assessing the FOAM-AMM system compared to an existing operational shelf seas forecast system POLCOMS-AMM. Harmonic analysis of the dominant tidal constituents show that in general FOAM-AMM is better than or equal to POLCOMS-AMM for SSH amplitude and phase. However, in the eastern Irish Sea FOAM-AMM is found to have weaker tides than observations and is an area that requires further refinement.

A two year fully baroclinic hindcast for 2007–2008 is also compared against archived operational fields from POLCOMS-AMM for the same period. The hindcasts reveal that the annual RMS SST errors in POLCOMS-AMM and FOAM-AMM without assimilation are similar, but with areas and seasons of weakness and strengths in each.

The addition of SST data assimilation markedly reduces the RMS SST errors. Furthermore, an analysis of the seasonal stratification on the shelf and tidal mixing fronts shows that the assimilation does not significantly alter the tidal mixing frontal positions. The locations of fronts in FOAM-AMM are in general closer to the ICES data set than POLCOMS-AMM with some exceptions including the German Bight.

The system continues to evolve and more detailed analysis of specific dynamics and regions continue to highlight specific features and areas that need to be addressed. Developments under investigation include the replacement of the climatological Baltic boundary condition with real-time data from a Baltic model. Specification from hydrological models of the river outflows is also being assessed. An improved coordinate system that allows a constant surface box domain wide is being developed to allow uniform specification of fluxes. The light attenuation scheme will be replaced by a three-band scheme and spatial variance of the light attenuation coefficient based on satellite climatologies is also being developed. Similarly, the coefficient of bottom friction may be varied depending on seabed types. A wetting and drying scheme is planned at NOC (following the one implemented in POLCOMS) which should allow for improved tidal dynamics, particularly in the Irish Sea. The data assimilation scheme will be updated to use NEMOVAR[68] and an improvement of the specification of the error covariance will be made. In addition to SST data assimilation, both profile data and altimeter data will be assimilated.

The FOAM-AMM system is also coupled to the ecosystem model ERSEM.[13] The coupled system continues to develop in parallel to the physical model and replaces the existing POLCOMS-ERSEM. Finally, a fully coupled atmosphere-ocean model using a version of FOAM-AMM for the ocean component focused on waters around the UK is being developed using the OASIS[69] coupler.

REFERENCES
1. Flather RA, Proctor R, and Wolf J. 1991. Oceanographic forecast nodels. In Computer Modelling In The Envirnomental Sciences, Farmer, DG and Rycroft, MJ, Eds. Clarendon Press, Oxford. pp. 15–30.
2. Flather RA. 2000. *Existing operational oceanography*. Coastal Engineering **41(1–3)**: 13–40.
3. Holt JT and James ID. 2001. *An s coordinate density evolving model of the northwest European continental shelf 1, Model description and density structure*. J. Geophys. Res. **106(C7)**: 14015–14034.
4. Holt M, Li Z, and Osborne J. 2003. Real-time forecast modelling for the NW european shelf seas. In Elsevier Oceanography Series, H. Dahlin, NCFKN and Petersson, SE, Eds. Elsevier. pp. 484–489.
5. Siddorn JR, Allen JI, Blackford JC, Gilbert FJ, Holt JT, Holt MW, Osborne JP, Proctor R, and Mills DK. 2007. *Modelling the hydrodynamics and ecosystem of the North-West European continental shelf for operational oceanography*. Journal of Marine Systems **65(1–4)**: 417–429.

6. Platt T, Sathyendranath S, White G, Fuentes-Yaco C, Zhai L, Devred E, and Tang C. 2010. *Diagnostic properties of phytoplankton time series from remote sensing*. Estuaries and Coasts **33(2)**: 428–439.

7. Bell MJ, Forbes RM, and Hines A. 2000. *Assessment of the FOAM global data assimilation system for real-time operational ocean forecasting*. Journal of Marine Systems **25(1)**: 1–22.

8. Annan JD and Hargreaves JC. 1999. *Sea surface temperature assimilation for a three-dimensional baroclinic model of shelf seas*. Continental Shelf Research **19**: 1507–1520.

9. Martin MJ, Hines A, and Bell MJ. 2007. *Data assimilation in the FOAM operational short-range ocean forecasting system: a description of the scheme and its impact*. Quarterly Journal of the Royal Meteorological Society **133(625)**: 981–995.

10. Storkey D, et al. 2010. *Forecasting the ocean state using NEMO: The new FOAM system*. Journal of Operational Oceanography **3**: 3–15.

11. Madec G. 2008. NEMO ocean engine. Note du Pole de modélisation. Institut Pierre-Simon Laplace (IPSL), France. No 27 ISSN No 1288–1619

12. Baretta JW, Ebenhöh W, and Ruardij P. 1995. *The European regional seas ecosystem model, a complex marine ecosystem model*. Netherlands Journal of Sea Research **33(3–4)**: 233–246.

13. Edwards KP, Barciela RM, and Butenschon M. In Preparation. *Validation of the NEMO-ERSEM operational ecosystem model for the North West European Continental Shelf*.

14. Proctor R and James ID. 1996. *A fine-resolution 3D model of the Southern North Sea*. Journal of Marine Systems **8(3–4)**: 285–295.

15. Holt JT, James ID, and Jones JE. 2001. *An s coordinate density evolving model of the northwest European continental shelf 2, Seasonal currents and tides*. J. Geophys. Res. **106(C7)**: 14035–14053.

16. Holt JT, Allen JI, Proctor R, and Gilbert F. 2005. *Error quantification of a high-resolution coupled hydrodynamic-ecosystem coastal-ocean model: Part 1 model overview and assessment of the hydrodynamics*. Journal of Marine Systems **57(1–2)**: 167–188.

17. Ryder P. 2007. *Fast track marine core serice: Startegic implementation plan*. Available from: http://www.gmes.info/pages-principales/library/implementation-groups/marine-core-service-mcs.

18. Huthnance JM. 1984. *Slope currents and 'JEBAR'*. Journal of Physical Oceanography **14(4)**: 795–810.

19. Hill AE, Hickey BM, Shillington FA, Strub PT, Brink KH, Barton ED, and Thomas AC. 1998. Eastern Ocean Boundaries: Coastal segment (E). In The Sea: The Global Coastal Ocean, Vol 11, Regional Studies and Syntheses, Robinson, AR and Brink, KH, Eds. John Wiley

20. Torres R and Barton ED. 2006. *Onset and development of the Iberian poleward flow along the Galician coast*. Continental Shelf Research **26(10)**: 1134–1153.

21. Haynes R and Barton ED. 1990. *A poleward flow along the atlantic coast of the iberian penninsula*. J. Geophys. Res. **95(C7)**: 11425–11441.

22. New AL and Pingree RD. 2000. *An intercomparison of internal solitary waves in the Bay of Biscay and resulting from Korteweg-de Vries-Type theory*. Progress In Oceanography **45(1)**: 1–38.

23. Pingree RD, Mardell GT, and New AL. 1986. *Propagation of internal tides from the upper slopes of the Bay of Biscay*. Nature **321(6066)**: 154–158.

24. Simpson JH. 1998. The Celtic Seas. In The Sea: The Global Coastal Ocean, Robinson, AR and Brink, KH, Eds. John Wiley and Sons, New York. pp. 659–698.

25. Hansen B and Østerhus S. 2000. *North Atlantic-Nordic seas exchanges*. Progress In Oceanography **45**: 109–208.

26. Johnson C, Sherwin T, Smythe-Wright D, Shimmield T, and Turrell W. 2010. *Wyville Thomson Ridge overflow water: Spatial and temporal distribution in the Rockall Trough*. Deep Sea Research Part I: Oceanographic Research Papers **57(10)**: 1153–1162.

27. Simpson JH and Bowers D. 1981. *Models of stratification and frontal movement in shelf seas*. Deep Sea Research Part A. Oceanographic Research Papers **28(7)**: 727–738.

28. Holt J and Proctor R. 2008. *The seasonal circulation and volume transport on the northwest European continental shelf: A fine-resolution model study*. J. Geophys. Res. 113(C6): C06021.

29. Rossiter JR. 1954. *The North Sea Storm Surge of 31 January and 1 February 1953*. Philosophical Transactions of the Royal Society of London. Series A, Mathematical and Physical Sciences **246(915)**: 371–400.

30. Souza AJ and Simpson JH. 1997. *Controls on stratification in the Rhine ROFI system*. Journal of Marine Systems **12(1–4)**: 311–323.

31. Bendtsen J, Gustafsson KE, Söderkvist J, and Hansen JLS. 2009. *Ventilation of bottom water in the North Sea-Baltic Sea transition zone*. Journal of Marine Systems **75(1–2)**: 138–149.

32. Otto L, Zimmerman JTF, Furnes GK, Mork M, Saetre R, and Becker G. 1990. *Review of the physical oceanography of the North Sea*. Netherlands Journal of Sea Research **26(2–4)**: 161–238.

33. Wakelin S, Holt J, and Proctor R. 2009. *The influence of initial conditions and open boundary conditions on shelf circulation in a 3D ocean-shelf model of the North East Atlantic*. Ocean Dynamics **59(1)**: 67–81.

34. Song Y and Haidvogel D. 1994. *A semi-implicit ocean circulation model using a generalized topography-following coordinate system*. Journal of Computational Physics **115(1)**: 228–244.

35. Levier B, Tréguier AM, Madec G, and Garnier V. 2007. Free surface and variable volume in the NEMO code. MERSEA IP report WP09-CNRS-STR03-1A.

36. Arakawa A and Lamb VR. 1981. *A potential enstrophy and energy conserving scheme for the shallow water equations*. Monthly Weather Review **109(1)**: 18–36.

37. Zalesak ST. 1979. *Fully multidimensional flux-corrected transport algorithms for fluids*. Journal of Computational Physics **31(3)**: 335–362.

38. Courant R, Friedrichs K, and Lewy H. 1928. *Über die partiellen Differenzengleichungen der mathematischen Physik*. Mathematische Annalen **100(1)**: 32–74.

39. Madec G, Delecluse P, Crépon M, and Lott F. 1996. *Large-scale preconditioning of deep-water formation in the northwestern Mediterranean Sea*. Journal of Physical Oceanography **26(8)**: 1393–1408.

40. Mellor GL, Ezer T, and Oey L-Y. 1994. *The pressure gradient conundrum of sigma coordinate ocean models*. Journal of Atmospheric and Oceanic Technology **11(4)**: 1126–1134.

41. Liu H and O'Dea EJ. In Preparation. *A new pressure Jacobian horizontal pressure gradient method for hybrid vertical coordinate ocean modelling.*

42. Flather RA. 1976. *A tidal model of the northwest European continental shelf*. Mem. Soc. R. Sci. Liege **10(6)**: 141–164.

43. Flather RA. 1981. Results from a model of the northeast Atlantic relating to the Norwegian coastal current. In The Norwegian Coastal Current, Sætre, R and Mork, M, Eds. Bergen University, Bergen, Norway. pp. 427–458.

44. Martinsen EA and Engedahl H. 1987. *Implementation and testing of a lateral boundary scheme as an open boundary condition in a barotropic ocean model*. Coastal Engineering **11(5–6)**: 603–627.

45. Umlauf L and Burchard H. 2003. *A generic length-scale equation for geophysical turbulence models*. Journal of Marine Research **61**: 235–265.

46. Canuto VM, Howard A, Cheng Y, and Dubovikov MS. 2001. *Ocean urbulence. Part I: One-point closure model-momentum and heat vertical diffusivities*. Journal of Physical Oceanography **31(6)**: 1413–1426.

47. Rodi W. 1987. *Examples of calculation methods for flow and mixing in stratified fluids* J. Geophys. Res. **92(C5)**: 5305–5328.

48. Umlauf L and Burchard H. 2005. *Second-order turbulence closure models for geophysical boundary layers. A review of recent work*. Continental Shelf Research **25(7–8)**: 795–827.

49. Holt J and Umlauf L. 2008. *Modelling the tidal mixing fronts and seasonal stratification of the Northwest European Continental shelf*. Continental Shelf Research **28(7)**: 887–903.

50. Craig PD and Banner ML. 1994. *Modelling wave-enhanced turbulence in the ocean surface layer*. Journal of Physical Oceanography **24(12)**: 2546–2559.

51. Galperin B, Kantha LH, Hassid S, and Rosati A. 1988. *A quasi-equilibrium turbulent energy model for geophysical flows*. Journal of the Atmospheric Sciences **45(1)**: 55–62.

52. Young EF and Holt JT. 2007. *Prediction and analysis of long-term variability of temperature and salinity in the Irish Sea*. J. Geophys. Res. **112(C1)**: C01008.

53. Haney RL. 1971. *Surface thermal boundary condition for ocean circulation models*. Journal of Physical Oceanography **1(4)**: 241–248.

54. Martin MJ, Hines A, and Bell MJ. 2007. *Data assimilation in the FOAM operational short-range ocean forecasting system: a description of the scheme and its impact*. Quarterly Journal of the Royal Meteorological Society **133**: 981–995.

55. Lorenc AC, Bell RS, and Macpherson B. 1991. *The Meteorological Office analysis correction data assimilation scheme*. Quarterly Journal of the Royal Meteorological Society **117**: 59–89.

56. Bloom SC, Takacs LL, Da Silva AM, and Ledvina D. 1996. *Data assimilation using incremental analysis updates*. Monthly Weather Review **124**: 1256–2170.

57. Annan JD and Hargrreaves JC. 1999. *Sea surface temperature assimilation for a three-dimensional baro-clinic model of shelf seas*. Continental Shelf Research **19**: 1507–1520.

58. Larson J, Høyer JL, and She J. 2007. *Validation of a hybrid optimal interpolation and Kalman filter scheme for sea surface temperature and assimilation*. Journal of Marine Systems **65**: 122–133.

59. Donlon CJ, et al. 2007. *The GODAE High Resolution Sea Surface Temperature Pilot Project (GHRSST-PP)*. Bulletin of the American Meteorological Society **88**: 1197–1213.

60. Lorenc AC and Hammon O. 1988. *Objective quality control of observations using Bayesian methods. Theory, and a practical implementaion*. Quarterly Journal of the Royal Meteorological Society **114**: 515–543.

61. Donlon CJM, M. J. Stark, J. Roberts-Jones, J. Fiedler, E. Wimmer, W. 2011. *The Operational Sea Surface Temperature and Sea Ice Analysis (OSTIA)*. Rem. Sens. Env In Press.

62. Montégut C, Madec G, Fischer AS, Lazar A, and Iudicone D. 2004. *Mixed layer depth over the global ocean: an examination of profile data and a profile-based climatology*. J. Geophys. Res. **109**: c12003.

63. Parrish DF and Derber JC. 1992. *The National Meteorological Center's spectral statistical-interpolation analysis system*. Monthly Weather Review **12**: 1747–1763.

64. Hollingsworth A and Lonnberg P. 1986. *The statistical structure of short range forecast errors as determined from radiosonde data*. Tellus **38A**: 111–136.

65. Howarth MJ and Pugh DT. 1983. Observations of tides over the continental shelf of northwest Europe. In Physical Oceanography of Coastal and Shelf Seas, Johns, B, Ed. Elsevier, Amsterdam. pp. 133–85.

66. Stark JD, Donlon CJ, Martin MJ, and McCulloch ME. *An operational, high resolution real time, global sea surface temperature analysis system*. in *Oceans '07 IEEE Aberdeen, conference proceedings. Marine challenges: coastline to deep sea*. 2007. Aberdeern, Scotland: IEEE.

67. *The International Council for the Exploration of the Sea database*. Available from: http://www.ices.dk/ocean/ aspx/HydChem/hydChem.aspx.

68. Mogensen KS, Balmaseda MA, Weaver A, Martin MJ, and Vidard A. *NEMOVAR: A variational data assimilation system for the NEMO ocean model*. in *ECMWF newsletter*. Summer 2009.

69. Redler R, Valcke S, and Ritzdorf H. 2010. *OASIS4 – a coupling software for next generation earth system modelling*. Geosci. Model Dev. **3(1)**: 87–104.
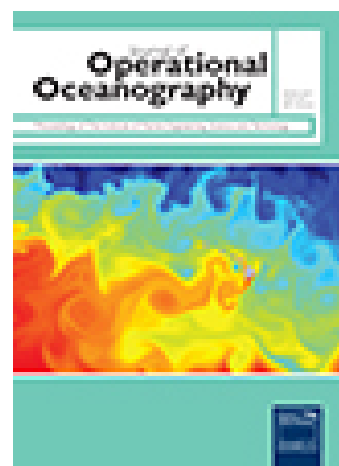
Journal of Operational Oceanography

Forecasting the ocean state using NEMO:The new FOAM system

D Storkey[a], E W Blockley[a], R Furner[a], C Guiavarc'h[a], D Lea[a], M J Martin[a], R M Barciela[a], A Hines[a], P Hyder[a] & J R Siddorn[a]

[a] all of the Met Office Exeter, UK
Published online: 01 Dec 2014.

PLEASE SCROLL DOWN FOR ARTICLE

Forecasting the ocean state using NEMO: The new FOAM system

D Storkey, EW Blockley, R Furner, C Guiavarc'h, D Lea, MJ Martin, RM Barciela, A Hines,
P Hyder, JR Siddorn, all of the Met Office, Exeter, UK

The Forecasting Ocean Assimilation Model (FOAM) deep ocean analysis and forecasting system has been running operationally at the Met Office for over 10 years. The system has recently been transitioned to use the Nucleus for European Modelling of the Ocean (NEMO) community model as its core ocean component. This paper gives an end-to-end description of the FOAM-NEMO operational system and presents some preliminary assessment of operational and hindcast integrations including verification statistics against observations and forecast verification against model best guess fields. Validation of the sea surface height fields is presented, which suggests that the system captures and tracks the major mesoscale features of the ocean circulation reasonably well, with some evidence of improvement in higher-resolution configurations.

LEAD AUTHOR'S BIOGRAPHY

Dave Storkey joined the Met Office in 1997 after a PhD in fluid dynamics. He now works as a senior scientist in the Ocean Forecasting R&D group and has been involved in the transition of the FOAM and shelf seas forecasting systems to use the NEMO model. His main interests are in model dynamics and model validation.

INTRODUCTION

The Forecast Ocean Assimilation Model (FOAM) is a system for analysing and forecasting the properties of the deep ocean at global and basin scales. A global configuration of the system has been operational at the Met Office since 1997,[1] and in the interim a number of higher resolution, basin-scale configurations have been implemented operationally. The system runs on a daily cycle in the Met Office operational suite, producing analyses and 5-day forecasts of physical ocean parameters, including temperature, salinity, currents and sea-ice variables. The principal customer is the Royal Navy, who uses the 3D density structure in sonar propagation models and also has a requirement for surface currents and sea-ice extent. The system increasingly has uses commercially, in other government departments and for research purposes. FOAM was one of the contributing systems to the Global Ocean Data Assimilation Experiment (GODAE)[2, 3] and will contribute to the follow-on GODAE Ocean View[4] initiative. FOAM will form part of the Europe-wide operational oceanography capability that is being assembled for the Global Monitoring for Environment and Security (GMES) Marine Core Service.[5]

The hydrodynamic model at the core of the system has recently been changed to use the Nucleus for European Modelling of the Ocean (NEMO) modelling code.[6] NEMO offers several advantages over the previous FOAM ocean model, notably a more structured coding environment, access to more up-to-date numerical options, and the opportunity to collaborate with an extensive community of developers and users. It also provides opportunities for closer collaboration within the Met Office since the climate scale, decadal and seasonal forecasting groups use, or will use, NEMO for the ocean component of their systems, and the operational shelf seas forecast system will also transition to the NEMO code in the near future.

The FOAM-NEMO system became fully operational in December 2008. The first part of this paper gives a detailed description of the new operational system, including the core model and data assimilation components and other components such as the observation processing, product delivery and automated verification system. It also briefly describes some of the applications of the system. The second part provides some preliminary assessment of the system, including assessment of

hindcast integrations and operational verification statistics. Finally, some conclusions are presented including a look ahead to future areas of development.

SYSTEM DESCRIPTION

Physical model

The original FOAM system was based on the ocean component of the Met Office Unified Model (UM).[7] This has now been replaced by the NEMO code. Among other benefits, this has allowed a number of the numerical schemes to be updated. In this section, the main features of the physical model are summarised.

The FOAM-NEMO system is based on a new set of operational configurations. The global configuration is based on the ORCA025 configuration developed by Mercator-Océan.[8] This has a Mercator latitude-longitude grid over most of the domain with 1/4° (28km) grid spacing near the equator reducing to 6km grid spacing at high latitudes. There is a stretched grid with two poles in the Arctic to avoid the convergence of meridians at the geographic pole.[9] It has 50 vertical levels with a concentration of levels near the surface (1m near-surface resolution) in order to resolve shallow mixed layers and to give the potential to capture diurnal variability. There are three nested, regional configurations: in the North Atlantic (NATL12), the Mediterranean (MED12) and the Indian Ocean north of 25°S (IND12). These all have latitude-longitude grids with 1/12° horizontal resolution. The NATL12 grid is rotated so that the equator of the grid runs through the centre of the model domain, which gives a more uniform resolution across the domain. The regional configurations have the same 50 vertical levels as the global configuration.

The ORCA025 bathymetry was derived by Mercator-Océan[6] from a combination of ETOPO5[10] for the deep ocean, General Bathymetric Chart of the Oceans (GEBCO)[11] for the continental shelves and BEDMAP[12] for the Antarctic. The regional model bathymetries are derived from GEBCO.

The modelling code is currently version 3.0 of the NEMO primitive equation ocean model. The model uses a linear free surface with a filtered solver[13] for the depth-mean solution and an energy-and enstrophy-conserving form of the momentum advection.[14] The lateral boundary condition on the momentum equations is free slip for the global configuration and partial slip for the regional configurations. In the partial slip boundary condition the tangential velocity along lateral boundaries is reduced compared to the velocity at the nearest gridpoint, but is nonzero. It is used in the higher resolution models for stability reasons. The horizontal momentum diffusion uses a combination of laplacian and bilaplacian operators, since this has been found to better represent features like the Gulf Stream separation at intermediate model resolutions.[15] ORCA025 uses values for the laplacian and bilaplacian coefficients of 340m²s⁻¹ and 1.5x10¹¹ m⁴s⁻¹ respectively. The regional models use values of 50m²s⁻¹ and 1.0x10¹⁰m⁴s⁻¹. For ORCA025, the diffusion coefficients (for momentum and tracers) are scaled with the gridspacing. The laplacian operator scales linearly with the grid spacing and the bilaplacian coefficient scales with the cube of the grid spacing. This is to prevent instabilities caused by using a too-high diffusion coefficient at small grid spacing. The tracer equations use a total-variation-diminishing (TVD) advection scheme.[16] The tracer diffusion operator is laplacian and along-isopycnal. The tracer diffusion coefficient is 300m²s⁻¹ for ORCA025 and 100m²s⁻¹ for the regional models.

The vertical coordinate system is on geopotential levels with partial cell thicknesses allowed at the sea floor. Barnier *et al* (2006)[17] show that the combination of partial-cell bathymetry, an energy and enstrophy conserving momentum advection scheme and the free-slip momentum boundary condition gives an improved representation of the mesoscale flow field in models of intermediate horizontal resolution. The vertical mixing uses the turbulent kinetic energy (TKE) scheme of[18] embedded in NEMO by Blanke and Delecluse (1993).[19] There is a prognostic equation for the TKE and a diagnostic equation for the turbulent mixing length based on the local stability profile. Convection is parameterised using an enhanced vertical diffusion. A quadratic bottom friction boundary condition is applied.

The regional configurations are nested into the global configuration using one-way lateral boundary conditions with the flow relaxation scheme algorithm.[20] Temperature, salinity, velocities, and sea-ice concentration and thickness are relaxed to outer-model values over a 9-point zone at the edge of the model domain. The bathymetries of the regional models are matched to the bathymetry of the global model in this boundary zone. A correction is added to the velocities normal to the boundary at each timestep to ensure that the total volume of the model remains constant, taking into account both the flux through lateral boundaries and the freshwater flux across the free surface. In the NATL12 configuration a relaxation of the temperature and salinity fields to climatology is applied near the Strait of Gibraltar (which is closed in the model) to simulate Mediterranean outflow water.

Sea-ice is included in the ORCA025 and NATL12 configurations. The model used is the second version of the Louvain-le-Neuve sea-ice model (LIM2) as described by[21]. The thermodynamics uses a three-layer model (two-layers of ice and one of snow), with parameterisations of the sub-gridscale ice thickness distribution and the effect of brine pockets. The dynamical part treats the sea-ice as a two-dimensional field in balance with the atmosphere and ocean stress fields and uses the viscous-plastic constitutive relationship of Hibler.[22]

The model is forced at the surface by 6-hourly mean fluxes from the Met Office Numerical Weather Predication (NWP) model. A Haney flux correction[23] is applied based on the difference between the model sea surface temperature (SST) and a climatological SST field.[24] River outflow is input to the model as a surface freshwater flux with an enhanced vertical diffusion to mix the fresh water to depth. The climatological river runoff fields for ORCA025 were derived by[25] based on estimates given in[26]. The river outflow fields for the regional models were derived from the Global Runoff Data Centre (GRDC)[27] climatology.

Assimilation system

The data assimilation scheme used in FOAM-NEMO is based on the OI-type scheme used in the original FOAM system which is described in detail in Martin *et al* (2007)[28]. There have been a number of improvements since the move to NEMO, notably: the introduction of a first-guess-at-appropriate-time

(FGAT) scheme for calculating model-observation differences; the use of high-resolution SST data; improved error covariances; and the assimilation of large-scale sea-level anomaly (SLA) increments in addition to mesoscale SLA increments. Here the main features of the system are summarised.

FOAM assimilates *in-situ* and satellite SST data, satellite altimeter SLA data, satellite sea-ice concentration data, and temperature and salinity profile data. The satellite SST data includes sub-sampled level 2 data from Advanced Microwave Scanning Radiometer–Earth Observing System (AMSRE), Advanced Very High Resolution Radiometer (AVHRR), Advanced Along-Track Scanning Radiometer (AATSR), and MetOp supplied by the Global High-Resolution Sea Surface Temperature (GHRSST) project.[29] Altimeter SLA data is along-track data provided by Collecte Localisation Satellite (CLS),[30] which currently includes data from the Jason-1, Jason-2 and Envisat platforms. A mean dynamic topography field (MDT) is required to give the full dynamic topography. For the FOAM-NEMO system the Rio *et al* [31] (2007) climatology is used. This climatology was found to be problematic in certain coastal regions. It was, therefore, modified in the Bay of Biscay and masked out in the Persian Gulf, Gulf of Oman and Gulf of Aden. In the masked areas, no assimilation of SLA data takes place. The bulk of the profile data now originates from the Argo[32] array of profiling floats. The sea-ice concentration data is Special Sensor Microwave/Imager (SSM/I) data provided by the EUMETSAT Ocean Sea Ice Satellite Application Facility (OSI-SAF).

There is automated quality control of all data. The SST, SLA and sea-ice data is compared with the model background using a Bayesian procedure.[33] The profile data are processed using the comprehensive method described in the literature.[34] The variances used in the quality control are the same as those used in the assimilation. The assimilation scheme currently runs on a 24-hour cycle. Model forecast fields are temporally and spatially interpolated to observation points over the period T-24h to T+0h. The model-observation differences at observation points are then used by the assimilation scheme to generate fields of daily increments. The model is rerun for the period T-24h to T+0h and the increments are nudged in evenly over the period in an incremental analysis update (IAU) step.[35] Owing to the delayed arrival time of many observations, the 24-hour observation window causes the system to miss a significant number of observations. It is therefore planned to perform an additional 24-hour cycle between T-48h and T-24h each day in future versions of the system.

The assimilation scheme is a version of an analysis correction scheme,[36] which calculates an iterative solution to the generalised optimal interpolation (OI) equations. FOAM uses a fixed number of 10 iterations of this scheme. For all observation types (apart from sea-ice), the analysis is separated into horizontal and vertical parts. For the surface observation types, a horizontal analysis is performed which is projected to depth. The SST increments are applied over the extent of the model mixed layer down to a maximum depth of 660m. SST increments are not applied in regions where there is a temperature inversion or a marginally stable water column as this can cause instabilities. Mesoscale SLA increments are projected to depth using a version of an existing scheme.[37]

Synoptic scale SLA increments are applied directly to the model SLA field, and the model allowed to adjust the 3D fields. For profile data, a vertical analysis is first performed at each observation point, and then a horizontal analysis performed at each model level. After 3D temperature and salinity increments have been derived from all the observation types, geostrophic balancing increments are applied to the baroclinic velocity field. The balancing velocity increments are applied poleward of 5° ramping down to zero at 1°. Surface salinity increments are calculated to balance sea-ice increments. The salinity over the depth of the mixed layer is adjusted to take account of the volume of freshwater added or taken from the ocean due to the sea-ice increments. The mesoscale surface height increments are recalculated to ensure that they are in balance with the temperature and salinity increments using hydrostatic balance.

The model and observation spatial error covariance matrices used in the assimilation scheme are univariate, with cross-correlations between state variables being provided by dynamical balancing relationships as described in the previous paragraph. The covariance matrices are static in time but spatially varying. The model and observation error covariance matrices are calculated using an observation-based technique[38] making the assumption that there are no cross-correlations between observations. Because of the sparseness of ocean observations this gives a low spatial resolution for the model error covariance matrix. The model error covariance matrix is therefore also calculated using a model-based method.[39] The model-based based method uses the difference between 48h forecast fields and 24h forecast fields as a proxy for model error. These difference fields are then fitted by a linear combination of two second-order autoregressive (SOAR) functions. The combination of two functions is used to represent two sources of model error: synoptic-scale due to errors in the atmospheric forcing and ocean mesoscale errors due to errors from the internal model dynamics. A length-scale of 400km is assumed for the synoptic errors and a length-scale of 40km for the mesoscale errors. The model-based method provides high spatial resolution, but underestimates the magnitude of the covariances. The model-based estimates are therefore inflated based on values generated by the observation-based technique. The covariances for all configurations were calculated using output from a 2-year hindcast of the ORCA025 model. Ideally, covariances for the high-resolution models should be calculated from integrations of these models and this is planned as a future upgrade.

A number of bias correction schemes are used to deal with systematic errors in the model and observations. Systematic errors in the wind forcing or deficiencies in the vertical mixing of momentum can cause spurious circulations in the tropics when the pressure gradients are altered by assimilation of temperature and salinity observations. One scheme[40] adds a correction term to the subsurface pressure gradients in the tropics to counter this and ensure that temperature and salinity increments are retained by the model. Errors in the MDT field can lead to time-correlated biases in the observations of surface height which are assimilated into the model. These are detected and corrected using the method described in the literature.[41] The different sources of satellite SST data have systematic differences due to sensor type, retrieval method

and atmospheric phenomena. These are corrected by treating the in-situ and AATSR data sets as reference data sets against which the other satellite types are individually calibrated, using the scheme developed for the Operational Sea Surface Temperature and Sea Ice Analysis (OSTIA) SST analysis system.[42]

Operational implementation

The FOAM system runs daily as part of the Met Office operational suite, performing the following steps for each daily cycle:

1. Observations for the correct time window are extracted from the Met Office observations database and quality controlled. The quality control flags are merged back to the observations database for future reference.
2. Fluxes produced by the operational, global 40km NWP model are processed and interpolated onto the model grid. The NWP system runs a main forecast run in the early morning and then several update runs during the day to take advantage of more recent observations. Each of these runs produce fluxes for the ocean model, and the flux processing system merges this output to give the most up-to-date fluxes at each validity time.
3. For the regional models, lateral boundary data produced by the ORCA025 model are copied and processed.
4. The model is integrated forward for 24 hours from the previous best guess at T-24h and model equivalents of the observations are calculated online and stored in netcdf files together with the observation values and quality control information.
5. The assimilation system reads in the model and observation values and calculates model increments and bias fields, which are written out to netcdf files.
6. A 24-hour incremental analysis updating (IAU) step is performed by running the model from the previous best guess at T-24h and adding in the assimilation increment fields evenly up to T+0.
7. The model is run forward from T+0 for 5 days to give the forecast.

The system currently operates as two daily suites: the global ORCA025 configuration in one suite and the three regional configurations in another suite. Both of these suites complete the daily cycle detailed above in about one hour on four 32-processor nodes of an IBM Power 6 cluster.

Once the core suite is complete, separate batch jobs are submitted to perform post-processing of diagnostic output, interpolation of boundary conditions for nested FOAM and shelf seas models, and the automated production of verification statistics. Diagnostic output for Navy forecasters is provided via a dedicated communications link. Output for general users will be provided via the Global Monitoring for Environmental Security (GMES) Marine Core Service framework[3] in two ways. For users requiring a robust, operational feed of data, data will be provided via password-protected FTP. This system is fully robust and used in the context of other critical operational services and thus provides a high specification service in terms of timeliness and delivery to requirement. The systems operate a failover mechanism,

whereby a failure in one or more of the servers will result a switch to secondary servers. For users with less stringent requirements, data will be provided via File Transfer Protocol (FTP), Open-source Project for a Network Data Access Protocol (OpENDAP) and WebMap services from FTP and Thematic Real-time Environmental Distributed Data Services (THREDDS) servers on a third-party hosting service.

A web-based monitoring system has been developed at the Met Office to allow developers quick access to daily output to check for potential problems in the operational system. Up-to-date output from all the FOAM configurations can be viewed as horizontal fields or cross-sections. Also available are visualisations of the daily model-observation differences, temperature and salinity anomalies from climatology, and maps of forecast errors versus analysis.

Applications of the system

The FOAM system has a variety of applications both for real-time products and reanalyses. The original application was for use in Navy operations. Information about the 3D temperature and salinity fields is fed into sonar propagation models for use in anti-submarine warfare. The Navy also have requirements for surface currents and sea-ice extent.

Another important application for real-time products is the provision of lateral boundary data for operational regional models. FOAM data is used to provide boundary conditions for the Met Office operational Shelf Seas models on the north-west European Shelf,[43] and also for regional models at other European centres within the GMES Marine Core Service framework.

Surface and subsurface currents are important in the context of ship-routing and offshore operations. Surface currents from the global FOAM system are supplied both as a real-time product to aid the planning of shipping routes and also as historical data for use in legal disputes. Offshore operations such as oil drilling and undersea cable repair are vulnerable to strong currents throughout the water column. FOAM currents are supplied in real-time on a case-by-case basis to give early warning of strong currents, and also as historical data to provide climatologies of the current variability at future locations of operations. Other potential use for real-time surface currents include search and rescue and oil spill tracking. At the time of writing, there has been limited direct validation of model currents against observations, so these products are still viewed as experimental.

The 3D analyses of temperature and salinity provided by FOAM are useful in the context of long-timescale applications such as seasonal forecasting and climate monitoring. FOAM analyses are used as part of a system to predict winter temperatures in northern Europe.[44] Knowledge of the pattern of SST in the North Atlantic in late spring has been shown to enable a forecast to be made of the conditions in northern Europe in the following winter. This is because the SST pattern in late spring is capped by summertime shallow mixed layers, but then re-emerges in the autumn as deeper water is mixed to the surface again. FOAM is used to track these submerged temperature patterns over the summer when they are not visible from satellite observations.

Historical analyses of the physical state of the ocean are of interest both to the research community and to commercial
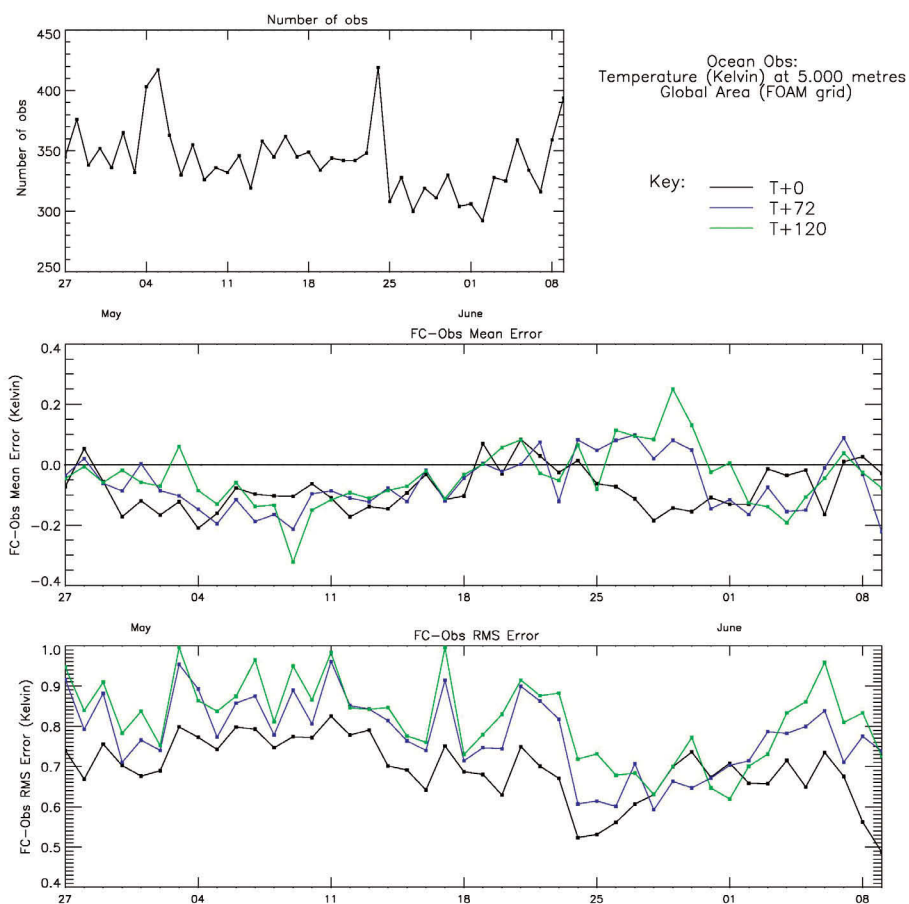
Fig 1: Example of output from automated verification of the operational FOAM system, showing verification of 5m temperature fields between 27 April and 9 June 2009. Top: timeseries of number of observations processed each day. Middle: timeseries of daily mean error statistics for three forecast lead times. Bottom: timeseries of daily rms. error statistics for three forecast lead times

users and will be more readily available for research use through the GMES Marine Core Service portals as described in the previous section. Observing system experiments have been used to feed back information on the design of observing arrays. For example, experiments assimilating different numbers of altimeter platforms have shown that using more platforms gives a better comparison with unassimilated surface drifter data.[45]

SYSTEM VALIDATION

Operational verification

Automated verification of the operational system is run on a daily basis a week behind real time. Verification of the model forecasts is performed against *in-situ* observations (surface and profile) and also against model analysis fields. The raw differences are archived, and from these the system can generate a variety of statistics and skill scores based on the full model domains or subdomains and for any time period. A selection of statistics are generated and plotted automatically on a daily basis as a monitoring tool. Fig 1 provides an example of these daily plots, showing surface temperature verification against *in-situ* observations for 50 days between April and June 2009 for ORCA025. There are timeseries of: number of observations ingested, mean errors and (root mean square) rms errors. Errors are shown for T+0 (best guess), T+72, and T+120 forecasts. Because these statistics are calculated daily, the number of observations available for each comparison is small, which leads to a noisy timeseries. The magnitude of the errors for the best guess fields is generally similar to the errors found in the

hindcast runs (Table 1), although it will not be possible to make a rigorous comparison until there is a year's worth of operational output.

Fig 2 shows an example of the statistics that can be generated from the system on an ad-hoc basis. It shows verification of surface height forecasts against model best guess fields using rms scores and anomaly correlations, where the anomalies are calculated relative to the MDT field. These were generated from 60 days of operational output in June and July 2009. Comparisons are shown with persistence errors to give an indication of model skill. By both measures the model forecasts perform better than persistence. An anomaly correlation score of 0.6 or above is often taken to indicate a forecast that is accurate enough to be useful.[46] By this measure, the model forecasts may have useful skill for a considerable time beyond the current 5-day lead time. [47]shows anomaly correlation scores for SLA above 0.6 out to 20–30 days lead time depending on the area examined.

It should be emphasised that Fig 2 shows verification against model best guess fields rather than against observations. This is an easier test for the system since where there are no observations assimilated in a particular period then the best guess field at the end of the period is identical to the forecast field. For satellite SSH there is reasonable coverage of the observations even within a one-day window, so this measure should provide some useful information about the skill of the system.

Hindcasts

In order to validate the system prior to operational implementation, all the configurations were run in hindcast mode for periods of 1–2 years. The integrations were initialised with

		SST (°C)	SSH (m)	MLD (m)	Temperature (°C) surface to 2000m	Salinity (psu) surface to 2000m
Global	ORCA025	0.66 (-0.14)	0.10 (0.00)	30.0 (+1.6)	0.64 (+0.01)	0.10 (0.00)
North Atlantic	ORCA025	0.84 (-0.05)	0.10 (+0.01)	40.1 (-0.5)	1.05 (+0.02)	0.23 (+0.01)
	NATL12	0.95 (-0.04)	0.11 (-0.01)	41.8 (-0.05)	1.06 (+0.07)	0.21 (0.00)
Indian Ocean	ORCA025	0.59 (-0.08)	0.07 (-0.02)	26.7 (+1.2)	0.56 (+0.02)	0.12 (0.00)
	IND12	0.73 (-0.13)	0.07 (0.00)	27.9 (+3.0)	0.61 (0.00)	0.12 (0.00)
Mediterranean	ORCA025	0.80 (+0.05)	0.08 (-0.04)	37.1 (-3.3)	0.72 (+0.04)	0.09 (0.00)
	MED12	0.73 (+0.01)	0.07 (-0.00)	30.4 (+0.1)	0.69 (0.00)	0.09 (0.00)

Table 1: Rms (bold) and mean (bracketed) errors for various fields from the hindcast validation runs of the FOAM models. Errors are calculated using the differences between the observations and model background fields at observation points. Fields shown are sea-surface temperature (SST), sea-surface height (SSH), mixed-layer depth (MLD), and 3D temperature and salinity. The mixed-layer depth is calculated according to the density criterion of[57] for both observations and model fields. Global statistics are shown for the ORCA025 configuration, then regional statistics for the North Atlantic, Indian Ocean and Mediterranean, showing comparisons of statistics from the regional model and the region of the ORCA025 model
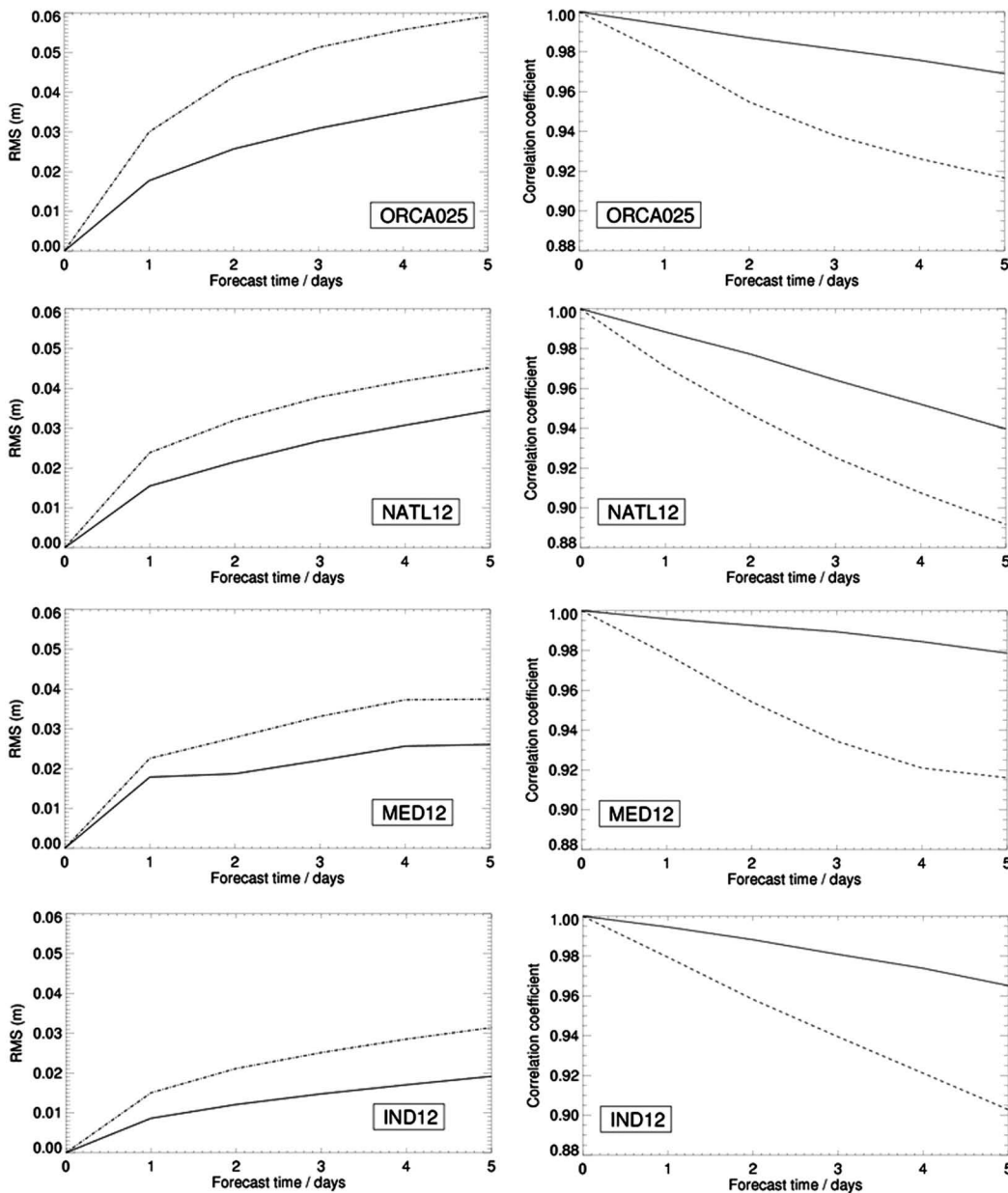

Fig 2: Plots showing forecast error statistics calculated versus the model best guess (solid lines) compared with persistence errors versus model best guess (dashed lines). Left hand column: rms errors. Right-hand column: anomaly correlation scores. Statistics are calculated from the operational system using 60 day's worth of output in June and July 2009

operational temperature and salinity fields and zero velocity fields and then spun up for 3 months with no data assimilation and for a further 3 months with data assimilation. The hindcast validation period began in April 2005 and ran for two years for ORCA025 and MED12 and for one year for NATL12 and IND12. The hindcasts operate on the same 24-hour cycle described previously with the exception that the IAU step was run for 24 hours and no further forecast was run (ie, steps 1–6 of the operational cycle). The hindcasts were forced with archived 6-hourly mean NWP fluxes and assimilated all observations valid for the 24-hour period, including those that would have been missed by the operational system due to late delivery times. The hindcast period was chosen to facilitate comparison with hindcasts performed with the previous FOAM system; it had the disadvantage that some observation types were not available for the whole period. High-resolution GHRSST SST data is only available in the Met Office database from July 2006. Prior to this AVHRR Pathfinder data[48] was used, binned onto a 1° global grid. The EUMETSAT OSI-SAF sea-ice concentration fields are only available in the database from January 2006, so prior to this no sea-ice data was assimilated.

Table 1 shows a summary of the rms and mean error versus observations from the hindcast integrations. These errors are derived using the model-observation differences calculated at observation locations for the assimilation step. They, therefore, represent the difference between the model background field (a forecast from the previous best guess) and the observations prior to their assimilation into the model. The table shows global statistics for the ORCA025 model and regional statistics comparing the statistics for the regional models with the statistics for the corresponding region of ORCA025. The temperature fields have rms errors of between 0.5°C and 1.0°C with full-depth biases of less than 0.1. The salinity fields have rms errors of between 0.1psu and 0.2psu with biases of 0.01psu or less. For the SSH field typical rms. errors are around 10cm with a bias of 2cm or less. The scores for the North Atlantic are generally worse than for

other areas, both for the ORCA025 and NATL12 models. This probably reflects the fact that it contains several dynamically active regions, including the Gulfstream extension which is acknowledged as a particularly hard region to model accurately with intermediate-resolution models.[49]

In general, the statistics for the regions are very similar in ORCA025 and the regional models. With the exception of SST, the biases in ORCA025 are generally very small so that there is not much room for improvement in the regional models. An exception to this is the Mediterranean, where the MED12 biases seem to be significantly better than ORCA025 for most variables. Rms errors are similar and in some cases slightly worse in the regional models compared to ORCA025. This does not necessarily indicate that the regional models show no added value compared to ORCA025. As discussed in[50, 51] traditional verification metrics such as rms errors and skill scores can penalise a higher resolution model. Such a model will generally better represent the mesoscale eddy field, with more eddies and more intense eddies, but this will lead to a higher penalty when eddies are inevitably misplaced. In order to assess the added value of higher resolution models, one needs additional techniques such as object-oriented validation (one example is discussed in relation to Fig 7) or fuzzy verification techniques.[48]

Table 2 shows a comparison of error statistics between the FOAM-NEMO system and the old FOAM UM-based system. This comparison is for only part of the period of the main hindcast integrations (April to December 2005), so the statistics in Tables 1 and 2 are not directly comparable. In particular, the period for the error statistics in Table 2 does not cover a full annual cycle. The results show that for most variables the mean and rms errors in the new system are the same or slightly better than the mean and rms errors in the old system. The horizontal and vertical resolution is increased in the new system compared to the corresponding configurations in the old system (eg, the resolution of the global model is increased from 1°, 20 levels to 1/4°, 50 levels). Therefore, as discussed above, maintaining or improving the errors in the new system compared to the old

		SST (°C)	SSH (m)	MLD (m)	Temperature (°C) surface to 2000m	Salinity (psu) surface to 2000m
Global	Old FOAM 1° global	0.96 (+0.05)	0.11 (-0.01)	19 (+1.5)	0.93 (-0.08)	0.22 (-0.05)
	ORCA025	0.84 (-0.08)	0.10 (+0.01)	22 (-0.2)	0.92 (+0.02)	0.19 (+0.01)
North Atlantic 20N – 70N	Old FOAM 1/3° Atlantic	1.1 (+0.08)	0.11 (0.00)	16 (+0.5)	1.1 (-0.08)	0.20 (+0.01)
	Old FOAM 1/9° North Atlantic	1.2 (+0.11)	0.13 (-0.01)	17 (+0.7)	1.1 (-0.07)	0.22 (+0.03)
	NATL12	0.98(-0.04)	0.10 (0.00)	23 (-0.3)	0.94 (-0.07)	0.17 (0.00)

Table 2: Table showing comparison of error statistics between the old and new FOAM systems. Rms. (bold) and mean (bracketed) errors for various fields are shown for the period April to December 2005. Errors are calculated using the differences between the observations and model background fields at observation points. Fields shown are sea-surface temperature (SST), sea-surface height (SSH), mixed-layer depth (MLD), and 3D temperature and salinity. The mixed-layer depth is calculated according to the density criterion of[57] for both observations and model fields. Comparisons are shown between the old FOAM global 1° model and the ORCA025 model on the global domain; and for the old FOAM 1/3° and 1/9° Atlantic models with NATL12 on the North Atlantic domain between 20°N and 70°N. The statistics for the new FOAM models are generally similar or slightly improved compared to the old FOAM models. An exception is the rms error for the mixed layer depth which is slightly degraded in the new system
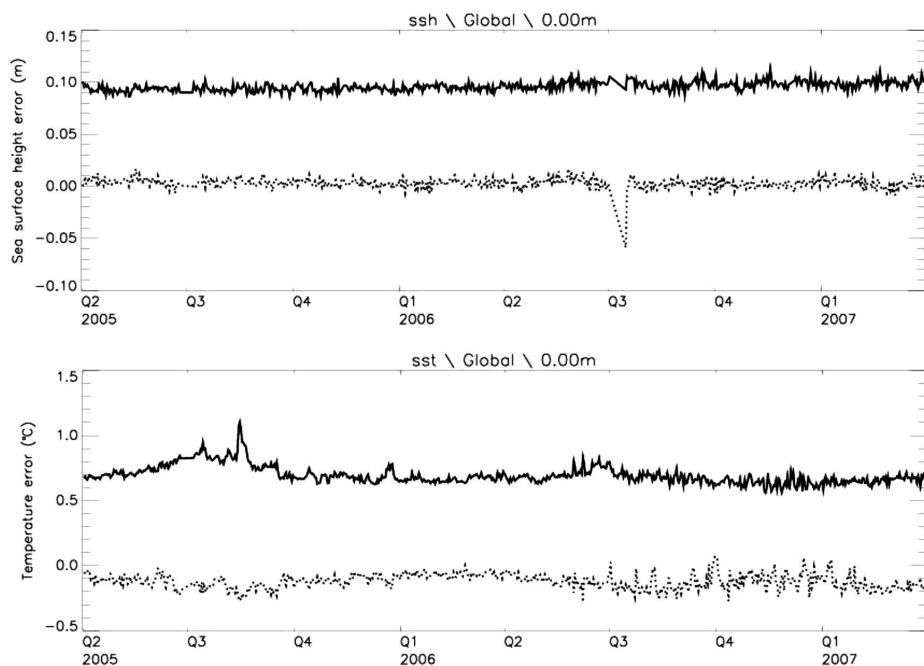
Fig 3: Timeseries of model background versus observation errors from a 2-year hindcast of ORCA025. Timeseries of mean (dotted lines) and rms (solid lines) best-guess minus observation errors for surface height (top) and sea surface temperature (bottom). There was no surface height data available for a week in the third quarter of 2006
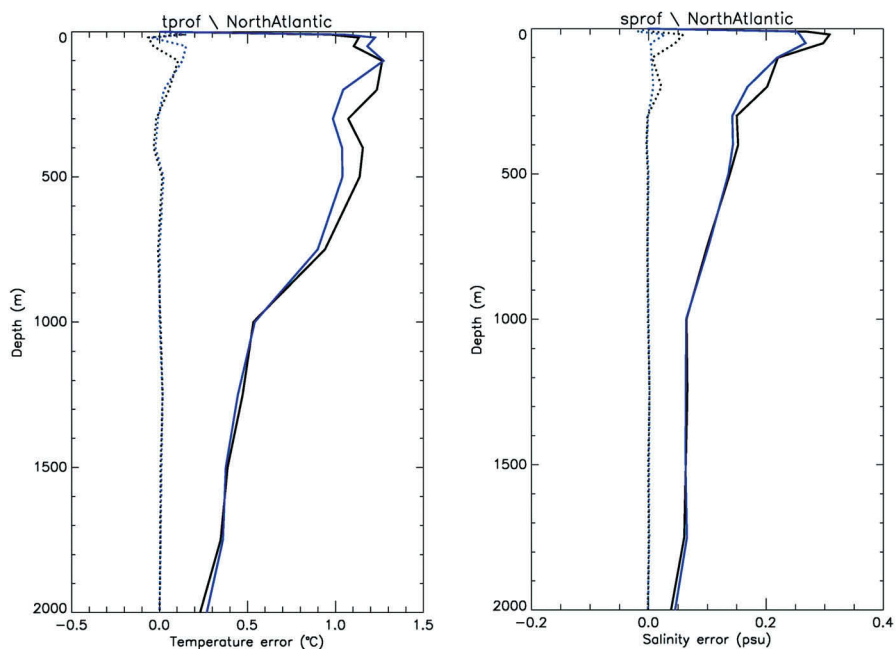
Fig 4: Profiles of error statistics from hindcasts of ORCA025 and NATL12. Profiles of mean (dotted lines) and rms. (solid lines) model background minus observation errors accumulated over the one-year hindcast period of NATL12 for left: temperature; and right: salinity. Results for the North Atlantic region of ORCA025 are shown in black and for the NATL12 model in blue. [From[3]]

system is a reasonable result, especially for the rms errors which usually punish an increase in model resolution.

Timeseries of the global statistics for the 2-year integrations for ORCA025 are shown in Fig 3 for SST and surface height. The timeseries for the surface height field is stable over the hindcast period. The timeseries for SST shows some variability in the first part of the hindcast period but is more stable in the later period when the high-resolution SST data is being assimilated. The bias in the SST is consistently around -0.1°C (see also Table 1), which is large compared to the subsurface biases. This is partly due to the fact that the verification is done against all SST observation types before they are bias-corrected as described previously. The value of -0.1°C therefore includes the observation bias as well as the model bias.

Fig 4 shows profiles of the errors for temperature and salinity for the North Atlantic region from ORCA025 and NATL12 down to 2000m (the limit of most Argo floats). As expected the highest errors are in the most active regions near the surface. The NATL12 model has similar errors to ORCA025 throughout the water column with small improvements visible in the rms. errors at mid-depths but slightly worse rms errors near the surface. The comparison of the other regional models with ORCA025 (not shown) shows that the mean and rms. profile errors are similar throughout the water column.

One of the principal aims of the system is to capture and forecast mesoscale features such as eddies and fronts. Fig 5 shows the standard deviation of the surface height field comparing model best-guess fields with observations for the one year of the NATL12 hindcast. In order to generate temporal statistics, the along-track data was binned into 1°x1° grid boxes. This gave on average 250 observations per grid box

Fig 5: Comparison of sea surface height variability between observations and model for the NATL12 configuration. Top: standard deviation of surface height (m), calculated by binning the along-track observations into 1°x1° gridboxes and calculating statistics for each gridbox. Bottom: standard deviation of surface height (m), calculated from the NATL12 hindcast by using the model equivalent values to the observations, binned in the same way
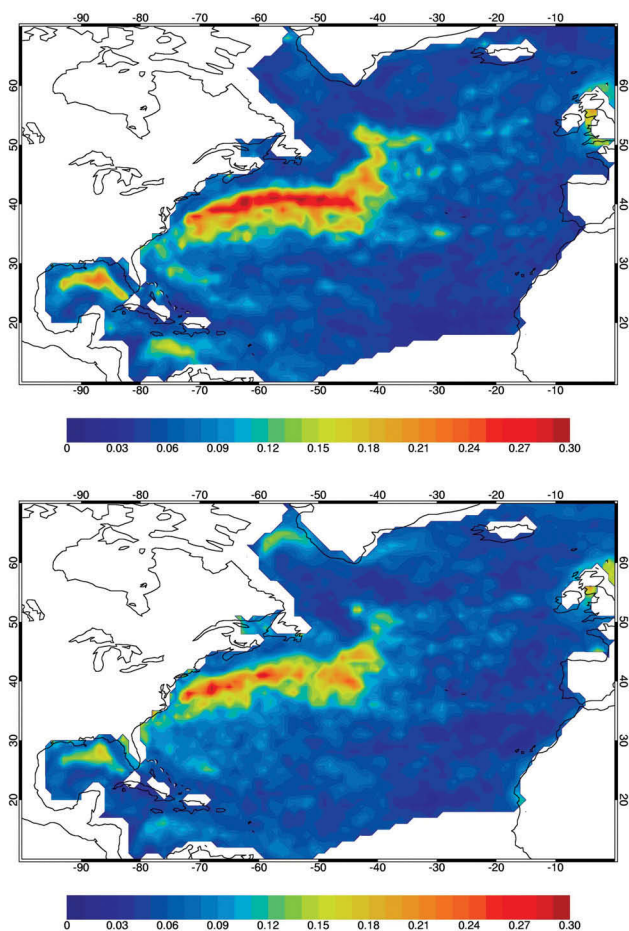
over the one year period. The model field was calculated by using the model values at the observation points binned into the same 1°x1° grid boxes. The spatial pattern of the variability is captured reasonably well by the model, but the overall magnitude is too low. This is likely due to insufficient horizontal resolution. It can be shown[47] that for a model without data assimilation, a resolution of at least 1/32° is required to adequately simulate the variability in the Gulfstream extension. As already noted the error covariance fields for the regional models were calculated using output from the ORCA025 model and this may restrict the variability in the regional models.

As well as capturing the distribution of mesoscale variability, one wants to constrain the evolution of individual eddies. As one way of trying to assess how well the model does this, we have generated animations comparing the SLA and SST anomaly fields output from the model with gridded observation products. Animations have been generated for areas of high variability including the Gulf Stream and Kuroshio extensions, and in general show that the models

reproduce and track most of the larger features seen in the observations, with some improvement in the representation noticeable as one moves to higher resolution. Fig 6 shows examples of stills from these animations, comparing the ORCA025 output with a mapped product from CLS[34] for the Kuroshio region and the IND12 output with the CLS data for the Indian Ocean. These illustrate typical comparisons: there are many differences of detail, but the models capture the positions of the major features in the mesoscale field.

Following[52] satellite ocean colour data has also been used as an independent observation set to try to determine how well the mesoscale eddies are reproduced on a case-by-case basis. Fig 7 shows an example of this kind of comparison for ORCA025 and IND12 in the north-west Arabian Sea. An 8-day composite, merged chlorophyll concentration product is shown in colour, overlaid with contours of the 8-day mean model SLA. In the northern hemisphere, cyclonic eddies have upwelling at their centre and therefore show up as high-biomass-centre eddies in the colour plot with anticyclonic eddies showing up as low-biomass-centre eddies. The main features of the circulation are captured by both models, for instance the intense cyclonic eddy at the entrance to the Gulf of Oman and the cyclonic eddy off the south-east coast of Oman which is advecting high-productivity coastal waters into the deep ocean. Some improvement in the representation of the eddy field can be seen in the IND12 model compared to the ORCA025 model; for instance the match of the SSH field to the filament of high-productivity water across the entrance to the Gulf of Aden is better in the IND12 model.

To more objectively assess the skill of the mesoscale representation in this case, an eddy-matching technique has been applied, similar to that described in[52]. 20 cyclonic and anticyclonic eddies with diameters of 50km or more were identified in the ocean colour field. Corresponding eddies (where they exist) were identified in the model fields and an eddy-position error calculated based on the eddy centres. The results are summarised in Table 3. ORCA025 represents 65% of the eddies with a median position error of 77km, whereas IND12 represents 80% of the eddies with a median position error of 67km. For comparison, previous results[52] from a 1/16° forecasting system showed 70% of eddies are represented with a median error of 35km. It should be noted that this previous study included smaller eddies in the comparison with a minimum diameter of 25km. Both models, therefore, represent the majority of the eddies with position errors of the

	ORCA025	IND12
% of eddies present	65%	80%
Median eddy centre position error (km)	77.8	67.3
% of eddies with most accurate position	37%	63%
% eddies with position error < 30 km	7%	31%
% eddies with position error between 30 and 60 km	28%	31%
% eddies with position error > 60 km	64%	37%

Table 3: Validation of eddy-centre locations in the north-west Arabian Sea for the ORCA025 and IND12 models against ocean colour data. The region verified is shown in Fig 7 and the verification period is the 7–14 April 2005
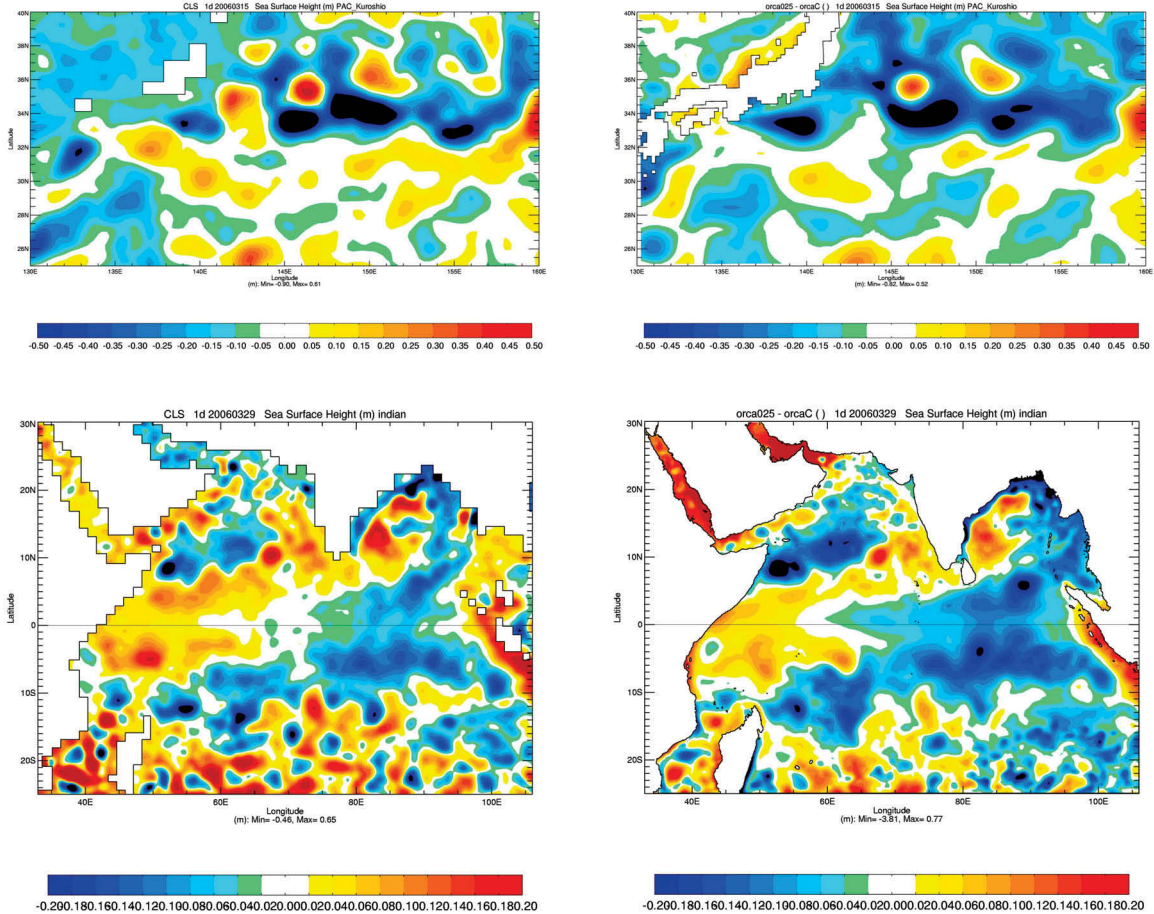
Fig 6: Stills from animations of SLA taken from hindcast integrations. Top: comparison of SLA analysis from CLS mapped product (left) and ORCA025 hindcast field valid for 16 March 2006; Bottom: comparison of SLA analysis from CLS mapped product (left) and IND12 hindcast field valid at 4 April 2006
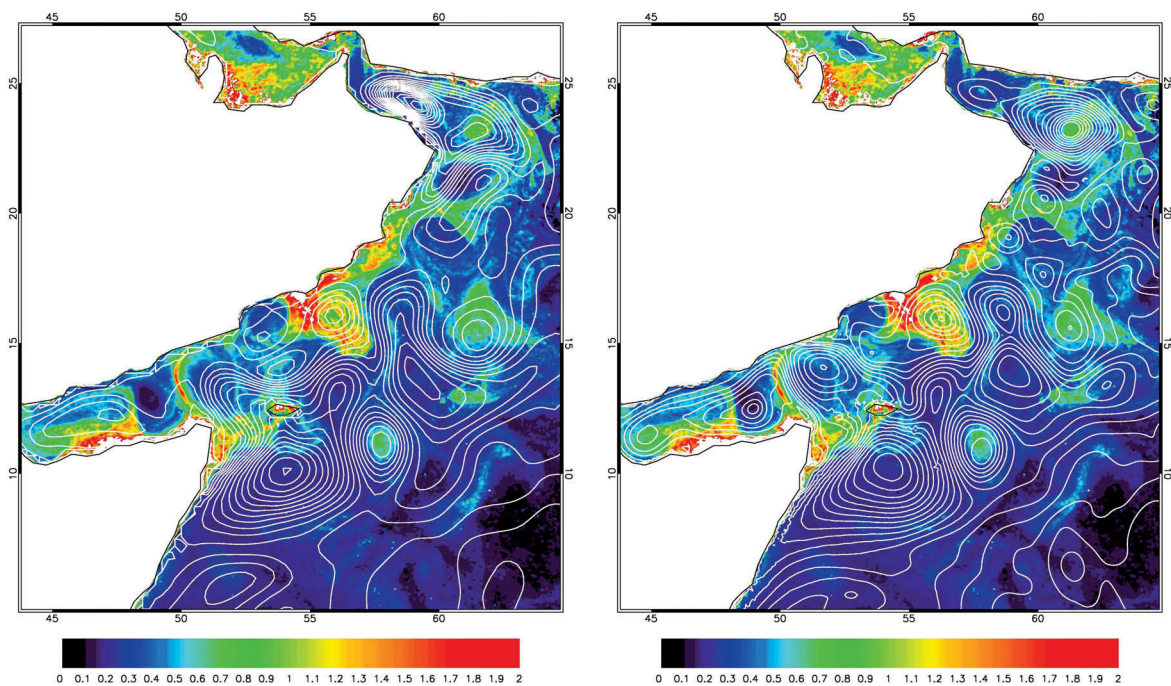
Fig 7: Comparison of surface height fields (contours) from the hindcast integrations with a merged chlorophyll concentration product (colour field) from GlobColour[58] in the north-west Arabian Sea. Model fields are 8-day means and chlorophyll fields are 8-day composites valid between 7–14 April 2005. Left: ORCA025. Right: IND12

same order of magnitude as the eddy diameters, but there is a clear improvement at higher resolution. These comparisons are important to demonstrate the added value of higher resolution models which is not evident in the error statistics in this case.

CONCLUSIONS AND FUTURE DEVELOPMENTS

The FOAM system now uses the NEMO code as its core hydrodynamic model. A detailed description of the operational implementation of the new system has been provided. Verification statistics against observations have been shown for hindcast integrations. Rms errors for the higher resolution models are similar to those from the global model. Subjective assessment of the hindcast fields by comparison to gridded SST, SLA and ocean colour products suggests that the models capture and track the major mesoscale features of the ocean circulation, with some improvement evident in the higher resolution configurations. Verification of forecasts against analyses from the operational system indicate that the models have skill out to the 5-day forecast lead time.

The preliminary assessments of the system presented in this paper have focussed on comparing the model background fields (that is short lead-time forecasts) with data that is subsequently assimilated into the model. Further assessments will include more detailed assessment of forecast skill and verification against independent data sets. Forecast error statistics against analyses and observations will be generated by spinning a number of forecasts off the hindcast integrations. Surface currents are an important output parameter from the model and will be assessed against surface drifter data and mooring observations.

A weakness of the current operational system is the fact that a significant number of observations are not used owing to late delivery. It is planned to improve this by starting the assimilation cycle at T-48h each day instead of T-24h. A 24-hour assimilation and IAU step will be performed between T-48h to T-24h to produce a best guess at T-24h and then a second 24-hour assimilation and IAU step will be performed between T-24h and T+0 to produce a preliminary best guess from which the forecasts are initialised. It is estimated that for the Argo data this will result in a 50% increase in the observations being assimilated into the system. Other developments to the assimilation system include the calculation of error covariances for the regional models based on regional model integrations rather than global model integrations. In the medium term, it is planned to upgrade the assimilation scheme to use a 3D Variational (3DVAR) First Guess at Appropriate Time (FGAT) scheme, using the NEMO Variational (NEMOVAR) code[53] that is being developed for use with NEMO.

The high vertical resolution near the surface in the models gives the potential to capture diurnal mixed layers. However, the 6-hourly frequency of the fluxes means that the diurnal cycle is barely resolved. It is planned to trial higher-frequency NWP fluxes to resolve the diurnal cycle more fully.

It is planned to replace the Louvain-la-Neuve Sea-Ice Model (LIM2) with the Los Alamos CICE code.[54] This will open the possibility of using an ice thickness distribution (ITD) scheme and elastic-viscous-plastic (EVP) rheology, and align the work more closely with the Met Office Hadley Centre climate model configuration.

Development and application of models of the ocean ecosystem is currently an area of increasing activity, with applications ranging from short-term information for limited areas for fisheries management through to climate time-scale applications to the global carbon cycle. The FOAM system is being used as the basis for the development of a coupled physical-biological analysis and forecasting system, which will provide products for the GMES Marine Core Service. A low-resolution global configuration of the physical model is coupled to the Hadley Centre Ocean Carbon Cycle (HadOCC) model,[55] a simple NPZD (Nutrient, Phytoplankton, Zooplankton, Detritus) model that also includes dissolved inorganic carbon (DIC) and alkalinity. Assimilation of satellite ocean colour data is being tested, using the scheme given in the literature.[56]

ACKNOWLEDGEMENTS

REFERENCES

1. Bell MJ, Forbes RM, and Hines A. 2000. *Assessment of the FOAM global data assimilation system for real-time operational ocean forecasting*. J. Marine Sys. **25**: 1–22

2. Bell MJ, Le Traon P-Y, Smith N, Lefebvre M, and Wilmer-Becker K. 2009. *The Global Ocean Data Assimilation Experiment (GODAE)*. Oceanography **22(3)**: 14–21

3. Dombrowsky E, Bertino L, Brassington GB, Chassignet EP, Davidson F, Hurlburt HE, Kamachi M, Lee T, Martin MJ, Mei S, and Tonani M. 2009. *GODAE Systems in Operation*. Oceanography **22(3)**: 80–96

4. Le Traon P, Bell M, Dombrowsky E, Schiller A, and Wilmer-Becker K. 2010. GODAE OceanView: from an experiment towards a long-term ocean analysis and forecasting international program. Proceedings of the OceanObs09 Conference: Sustained Ocean Observations and Information for Society, Venice, Italy, 21–25 Sep 2009, vol. 2. (ESA Publication WPP-306, 2010)

5. Ryder P. 2007. GMES Fast Track Marine Core Service: Strategic Implementation Plan. Available from: http://www.gmes.info/pages-principales/library/implementa-tion-groups/marine-core-service-mcs/

6. Madec G. 2008. NEMO ocean engine. Note du Pole de modélisation, Institut Pierre-Simon Laplace (IPSL), France, No 27 ISSN No 1288–1619

7. Gordon C, Cooper C, Senior CA, Banks H, Gregory JM, Johns TC, Mitchell JFB and Wood RA. 2000. *The simulation of SST, sea-ice extents and ocean heat transports in a version of the Hadley Centre coupled model without flux adjustments*. Clim. Dyn. **16**: 147–168

8. Drévillon M, Bourdallé-Badie R, Derval C, Drillet Y, Lellouche JM, Rémy E, Tranchant B, Benkiran M, Greiner E, Guinhut S, Verbrugge N, Garric G, Testut CE, Laborie M, Nouel L, Bahurel P, Bricaud C, Crosnier L, Dombrowsky E, Durand E, Ferry N, Hernandez F, Le Galloudec O, Messal F, and Parent L. 2008. *The GODAE/Mercator-Océan global ocean forecasting system: results, applications and prospects.* J. Operational Ocean. **1 (1)**: 51–57

9. Madec G, and Imbard M. 1996. *A global ocean mesh to overcome the North Pole singularity.* Climate Dynamics **12**: 381–388

10. NOAA/NGDC. 2001. ETOPO2: Global Gridded Databases Combining Bathymetry & Topography (Global Relief), NOAA/NGDC database.

11. IOC, IHO and BODC. 2003. Centenary Edition of the GEBCO Digital Atlas. Published on CD-ROM on behalf of the Intergovernmental Oceanographic Commission and the International Hydrographic Organization as part of the General Bathymetric Chart of the Oceans; British Oceanographic Data Centre, Liverpool, UK

12. Lythe MB, Vaughan DG, and The Bedmap Consortium. 2001. Bedmap: a new ice thickness and sub-glacial topographic model of Antarctica. J. Geophys. Res. **106(B6)**: 11,335–11,351

13. Roullet G, and Madec G. 2000. *Salt conservation, free surface and varying levels: a new formulation for ocean general circulation models.* J. Geophys. Res. **105(C10)**: 23927–23942

14. Arakawa A, and Lamb, VR. 1980. *A potential enstrophy and energy conserving scheme for the shallow water equations.* Mon. Weath. Rev. **109**: 18–36

15. Chassignet EP, and Garraffo ZD. 2001. Viscosity parameterization and the Gulf Stream separation". In "From Stirring to Mixing in a Stratified Ocean. Proceedings 'Aha Huliko'a Hawaiian Winter Workshop. U. of Hawaii. January 15–19, P. Muller and D. Henderson, Eds., 37–41

16. Zalesak ST. 1979. *Fully multidimensional flux corrected transport algorithms for fluids.* J. Comput. Phys. **31**: 335–362

17. Barnier B, Madec G, Penduff T, Molines J-M, Treguier A-M, Le Sommer J, Beckman A, Biastoch A, Böning C, Dengg J *et al.* 2006. *Impact of partial steps and momentum advection schemes in a global ocean circulation model at eddy-permitting resolution.* Ocean Dynamics **56**: 543–567

18. Gaspar P, Gregoris Y, and Lefevre JM. 1990. *A simple eddy-kinetic-energy model for simulations of the ocean vertical mixing: tests at station Papa and Long-Term Upper Ocean Study Site site.* J. Geophys. Res. **95(C9)**: 16179–16193

19. Blanke B, and Delecluse P. 1993. *Variability of the tropical Atlantic Ocean simulated by a general circulation model with two different mixed-layer physics.* J. Phys. Ocean. **23**: 1363–1388

20. Martinsen EA, and Engerdahl H. 1987. *Implementation and testing of a lateral boundary scheme as an open boundary condition in a barotropic ocean model.* Coastal Engineering **11**: 603–627

21. Timmermann R, Goosse H, Madec G, Fichefet T, Ethe C and Duliere V. 2005. *On the representation of high latitude processes in the ORCA-LIM global coupled sea ice-ocean model.* Ocean Modelling **8**: 175–201

22. Hibler III, WD. 1979. *A dynamic thermodynamic sea ice model.* J. Phys. Ocean. **9(4)**: 815–846

23. Haney RL. 1971. *Surface thermal boundary condition for ocean circulation models.* J. Phys. Ocean. **1**: 241–248

24. Locarnini RA, Mishonov AV, Antonov JI, Boyer TP, and Garcia HE. 2006. World Ocean Atlas 2005, US Government Printing Office, Washington DC, USA, 182 pp.

25. Bourdalle-Badie R and Treguier AM. 2006. A climatology of runoff for the global ocean-ice model ORCA025. Report, Mercator-Ocean. Reference: MOO-RP-425-365-MER

26. Dai A and Trenberth KE. 2002. *Estimates of Freshwater Discharge from Continents: Latitudinal and Seasonal Variations.* Journal of Hydrometeorology **3(6)**: 660–687

27. http://www.bafg.de/GRDC/Home/homepage_node.html

28. Martin MJ, Hines A and Bell MJ. 2007. *Data assimilation in the FOAM operational short-range ocean forecasting system: a description of the scheme and its impact.* Q.J.R. Meterol. Soc. **133**: 981–995

29. Lorenc AC, Bell RS and MacPherson B. 1991. *The Met Office analysis correction data assimilation scheme.* Q.J.R. Meterol. Soc. **117**: 59–89

30. Bloom SC, Takacs LL, Da Silva AM, and Ledvina D. 1996. *Data assimilation using incremental analysis updates.* Mon. Weath. Rev. **124**: 1256–1271

31. Rio MH, Schaeffer P, Hernandez F and Lemoine JM. 2005. The estimation of the ocean Mean Dynamic Topography through the combination of altimetric data, in-situ measurements and GRACE geoid: From global to regional studies. Proceedings of the GOCINA international workshop, Luxembourg

32. Argo Science Team 1998. On the design and implementation of Argo: An initial plan for a global array of profiling floats. ICPO Report 21, GODAE Report 5, Met Office, Exeter, UK.

33. Ingleby NB, and Lorenc A. 1993. *Bayesian quality control using multivariate normal distributions.* Q. J. R. Meteor. Soc. **119**: 1195–1225

34. Ingleby NB and Huddleston M. 2007. *Quality control of ocean temperature and salinity profiles – historical and real-time data.* J. Mar. Sys. **65**: 158–175

35. Ssalto/Duacs User Handbook : (M)SLA and (M)ADT Near-Real Time and Delayed Time Product, March 2009. Available from: http://www.aviso.oceanobs.com/en/data/tools/aviso-user-handbooks/index.html

36. Group for High Resolution Sea Surface Temperature. http://www.ghrsst-pp.org/

37. Cooper, M, and Haines K. 1996. *Altimetric assimilation with water property conservation.* J. Geophys. Res. **101(C1)**: 1059–1077

38. Hollingsworth A and Lönnberg P. 1986. *The statistical structure of short-range forecast errors as determined from radiosonde data. Part I: The wind field.* Tellus **38A**: 111–136

39. Parrish DF and Derber JC. 1992. *The National Meteorological Center's spectral statistical interpolation analysis system.* Mon. Weather Rev. **120**: 1747–1763

40. Bell MJ, Martin MJ, and Nichols NK. 2004. *Assimilation of data into an ocean model with systematic errors near the equator.* Q.J.R. Meteorol. Soc. **130**: 873–893

41. Lea D, Drecourt J-P, Haines K, and Martin MJ. 2008. *Ocean altimeter assimilation with observational and model bias correction.* Q. J. R. Meteorol. Soc. **134**: 1761–1774

42. Stark JD, Donlon CJ, Martin MJ, and McCulloch ME. 2007. OSTIA: An operational, high resolution, real time, global sea surface temperature analysis system. Oceans '07 IEEE Aberdeen, conference proceedings. Marine challenges: coastline to deep sea. Aberdeen, Scotland. IEEE. 21 June 2007

43. Siddorn JR, Allen JI, Blackford JC, Gilbert FJ, Holt JT, Holt MW, Osborne JP, Proctor R and Mills DK. 2006. *Modelling the hydrodynamics and ecosystem of the North-West European continental shelf for operational oceanography.* J. Marine Systems **65 (1–4)**: 417–429

44. Graham R, Gordon C, Huddleston MR, Davey M, Norton W, Colman AW, Scaife AA, Brookshaw A, Ingleby B, McLean P, Cusack S, McCallum E, Elliot W, Groves K, Cotgrove D, and Robinson D. 2006. The *2005/2006 winter in Europe and the United Kingdom: Part 1 – How the Met Office forecast was produced and communicated.* Weather **61**: 327–336

45. Oke PR, Balmaseda MA, Benkiran M, Cummings JA, Dombrowsky E, Fujii T, Guinehut S, Larnical G, Le Traon PY and Martin M. 2008. Observing System Evaluation. Proceedings of the Final GODAE Symposium, GODAE Project Office, Met Office, Exeter, UK

46. Murphy AH and Epstein ES. 1989. *Skill scores and correlation coefficients in model verification. Mon. Weath.* Rev. **117**: 572–581

47. Smedstad OM, Hurlburt HE, Metzger EJ, Rhodes RC, Shriver JF, Wallcraft AJ, and Kara AB. 2003. *An operational eddy resolving $1/16^o$ global ocean nowcast/forecast system.* J. Mar. Sys. **(40–41)**: 341–361

48. http://www.nodc.noaa.gov/SatelliteData/pathfinder4km/

49. Hurlburt HE and Hogan PJ. 2000. *Impact of $1/8^o$ to $1/64^o$ resolution on Gulfstream model-data comparisons in basin-scale subtropical Atlantic Ocean models.* Dyn. Atmos. Ocean. **32**: 283–329

50. Ebert EE. 2008. *Fuzzy verification of high-resolution gridded forecasts: a review and proposed framework. Meteorol.* Appl. **15**: 51–64

51. Mass CF, Ovens D, Westrick K and Cole BA. 2002. *Does increasing horizontal resolution produce more skillful forecasts?* Bulletin of the American Meteorological Society **83**:407–430

52. Shriver JF, Hurlburt HE, Smedstad OM, Wallcraft AJ, and Rhodes RC. 2007. *$1/32^o$ real-time global ocean prediction and value-added over $1/16^o$ resolution.* J. Marine Systems **65**: 3–26

53. Weaver AT, Deltel C, Machu E, Ricci S and Daget N. 2005. *A multivariate balance operator for variational ocean data assimilation.* Quarterly Journal of the Royal Meteorological Society **131**: 3605–3625

54. Hunke EC and Lipscomb WH. 2008. CICE: the Los Alamos Sea Ice Model. Documentation and Software Users Manuall Version 4.0. Fluid Dynamics Group, Los Alamos National Laboratory, Los Alamos

55. Palmer JR and Totterdell IJ. 2001. *Production and export in a global ocean ecosystem model.* Deep-Sea Research Part I **48**: 1169–1198

56. Hemmings JCP, Barciela RM and Bell MJ. 2008. *Ocean color data assimilation with material conservation for improving model estimates of air-sea CO_2 flux.* Journal of Marine Research **66**: 87–126

57. Kara AB, Rochford PA and Hurlburt HE. 2000. *An optimal definition for ocean mixed layer depth.* J. Geophys. Res. **105 (C7)**: 16803–16822.

58. http://www.globcolour.info

Assessing equatorial surface currents in the FOAM Global and Indian Ocean models against observations from the global tropical moored buoy array

P Hyder, D Storkey, E Blockley, C Guiavarc'h, J Siddorn, M Martin and D Lea, Met Office, Exeter, UK

Surface currents from 2007–2008 hindcasts of the Forecast Ocean Assimilation Model (FOAM) Global and Indian Ocean models are assessed against observations at 46 global tropical moored buoy array sites. Zonal (u) currents are less challenging to model than meridional flows (v) due to their lower frequency variability. The assimilative global model has reasonable skill for zonal currents but less skill for meridional currents. The assimilative models have higher skill than the corresponding non-assimilative models. A too-strong westward bias of the order of 20cm/s is evident along the equator in all model versions used in this study. No extra skill is evident in the high resolution (1/12°) regional model compared to the coarser resolution (1/4°) global model.

LEAD AUTHOR'S BIOGRAPHY

Pat Hyder has worked on ocean model evaluation and development at the Met Office since 2004. He has also worked since 1988 as an oceanographer, in research for the University of Wales, Bangor; Aristotle University of Thessaloniki; Bermuda Institute for Ocean Sciences; and NOAA fisheries, and for commercial companies, including FUGRO GEOS.

INTRODUCTION

There has been much work undertaken to evaluate assimilative ocean models.[1,2] However, to date, evaluation of simulated currents, and in particular, site specific comparisons, has been more limited.[3] Considerable effort was focused on site specific comparisons for oil drilling and production locations, particularly in the Gulf of Mexico, by the commercial company Ocean Numerics, but due to commercial confidentiality, only a small proportion of this effort was published.[4] Relevant effort has, however, been undertaken to evaluate observational current products.[5–9] There has also been considerable site specific evaluation effort in the meteorology community.[10] The observational constraint on mesoscale and sub-mesoscale ocean variability, through altimeter observations which are assimilated into models, has also been discussed in detail.[11,12]

This paper compares the simulated currents from two operational configurations of the Global 1/4° and Indian Ocean 1/12° FOAM models with and without data assimilation with surface current observations undertaken through the Global Tropical Moored Buoy (GTMB) array programme (www.pmel.noaa.gov/tao/global/global.html). These current data are independent since they are not assimilated by the models. However, the associated temperature and salinity observations at the same sets of moorings are assimilated.

The main aims of this study are to:

- Quantify skill in surface currents, against global tropical moored buoy observations, and identify any biases and regional differences.
- Assess whether skill is improved by data assimilation, increased model resolution and other model upgrades.
- To compare several skill scores.

The 46 observational sites with surface currents during the hindcast period are in the tropics between 12°S and 20°N (mainly between 10°S and 10°N). On inter-annual timescales, zonal surface currents in these locations are mainly influenced by the well-known equatorial climate modes, such as the El Niño Southern Oscillation[13] and Indian Ocean Dipole.[14] In the Indian Ocean, seasonal reversals in the major equatorial flows are also observed, associated with the monsoon reversals. In the eastern Atlantic and Pacific meridional flows are dominated by Tropical Instability Waves (TIW), which have relatively short periods of around 20 to 30 days. Surface currents are influenced both by the wind driven Ekman transport and the density driven flows which, away from the equator (>2°N/S), are in geostrophic balance but closer to the equator can be approximated using beta plane dynamics.[13] The vertical structure of both Ekman and geostrophic flows depend on ocean mixing. It should be noted, however, that the focus of this study is on model skill rather than equatorial dynamics.

The next section covers the background to models and methods. This is followed by sections on the results, a discussion of the results and conclusions.

BACKGROUND TO MODELS AND METHODS

Forecast Ocean Assimilation Model (FOAM)

The Forecast Ocean Assimilation Model (FOAM) is a system for analysing and forecasting the properties of the deep ocean at global and regional scales.[15,16] The Met Office runs daily analyses and five-day forecasts using several operational configurations, including the 1/4° resolution Global model and the nested high resolution Indian Ocean model (1/12° resolution). Both configurations employ the FOAM system using the coupled NEMO ocean and LIM2 sea ice models.

The hydrodynamic model at the core of the system has recently been changed to use the NEMO (Nucleus for European Modelling of the Ocean) modelling code. The global configuration is based on the 'ORCA025' configuration developed by Mercator-Océan. Full details of the model and data assimilation and their original configuration, termed V0, have been published,[15] while details of the data assimilation system employed in FOAM have also been reported.[17] Of particular relevance to model performance in the tropics are systematic errors in the wind forcing or deficiencies in the vertical mixing of momentum, which can cause spurious circulations when the pressure gradients are altered by assimilation of temperature and salinity observations. A scheme is therefore employed to add a correction term to the subsurface pressure gradients in the tropics to counter this and ensure that temperature and salinity increments are retained by the model.[18]

Hindcasts of the operational configurations were run for the period 2007 to 2008 with and without data assimilation for the original V0 operational configuration. Subsequently, and only with data assimilation, an additional 2007–2008 hindcast was completed using an updated configuration, termed V1. A series of corrections and upgrades were undertaken at V1 which include:

- An updated version of the mean dynamic topography (MDT)[19] termed CNES-CLS v1.1. (www.aviso.oceanobs.com) is used in the assimilation of sea surface height data.
- New seasonally varying error covariance fields in the assimilation scheme.
- The version of the NEMO code used was upgraded from version 3.0 to version 3.2.
- At V0, only Laplacian viscosity was applied resulting in grid scale noise. At V1, this was corrected to apply mixed Laplacian and BiLaplacian viscosity which reduces grid scale noise (and increases Eddy Kinetic Energy).
- A modified version of the TKE scheme is used which is theoretically similar to that used for V0 but designed to be dynamically consistent with the momentum advection scheme.[20]
- At V0, the Haney forcing term in the surface heat flux used monthly-mean climatological fields for the reference SST field. At V1, the Haney forcing term uses the Operational Sea surface Temperature and sea Ice Analysis (OSTIA) SST analysis that is seen by the Numerical Weather Prediction model.

Observational products

To evaluate the equatorial variability and currents in FOAM the following observational products were used:

- For sea surface height comparisons, the AVISO 1/4° delayed time gridded global product – Ssalto/Duacs Gridded Sea level anomalies. For details see www.aviso.oceanobs.com.
- For sea surface temperature comparisons, the daily OSTIA Sea Surface Temperature analysis.[21,22]
- The ocean surface current observations come from the global tropical moored buoy array observations (www.pmel.noaa.gov/tao/global/global.html).

Skill scores

A large number of different skill scores have been employed in the evaluation of ocean models. Essentially, all of these metrics attempt to summarise the distribution of observational versus simulated current components. Efforts were focused on the skill scores used to evaluate the Met Office operational models, which include Taylor diagrams, Root Mean Square Error (RMSE) and Mean Error (or bias). Taylor diagrams plot the Pearson correlation and model standard deviation (SD) divided by observed standard deviation (SD), from which the RMSE can also be derived.[23] To facilitate comparison the following metrics (employed by Allen et al[24] and Holt et al[25]) were also used:

(1) Holt cost function, HCF = RMSE/SD(observations).[25]
(2) Allen cost function, ACF = Mean(Absolute(error))/SD(observations).[24]

(3) Model Efficiency, ME = 1 − (RMSE/SD(observations))^2.[24]
Note – there is a direct relationship between ME and HCF such that ME = 1 − HCF^2.

(4) Normalised Standard Deviation, NSD = SD(error)/SD (observations).

It should be noted that the above-mentioned commonly employed metrics are related to each other. For example, the HCF and ACF are similar but the ACF penalises outliers less. Both of these scores penalise bias (or time mean error) since the denominator does not include bias but the numerator does. The NSD metric gets round this issue since neither term includes bias.

All metrics are calculated on daily mean observational and daily mean model analysis values.

RESULTS

Representation of equatorial variability and vertical structure

Fig 1 presents the sea surface height anomaly along the equator for the AVSIO observational product, together with the V0 assimilative (ASM) and non-assimilative (FREE) runs. The model and AVISO anomalies are relative to the mean dynamic topography. The model climatology was not used since the hindcast was limited to 2007–2008 and was therefore influenced by the predominantly La Niña state. There is reasonable agreement between the V0 assimilative run and the AVISO observational product. It should also be noted that plotting the anomalies relative to the two-year local mean (not shown as a figure) suggests that most of the major differences (including the large differences close to Southeast Asia) arise
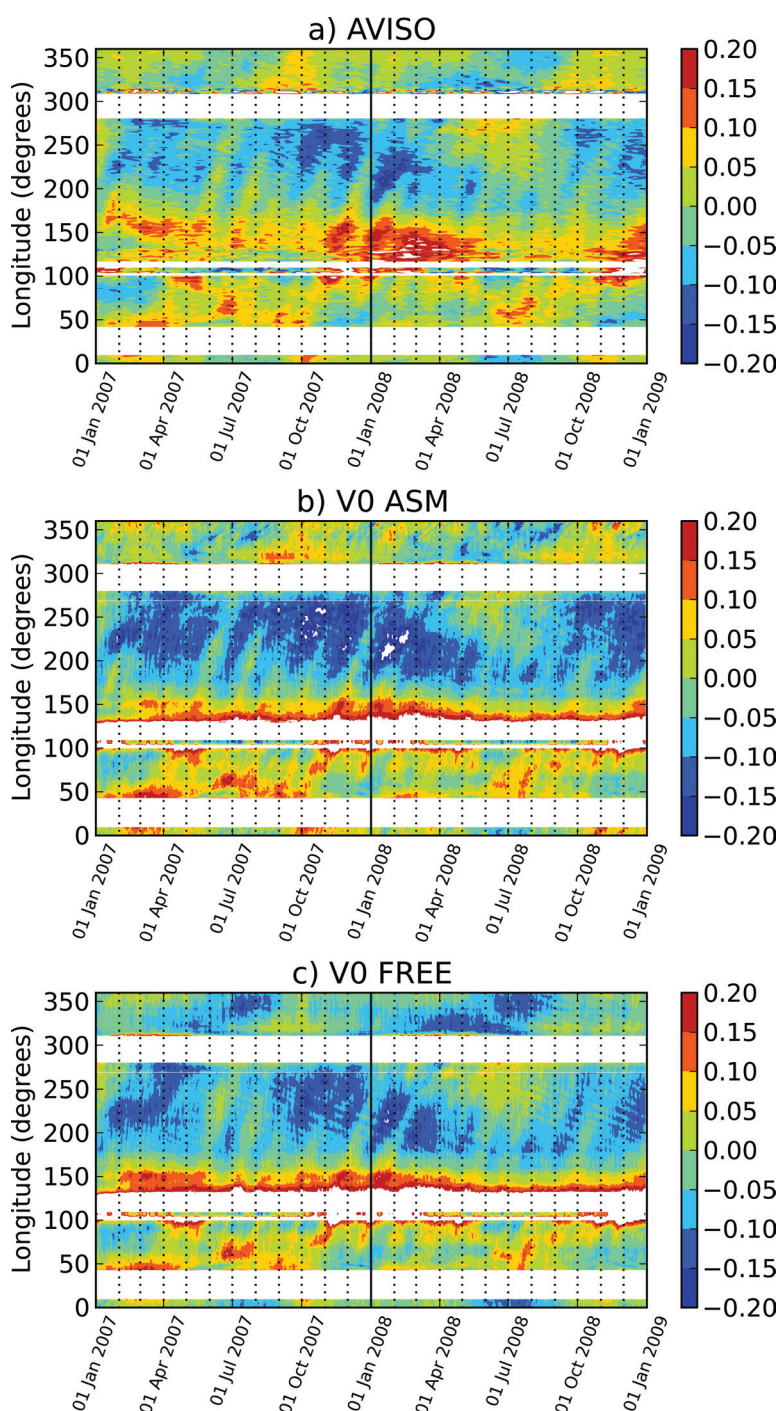

Fig 1: The sea surface height anomaly (m) variations along the equator over the 2007 to 2008 hindcast period for (a) the AVISO gridded observations (AVISO), (b) the V0 assimilative global model (V0 ASM) and (c) the V0 non-assimilative model (V0 FREE)

from differences in the mean state over the two years, rather than differences in the variability.

This agreement is perhaps not surprising since the same altimeter observations are used by FOAM as the AVISO product (albeit assimilated in very different ways) but it confirms adequate performance of the assimilation system. The non-assimilative run sea surface heights had a ~20cm/year increasing trend in sea surface height associated with a freshwater imbalance (ie, too much precipitation and river input compared to evaporation). This drift was corrected for in Fig 1 by removing, for each day, the mean sea surface height across the global equator relative to its initial level. Once corrected, the V0 non-assimilative run, sea surface heights agree reasonably with both the assimilative run and the observations for the large scale and inter-annual variations. However, significant errors are evident in short period and short scale variations in the non-assimilative run.

A similar analysis was undertaken (not shown) for SST against the OSTIA SST product. Visual analysis suggests that Tropical Instability Waves propagate at closer to their observed speeds in the assimilative V0 run than the non-assimilative V0 run, presumably due to improved representation of vertical density structure that affects the wave speed. These comparisons also suggest that SST equatorial variability is reasonably well represented in the assimilative V0 run but a warm bias of 1–2°C was evident in the non-assimilative V0 run.

Annual mean 2008 vertical current structure for a section at 140°W for V0 assimilative run and non-assimilative run are presented together with the corresponding mean observational section for 1991–1998 (present in[26] their Fig 1). The vertical current structure for the assimilative model agrees rather well the observations. Flow structure is generally similar, except for small differences in vertical extent and a failure to fully resolve the Sub Surface Counter Currents or Tsuchiya Jets.[26] It should be noted that differences might be expected in both the flow magnitudes and vertical extents due to the predominantly La Niña state during 2008. The main flows, eg, South Equatorial Current and Equatorial Under-Current were also reproduced by the non-assimilative model (Fig 2). However, in the non-assimilative model the Equatorial Under-Current is too strong and the South Equatorial Current is too strong on the equator and too weak in its southern branch.

Time-series comparison example at 170°W 0°N

Example time-series comparisons for zonal (u) and meridional (v) components of the surface currents for the V0 assimilative and V0 non-assimilative runs are presented in Fig 3. For the zonal (u) component there is clearly skill in the model at seasonal to inter-annual timescales. However, it is difficult to visually differentiate skill between the runs so a skill score is certainly required. The meridional (v) component is considerably more challenging to model since it is dominated by higher frequency variability of less than ~60 days. It is therefore difficult to assess skill by visual inspection so a skill score is again needed.

Relationship between skill scores

To decide on which skill score to employ, for all the model runs, all of the skill scores (detailed earlier) were calculated at each mooring location with surface current observations.
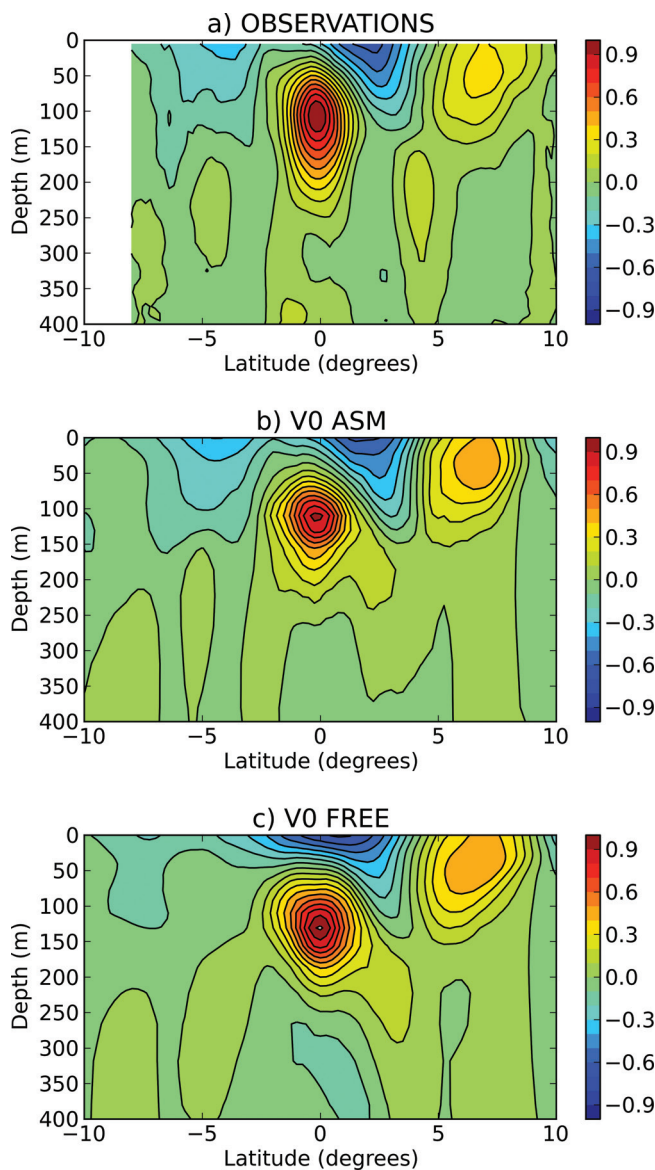
Fig 2: Mean zonal currents (m/s) in upper 400m of water column along 140°W for (a) Observations (redrawn, after Wang[26]), (b) the V0 global assimilative model (V0 ASM) and (c) the V0 global non-assimilative model (V0 FREE)

Fig 4 inter-compares the skill scores at each of the 46 locations for the global V0 assimilative model with values of the model efficiency parameter discussed by Allen *et al*.[24] This skill score was chosen as the baseline since thresholds for good, average and poor scores had already been defined, initially for river routing model evaluation.[24]

As expected from their derivations, there is a generally non-linear relationship with little scatter between model efficiency and the Holt cost function (which are directly related), the Allen cost functions and the correlation (except for low correlations). This is not the case for mean error or RMS error (neither of which incorporates information about the observational spread or standard deviation). Hence, careful interpretation of RMS and mean error is obviously essential, to avoid potentially misleading inferences. The low scatter (ie, relatively few outliers) in the relationship between model efficiency and both the two cost functions and correlation suggests that equivalent thresholds for each of the descriptors, already defined for model efficiency, can be estimated. These are included for
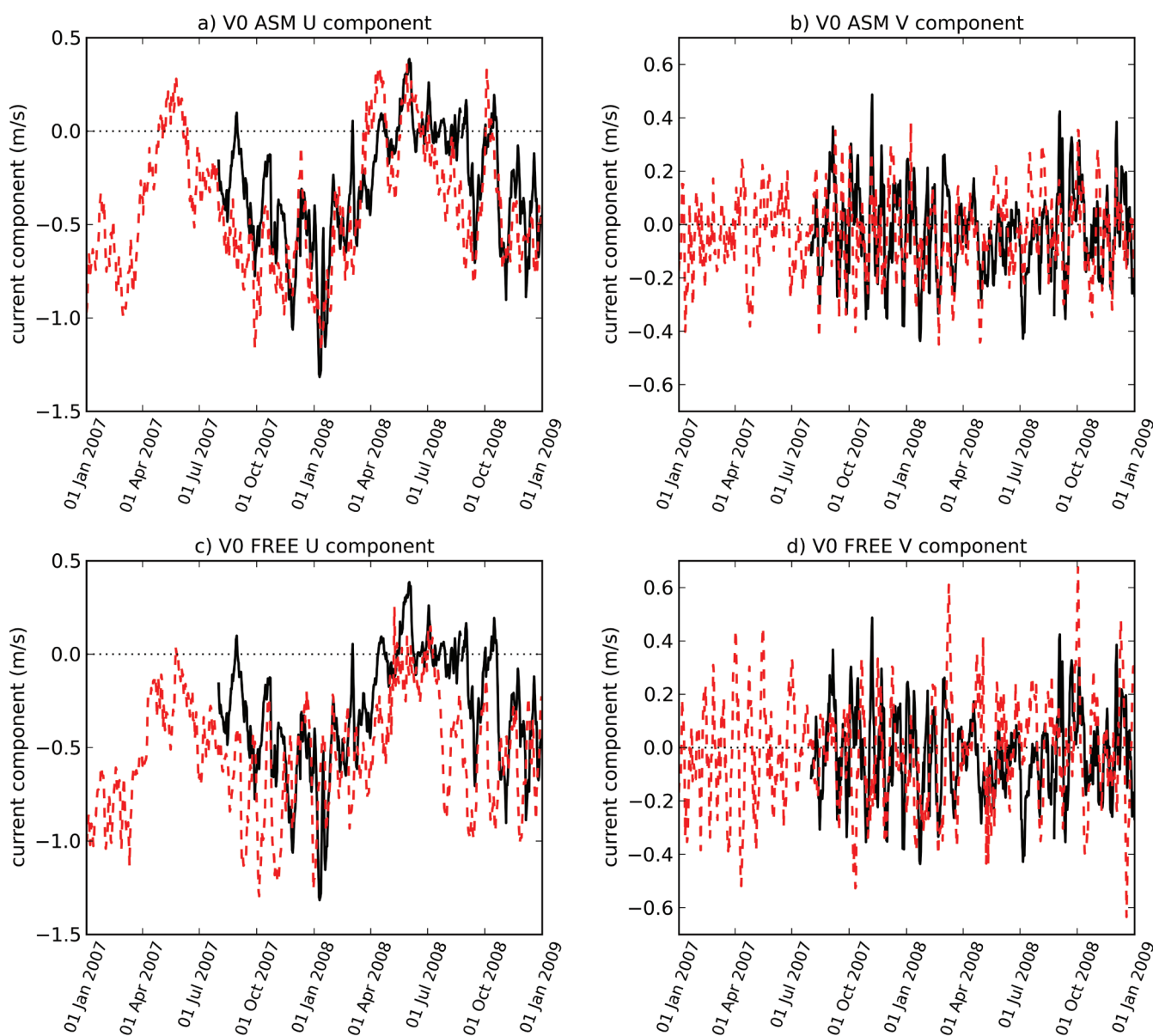
Fig 3: Time-series of zonal (u) and meridional (v) component surface current (m/s) at 170°W 0°N for (a & b) the V0 assimilative global model (V0 ASM), and (c & d) the V0 global non-assimilative model (V0 FREE). The model is marked with a dashed red line and the observations are marked with a solid black line

Descriptor (subjective)	ME upper threshold	ME lower threshold	R upper threshold	R lower threshold	Holt CF upper threshold	Holt CF lower threshold
Excellent	-	0.65	-	0.85	-	0.60
Very Good	0.65	0.50	0.85	0.80	0.60	0.70
Good	0.50	0.20	0.80	0.70	0.70	0.90
Average*	0.2	−0.20	0.70	0.60	0.90	1.20
Poor*	<−0.2	-	0.60	-	1.20	-

Table 1: The equivalent correlation and Holt[25] cost function skill score thresholds for the descriptors bands defined originally for model efficiency.[24]
*Note that the original 'poor' band has been split into average and poor bands
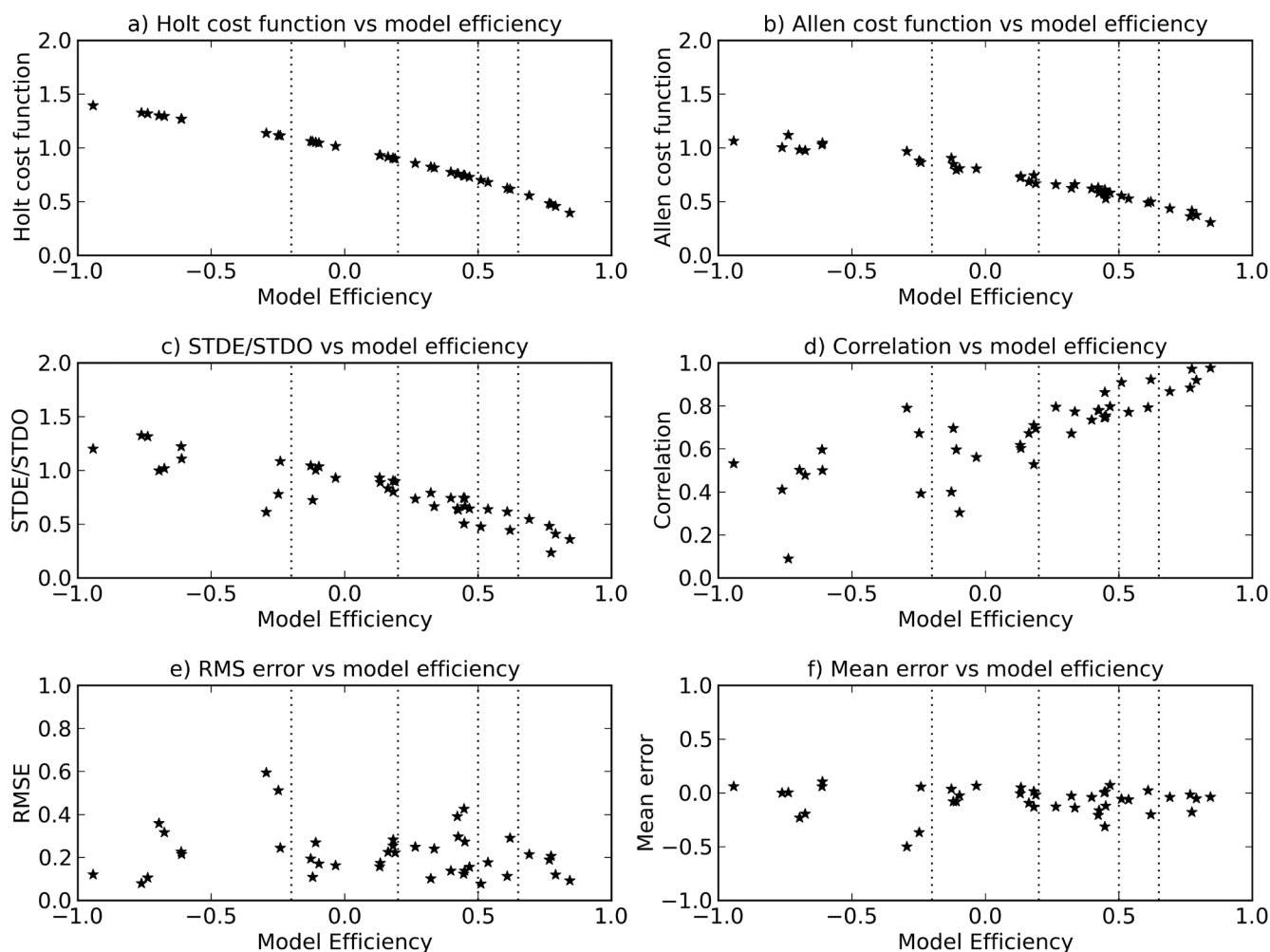
Fig 4: Relationship between the different skill scores at the 46 mooring locations for the V0 global assimilative model. The model efficiency parameter is presented on the x axis versus on the y axis: a) the Holt cost function; b) the Allen cost function; c) the standard deviation of the error divided by the standard deviation of the observations (STDO/STDE); d) the correlation coefficient, r; e) the Root Mean Square Error (RMSE) and f) the Mean Error

Global region	comp	n	rmserr (m/s)	mnerr (m/s)	r	std (mod/obs)	model efficiency	cost function (Allen)	cost function (Holt)	rmsnorm
V0 ASM	U	16627	0.25	−0.07	0.77	1.13	0.41	0.54	0.77	0.75
V0 ASM	V	16627	0.20	0.00	0.46	1.01	−0.08	0.76	1.04	1.04
V0 FREE	U	16627	0.28	−0.04	0.66	1.09	0.23	0.63	0.88	0.85
V0 FREE	V	16627	0.22	0.01	0.36	1.00	−0.28	0.81	1.13	1.13
V1 ASM	U	16627	0.28	−0.10	0.77	1.24	0.27	0.59	0.85	0.83
V1 ASM	V	16627	0.19	0.00	0.52	1.05	−0.01	0.73	1.01	1.00

Table 2: Skill score table for zonal (u) and meridional (v) surface currents for all the Global model hindcasts. The table includes velocity component (comp); number of values (n); Root Mean Square Errors (rmserr); Mean Errors (mnerr); Correlation coefficent (r); Standard deviation of model divided by standard deviation of observations (std (mod/obs)); Model Efficiency Parameter (model efficiency); Cost Function (Allen[24]); Cost Function (Holt[25]); and Normalised Root Mean Square Error (rmsnorm)

Indian region	comp	n	rmserr (m/s)	mnerr (m/s)	r	std (mod/obs)	ME	cost function (Allen)	cost function (Holt)	rmsnorm
V0 ASM	U	3700	0.22	−0.07	0.77	0.94	0.50	0.52	0.70	0.70
V0 ASM	V	3700	0.17	0.00	0.63	0.94	0.31	0.65	0.83	0.83
V0 FREE	U	3700	0.23	−0.02	0.73	1.02	0.45	0.57	0.74	0.74
V0 FREE	V	3700	0.16	0.00	0.66	0.94	0.35	0.62	0.80	0.80
V0 HRS ASM	U	3696	0.22	−0.06	0.75	0.95	0.49	0.53	0.71	0.71
V0 HRS ASM	V	3696	0.18	0.00	0.62	1.00	0.23	0.67	0.88	0.88
V0 HRS FREE	U	3696	0.23	−0.02	0.70	0.95	0.43	0.58	0.75	0.75
V0 HRS FREE	V	3696	0.17	−0.01	0.62	0.95	0.27	0.65	0.86	0.85
V1 ASM	U	3700	0.21	−0.07	0.78	0.92	0.53	0.50	0.68	0.68
V1 ASM	V	3700	0.17	0.00	0.64	0.98	0.30	0.65	0.84	0.84
V1 HRS ASM	U	3696	0.22	−0.06	0.77	0.99	0.51	0.52	0.70	0.70
V1 HRS ASM	V	3696	0.18	−0.01	0.62	1.05	0.21	0.69	0.89	0.89

Pacific region	comp	n	rmserr (m/s)	mnerr (m/s)	r	std (mod/obs)	ME	cost function (Allen)	cost function (Holt)	rmsnorm
V0 AMM	U	9417	0.28	−0.10	0.78	1.13	0.40	0.56	0.77	0.73
V0 ASM	V	9417	0.22	0.01	0.43	1.02	−0.18	0.81	1.09	1.08
V0 FREE	U	9417	0.33	−0.06	0.63	1.08	0.16	0.68	0.92	0.86
V0 FREE	V	9417	0.25	0.02	0.26	1.03	−0.54	0.93	1.24	1.24
V1 ASM	U	9417	0.33	−0.14	0.78	1.29	0.18	0.65	0.90	0.85
V1 ASM	V	9417	0.22	0.01	0.48	1.08	−0.14	0.79	1.07	1.06

Atlantic region	comp	n	rmserr (m/s)	mnerr (m/s)	r	std (mod/obs)	ME	cost function (Allen)	cost function (Holt)	rmsnorm
V0 ASM	U	3510	0.17	0.01	0.58	1.46	−0.46	0.82	1.21	1.16
V0 ASM	V	3510	0.15	−0.02	0.33	1.02	−0.39	0.82	1.18	1.17
V0 FREE	U	3510	0.17	0.00	0.56	1.37	−0.35	0.78	1.16	1.12
V0 FREE	V	3510	0.14	0.00	0.40	0.88	−0.08	0.71	1.04	1.03
V1 ASM	U	3510	0.16	−0.03	0.59	1.30	−0.20	0.73	1.10	1.06
V1 ASM	V	3510	0.13	0.00	0.53	0.98	0.07	0.68	0.96	0.96

Table 3: Regional skill score tables for each ocean basin for zonal (u) and meridional (v) surface currents for all the Global and Indian Ocean model hindcasts. The table includes velocity component (comp); number of values (n); Root Mean Square Errors (rmserr); Mean Errors (mnerr); Correlation coefficent (r); Standard deviation of model divided by standard deviation of observations (std (mod/obs)); Model Efficiency Parameter (ME); Cost Function (Allen); Cost Function (Holt); and Normalised Root Mean Square Error (rmsnorm)

correlation and the Holt cost function in Table 1. Note that an 'average' band has been added to the bands (discussed in[24]) by splitting their original 'poor' band which had an upper threshold for correlation of 0.7 and therefore contained apparently useable skill. Note also that these new equivalent thresholds may well be specific to this dataset. Thresholds of correlation were used to define the descriptors (although for completeness associated values of the other skill scores are also included in Tables 2 and 3). The thresholds for these descriptor bands remain rather arbitrary; they are therefore used simply to attach approximate descriptors to bands of correlation and to facilitate future verbal inter-comparison between different systems. The 'poor' upper threshold for correlations of 0.6, in particular, corresponds to an explained variance 36% but may in some circumstances still represent useable skill.

a) V0 ASM U

b) V0 FREE U

c) V1 ASM U

d) V1 ASM U - IND REG

e) V1 HRS ASM U - IND REG

Fig 5: Taylor diagrams for zonal (u) current component for a) the V0 global assimilative model (V0 ASM), b) the V0 global non-assimilative model (V0 FREE) and c) the V1 global assimilative model (V1 ASM). The equivalent diagrams for the Indian Ocean region only are also presented for d) the V1 global assimilative run (V1 ASM – IND REG) and e) the V1 high resolution Indian Ocean assimilative model (HRS ASM – IND REG). '*'s represent the overall values for the full datasets for the relevant region

a) V0 ASM V

b) V0 FREE V

c) V1 ASM V

d) V1 ASM V - IND REG

e) V1 HRS ASM V - IND REG
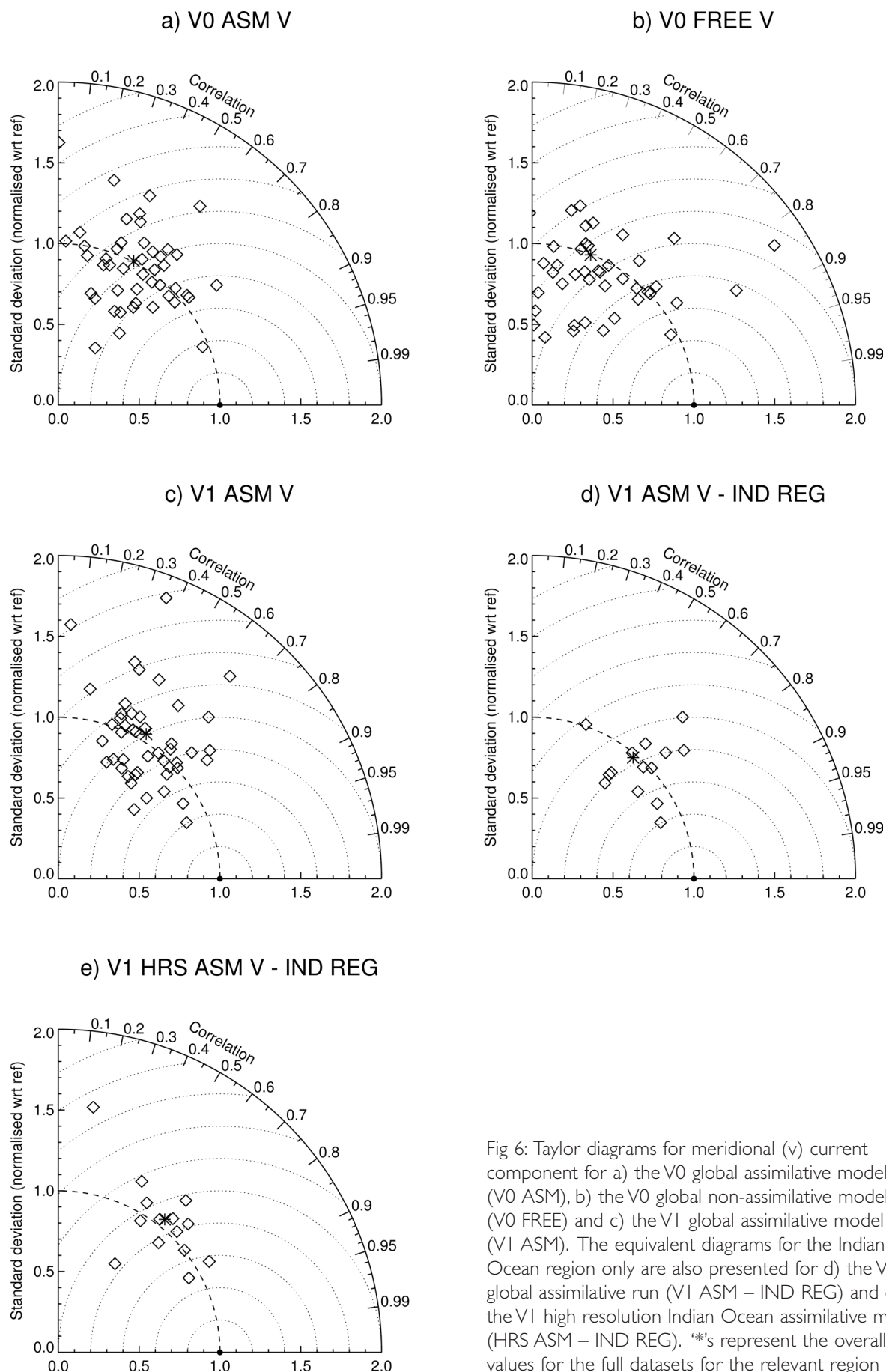
Fig 6: Taylor diagrams for meridional (v) current component for a) the V0 global assimilative model (V0 ASM), b) the V0 global non-assimilative model (V0 FREE) and c) the V1 global assimilative model (V1 ASM). The equivalent diagrams for the Indian Ocean region only are also presented for d) the V1 global assimilative run (V1 ASM – IND REG) and e) the V1 high resolution Indian Ocean assimilative model (HRS ASM – IND REG). '*'s represent the overall values for the full datasets for the relevant region

Inter-comparing skill across the models and regions

Taylor diagrams for all model runs are included in Figs 5 and 6. Overall values for the metrics across all sites (weighted by number of observations at each site) are labelled with stars and are also presented in Table 2.

For zonal current (Fig 5) for the V0 hindcasts there is a notable improvement in skill for the assimilative run (V0 ASM), compared to the non-assimilative run (V0 FREE). In particular, there are considerably fewer locations where correlation falls below the 0.6 'average' or 'usable' skill threshold for the assimilative run than for the non-assimilative run. For meridional current (Fig 6), as expected, skill is generally considerably lower than for zonal. Again there are fewer sites with very low correlation for the assimilative hindcast than the non-assimilative hindcast but the assimilation does not appear to improve skill sufficiently to move these locations into the region above the 0.6 correlation or 'useable' band (although it should again be noted that the threshold for this band is somewhat arbitrary).

The same data is presented in the regional skill diagrams for zonal current in Fig 7 and for meridional current in Fig 8, together with overall regional skills which are included in Table 3. It can be clearly seen that for both current components skill is best in the Indian Ocean, then medium in the Pacific Ocean and worst in the Atlantic. This is confirmed statistically for the global V0 and V1 runs in Table 3.

Tables 2 and 3 also indicate that there is a minor improvement in skill for the V1 run compared to the V0 run. Unfortunately, in combination with regional skill diagrams (Fig 9) they also demonstrate that that skill scores are no higher in the 1/12° high resolution Indian Ocean model compared to the 1/4° global model, for either V0 or V1 runs.

Skill, ie, correlation, was also plotted against a range of parameters to try to determine potential causes of increased skill (not shown as a figure). The relationship between longitude and skill score confirmed the aforementioned regional skill variations between ocean basins. However, there is no clear relationship between skill and latitude. There is, though, a clear relationship between correlation and the observational standard deviation for both u and v component currents. This indicates that skill is generally highest when variability in the currents is strongest. In particular, skill for both u and v is consistently above the 0.6 'useable' correlation threshold for all sites where observational standard deviation was more than 0.3m/s (note that correlation is also above this threshold for some sites where the observational standard deviation is lower but not for all sites). Further investigation is required to understand this relationship, whether it might also be related to the aforementioned variations in skill between ocean basins, and its potential value to model users.

Westward equatorial current bias

A westward (ie, too strong) equatorial current bias of around 20cm/s is evident in this comparison with the global tropical moored buoy data (Figs 7, 8 and 9). This bias is evident in the assimilative and non-assimilative runs; in all ocean basins; and in the global and high resolution nested Indian Ocean model. In a comparison of simulated surface currents with drifter derived flows (not shown) this westward bias is also clearly evident and extends from around 2°N to 2°S. Initial

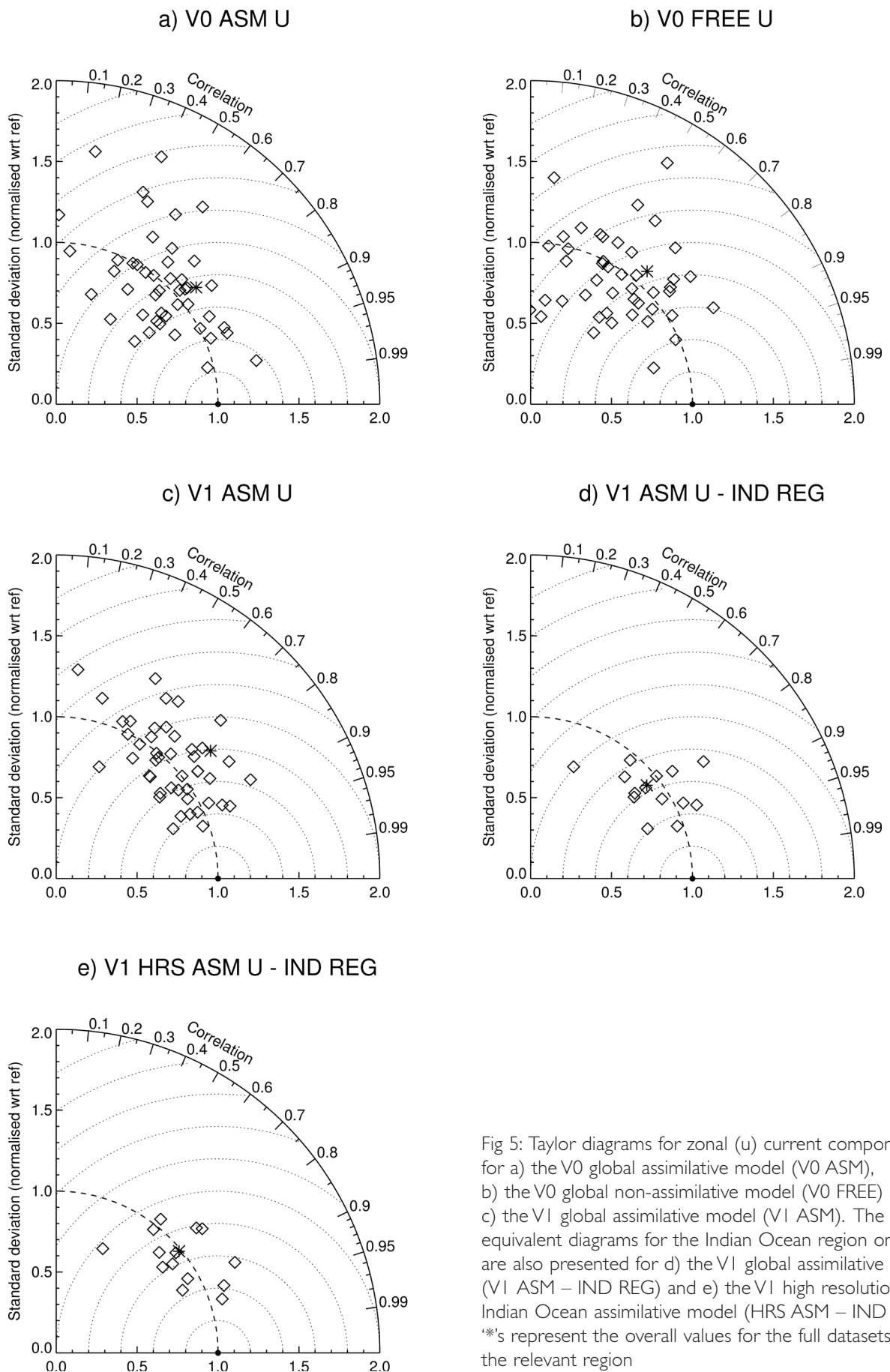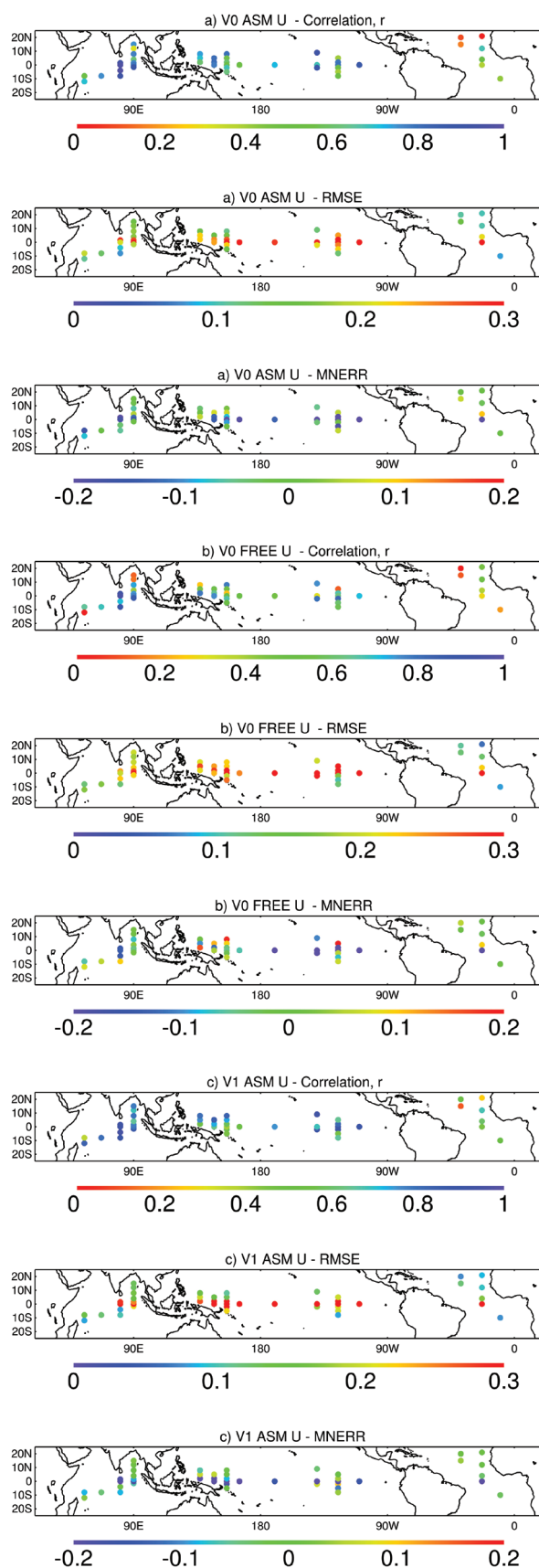Fig 7: Regional skill diagrams presenting correlation, RMS error and mean error for zonal (u) current for a) the V0 global assimilative model (V0 ASM), b) the V0 global non-assimilative model (V0 FREE) and c) the V1 global assimilative model (V1 ASM)
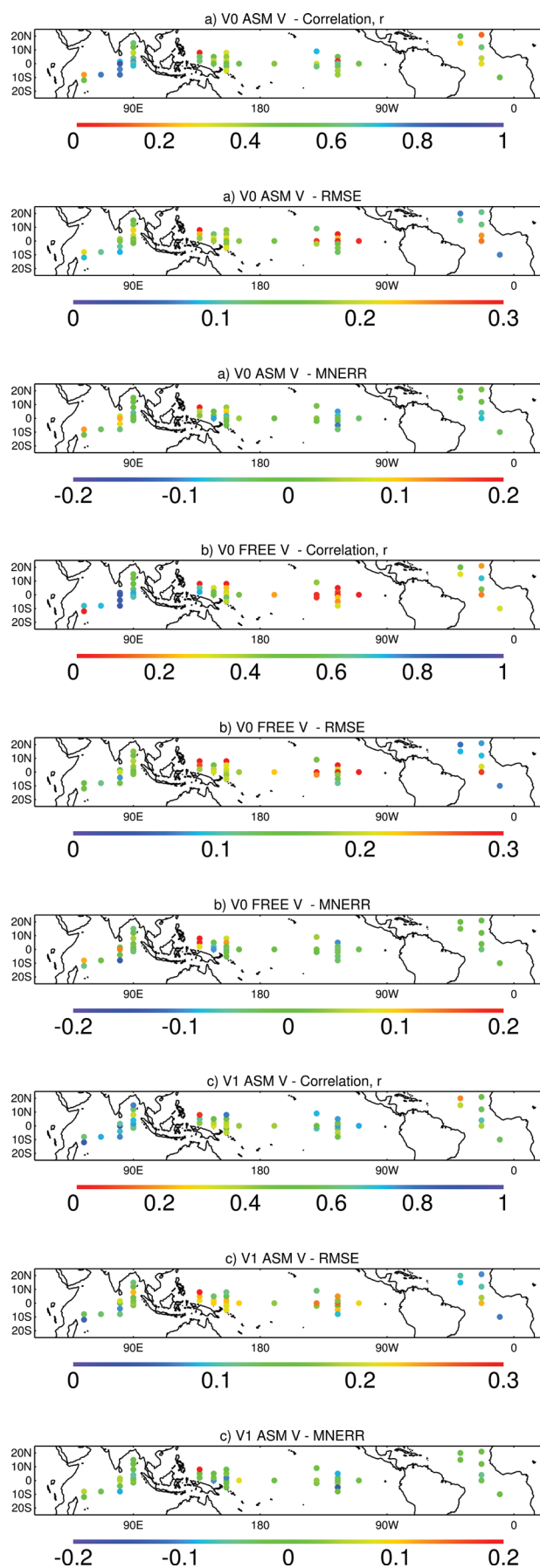
Fig 8: Regional skill diagrams presenting correlation, RMS error and mean error for meridional (v) current for a) the V0 global assimilative model (V0 ASM), b) the V0 global non-assimilative model (V0 FREE) and c) the V1 global assimilative model (V1 ASM)

findings of comparisons with sub-surface current meters at 110, 140 and 170°W suggests the westward bias extends down to around 200m depth, although the vertical structure of the bias varies between the non-assimilative and assimilative run and also between longitudes.

DISCUSSION

The results demonstrate that the FOAM global assimilative model skill scores, including correlation, are reasonable for zonal current but lower for meridional. There are two possible causes for this apparent difference in skill. Firstly observational studies expect zonal flows to be better constrained than meridional flows due to the angle of the altimeter tracks, which is much closer to north-south than east-west near the equator (ie, the north-south sea surface slopes which influence zonal flows are better resolved than east-west slopes). Secondly, the meridional flows tend to be dominated by short period mesoscale variability whilst the zonal flows tend to be dominated by seasonal to inter-annual variations in the major equatorial currents. In the Eastern Atlantic and Pacific, in particular, equatorial meridional flow variability would be expected to be dominated by tropical instability waves whose period is generally around 20 to 30 days.

It cannot be expected to constrain these waves with the altimeter observations since the Niquist or shortest detectable period of the JASON altimeter is 20 days and the corresponding Niquist periods for GFO and ENVISAT are 35 day and 70 days, respectively. Although sea surface temperature is assimilated daily at much higher spatial resolution than the altimeter, these data are only assimilated into the ocean mixed layer and therefore also cannot be expected to properly constrain the dynamics of the tropical instability waves. It is therefore not surprising that current variations, which are expected to be dominated by tropical instability waves, do not appear to be well represented. These limitations to the observational constraint on the ocean mesoscale, including tropical instability waves, provide possible explanations for the poor meridional surface current skill scores evident both in this study and in similar evaluations of observational surface current products.[7]

The data assimilation consistently improves skill compared to the non-assimilative model, although currents are not directly assimilated. This is encouraging and suggests that observations (including temperature and salinity profiles and altimeter) are helping to constrain flows, at least for large scales and long period variability. There is also a slight improvement in skill score for the upgraded V1 model, compared to the V0 model configuration. Skill for both the V0 and V1 models appears to be highest in the Indian Ocean, then medium in the Pacific and lowest in the Atlantic. It should be noted, however, that this may well be related to the dominant variability in the different oceans (eg, the Indian Ocean variability in surface currents is dominated by seasonal monsoonal reversals).

There is a ~20cm/s too strong westward surface current bias on the equator (within ±~2°) for all of the assimilative and non-assimilative hindcasts. In 2007–2008 the short-range Numerical Weather Prediction wind speed was about 10% too weak (ie, not westward enough) compared to tropical moored buoy observations.[27] The Eastern Pacific thermocline is also
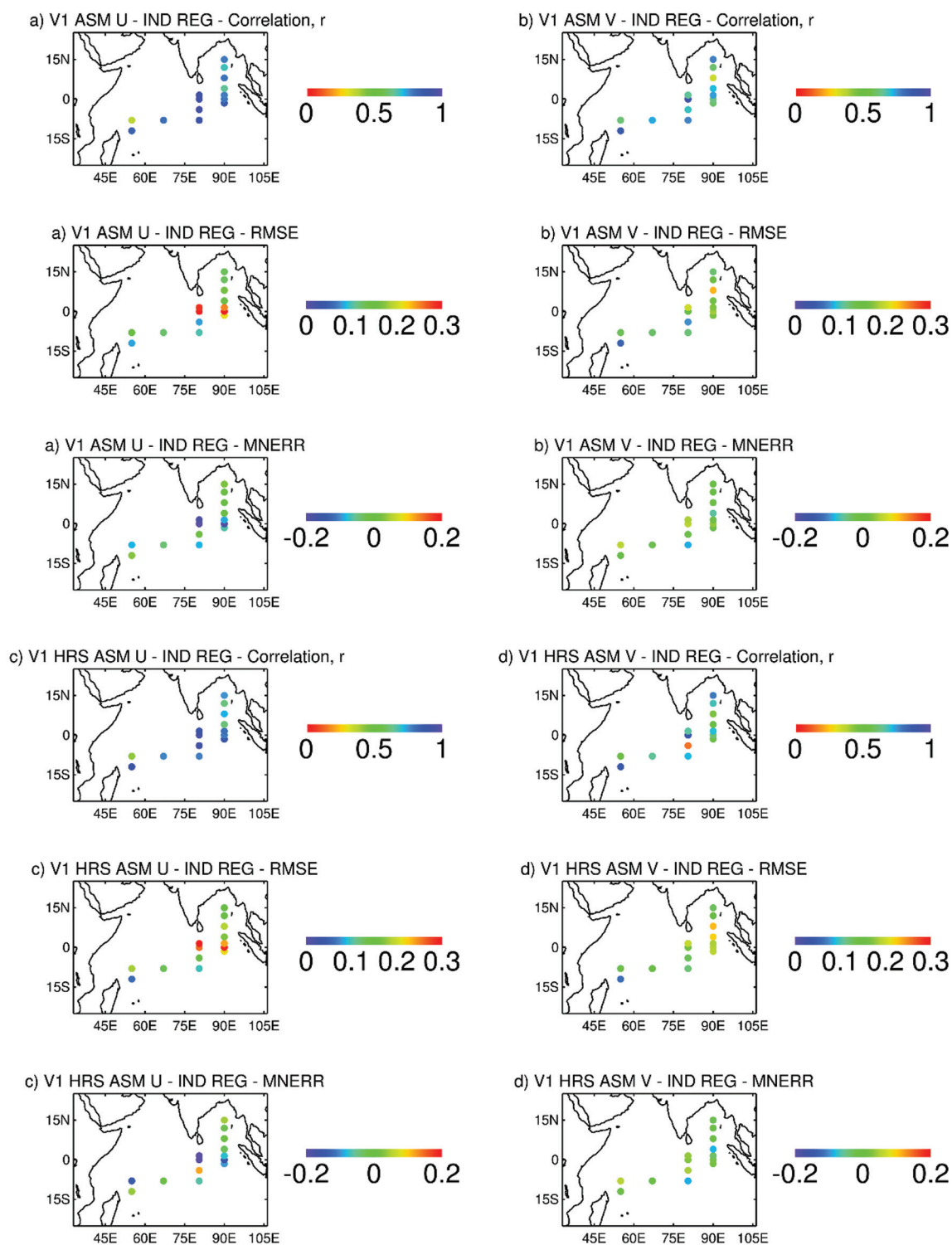
Fig 9: Regional skill diagrams for zonal (u) and meridional (v) current component in the Indian Ocean region for (a & b) the V1 global assimilative model (V1 ASM) and (c & d) the V1 high resolution Indian Ocean assimilative model (V1 HRS ASM)

too deep (ie, the east-west thermocline slope is less than observed) in the non-assimilative V0 run compared to the assimilative V0 run (not shown), which is also consistent with a too weak westward equatorial wind stress. The westward surface current error is evident in the assimilative run which assimilates a high volume of temperature and salinity profiles from the moored buoy array and therefore might be expected to have a reasonably accurate representation of the near equatorial density structure (and associated density driven flows).

It is also evident in the non-assimilative run, so it also cannot be solely related to the assimilation process, and, in particular, the pressure correction scheme applied near the equator.

It is possible that the error is related to the magnitude and vertical structure of the locally wind-forced Ekman transport currents. An eastward wind error would therefore not be expected to be the direct cause of the westward surface current bias. The vertical structure of the Ekman currents is controlled both by wind stress and by vertical mixing

of momentum. In short runs of the non-assimilative global model (not shown), applying wind versus current stress, ie, relative stress rather than the absolute stress which was prescribed for the runs presented herein, reduces the westward surface current which would be expected to reduce the surface current bias. However, it remains uncertain whether using relative stresses improves the surface currents for the correct reasons (and how this change might impact on the representation of the east-west Pacific thermocline slope variations). Further analysis of simulated currents with Acoustic Doppler Current Profiler current (and temperature and salinity) profiles, co-located in time, is therefore required to better understand the cause of this westward surface current error.

Even in the updated V1 FOAM model runs skill scores are still not improved in the high resolution 1/12° regional Indian Ocean model, compared to those for the 1/4° global model. This is disappointing, given that:

- high resolution models have been found to provide better estimates, ie, reduced underestimation, of eddy kinetic energy, compared to altimeter observations, and the V1 high resolution Indian Ocean model has more eddy kinetic energy than the V1 Global model;
- the V1 Indian Ocean model has lower RMS errors (0.048m) against the altimeter observations than the global model (0.054m) (for V0 their RMS errors were identical)[15];
- qualitative comparisons with animated drifter tracks overlaid on simulated sea surface height appear to suggest there may be some improved skill in the currents from the high resolution model.

On further consideration, however, there are several reasons why this apparent lack of additional skill for the high resolution model might be expected. Errors in assimilative models at any location depend on both the *initialisation errors* and the *total error growths*.

$$error = initialisation\ errors + total\ error\ growths$$

The *total error growth* at any location or grid point depends in a rather complex manner on the integrated *error growth rates* along multiple wave or fluid paths moving back in time to the time at which they were initialised with observations (ie, the *time since initialisation*). The *error growth rates* themselves depend on *initialisation errors* both locally and at locations upstream of the location considered. However, they also depend both on model errors/biases and how chaotic or unstable the flow is, which would be expected to depend on the baroclinic instability (Eady growth rate), barotropic instability, topographic instabilities, etc. Higher frequency and short period flows might be expected to be more chaotic and unstable, and therefore, to have faster error growth rates.

$$total\ error\ growths = function\ (time\ since\ initialisation,\\ error\ growth\ rate)$$

$$error\ growth\ rate = function\ (initialisation\ errors,\\ model\ biases,\ flow\ instability)$$

For a single wave type, the *time since initialisation* could, to a first order, be considered to be the time since a particular feature was last over an observational track, which in turn depends on the speed at which features propagate over the tracks, eg, the Rossby or tropical instability wave speed. An order of magnitude estimate for the maximum *time since initialisation*, assuming a typical distance between tracks of ~100km and a Rossby wave speed of ~10cm/s, would be up to around 10 days.

In practice, *total error growths and error growth rates* for each model (including model error) could be estimated from time-varying differences for a series of paired model experiments, where a small perturbation (at a different location for each pair of experiments) is applied to one model but not the other. Adjoint techniques are also employed in the meteorological community to estimate model sensitivity to perturbations at different locations although it should be noted that these estimates depend on assumptions of linearity in the adjoint model.

Considering next the *initialisation errors*, it has been stated[11] that for merged altimeter datasets 'for Gaussian shaped eddies, this wavelength resolution corresponds to being able to detect mesoscale features with e-folding scales of about 0.4°'. This represents a fundamental resolution limit for initialisation of observational products. Dynamic assimilative models, however, have the advantage that they should be able to propagate information away from the observational tracks to build up a picture over time, albeit with the aforementioned error growths and observational Niquist period limitations. However, even the along track data is only able to detect mesoscale features of e-folding scales of around 0.2°.[12] There are also additional contributions to *intialisation errors* through limitations of the accuracy of the data assimilation (including the impact of model errors) and its configuration. In particular, the error covariance scale used in the data assimilation is also 40km or ~0.4°. This means that at each observational location information is spread over a region, ie, away from the altimeter tracks, of e-folding radius ~0.4°. For sparse observations, this would also be expected to limit the minimum scales which might be expected to be accurately initialised.

In view of the above-mentioned limitations, one might expect large *initialisation errors*, faster *error growth rates* and, in consequence, a poor constraint on the shorter scale variability, ie, scales less than ~0.4° (a coarser scale than either the global or Indian Ocean model resolutions of 0.25° and 0.08°, respectively). It should also be noted that the minimum Niquist period of ~20 days (for JASON observations) means that higher frequency variability than ~20 days will not be adequately initialised in either model. One could, however, expect the high resolution model to more accurately represent the scales greater than 0.4° (and periods longer than 20 days) because of the expected improved model dynamics, including eddies (and associated eddy statistics) and mesoscale. This would be expected to result in improved propagation of observational information away from altimeter tracks, ie, slower error growth rates at these larger spatial scales. For example, in a high resolution model improved topographic and coastal constraints might be expected (with the caveat of sparse observation coverage in coastal regions, either for data assimilation or for evaluation); improved equatorial and boundary current width, location and strength; and improved mesoscale and eddy dynamics, statistics and feedbacks on mean flows.

Since the assimilative model performs consistently better than the non-assimilative model, clearly the observations are providing a useful constraint, at least for large scale, low frequency variability. The question remains, however, as to why improved skill scores for the high resolution Indian Ocean model are not being seen. An alternative potential reason for the similar skill scores is that in the statistical analysis the high resolution model is being penalised by its higher resolution of short-scale variability, which would not be expected to be well constrained. Filtering the high resolution model onto the same resolution as the global model prior to the comparison with observations might therefore provide a fairer comparison.

It should also be noted that no tuning of the high resolution model has been undertaken to date. In particular, the error covariances used in data assimilation of the high resolution model are those derived from the low resolution global model output. These error covariances are not expected to be optimal for use in the high resolution Indian Ocean model and could therefore be limiting the benefits of the high resolution model. Recalculating error covariances using data from the high resolution Indian Ocean model and tuning model parameters might help to improve the performance of the high resolution model. Hence, although it remains disappointing that additional skill at high resolution has not been demonstrated, it is hopeful that with further tuning, appropriate filtering and use of an appropriate skill measure it will become possible to demonstrate extra skill at high resolution.

CONCLUSIONS

This short note presents a simple statistical assessment of surface currents simulated by the Met Office FOAM models. The initial aims have largely been met, which were to quantify skill in simulating surface currents in the tropics; to assess whether skill for an independent variable is improved by data assimilation, model resolution and model upgrades; and to compare several skill scores. If adopted as a standard, the approach discussed in this paper could represent a good method to inter-compare skill across different modelling systems, for a truly independent variable.

Improved skill in analysed ocean surface currents has been demonstrated through the employment of data assimilation. Useful skill has also been demonstrated for the zonal surface currents at many locations. However, skill appears to be more limited for the meridional component which is dominated by high frequency variability, including tropical instability waves at many locations. This appears to be, at least in part, related to limitations associated with the altimeter observational constraint, including its repeat cycles and associated Niquist periods. The absence of improved skill scores for the nested high resolution Indian Ocean model compared to the Global model is disappointing and probably also, at least in part, related to the limited altimeter observational constraint.

Further investigation is required and planned to filter the high resolution output onto a lower resolution grid prior to comparison with observations; to optimise the error covariances and model configuration for the high resolution model; to investigate the regional differences in skill scores in different ocean basins; and to better understand large scale model temperature and salinity biases. Work is also planned to use these statistics, against the Global Tropical Moored Buoy observations, to benchmark an evaluation over an equivalent region using drifter observations, which could then be extended to a full global analysis. Drawing on experience from the meteorological community, the authors are also planning to trial a range of statistical approaches for evaluating ocean currents against mooring observations, including comparisons with adjacent model grid points (within a search radius).

This initial study focuses on evaluating analysed surface currents. Clearly, forecast currents would become progressively more challenging to accurately simulate at increasing lead times, due to the increasing timescales for model errors to grow. Surface currents would also be expected to be better represented than deeper currents, whose representation relies on the propagation of observed sea surface height information through the water column and the associated assumptions and errors in the simulated density structure. Comparisons with Global Tropical Moored Buoy Acoustic Doppler Current Profiler observations of vertical current structure would therefore be valuable. This analysis might also provide more information on the potential cause of the westward current bias, eg, wind or mixing errors, etc.

To better inform engineering users of assimilative model products, increased effort would be valuable (drawing on considerable experience in the meteorological community) to better understand site-specific model performance, particularly representation of the mesoscale. Improved understanding of the dynamics of tropical current variability might also help modellers to relate errors to deficiencies in process representation. The SWOT wide swath altimeter, planned for 2014–16, with ~10km resolution, could significant improve the observational constraint for mesoscale and sub-mesoscale ocean variability. This instrument might therefore be expected to result in significant improvements in observing and forecasting ocean currents, which would be particularly valuable for engineering users.

ACKNOWLEDGEMENTS

REFERENCES

1. Bell MJ, Lefèbvre M, Le Traon PY, Smith N and Wilmer-Becker K. 2009. *GODAE: The Global Ocean Data Assimilation Experiment*. Oceanography, 22(3), 14–21.

2. Hurlburt HE, Brassington GB, Drillet Y, Kamachi M, Benkiran M, Bourdallé-Badie R, Chassignet EP, Jacobs GA, Le Galloudec O, Lellouche JM, Metzger EJ, Oke PR, Pugh TF, Schiller A, Smedstad OM, Tranchant B, Tsujino H, Usui N and Wallcraft AJ. 2009. *High-resolution global and basin-scale ocean analyses and forecasts*. Oceanography, 22(3), 110–127.

3. Metzger EJ, Hurlburt HE, Xu X, Shrivera JF, Gordon AL, Sprintall J, Susanto RD and van Aken HM. 2010. *Simulated and observed circulation in the Indonesian Seas: 1/12° global HYCOM and the INSTANT observations*. Dynamics of Atmospheres and Oceans, 50, 275–300.

4. Giraud St Albin S, Crosnier L and Stephens R. 2005. *Evaluation du nouveau système du assimilation multi-varié multidonnées Mercator-Océan pour la prévision du Loop Current et des positions des tourbillons frontaux dans le Golfe du Mexique*. La lettre trimestrielle Mercator Océan, 19 October 2005, 22–43.

5. Bonjean F and Lagerloef GSE. 2002. *Diagnostic model and analysis of the surface currents in the tropical Pacific Ocean*. Journal of Physical Oceanography, 32, 2938–2954.

6. Johnson ES, Bonjean F, Lagerloef GSE, Gunn JT and Mitchum GT. 2007. *Validation and error analysis of OSCAR sea surface currents*. Journal of Atmosphere and Ocean Technology, 24, 688–701.

7. Sudre J and Morrow RA. 2008. *Global surface currents: a high-resolution product for investigating ocean dynamics*. Ocean Dynamics, 58, 101–118, DOI 10.1007/s10236-008-0134-9.

8. Dohan K and Maximenko N. 2010. *Monitoring ocean currents with satellite sensors*. Oceanography, 23(4), 94–103.

9. Jeans DG and Lefevre F. 2008. *Evolving synergies in applied ocean current merasurement*. Journal of Operational Oceanography, 1, 45–49.

10. Gilleland E, Ahijevych D, Brown BG, Casiti B and Ebert EE. 2009. *Intercomparison of spatial forecast verification methods*. Weather and forecasting, 24, 1416–1430.

11. Fu LL, Chelton DB, Le Traon PY and Morrow R. 2010. *Eddy dynamics from satellite altimetry*. Oceanography, 23(4), 14–25.

12. Chelton DB, Schlax MG and Samelson RM. 2011. *Global observations of nonlinear mesoscale eddies*. Progress in Oceanography, 91, 167–216, doi:10.1016/j.pocean.2011.01.002.

13. Lagerloef GSE, Mitchum GT, Lukas RB and Niiler PP. 1999. *Tropical Pacific near-surface currents estimated from altimeter, wind and drifter data*. Journal of Geophysical Research, 104, 22313–22326.

14. Saji NH, Goswami BN, Vinayachandran PN and Yamagata T. 1999. *A dipole mode in the tropical Indian Ocean*. Nature, 401, 360–363.

15. Storkey D, Blockley EW, Furner R, Guiavarc'h, C, Lea D, Martin MJ, Barciela, RM, Hines A, Hyder P and Siddorn JR. 2010. *Forecasting the ocean state using NEMO: The new FOAM system*. Journal of Operational Oceanography, 3(1), 3–15.

16. Bell MJ, Forbes RM and Hines A. 2000. *Assessment of the FOAM global data assimilation system for real-time operational ocean forecasting*. Journal of Marine Systems, 25, 1–22.

17. Martin MJ, Hines A and Bell MJ. 2007. *Data Assimilation in the FOAM operational short-range ocean forecasting system: a description of the scheme and its impact*. Quarterly Journal of the Royal Meteorological Society, 133, 981–995.

18. Bell MJ, Martin MJ and Nichols NK. 2004. *Assimilation of data into an ocean model with systematic errors near the equator*. Quarterly Journal of the Royal Meteorological Society, 130, 873–893.

19. Rio MH, Schaeffer P, Hernandez F and Lemoine JM. 2005. *The estimation of the ocean mean dynamic topography through the combination of altimetric data, in-situ measurements and GRACE geoid: From global to regional studies*. Proceedings of the GOCINA international workshop, Luxembourg

20. Burchard H. 2002. *Energy-conserving discretisation of turbulent shear and buoyancy production*. Ocean Modelling, 4, 347–361.

21. Stark JD, Donlon CJ, Martin MJ and McCulloch ME. 2007. *OSTIA: An operational, high resolution, real time, global sea surface temperature analysis system*. Oceans '07 IEEE Aberdeen, conference proceedings, Marine challenges: coastline to deep sea, Aberdeen, Scotland.

22. Donlon CJ, Martin M, Stark JD, Roberts-Jones J, Fiedler E and Wimmer W. 2011. The Operational Sea Surface Temperature and Sea Ice Analysis (OSTIA) system, remote sensing of environment. Available online 27 August 2011, ISSN 0034-4257, 10.1016/j.rse.2010.10.017.

23. Taylor KE. 2001. *Summarizing multiple aspects of model performance in a single diagram*. Journal of Geophysical Research, 106, 7183–7192.

24. Allen JI, Holt JT, Blackford J and Proctor R. 2007. *Error quantification of a high-resolution coupled hydrodynamic-ecosystem coastal-ocean model: Part 2. Chlorophyll-a, nutrients and SPM*. Journal of Marine Systems, 68, 381–404.

25. Holt JT, Allen JI, Proctor R and Gilbert F. 2005. *Error quantification of a high-resolution coupled hydrodynamic – ecosystem coastal – ocean model: Part 1 model overview and assessment of the hydrodynamics*. Journal of Marine Systems, 57, 167–188.

26. Wang C. 2005. *Subthermocline tropical cells and equatorial subsurface countercurrents*. Deep-Sea Research I, 52, 123–135.

27. Ingleby B. 2010. *Factors affecting ship and buoy data quality: A data assimilation perspective*. Journal of Atmospheric and Oceanic Technology, 27, 1476–1489.

GO5.0: the joint NERC–Met Office NEMO global ocean model for use in coupled and forced applications

A. Megann[1], **D. Storkey**[2], **Y. Aksenov**[1], **S. Alderson**[1], **D. Calvert**[2], **T. Graham**[2], **P. Hyder**[2], **J. Siddorn**[2], and **B. Sinha**[1]

[1]Marine Systems Modelling, National Oceanography Centre, Southampton, SO14 3ZH, UK
[2]Met Office, Hadley Centre, Exeter, Devon, EX1 3PB, UK

Correspondence to: A. Megann (apm@noc.ac.uk)

Abstract. We describe a new Global Ocean standard configuration (GO5.0) at eddy-permitting resolution, developed jointly between the National Oceanography Centre and the Met Office as part of the Joint Ocean Modelling Programme (JOMP), a working group of the UK's National Centre for Ocean Forecasting (NCOF) and part of the Joint Weather and Climate Research Programme (JWCRP). The configuration has been developed with the seamless approach to modelling in mind for ocean modelling across timescales and for a range of applications, from short-range ocean forecasting through seasonal forecasting to climate predictions as well as research use. The configuration has been coupled with sea ice (GSI5.0), atmosphere (GA5.0), and land-surface (GL5.0) configurations to form a standard coupled global model (GC1). The GO5.0 model will become the basis for the ocean model component of the Forecasting Ocean Assimilation Model, which provides forced short-range forecasting services. The GC1 or future releases of it will be used in coupled short-range ocean forecasting, seasonal forecasting, decadal prediction and for climate prediction as part of the UK Earth System Model.

A 30-year integration of GO5.0, run with CORE2 (Common Ocean-ice Reference Experiments) surface forcing from 1976 to 2005, is described, and the performance of the model in the final 10 years of the integration is evaluated against observations and against a comparable integration of an existing standard configuration, GO1. An additional set of 10-year sensitivity studies, carried out to attribute changes in the model performance to individual changes in the model physics, is also analysed. GO5.0 is found to have substantially reduced subsurface drift above the depth of the thermocline relative to GO1, and also shows a significant improvement in the representation of the annual cycle of surface temperature and mixed layer depth.

1 Introduction

Coupled climate models developed at the UK Met Office have been at the forefront of international climate research and projections for the past 15 years. HadCM3 (Hadley Centre Coupled Model version 3; Gordon et al., 2000) was used in the Third and Fourth Assessment Reports (Houghton et al., 2001; Solomon et al., 2007) and is still widely used as a standard tool in climate research, while HadGEM1 (Hadley Centre Global Environmental Model version 1) (Johns et al., 2006), HadGEM2 (Collins et al., 2008) and HadGEM3 (Hewitt et al., 2011) have offered improvements in resolution, numerics and physics. All these models have an ocean on a horizontal grid of around 1°, although the HadGEM models have a refinement of the north–south grid scale close to the Equator down to 1/3°. In this paper we will refer to the model described by Hewitt et al. (2011) as HadGEM3, however newer versions currently in development, with a higher-resolution ocean, are also commonly referred to as HadGEM3.

Global ocean models are also used at the Met Office as part of seasonal and decadal forecasting systems (Arribas et al., 2011; Smith et al., 2007) and for ocean analysis and short-range forecasting (Storkey et al., 2010). At the Met Office and elsewhere there is increasing interest in using a seamless modelling system for use at all timescales from short range forecasting to climate prediction (Brown et al., 2012).

Increased horizontal resolution in the ocean has been shown to have several benefits for modelling climate. In the North Atlantic the improved path of the Gulf Stream and North Atlantic Current (NAC) reduces the magnitude of a large cold bias off Grand Banks seen in many low-resolution climate models (e.g. Gnanadesikan et al., 2007; Danabasoglu et al., 2010). Reducing this bias has been shown

to improve the frequency of blocking in a climate model (Scaife et al., 2011). In the tropical Pacific Ocean, eddy permitting resolution in HiGEM (High-resolution Global Environment Model) has been shown to help reduce the equatorial cold tongue bias (Shaffrey et al., 2009; Roberts et al., 2009) and the double intertropical convergence zone (ITCZ) bias, and also to more realistically simulate the westward extent of El Niño. Furthermore, teleconnections to the North Pacific Ocean associated with ENSO were also improved as a result of increased ocean resolution (Dawson et al., 2012). Eddy permitting models have an order of magnitude more eddy kinetic energy (EKE) than low-resolution models (Delworth, 2012) and the $1/4°$ ORCA025 configuration has been shown to simulate 81 % of observed sea level variability on interannual timescales (Penduff et al., 2010).

Ocean models run on horizontal grids fine enough to resolve eddies in the Southern Ocean show "eddy saturation", where increased vertical transport of momentum and meridional transport of heat away from the Antarctic Circumpolar Current (ACC) by the eddy field in response to increases in wind stress means that the isopycnal slopes and therefore the circumpolar transport is relatively insensitive to changes in the wind forcing (Tansley and Marshall, 2001; Hallberg and Gnanadesikan, 2006; Munday et al., 2013). This is not observed in lower-resolution models where the eddy transports are parameterised by diffusive schemes. A similar insensitivity of the global overturning circulation to the Southern Ocean wind forcing ("eddy compensation") is also seen in eddy-resolving models (Viebahn and Eden, 2010; Farneti et al., 2010) although some studies have suggested that eddy compensation can be achieved in lower-resolution models using a variable Gent–McWilliams coefficient and modified tapering scheme at the base of the mixed layer (Gent and Danabasoglu, 2011; Farneti and Gent, 2011).

Here we describe a new Global Ocean standard configuration (GO5.0) at eddy-permitting resolution, developed jointly between the National Oceanography Centre and the Met Office as part of the Joint Ocean Modelling Programme (JOMP), a working group of the UK's National Centre for Ocean Forecasting (NCOF) and part of the Joint Weather and Climate Research Programme (JWCRP). The configuration has been developed with the seamless approach to modelling in mind and is therefore intended to be used as the basis for ocean modelling across timescales and for a range of applications, from short-range ocean forecasting, through seasonal forecasting, to climate predictions as well as research use. The configuration has been developed for use throughout the UK academic and operational modelling communities. It has been coupled with the sea ice (GSI5.0), the atmosphere (GA5.0) and the land-surface (GL5.0) configurations to form a standard coupled global model (GC1). Additionally we take this opportunity to improve upon known deficiencies in the vertical mixing scheme and to take advantage of recent releases of NEMO and improvements in bathymetry data sets. The GO5.0 model will become the

basis for the ocean model component of the Forecasting Ocean Assimilation Model (FOAM, Storkey et al., 2010), which presently provides forced short-range forecasting services to MyOcean (www.myocean.eu) and other users. The global coupled model will be used in coupled short-range ocean forecasting (as future versions of FOAM evolve into coupled systems), for seasonal forecasting as part of the GloSea4 (Global Seasonal forecasting system version 4) system (Arribas et al., 2011), for decadal prediction as part of the DePreSys (Decadal climate Prediction System; Smith et al., 2007) and for climate prediction as part of the UK Earth System Model (UKESM). The latter will be the UK's contribution to the upcoming IPCC (Intergovernmental Panel on Climate Change) Sixth Assessment Report and to the Coupled Model Intercomparison Project phase 6 (CMIP6).

We use the term "standard configuration" to denote all the items required to run the model, i.e. model code, input parameters and data sets, and compilation keys, and these are summarised in the Appendices A–E.

The main aim of this paper is to introduce the ocean model constituting GO5.0, and to evaluate its performance in ocean-only configuration, according to a set of first-order metrics. We will also compare the performance of GO5.0 with the previous global ocean configuration, which we denote GO1, and attribute the salient differences between the two model implementations to specific changes in model physics and parameter sets. Documentation of the attribution of changes in model behaviour to specific choices in a configuration will allow model developers using this or other models to make informed decisions and interpret model simulations with more clarity. Section 2 describes the ocean and ice models and the surface forcing fields. Section 3 summarises the main physics choices, and in Sect. 4 the experimental design is described. In Sect. 5 we present the results of the analysis: firstly the GO5.0 configuration is validated against observations; then GO5.0 is compared with the previous global model GO1; and the main improvements identified in GO5.0 are attributed to specific physics choices. Finally in Sect. 6 we summarise the results and discuss upgrades to the model currently under development.

2　Model description

GO5.0 is based on version 3.4 (v3.4) of NEMO (Nucleus for European Models of the Ocean) (Madec, 2008), and is closely related to the global DRAKKAR ORCA025 configuration (Barnier et al., 2006) sharing many of the same dynamics and physics choices. The horizontal grid, known as ORCA025, has $1/4°$ resolution (1442 grid points $\times$ 1021 grid points) at global scale decreasing poleward (an isotropic Mercator grid in the Southern Hemisphere, matched to a quasi-isotropic bipolar grid in the Northern Hemisphere with poles at $107°$ W and $73°$ E). The effective resolution is approximately 27.75 km at the Equator, but increases with latitude to be, for example, 13.8 km at $60°$ S or $60°$ N. The model

has 75 vertical levels where the level thickness is a double tanh function of depth such that the level spacing increases from 1 m near the surface to 200 m at 6000 m (I. Culverwell, personal communication, 2009). This level set was chosen to provide high resolution near the surface for short to mid-range forecasting purposes while retaining reasonable resolution at mid-depths for long-term climate studies.

The model's bathymetry (DRAKKAR v3.3) is based on the ETOPO1 data set (Amante and Eakins, 2009) with additional data in coastal regions from GEBCO (General Bathymetric Chart of the Oceans; IOC, 2003). This is a change from the GO1 configuration, which used the DRAKKAR G70 bathymetry based on the lower-resolution ETOPO2 with corrections from satellite-based bathymetry and other sources (Remy et al., 2003). Bottom topography is represented as partial steps (Barnier et al., 2006). The derivation of DRAKKAR bathymetry data sets is described by Barnier et al. (2006). Initially, each model grid cell is assigned the median of all observations falling within the boundaries of that grid cell. The initial estimate is then modified by application of two passes of a uniform Shapiro filter and, finally, hand editing is performed in a few key areas.

The model uses a linear free surface and an energy and enstrophy conserving momentum advection scheme. The horizontal viscosity is bi-Laplacian with a value of 1.5×10^{11} m^4 s^{-1} at the Equator, reducing polewards as the cube of the maximum grid cell dimension: thus at 60° N the horizontal viscosity is approximately one-eighth of its value at the Equator. Tracer advection uses a total variance dissipation (TVD) scheme (Zalesak, 1979). Lateral tracer mixing is along isoneutral surfaces with a coefficient of 300 m^2 s^{-1}. The isopycnal mixing scheme of Gent and McWilliams (1990) is not used in this configuration.

With regard to diapycnal mixing processes, the vertical mixing of tracers and momentum is parameterised using a modified version of the Gaspar et al. (1990) turbulent kinetic energy (TKE) scheme (described in Madec, 2008). Unresolved vertical mixing processes are represented by a background vertical eddy diffusivity of 1.2×10^{-5} m^2 s^{-1}, which decreases linearly from ±15° latitude to a value of 1.2×10^{-6} m^2 s^{-1} at ±5° latitude (Gregg et al., 2003) and a globally constant background viscosity of 1.2×10^{-4} m^2 s^{-1}. A parameterization of double diffusive mixing (Merryfield et al., 1999) is included at GO5.0.

Bottom friction is quadratic with an increased coefficient in the Indonesian Throughflow, Denmark Strait and Bab al Mandab regions. An advective and diffusive bottom boundary layer scheme is included (Beckmann and Doescher, 1997). The tidal mixing parameterisation of Simmons et al. (2004) is included with a special formulation for the Indonesian Throughflow (Koch-Larrouy et al., 2008). At GO5.0 a climatological geothermal heat flux (Stein and Stein, 1992) is added as a bottom boundary condition; this was not used at GO1.

The sea ice component is the latest public release of the Los Alamos National Laboratory sea ice model version 4.1 (CICE v4.1; Hunke and Lipscomb, 2010). The model includes elastic-viscous-plastic ice dynamics (Hunke and Dukowicz, 1997), energy-conserving thermodynamics (Bitz and Lipscomb, 1999) and multicategory ice thickness (Bitz et al., 2001). The setup of CICE is the same as in the lower-resolution version of HadGEM3 described by Hewitt et al. (2011) with five sea ice thickness categories. Both GO5.0 and HadGEM3 use the zero-layer Semtner thermodynamics scheme (Semtner, 1976). We also note that in both the GO5.0 and HadGEM3 configurations the sea ice model is not on the same grid as the ocean (sea ice is on the Arakawa B-grid and ocean is on the Arakawa C-grid; Arakawa, 1966) and an interpolation routine is used to couple these model components. As in HadGEM3, the ice and ocean components are combined into a single executable, so there is no need for a coupler.

We shall also discuss the preceding version of the Met Office ocean model, GO1. This was based on NEMO version 3.2 (v3.2) and CICE v4.1, and was implemented on the same grid as GO5.0, with the same surface forcing.

The ocean and ice code are managed using the Subversion code-management software, allowing unique identification of the respective code bases using a code version number. Ocean and ice model code version numbers, compilation keys and name lists are listed in the Appendices A–E.

The model was run on the MONSooN supercomputer, jointly owned by NERC and the Met Office. The ocean was distributed over 480 cores with the MPI communications harness, with CICE running on a single node, and an acceptable throughput of one model year in 6 h was achieved.

3   Summary of main physics choices

The main physics change between GO1 and GO5.0 is a set of changes to the vertical mixing parameters based on the work of Calvert and Siddorn (2013). Vertical mixing in the model is achieved using a turbulent closure scheme with an algebraic mixing length (Gaspar et al., 1990; Madec, 2008). Additionally, the NEMO implementation of the scheme includes a number of parameterisations to represent additional unresolved turbulent processes, including surface wave breaking (Craig and Banner, 1994) and Langmuir turbulence (Axell, 2002). A further parameterisation represents the enhanced mixing due to breaking of near-inertial waves as an additional source of TKE exponentially decaying from the surface. Users of previous versions of the NEMO ORCA025 model have found significant biases, particularly in the mid-latitudes, and this has been highlighted as a priority bias to reduce with this configuration. Calvert and Siddorn (2013) explored the sensitivity of the model to realistic ranges of parameters in the TKE scheme using 10-year integrations of NEMO at ORCA1 (1°) lateral resolution. As a result of this work they found that altering the vertical length scale for this

TKE source term (controlled by the parameter *nn_htau*) from 30 to 10 m at mid to high latitudes and from 0.5 to 10 m in the tropics was able to significantly alleviate an excessively diffuse midlatitude thermocline. This was seen to result in reduced summertime mixed layer depths and a significant reduction of near-surface temperature biases at midlatitudes. Additionally, Calvert and Siddorn (2013) suggested that a small increase in the Craig and Banner (1994) wind-wave energy coefficient (controlled by the parameter *rn_ebb*) would be more consistent with theory, but was shown to have a very small impact on model results. Similarly, a minor change in the minimum permitted surface mixing length (controlled by the parameter *rn_mxl0*) suggested by Calvert and Siddorn (2013) for consistency with other vertical mixing parameters was shown to have a negligible impact.

Convection in the model is parameterised as an enhanced vertical diffusivity of $10 \, \text{m}^2 \, \text{s}^{-1}$ for momentum and tracer fields where the water column is unstable. At NEMO v3.2 this enhanced vertical diffusivity was erroneously used in the prognostic equation for the TKE, instead of the vertical diffusivity calculated by the TKE scheme. This was shown to result in a deep bias in wintertime mixed layer depths owing to the non-conservative increase in the calculated TKE. This has since been addressed with NEMO v3.4 and therefore constitutes another difference between GO5.0 and GO1.

Other changes between GO1 and GO5.0 are changes to other vertical mixing parameters between GO1 and GO5.0 as noted in Table 1; the inclusion of a double diffusive mixing parameterisation at GO5.0; the addition of the bottom boundary layer scheme of Beckmann and Doescher (1997); and the inclusion of a climatological geothermal heating parameterisation at GO5.0.

The inclusion of the particular new processes and parameter choices described above is based on a mixture of recommendations from the recent literature (from low-resolution model studies), and on changes considered desirable on strong theoretical or observational grounds.

4 Experimental design

The GO5.0 configuration can be viewed as a set of incremental changes in the model physics relative to the GO1 configuration. In order to evaluate the GO5.0 configuration and to understand the model improvements over GO1, a series of forced ocean–sea ice integrations was performed to assess the effects of each individual change.

4.1 Model initialisation and forcing

All of the integrations described here are driven over the period 1976–2005 by the CORE2 surface forcing data set (Large and Yeager, 2009). CORE2 supplies monthly precipitation and daily downward shortwave and longwave radiation which are used to force the model directly, and 6-hourly 10 m wind, 2 m air humidity and 2 m air temperature which

are used to compute turbulent air–sea and air–sea ice fluxes during model integration using the bulk formulae proposed by Large and Yeager (2009). The source data for precipitation and radiative fluxes are only available from 1979 and 1984 onward, respectively. Prior to these dates the respective climatologies are used. Climatological monthly runoffs derived from the Dai and Trenberth (2002) climatology are applied along the land mask (Bourdalle-Badie and Treguier, 2006). No diurnal cycle is imposed in the radiative forcing.

Initial conditions for temperature and salinity for all the integrations are obtained from an average of years 2004–2008 of the EN3 monthly objective analysis (Ingleby and Huddleston, 2007) and the model is started from a state of rest. To avoid unacceptable drifts in salinity and an excessive spin-down of the overturning circulation, the sea surface salinity (SSS) is restored toward monthly mean climatological values: the vertical velocity for restoration *rn_deds* is set to $-33.33 \, \text{mm} \, \text{day}^{-1} \, \text{psu}^{-1}$ over the open ocean. Model outputs are archived as successive 5-day means throughout the whole integration and post-processed to monthly means. More details about the model configuration may be found in Storkey et al. (2010), Barnier et al. (2006), and Penduff et al. (2007).

4.2 Model integrations

A 30-year integration of GO5.0 was carried out with the final set of modifications and parameter values, from the initial state described above. This was compared with the reference integration, from the same initial state and of the same length, of the pre-existing GO1 model based on NEMO v3.2. To estimate the effect of the code change alone, a further 30-year integration of NEMO 3.4 was made with initial state and all parameters and physics choices identical, or as close as possible, to those of GO1. We compare annual and seasonal means from each of these three integrations and also with observations in the form of the EN3 climatology for subsurface temperature and salinity (Ingleby and Huddleston, 2007), the HadSST3 surface temperature climatology (Kennedy et al., 2011), satellite-derived sea ice extent (Cavalieri et al., 1996, updated yearly), the PIOMAS (Pan-Arctic Ice-Ocean Modeling and Assimilation System) reanalysis for Northern Hemisphere sea ice volume (Zhang et al., 2003), and measured transports through key straits from a variety of observational studies.

An additional set of 10-year simulations was made to attribute changes between GO1 and GO5.0 to individual changes in configuration. These are summarised as follows:

– The bathymetry was upgraded from the original DRAKKAR ORCA025 data set as described in Sect. 2.

– The background vertical diffusivity *rn_avt0* and viscosity *rn_avm0* were increased from 1.0×10^{-5} to $1.2 \times 10^{-5} \, \text{m}^2 \, \text{s}^{-1}$ and from 1.0×10^{-4} to $1.2 \times 10^{-4} \, \text{m}^2 \, \text{s}^{-1}$, respectively.

Table 1. Parameter changes between GO1 and GO5.0.

Parameter	GO1 (where different from GO5)	GO5
Horizontal bi-Laplacian viscosity	Same as in GO5.0	$-1.5 \times 10^{11}\,\mathrm{m^4\,s^{-1}}$
Isoneutral Laplacian tracer diffusion	Same as in GO5.0	$300\,\mathrm{m^2\,s^{-1}}$
Background vertical viscosity	$1.0 \times 10^{-4}\,\mathrm{m^2\,s^{-1}}$	$1.2 \times 10^{-4}\,\mathrm{m^2\,s^{-1}}$
Background vertical diffusivity	$1.0 \times 10^{-5}\,\mathrm{m^2\,s^{-1}}$	$1.2 \times 10^{-5}\,\mathrm{m^2\,s^{-1}}$
Energy coefficient for Craig and Banner (1994) surface wave breaking parameterisation	60.0	67.83
Length scale for near-inertial wave breaking parameterisation	0.5 m in tropics, rising to 30 m at midlatitudes	10 m everywhere
Minimum value of surface mixing length scale	0.01 m	0.04 m
Minimum value of interior mixing length scale	0.001 m	0.01 m

– Changes were made to the TKE scheme parameters *rn_ebb* (coefficient of the surface input of TKE), *rn_mxl0* (minimum surface mixing length scale) and *nn_htau* (changing the TKE penetration depth scale from a constant 10 m to varying from 0.5 m at the Equator to 30 m poleward of 40° N and 40° S).

– Geothermal heat flux was applied, as in Stein and Stein (1992) via the parameter *nn_geoflx*.

– Double diffusion of tracers was added.

– A scheme for a bottom boundary layer as in Beckmann and Doescher (1997) was added.

– The ice model (CICE) was modified to include a salinity-dependent freezing point. The thermal conductivity of the ice was changed from 2.00 to $2.63\,\mathrm{W\,m^{-1}\,K^{-1}}$ and the fixed ice salinity was changed from 4.0 to 8.0 psu (practical salinity units), following Rae et al. (2014).

The attribution study will compare the above experiments with one another, as well as with the v3.2 model GO1 and the original v3.4 integration with the GO1 parameter set. The strategy of adjusting parameters according to individual sensitivity studies may not be the optimal method for finding the most appropriate parameter set, since the parameters and physics choices may interact non-linearly, but resources were insufficient for a systematic investigation of parameter space such as that carried out with HadCM3 by Williamson et al. (2013).

Table 2 summarises the integrations carried out, including the values of the principal parameter changes at each step.

We note that the pair of runs comparing NEMO 3.2 and 3.4 (namely GO1 and N3.4) differ further in one minor respect. The v3.4 parameter *rn_mxl0*, the minimum permitted surface mixing length, was erroneously set to 0.001 in the latter experiment to match the value of the parameter *rn_lmin* in v3.2. The latter is an interior minimum length scale in v3.2 but is absent in v3.4, and the equivalent parameter in v3.2 is in fact

rn_lmin0, which was set to 0.01. An additional 10-year integration (N3.4_mxl0) similar to N3.4 was performed, with a value of 0.01: the consequent surface changes were not considered to be significant, with the two simulations being qualitatively the same with mean surface temperature differences in years 6–10 of less than 0.05 °C everywhere.

5 Results

5.1 Validation of GO5.0 against observations

5.1.1 Surface biases and mixed layer depth

Figure 1 shows the sea surface temperature (SST) and salinity (SSS) errors in years 21–30 of the GO5.0 model, relative to the mean of the Reynolds et al. (2002) and EN3 (Ingleby and Huddleston, 2007) respective monthly climatology over the same period. There is overall a warm bias over most of the global ocean, with a global mean bias of +0.72 °C, and with the largest biases (of over 1 °C) in the tropics, the Southern Ocean, the subpolar North Atlantic and over the separated western boundary currents in the North Atlantic and North Pacific. There are cool biases of 0.25–0.50 °C extending over much of the subtropical North Atlantic and North Pacific. GO5.0 is too fresh in most of the Atlantic, except in the subpolar gyre, where the salty bias of 0.5–1.0 psu is co-located with the warm bias mentioned above. It is worth noting that the largest surface errors occur at high latitudes, and therefore are perhaps unduly emphasised in the cylindrical projection used in Fig. 1. Generally the regions where there is a surface warm bias (especially in the Southern Ocean and the Pacific) correspond to a positive surface salinity error: these may result from forcing errors, but are not inconsistent with an excessive evaporation from surface waters with a warm bias. The exception is in the Arctic, where there is a positive surface salinity error of up to 2 psu, due to excessive autumn sea ice formation on the Siberian shelves and in the Beaufort Sea (Fig. 1); the reason for this error is unclear, but is most

Table 2. Summary of integrations carried out. The UM (Unified Model) job ID (identification) is a unique identifier for each run within the Met Office Unified Model system, and allows any configuration to be replicated by another user. The parameters listed are *rn_avt0* (background vertical tracer diffusivity), *rn_mxl0* (minimum surface mixing length scale), and *rn_ebb* (coefficient of the surface input of TKE). The switch *nn_htau* enables a spatially varying TKE penetration depth scale, while *nn_geoflx* applies an abyssal geothermal heat flux (bathy – bathymetry data set).

| Run name	UM job ID	NEMO v	$rn\_avt0 \times 10^{-5}$	bathy	rn_mxl0	rn_ebb	nn_htau	nn_geoflx	Run (years)
GO1	xexoc	3.2	1.0	G70	n/a	60.0	1	0	30
N3.4	xhiml	3.4	1.0	G70	0.001	60.0	1	0	30
N3.4_mxl0	xhimq	3.4	1.0	G70	0.01	60.0	1	0	30
N3.4_bath	xhimj	3.4	1.0	GO5	0.001	60.0	1	0	10
N3.4_vmix	xhkfg	3.4	1.2	GO5	0.001	60.0	1	0	10
N3.4_tke	xhkfi	3.4	1.2	GO5	0.04	67.83	0	0	10
N3.4_geo	xhimt	3.4	1.2	GO5	0.04	67.83	0	2	10
N3.4_DD	xhimp	3.4	1.2	GO5	0.04	67.83	0	2	10
N3.4_ice	xhimm	3.4	1.2	GO5	0.04	67.83	0	2	10
N3.4_bbl	xhimn	3.4	1.2	GO5	0.04	67.83	0	2	10
GO5.0	xhimo	3.4	1.2	GO5	0.04	67.83	0	2	30
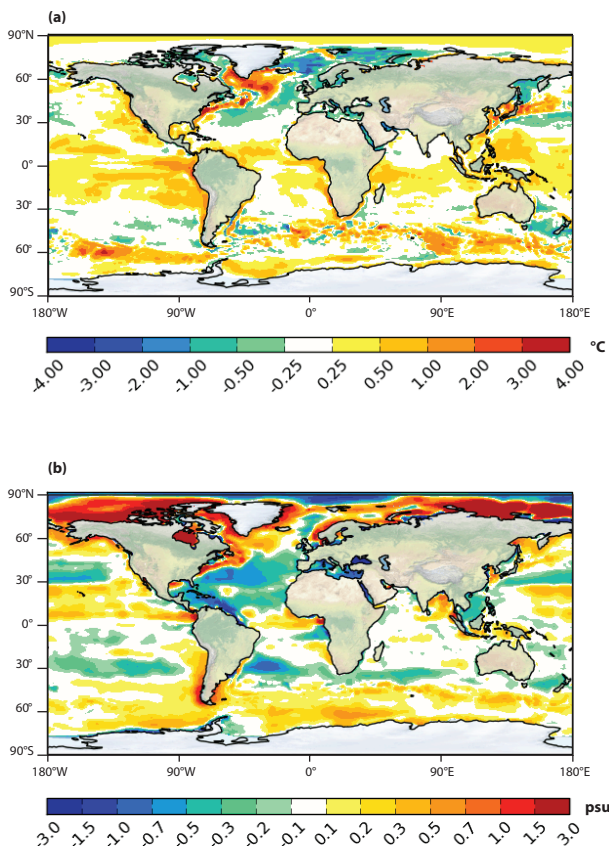
Figure 1. Surface biases in years 1996–2005 of GO5.0: **(a)** mean surface temperature bias with respect to the Reynolds et al. (2002) climatology, and **(b)** mean surface salinity bias with respect to the EN3 climatology.

likely to be related to the air temperature and radiative biases in the atmospheric forcing (Barnier et al., 2006). The sea ice biases are discussed further in Sect. 5.1.4.

Figure 2 shows the annual minimum and maximum mixed layer depth (MLD) calculated for years 1996–2005, corresponding to the shallowest depth of the mixed layer in the local hemispheric summer and the deepest mixed layer in the local hemispheric winter, alongside the same quantity from the de Boyer Montégut et al. (2004) climatology. The model's mixed layer depth is calculated from 5-day data using the same criterion of a 0.2 °C change relative to the surface value as used in the climatology. The ocean data points masked by hatching in the model output (panels a, c) and by white in the climatology (panels b, d) represent the locations where a full annual cycle of observations was not available as a result of sea ice coverage. The GO5.0 model realistically reproduces the spatial patterns of both summer and winter surface mixing: in particular, the regions of wintertime, dense water formation in the North Atlantic and Nordic Seas correspond quite closely to those in the observations, as do the near-zonal bands of deep turbulent mixing in the Southern Ocean (Fig. 2c, d). There is a consistent bias, however, to an unrealistically shallow summer mixed layer over the whole ocean, with maximum values of 30–50 m in the tropics and Southern Ocean in the model, contrasting with a range of 50–70 m in the same regions in the climatology (Fig. 2a, b). This is consistent with the warm surface bias in the same regions seen in Fig. 1. Also, the winter mixing in the dense water formation regions in the North Atlantic is much deeper than in the climatology, reaching to over 1000 m in many instances. The patch of very deep mixing extending from the Weddell Sea eastwards to 50° E is also seen in HadGEM1 and HiGEM: in GO5.0 this feature develops after year 20 of the integration, but it does not occur in GO1. It seems to be associated with a gradual modification of the water masses in the region and the development of the extensive polynya visible in Fig. 6c, which together precondition for the deep mixing, but the exact mechanisms are yet unclear.
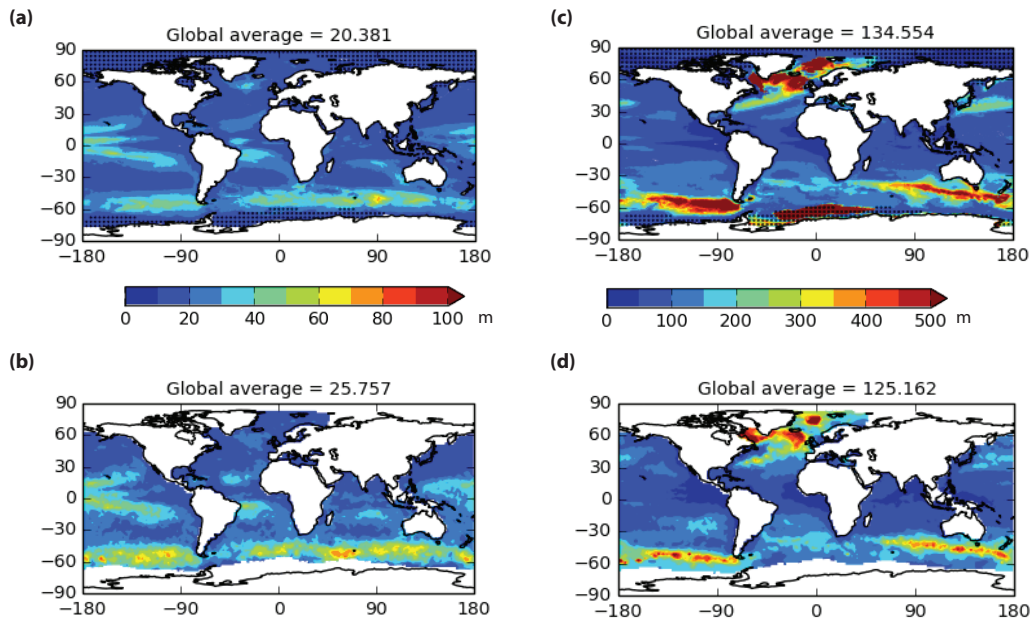
Figure 2. Seasonal cycle of MLD in GO5.0: **(a)** minimum monthly MLD in years 1996–2005, **(b)** minimum monthly MLD in the de Boyer Montegut et al. (2004) climatology, **(c)** maximum monthly MLD in years 1996–2005, and **(d)** maximum monthly MLD in the de Boyer Montégut et al. (2004) climatology. The hatching in panels a and b correspond to the areas of missing ocean data in panels **(c)** and **(d)**, where a full annual cycle of MLD is not observed in the de Boyer Montégut climatology.

The simulated deep, winter, mixed layer in the eastern Weddell Sea in the 1990s and 2000s is likely to be unrealistic, although the limited winter data in the area (e.g. Sirevaag et al., 2010) prevents us from making any definitive conclusion. From the conductivity, temperature and depth (CTD) data collected using Weddell seals, Årthun et al. (2013) surmised that the maximum MLD in the region of the Antarctic Bottom Water formation in the southern Weddell Sea is in excess of 500 m, which is consistent with the model results (Fig. 2c).

The surface biases of the model when forced by prescribed surface boundary conditions are to a large degree constrained by the forcing fields, but the subsurface drifts are a stronger test of the model, revealing discrepancies in diapycnal mixing and advection pathways. Figure 3 shows the zonal mean temperature and salinity anomalies in GO5.0 averaged from 1996 to 2005, with reference to the EN3 climatology. The black contours show the zonal mean potential density σ_0, with a 0.5 kg m^3 contour interval, to illustrate the position of the biases with respect to the main pycnocline. The largest biases are in the top 700 m of the water column: these include a cold subsurface bias ($\sim 2\,°C$) around Antarctica; a warm salty bias ($\sim 1.5\,°C$ and 0.25 psu) between 45 and 60° S; a warm bias in the tropics of up to 2.5 °C down to about 200 m; cold, fresh biases in the main thermocline (45° S–45° N, with maximum discrepancies of 1 °C and 0.5 psu); and a warm salty bias in the Northern Hemisphere subpolar gyre regions ($\sim 1\,°C$, 0.25 psu).
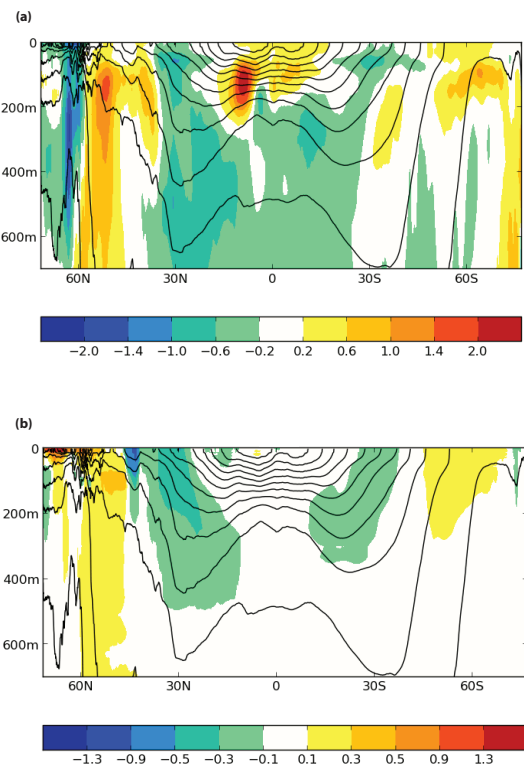

Figure 3. Zonal mean **(a)** temperature and **(b)** salinity biases in years 1996–2005 of GO5.0. The solid contours are of the zonal mean potential density σ_0, with a spacing of 0.5 kg m^3.

5.1.2 Atlantic meridional overturning

Figure 4a shows a time series of the strength of the Atlantic meridional overturning circulation (AMOC) at 26° N for the full 30-year integration of GO5.0, alongside that in GO1. Also shown is the potential density averaged over the upper 200m in the central Labrador Sea (55–58° N, 48–50° W). Figure 4b illustrates the meridional overturning stream function in years 1996–2005 in both models. In both GO1 and GO5.0 the overturning circulation reaches a maximum in the second decade of the integration, decreasing by 2–3 Sv by year 30; the run length is however not sufficient to determine whether the circulation has settled at that stage. In both runs both the AMOC (meridional overturning circulation) and the Labrador Sea density increase over the first decade and decrease later in the second decade, consistent with the hypothesis that the Labrador Sea surface density controls the overturning, although a longer time series would be required to establish a statistically robust correlation. The overturning strength at 26° N in the final decade is between 21 and 22 Sv, which is significantly stronger than the value of 18.5 ± 1 Sv observed between 2004 and 2008 by the RAPID WATCH/MOCHA array (McCarthy et al., 2012). Interestingly, the downward trend we see in the last decade of the model runs ($\sim 2-3$ Sv decade^{-1}) is similar to that recently reported from the RAPID array (Smeed et al., 2014). The modelled annual means for 2 years overlapping the observations, namely 2004 (19 Sv) and 2005 (20 Sv) match well with the observations (17.8 and 20.1 Sv, respectively), and the strength of the modelled AMOC over the latter decade of the run is entirely plausible, particularly since recent studies indicate that a substantial fraction of the variability in the strength of the AMOC originates from surface forcing (Roberts et al., 2013; Blaker et al., 2014). We cannot expect the model to simulate the measured AMOC perfectly, since a significant fraction of the AMOC variability is inherently unpredictable, arising as a consequence of the baroclinic wave field and mesoscale eddy field (Hirschi et al., 2013; Thomas and Zhai, 2013). Hirschi et al. (2013), performed forced 1/4° simulations similar to those described in this paper with different initial conditions: in the simulations of Hirschi et al. (2013) about 70 % of the AMOC variability is determined by the surface-forcing, and 30 % from intrinsic ocean variability. We expect this to be an underestimation, since our model configuration is eddy-permitting, rather than eddy-resolving. The question of the physical processes contributing to AMOC variability in models and observations (for example, Ekman transport, advection of density anomalies and Rossby waves) is complex and has been explored in a number of recent papers (e.g. Sinha et al., 2013; Roberts et al., 2013; Robson et al., 2014), but is beyond the scope of the current paper. We note that the modelled annual means quoted here are January–December, whilst the observational array figures are April–March.
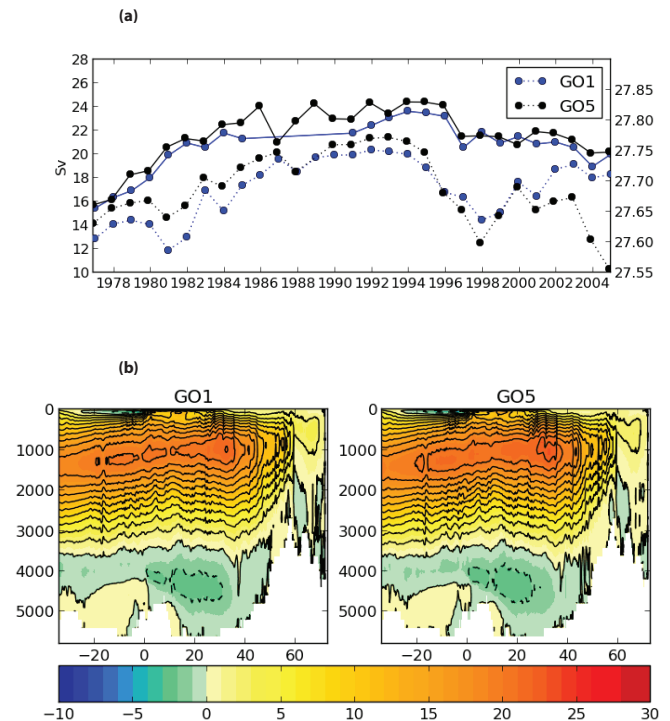

Figure 4. (a) Time series of annual mean AMOC at 26° N in GO1 and GO5.0, with the potential density σ_0 in the upper 200 m in the central Labrador Sea; and **(b)** mean Atlantic overturning stream function in years 1996–2005 of GO1 (left) and GO5.0 (right). Note that velocity data are missing in years 1986–1990 of GO1.

Figure 4b also shows that the depth of the North Atlantic Deep Water (NADW) return flow is too shallow. At 26° N the depth of the NADW return flow (usually defined as the depth of the zero contour in the stream function) is around 3500 m for most of the model run compared to deeper than 4000 m in the RAPID array data. This is a common bias in many ocean GCMs (global circulation models) using depth coordinates, and is usually attributed to spurious mixing of overflow waters as they descend from passages in the Greenland–Iceland–Scotland ridges to the deep ocean (Saunders et al., 2008; Danabasoglu et al., 2010). It is worth noting that substantial variation in the depth profile can arise from the method used to compute the overturning. Computing the overturning from a model using the RAPID array methodology and assuming a geostrophic reference depth of 4740 m can yield a transport profile much more similar to the observations at 26° N than integrating the model velocities (Roberts et al., 2013).

The increase in the AMOC over the first decade of the model run is a phenomenon often seen in ocean GCMs using mixed surface boundary conditions in which the high-latitude oceans become overly sensitive to salinity perturbations (Rahmstorf and Willebrand, 1995; Lohmann et al., 1996; Greatbach and Peterson, 1996; Griffies et al., 2009; Yeager and Jochum, 2009). In the GO5.0 model run, an initial

error in the path of the NAC causes warm, salty water to be advected into the subpolar gyre where it joins the Greenland current and enters the Labrador Sea. The prescribed surface air temperature causes excessive surface heat loss in the Labrador Sea, increasing the density of the surface waters and leading to excessive deep water formation in this region. The increase in the AMOC causes more warm, salty water to be advected into the subpolar gyre in a positive feedback. Yeager and Jochum (2009) show that stronger sea surface salinity restoration can reduce this feedback mechanism by reducing the surface salinity in the Labrador Sea. This improvement, however, comes at the expense of realistic interannual variability in the global climate.

5.1.3 Critical sill and strait transports

Table 3 lists the volume transports through the major straits and across critical sills, evaluated from the model velocities averaged over the last 10 years of the 30-year integrations of GO1 and GO5.0, together with recent observed estimates and their sources. The sign convention is positive for northward and eastward flow. Overall, the models simulate these transports acceptably: in particular, the Drake Passage throughflow is much closer to observations than those in the lower-resolution coupled models HadCM3 and HadGEM1, both of which at ~ 200 Sv (Johns et al., 2006) are unrealistically strong. HadGEM2 (Collins et al., 2008) gave a comparable simulated Drake Passage transport of ~ 140 Sv (Meijers et al., 2012). In contrast to these aforementioned coupled models, the $1/4°$ resolution of the ORCA025 grid allows the present model to at least approach an explicit resolution of the narrower passages: in particular, it can be seen that both GO1 and GO5.0 have transports through the Bering Strait of well within a factor of two of the observed values.

The Indonesian Throughflow is too strong in both GO1 and GO5.0, which may be due to insufficient enhancement of the tidal mixing in this region (Koch-Larrouy et al., 2008).

Comparing the model-derived and observation-based estimates of the Arctic–Atlantic exchanges across the Greenland–Scotland Ridge, through the Fram and Davis straits, and through the Barents Sea shows that in both 30-year model runs the volume transports are within 10–20 % of the observed long-term mean values and within the range of the observational uncertainties, except for the Denmark Strait overflow where the model estimates are 33 % (GO1) and 45 % (GO5.0) higher than the observational estimate (Table 3). Although the simulated net outflow from the Arctic Ocean, of 4.8 Sv in GO1 and 4.6 Sv in GO5.0, is very close to the observed value of 4.6 Sv, the model shows a different partitioning of the exports west and east of Greenland: the simulated flow through the Canadian Archipelago is larger than the export through the Fram Strait, which is opposite to the observations. The bias is stronger in summer than in winter and is due to excessive Ekman convergence in the Beaufort Sea; this in its turn is caused by the summer sea

ice extent being too low (see next section). The simulated Pacific inflow in the Bering Strait is higher than in the observations, even considering the recent update in the latter estimate (Woodgate et al., 2012). The simulated northward ocean velocities in the strait are about 35 % higher then those observed at the long-term moorings (Clement Kinney et al., 2014). Aagaard et al. (2006) suggested that the flow through the Bering Strait is partly driven by the local wind and partly by the steric height difference between the Bering and Chukchi seas. The latter is caused by the fresher, warmer waters present to the south of the strait and colder, more saline waters to the north of the strait (Aagaard et al., 2006). In the model the positive bias in salinity in the Chukchi Sea and the eastern Arctic (Fig. 1b) increases the steric height gradient from the North Pacific to the Arctic Ocean, increasing the northward flow through the Bering Strait. The stronger Pacific inflow brings extra heat into the Arctic Ocean, which may contribute to the excessive sea ice melting.

Overall, both runs, GO1 and GO5.0, present more vigorous northward flow of the Atlantic water than is observed ("Total Greenland–Scotland inflow" in Table 3 is a proxy for this) and stronger-than-observed return overflows across the Greenland–Scotland Ridge: the combined overflows in the Denmark Strait and in the opening between Iceland and the Faeroes and between the Faeroes and Scotland are 6.3 Sv from the data, 9.3 Sv in GO1 and 8.3 Sv in GO5.0. This is also consistent with the stronger simulated AMOC compared to observations.

It should be noted that the observational estimates of the exchange transports into and out of the Arctic should be treated with caution. First, in all straits, except for the moorings in Bering Strait, the hydrographic section in the Fram Strait and the one in the Barents Sea between Norway and Bjørnøya (Barents Sea opening), uninterrupted records from current meter moorings are no longer than 2 years. This aliases interannual variations and introduces large uncertainties in the observational transport estimates. Secondly, the instruments were not positioned in the top 50 m or on shallow shelves, in order to prevent the moorings being damaged by sea ice keels. Lastly, the distances between the moorings were too great to resolve mesoscale variability of the flows and in Bering Strait the transports were derived from velocity measurements obtained from three separate moorings (e.g. Woodgate et al., 2012). All this introduces spatial aliasing in the interpolating procedures and uncertainties in the transports. For a detailed discussion of uncertainties in observed transports, please refer to e.g. Curry et al. (2011) and Olsen et al. (2008). It also should be noted that, while the model's standard deviations in the table represent variability of the transports on synoptic to interannual timescales, the standard deviations of the observational estimates include uncertainty inherent in the estimation methods as well as the variability of the transports, thus rigorous comparison of the variability in the model and data requires additional analysis, not presented here.

Table 3. Volume transports (Sv), observed and model mean values and their standard deviations. Model values are means over the last 10 years of the 30-year spin up. Model standard deviations are obtained from the 5-day averages. Sign convention is positive northwards and eastwards, and is negative southwards and westwards.

Location	Observed value	GO1	GO5.0
AMOC at 26° N	18.5 ± 1 [a]	21.0 ± 4.2	22.0 ± 4.2
Barents Sea opening net	2.8 ± 0.6 [b,c,d]	3.3 ± 2.0	3.0 ± 2.0
Fram Strait net	-2.3 ± 4.3 [e]	-1.9 ± 2.4	-1.6 ± 2.3
Denmark Strait net	$(-6.0 \text{ to } -3.6)$ [d]	-3.4 ± 3.3	-3.3 ± 3.3
Denmark Strait overflow[m]	-2.9 ± 0.6 [f]	-5.3 ± 2.9	-4.34 ± 2.1
Iceland–Faeroes net	2.8 ± 0.5 [g]	2.72 ± 1.2	2.6 ± 1.2
Iceland–Faeroes overflow[m]	-1.0 ± 0.5 [f]	-0.9 ± 0.5	-0.9 ± 0.5
Faeroes–Scotland net	1.8 ± 0.5 [g]	1.4 ± 2.3	1.7 ± 2.3
Faeroes–Scotland overflow[m]	-2.4 ± 0.4 [f]	-3.1 ± 0.8	-3.1 ± 0.9
Total Greenland–Scotland inflow[n]	8.5 ± 1.0 [g]	9.3 ± 1.8	10.0 ± 1.7
Bering Strait net	$0.8[1.1^{l}] \pm 0.2$ [i]	1.3 ± 0.9	1.4 ± 0.9
Davis Strait net[o]	$-2.6 \pm 1.0 \text{ to } -2.3 \pm 0.7$ [e,h]	-2.9 ± 1.2	-3.0 ± 1.1
Drake Passage	135 ± 20 [j]	119 ± 8	124 ± 8
Indonesian Throughflow	-15 ± 4 [k]	-19.7 ± 5.4	-19.8 ± 5.5

Key: [a] McCarthy et al. (2012), [b] Gammelsrod et al. (2009), [c] Skagseth et al. (2008), [d] Aksenov et al. (2010), [e] Curry et al. (2011), [f] Olsen et al. (2008), [g] Østerhus et al. (2005), [h] Cuny et al. (2005), [i] Woodgate et al. (2012), [j] Cunningham et al. (2003), [k] Sprintall et al. (2009), [l] climatological transport with the estimate for 2011 in parenthesis, [m] southward transport of waters with $\sigma_\theta > 27.8$, [n] Atlantic inflow derived as the residual flow after subtracting the southward transport of waters with $\sigma_\theta > 27.8$, [o] including transports on the West Greenland shelf.

5.1.4 Sea ice

In Fig. 5 time series of the sea ice extent and ice concentration in the Northern Hemisphere and Southern Hemisphere are compared with products from passive microwave satellites SSMR/I (special sensor microwave/imager) and AVHRR (advanced very high resolution radiometer; Cavalieri, 1996, updated 2013). In the Northern Hemisphere the simulated annual mean of $11.2 \times 10^6 \text{ km}^2$ and the amplitude of the seasonal cycle of $7 \times 10^6 \text{ km}^2$ are in good agreement with the data ($12.4 \times 10^6 \text{ km}^2$ and $5.8 \times 10^6 \text{ km}^2$, respectively), suggesting good model skill in simulating sea ice extent (Fig. 5a), although the model underestimates summer sea ice extent. The simulated and observed interannual trends also agree. Figure 5b compares the modelled Arctic sea ice volumes with these derived from the PIOMAS reanalysis (Zhang et al., 2003). Simulated sea ice volumes are about 60 % of those observed through the annual cycle, with winter (DJF – December-January-February) biases of around 30 % and in summer (JJA – June-July-August) of around 50 %. Despite this bias, the multidecadal trends in the modelled and observed sea ice extents are comparable, showing sea ice extent decline at a rate of $-44 \times 10^3 \text{ km}^2 \text{ year}^{-1}$ and $-45 \times 10^3 \text{ km}^2 \text{ year}^{-1}$, respectively. In the Southern Hemisphere the modelled sea ice extent is again in good agreement with observations (Fig. 5c), but with a moderate negative summer bias. At present no published sea ice volume time series are available for Antarctica, rendering formal validation of the model skills in simulating sea ice volumes in the Southern Hemisphere impossible. However,

comparing simulated sea ice thicknesses around Antarctica for the period 1996–2005 with the Antarctic Sea Ice Processes and Climate (ASPeCt) data (Worby et al., 2008) for the same period, we conclude that the simulations underestimate long-term mean annual sea ice thickness by about 15 % (0.76 m in the model and 0.89 m in the observations). The annual cycle in the model is in good agreement with the observations, with the maximum ice thickness (1.06 m and in the model and 1.02 m in the observations) occurring in the austral summer (DJF) and minimum ice thickness (0.58 m in the model and 0.60 m in the observations) in the austral winter (JJA). The simulated sea ice extent trend in the Southern Hemisphere is negative and around $-58 \times 10^3 \text{ km}^2 \text{ year}^{-1}$, in contrast to the positive trend of $13 \times 10^3 \text{ km}^2 \text{ year}^{-1}$ in the observations. The negative trend in Antarctic sea ice extent is a common feature of global ocean models, and is attributed by Holland and Kwok (2012) to biases in the surface winds around Antarctica in the forcing data.

Comparison between the simulated sea ice concentration fields and those from the HadISST (Hadley Centre Sea Ice and Sea Surface Temperature) observational data set (Rayner et al., 2003) show that the simulated winter sea ice distribution in both hemispheres is realistic (Fig. 6a–d), although we note that there is a tongue of reduced ice cover extending eastward from the central Weddell Sea, which has also been seen in HadGEM1 and the higher-resolution HiGEM (Shaffrey et al., 2009), and which corresponds to the very deep winter mixing described in Sect. 5.1.1. The summer sea ice concentration in the model is lower than in the data (Fig. 6e–h). In the Arctic Ocean this is likely to be caused by
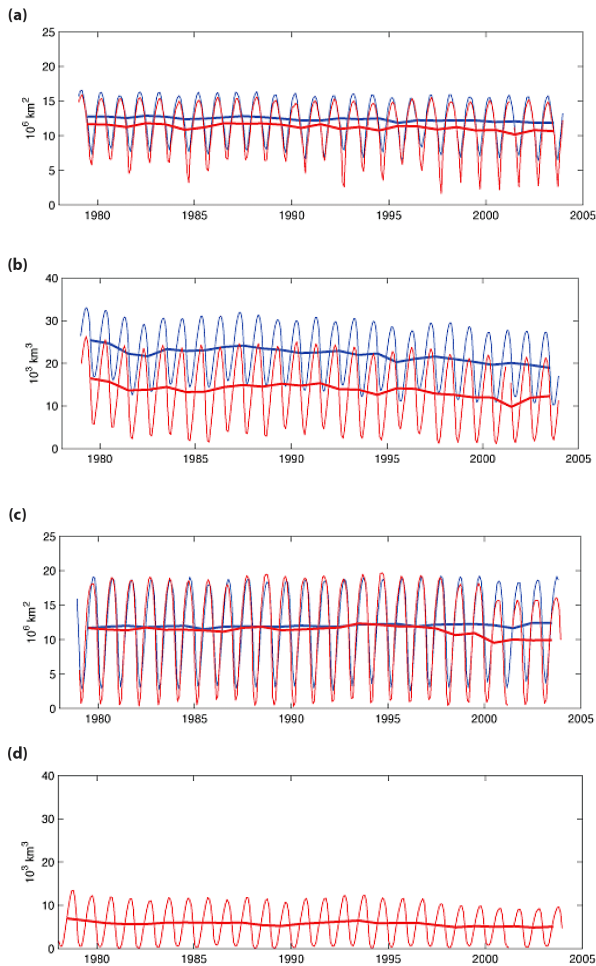
Figure 5. Time series of integrated sea ice properties in GO5.0 (red) and from observational estimates (blue): **(a)** Arctic mean ice extent, **(b)** Arctic mean ice volume, **(c)** Antarctic mean ice extent, and **(d)** Antarctic mean ice volume.

Figure 6. High-latitude sea ice extent in GO5.0 and in the HadISST observational data set: Arctic winter (DJF) ice extent in **(a)** GO5.0 and **(b)** observations; Antarctic winter (JJA) ice extent in **(c)** GO5.0 and **(d)** observations; Arctic summer (JJA) ice extent in **(e)** GO5.0 and **(f)** observations; and Antarctic summer (DJF) ice extent in **(g)** GO5.0, and **(h)** observations.

the negative bias in the sea ice thickness, which in turn results in lower ice strength, faster ice drift toward the Canadian Arctic archipelago and thus increased divergence of sea ice in the central Arctic Ocean. This, combined with the increased sea ice melting in summer, due to exposure of the ocean surface to the atmospheric heat, could sustain the lower thicknesses in the Arctic throughout the year. In the present forced simulations, the summer sea ice bias primarily affects polar regions and has a moderate effect on the global ocean circulation. However, in a fully coupled model atmospheric dynamics might cause a significant effect on regions remote from the ice-covered oceans.

5.2 Comparison of GO1 and GO5.0

As shown in Fig. 1, GO5.0 shows large-scale surface biases, which are nevertheless not untypical of comparable forced ocean models and are in part due to forcing errors. It is worth noting that the impact on the coupled model of the vertical
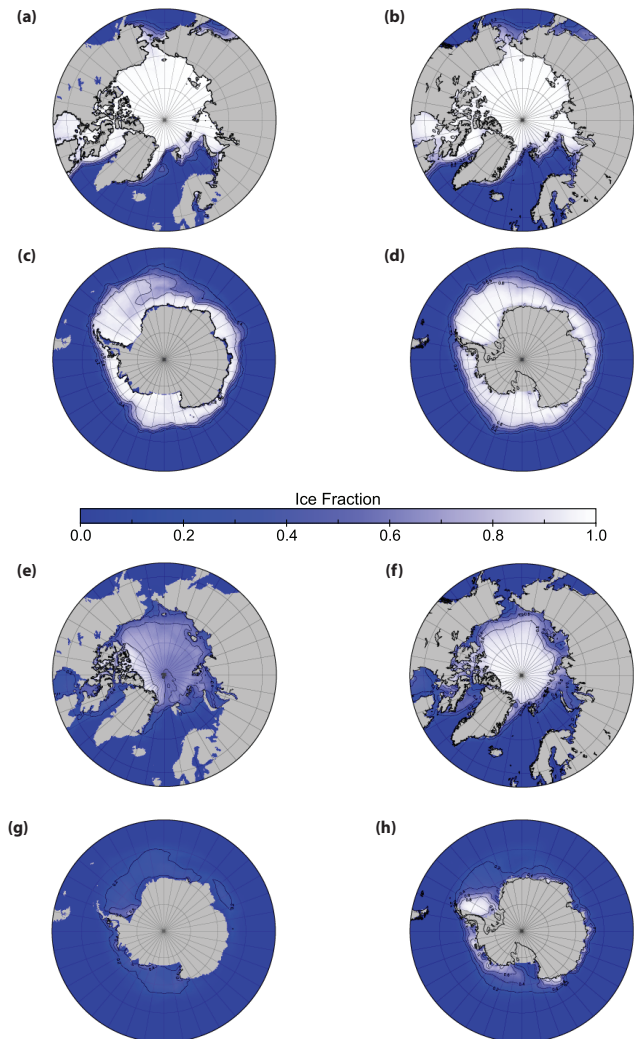
mixing changes is expected to be greater. We shall show in this section that, while the surface biases in the GO1 configuration are similar in most regions of the ocean to those already described in GO5.0, there are significant improvements in the subsurface drifts and the representation of the annual cycle of surface temperature in GO5.0, both of which are likely to lead to improvements in climate simulations.

5.2.1 Subsurface drifts

Figure 7 shows the global zonal mean temperature and salinity drifts of GO1 and GO5.0, defined as the difference between the respective mean for each year and the corresponding mean for the first year of integration, from the surface
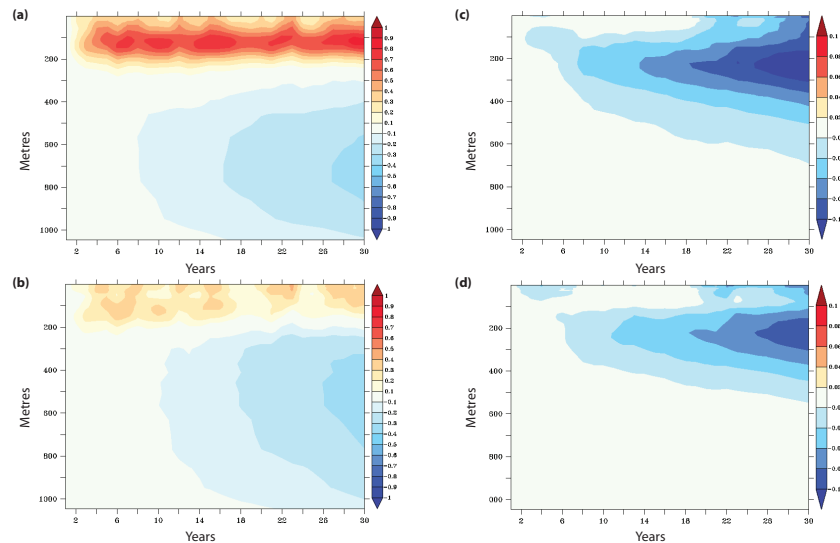
Figure 7. Subsurface drifts, defined as the difference of the horizontally averaged annual mean in any year from that in the first year of integration, as a function of depth: **(a)** GO1 temperature drift, **(b)** GO5.0 temperature drift, **(c)** GO1 salinity drift, and **(d)** GO5.0 salinity drift.

to a depth of 1000 m. We note that the drifts in both models are an order of magnitude larger that the comparable trends in the EN3 climatology (not shown). The temperature field in the upper 300 m reaches a quasi-equilibrium state after about 5 years of integration. Both models warm in the above depth range, with a maximum at about 120 m depth: in GO1 the maximum is up to 0.6 °C, while in GO5.0 the warming at the same depth only reaches 0.3 °C. Below 300 m both models cool, with a similar maximum rate at 600 m of around $-0.12\,°C\,decade^{-1}$. The salinity, by contrast, does not equilibrate, even in the upper ocean, and both GO1 and GO5.0 freshen globally, with a maximum rate at 200 m of $0.036\,psu\,decade^{-1}$ in the former and $0.025\,psu\,decade^{-1}$ in the latter. We note that the warm error in GO5.0 is mainly in the northwestern Atlantic and Southern Ocean, while this model is generally too fresh at the surface, with the exception at the Arctic (where there is a large salty surface bias of 1–2 psu), and the Southern Ocean. There is also interannual variability in the globally averaged surface temperature and salinity in the upper 200 m: this is not well correlated with that of the surface variability, so it is not likely to be a direct signature of the ENSO cycle.

It is interesting to relate the drifts in GO1 and GO5.0 to those over the first 30 years of HadGEM1 (Johns et al., 2006) and in CHIME and HadCM3 (Megann et al., 2010). All these except for CHIME (which uses a hybrid isopycnic-coordinate ocean, in contrast to the depth-coordinate ocean model in the other three) have a pronounced freshening in the upper ocean that steadily penetrates into the interior, and this is likely to be a consequence of the numerical diapycnal mixing typical of this model type (Griffies et al., 2000). HadCM3 and HadGEM1 (which shared an ocean model, albeit on a

slightly different grid) similarly had a negative surface temperature error over most of the ocean, offset in HadCM3 by a warm bias in the Southern Ocean, while CHIME had a warm surface error, consistent with a reduced drawdown of heat by numerical mixing.

5.2.2 Seasonal cycle of surface temperature and mixed layer depth

Figure 8 shows the mean biases of the sea surface temperature in GO1 and GO5.0 with respect to the interannual Reynolds et al. (2002) climatology in the boreal winter and boreal summer seasons, defined as the DJF and JJA periods respectively. It is clear that both configurations have substantial biases in the time-averaged surface fields, and as with the 10-year mean fields discussed in Sect. 5.1.1, in many regions these biases are very similar: for example, the tropics and Southern Ocean are generally too warm in both configurations, while the northern high latitudes are generally too cold, and there is a warm error in the subpolar North Atlantic with maximum values of 3–4 °C in the boreal winter. There are regions where the seasonal biases in GO1 are smaller than in GO5.0: for example, the cold boreal winter error in the subtropical North Atlantic is larger in GO5.0 south of the separated Gulf Stream (Fig. 8a, b), and in the Southern Ocean there is a substantial coherent warm error in GO5.0 in the austral summer that is not present to the same extent in GO1. Overall, however, there are large-scale reductions in seasonal bias, particularly in the northern summer (JJA) season: the cold errors in the North Atlantic and North Pacific are substantially reduced in GO5.0, as are the warm biases in the tropics and the Southern Ocean. To quantify the improvements, the global rms(root mean square) SST error in
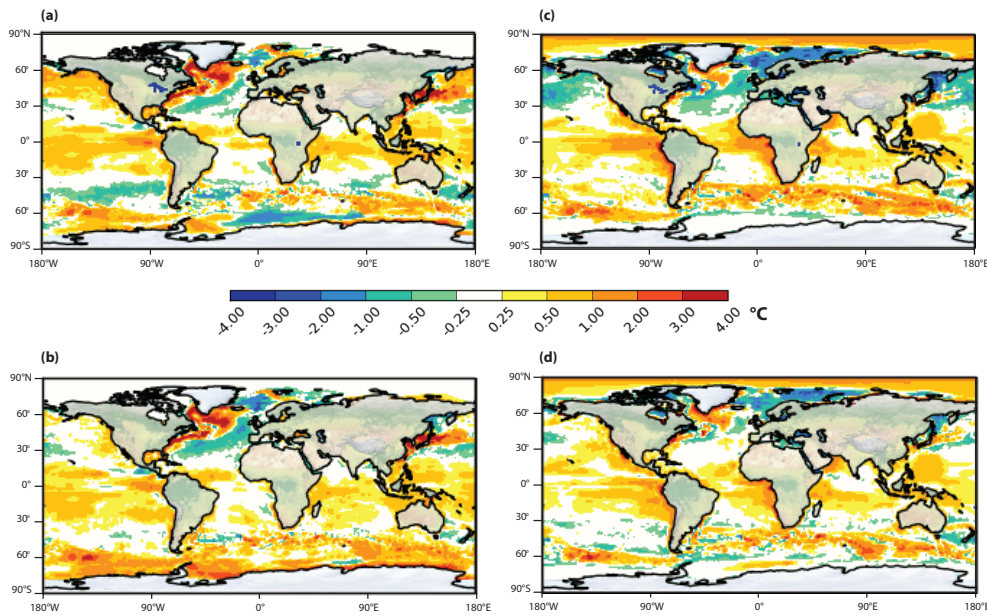
Figure 8. Seasonal SST biases against Reynolds et al. (2002) climatology: boreal winter (DJF) biases in **(a)** GO1 and **(b)** GO5.0, and boreal summer (JJA) biases in **(c)** GO1 and **(d)** GO5.0.

the boreal summer (JJA) is reduced from 0.93 °C in GO1 to 0.65 °C in GO5.0, while the global mean boreal winter (DJF) error is reduced from 0.79 to 0.67 °C.

To illustrate the latitude dependence of the large-scale seasonal biases in GO1 and GO5.0, Fig. 9 shows latitude-time plots of the zonally averaged surface temperature bias (referred to the climatology of Reynolds et al., 2002) and MLD error (referred to the data of de Boyer Montegut et al., 2004) in GO1 and GO5.0. This shows more clearly that the boreal summer warm bias in the tropics is reduced in GO5.0, as is also the large summer cold bias in the northern subtropics. As we have already noted, GO5.0 shows systematic biases in both the minimum and maximum MLD (Fig. 2): specifically, in both hemispheres winter mixed layers are generally too deep, while summer mixed layers are generally too shallow. The main difference between GO1 and GO5.0 is that mixed layer depths are generally shallower in GO5.0, leading to increased stratification and hence the warmer summer surface temperatures, especially in the Southern Ocean, seen in Figs. 8b and 9a. The winter MLD biases, in contrast, are generally reduced in GO5.0.

5.2.3 Surface heat fluxes

Although the model uses the CORE2 forcing data set, the use of bulk formulae to calculate some of the components of the heat flux means that the actual heat input to the ocean will be slightly different from the climatological field, and will reflect the surface temperature biases of the model. Figure 10a shows the zonal mean net downward surface heat flux in GO5.0 and GO1, alongside the corresponding mean from the

CORE2 data set, while Fig. 10b shows the difference in the surface heat flux between the two model configurations. The physics changes between GO1 and GO5.0 can be seen to lead to changes in the heat flux that are generally small compared with the difference between the models and the climatology. In tropical and subtropical latitudes the zonal mean surface flux in both model integrations is within 5–10 W m^{-2} of the observations, while the excessive heat loss of up to 20 W m^{-2} between 60 and 70° N and south of 60° S in both cases may be linked with the warm biases described in Sect. 5.1.1 in these latitude ranges. The regional differences in heat flux between the model versions correspond closely to differences in surface temperature, with the reduction in the warm bias in the tropical Atlantic and Pacific from GO1 to GO5.0 (visible in Fig. 9a and b) leading to an increase of up to 25 W m^{-2} in the heat flux into the ocean in these regions, and similarly the reduction in wintertime cold bias in subpolar latitudes seen in Fig. 9 corresponds to a decreased heat loss over the Labrador Sea. In the Southern Ocean the increased surface flux error is larger in GO5.0 relative to that in GO1, and is linked to the intense Weddell Polynya that develops in in GO5.0.

5.3 Attribution of changes

In this section we refer to the experimental design described in Sect. 4, where a series of shorter (10-year) integrations are made. The model code is first upgraded from NEMO v3.2 to v3.4, then other changes are progressively made within v3.4, to attribute the most significant changes in model fields to specific changes in the model physics. These changes are summarised in Table 2. We compare the mean fields in the
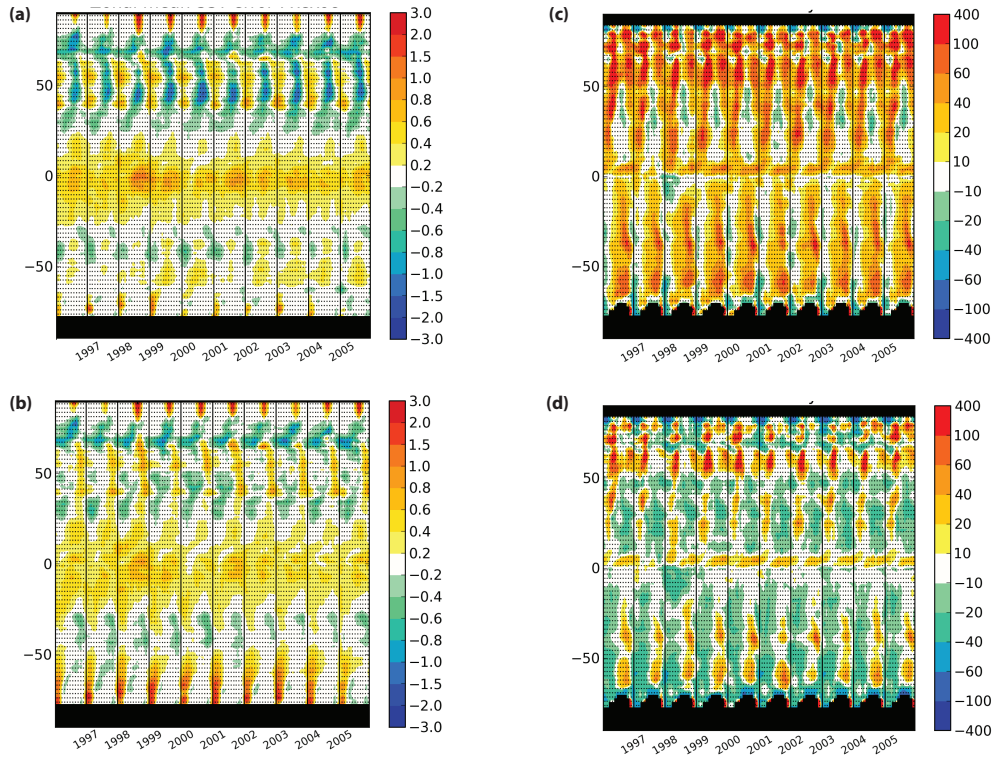
Figure 9. Monthly SST and MLD biases against Reynolds et al. (2002) and de Boyer Montégut et al. (2004) climatology, respectively, in years 1996–2005 as a function of latitude: **(a)** GO1 SST, **(b)** GO5.0 SST, **(c)** GO1 MLD, and **(d)** GO5.0 (monthly) MLD.
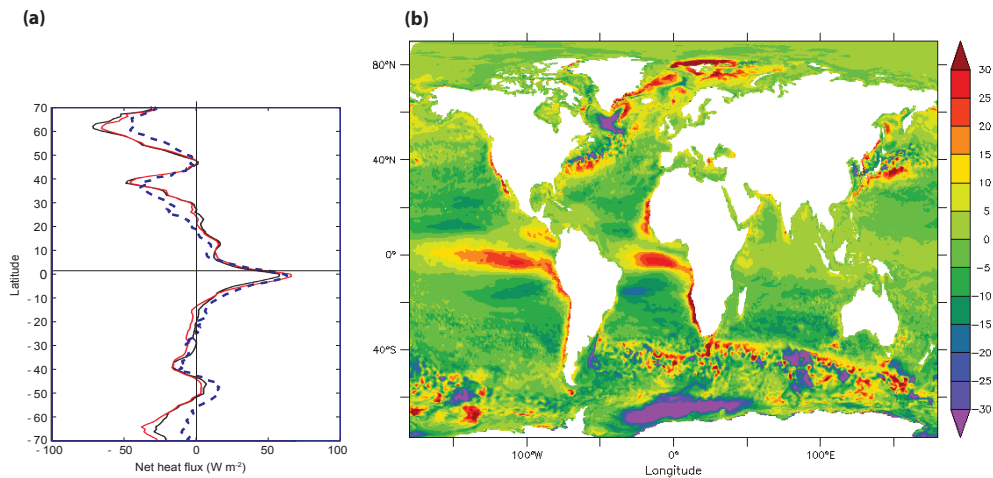

Figure 10. (a) Zonal mean net air–sea heat flux in GO1 (black), GO5.0 (red) and CORE2 data (dashed blue line) in years 1996–2005; and **(b)** surface net downward heat flux difference GO5.0 minus GO1. This panel is adapted from Fig. 5.10 of Josey et al. (2013).

final 5 years (1981–1985) of each 10-year integration; the main comparison will be of the surface fields, but the global subsurface biases down to 700 m will also be compared. We use an empirical criterion for the significance of the changes, since the variance of the fields discussed here was not available in the model output: we judge a modification to have a negligible effect if it leads only to differences in the 5-year mean field with the characteristic signature of the mesoscale eddy field, while modifications which lead to coherent large-scale changes in temperature or salinity are deemed to have a significant effect.
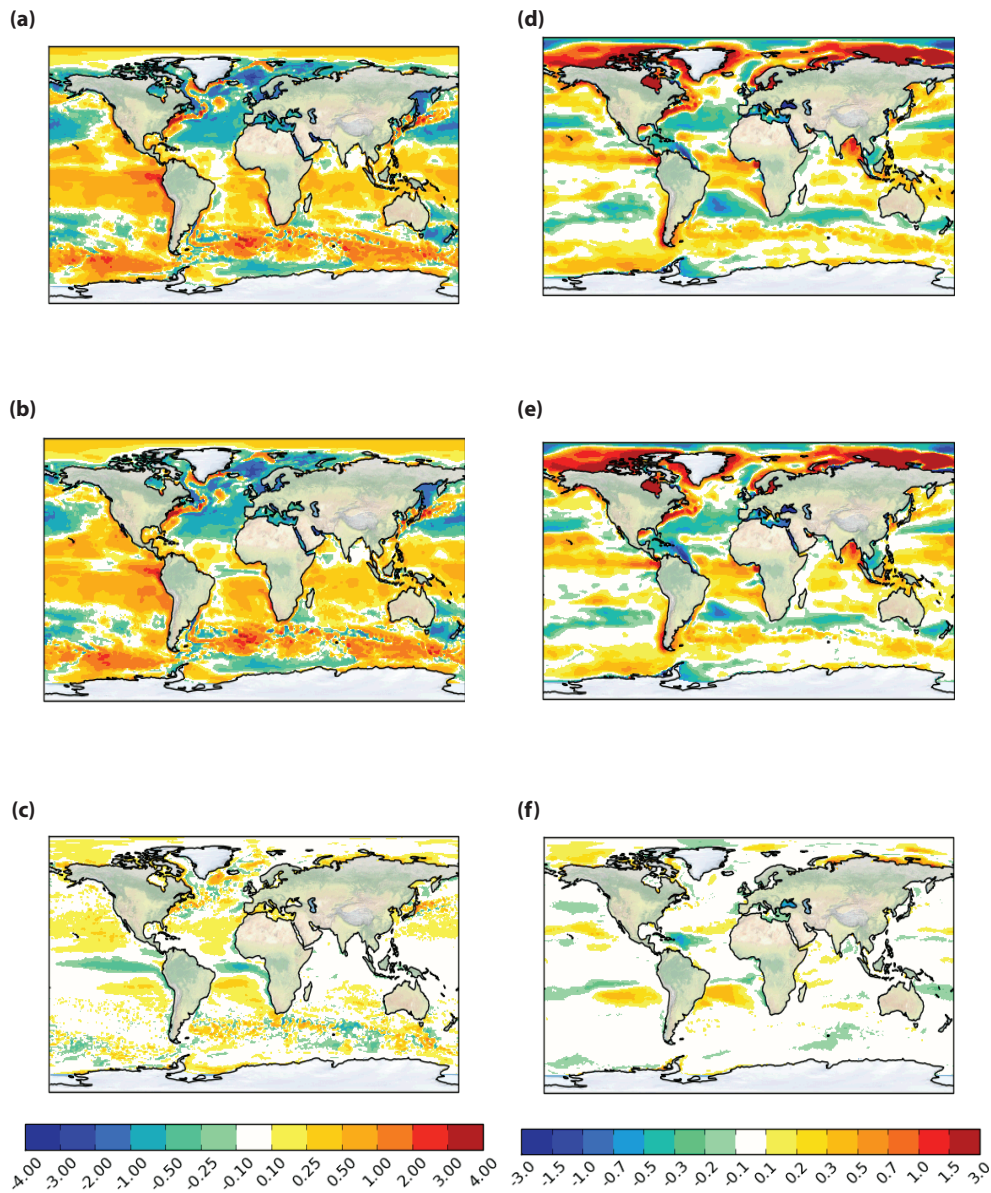
Figure 11. Effect on sea surface fields in years 1981–1985 of ocean code upgrade from v3.2 (GO1) to v3.4 (N3.4): **(a)** GO1 SST bias, **(b)** N3.4 SST bias, **(c)** N3.4 minus GO1 SST, **(d)** GO1 SSS bias, **(e)** N3.4 SSS bias, and **(f)** N3.4 minus GO1 SSS.

5.3.1 Correction to TKE convective mixing

The code changes from NEMO versions 3.2–3.4 have one main physics component, which is the correction to the treatment of convective mixing in the TKE scheme described in Sect. 3. As explained in Sect. 3, the expected change to the solution due to this correction is an improvement in the excessively deep wintertime mixing. Figure 11 shows that the code upgrade clearly has significant effects on the surface fields: there are basin-scale changes over almost the whole ocean, with warming of 0.1–0.2 °C over the Arctic and the subtropical gyres, but cooling by a similar magnitude on the Equator and coastal upwelling regions, in the Southern

Ocean and in the North Atlantic subpolar gyre. The surface salinity changes are also predominantly in zonal bands, with the largest increases of 0.2–0.4 psu between 15 and 30° S and between 15 and 30° N in the Atlantic and eastern Pacific and a surface freshening over much of the Southern Ocean. The code change overall, however, has little effect on the rms surface errors of the model: the rms SST error decreases from 0.665 to 0.657 °C, while the rms surface salinity error barely changes from 0.828 to 0.825 psu. There are, however, major subsurface effects resulting from the code upgrade, particularly from the correction to the treatment of convective mixing in the TKE scheme: comparing the temperature changes in the upper 700 m with the mean isopycnal depths (Fig. 12)
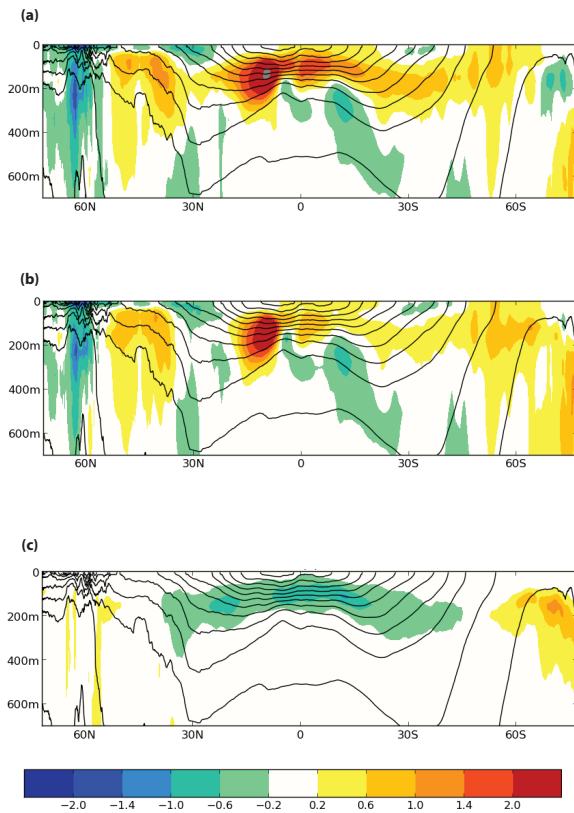
Figure 12. Effect on zonal mean temperature in years 1981–1985 of code upgrade from NEMO v3.2 (GO1) to v3.4 (experiment N3.4) in years 1981–1985. **(a)** Bias in GO1, **(b)** bias in N3.4, and **(c)** difference N3.4 minus GO1. The solid contours are of the zonal mean potential density σ_0 in N3.4, with a spacing of $0.5\,\mathrm{kg\,m^3}$.

shows that the upgrade removes much of the warm bias in the thermocline region between $50°$ S and $60°$ N, via a mean cooling of up to $1\,°\mathrm{C}$ in the depth range from 50 to $250\,\mathrm{m}$ over these latitudes. Additionally, the drastic reduction in winter MLD biases between v3.2 and v3.4 observed in Fig. 9 can be directly attributed to the convective mixing correction. The crescent shape of the temperature bias with respect to the observations (and of the difference between v3.2 and v3.4) in Fig. 12 reflects the deepening of the thermocline with increasing latitude.

5.3.2 TKE parameters

As a reminder to the reader we note that the main reason for performing this sensitivity test was to investigate the effect of altering the vertical length scale for the TKE source term at $1/4°$ resolution. In the $1°$ resolution experiments of Calvert and Siddorn (2013) reducing this length scale in midlatitudes and increasing it in the tropics significantly alleviated an excessively diffuse midlatitude thermocline, reduced summertime mixed layer depths and significantly reduced near-surface temperature biases at midlatitudes. For consistency with theory, we simultaneously made a small increase

in the wind-wave energy coefficient and the minimum permitted surface mixing length (controlled by the parameter *rn_mxl0*) but these are expected to have a negligible impact.

The changes to the TKE scheme parameters lead to a consistent surface warming of between 0.1 and $0.5\,°\mathrm{C}$ north of $30°$ N and south of $30°$ S (Fig. 13), while there is a small cooling of around $0.05\,°\mathrm{C}$ in the tropics. The pattern of the associated salinity changes is more complex, with freshening of up to 0.2 psu in the Arctic, in the subpolar North Pacific, and to a lesser extent in the tropics and along the path of the ACC; and an increase in salinity in the subtropical zones and, interestingly, in the regions dominated by the Amazon and Congo river plumes. The subtropical surface warming is balanced by a cooling down to 300 m in these latitudes (Fig. 14), consistent with reduced vertical mixing.

We conclude that changing the vertical length scale for the TKE source term has similar beneficial effects at $1/4°$ resolution as at $1°$ resolution and therefore recommend making this change to the existing scheme.

5.3.3 Bathymetry and background diffusivity and viscosity

The rationale for upgrading the bathymetry is that the new bathymetry is based on higher-resolution data (ETOPO1 instead of ETOPO2) and therefore more accurate. Upgrading the bathymetry (not shown) leads to small changes in the temperature and salinity in the Arctic, which overall cools by $0.05\,°\mathrm{C}$ or less and freshen by around 0.05 psu: this is likely to be a consequence of minor modifications to the North Atlantic sill topography. There are southward displacements of the path of the topographically steered ACC, north of the Kerguelen Plateau and north of the Pacific–Antarctic Ridge at 140–$150°$ W, along with a depression of the surface elevation in the Southern Ocean by 3–5 cm (not shown), which may be associated with alterations in the path and strength of the northward-flowing Antarctic Bottom Water.

The current consensus within the NEMO community is that background diffusivity and viscosity should be of the order of $1.2 \times 10^{-5}\,\mathrm{m^2\,s^{-1}}$ and $1.2 \times 10^{-4}\,\mathrm{m^2\,s^{-1}}$ respectively and since these increases do not degrade the model simulation we argue that these are appropriate values to employ. Increasing the background vertical diffusivity and viscosity parameters (*rn_avt0* and *rn_avm0* respectively) by 20 % (not shown) has a small effect on the surface fields, relative to the other parameter changes. There is a general surface freshening in the Arctic by 0.02–0.04 psu, and a hint of warming north of the ACC, but elsewhere any signal is small compared with the mesoscale noise. In the upper ocean the explicit representation of mixing processes by the TKE scheme dominates the background term, while it is also likely that over much of the ocean the numerical mixing in the model's advection scheme is at least as large as that associated with the $1.2 \times 10^{-5}\,\mathrm{m^2\,s^{-1}}$ explicit background diffusivity, as discussed in Griffies et al. (2000) and Lee et al. (2002).
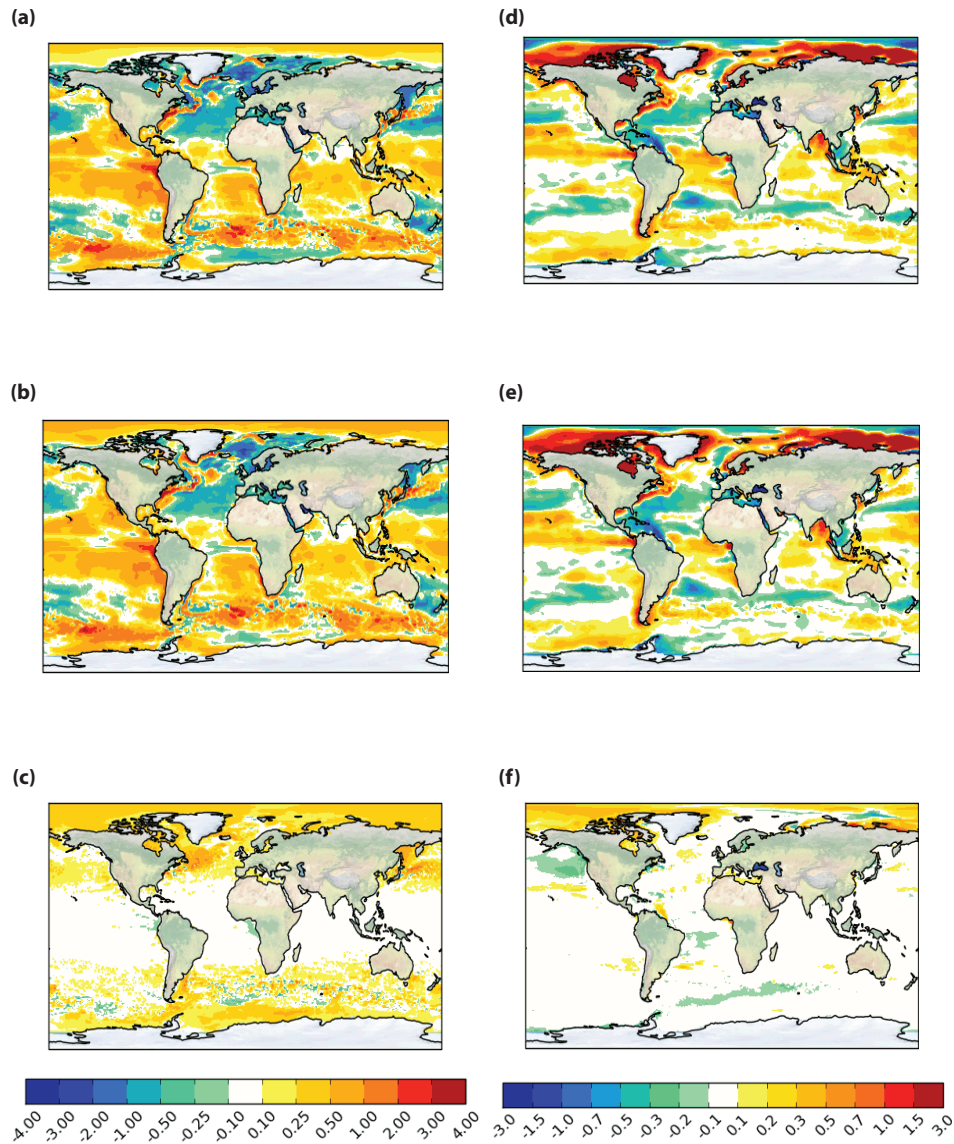
Figure 13. Effect on sea surface fields in years 1981–1985 of TKE scheme changes (from experiment N3.4_vmix to N3.4_tke): **(a)** N3.4_vmix SST bias, **(b)** N3.4_tke SST bias, **(c)** N3.4_tke minus N3.4_vmix SST, **(d)** N3.4_vmix SSS bias, **(e)** N3.4_tke SSS bias, and **(f)** N3.4_tke minus N3.4_vmix SSS.

We conclude that changing the bathymetry and the background vertical mixing parameters does not result in significant global effects on the solution. However we note that the more realistic bathymetry is likely to be important for local circulation, particularly in the Southern Ocean.

5.3.4 Geothermal heating, double diffusion, bottom boundary layer and ice model changes

Geothermal heating and double diffusion are physically present in the real ocean, but on the relatively short timescales discussed in this paper, their effects are expected to be small. Nevertheless, in order to make our model as complete as possible, and bearing in mind potential future ap-

plications, we explicitly perform sensitivity experiments to evaluate their significance. The addition of benthic geothermal heat input (not shown) leads to a surface freshening of 0.1–0.2 psu between 40 and 50° S in the southwestern Atlantic by the end of the 10-year integration, but little large-scale surface effects elsewhere. Adding double diffusion (also not shown) again has relatively little effect on the surface temperature, apart from a small localised cooling along the path of the ACC by 0.05 °C, but does produce a freshening of 0.05 psu over much of the Atlantic and the subtropical Pacific. Neither change was expected to have a large subsurface effect over the timescale discussed here, and this is confirmed by our experiments.
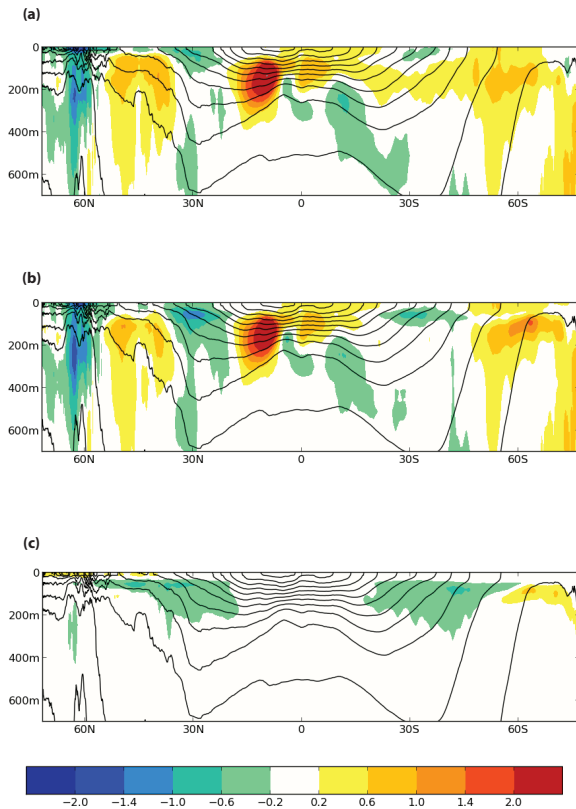
Figure 14. Effect on zonal mean temperature in years 1981–1985 of TKE scheme changes (from experiment N3.4_vmix to N3.4_tke). **(a)** Bias in N3.4_vmix, **(b)** bias in N3.4_tke, and **(c)** difference of N3.4_tke minus N3.4_vmix. The solid contours are of the zonal mean potential density σ_0 in N3.4_tke, with a spacing of $0.5\,\mathrm{kg\,m^3}$.

The rationale for inclusion of the bottom boundary layer scheme was to improve the representation of overflows, which are known to be a weak point of z-coordinate models such as NEMO. The bottom boundary layer scheme leads to a surface cooling of $\sim 0.2\,^\circ\mathrm{C}$ north of the separated Gulf Stream, while larger modifications of up to $1\,^\circ\mathrm{C}$ to the temperature are seen near the sea floor in the region downstream of the Denmark Strait overflow, but the relationship of the surface signal to the deep temperature signal and associated changes to the deep western boundary current are complex and require further analysis beyond the scope of the present paper.

As explained in Sect. 4, the ice model changes consisted of salinity dependence for the freezing point of water, and increases in the ice's thermal conductivity and salinity, in line with the latest observations. The addition of salinity dependence is justified on the grounds that it is more realistic, whilst the changes to the ice's salinity and thermal conductivity are based on the work of Rae et al. (2014) where the ice model parameters were tuned to reach agreement with the observed seasonal cycle of ice extent. The changes to the ice model (not shown) yield a surface cooling (of $\sim 0.2\,^\circ\mathrm{C}$) and

freshening (of ~ 0.1 psu) in the Southern Ocean and a similar cooling in the Arctic. The change in salinity is consistent with increased salt export from the polar regions (both polar regions are associated with net ice export). The increased thermal conductivity is expected to increase ice formation and overall ice cover and hence to reduce the annual mean surface water temperature (since at a given location there will be a longer ice-covered period annually compared to the previous model configuration, GO1).

5.3.5 Attribution study summary

In summary, we find that the largest changes result firstly from the ocean code version upgrade from NEMO v3.2 to v3.4, due to an improvement in handling of diffusion of TKE when convection occurs; and secondly from the changes to the parameters of the TKE scheme; namely, the parameters *rn_ebb*, *rn_mxl0*, and *nn_htau*. These have only a small effect on the surface errors, but in combination the two changes result in much more substantial improvement of the subsurface temperature field and the seasonal cycle, as described in Sect. 5.2.

6 Summary and discussion

We have introduced a new ocean model configuration, GO5.0, developed jointly between the Met Office and NERC. This is an implementation of version 3.4 of the NEMO model, on the ORCA025 grid, with horizontal resolution of at least $1/4^\circ$ everywhere, together with the CICE sea ice model on the same grid. The GO5.0 model configuration is derived from the previous GO1 through an upgrade of the NEMO code version from version 3.2, and a set of parameter changes. A 30-year integration of GO5.0, run with CORE2 surface forcing from 1976 to 2005, has been compared with GO1 with the same forcing. We have additionally described a set of 10-year sensitivity studies carried out to attribute changes in the model performance to individual changes in the model physics.

The GO5.0 configuration was validated against observations during the final 10 years of the 30-year integration. It was found to have a generally warm surface bias, with respect to the EN3 climatological data set, of 0.5–$1\,^\circ\mathrm{C}$ in the tropics, a cool bias of similar magnitude in the extratropics and a warm bias of around $2\,^\circ\mathrm{C}$ in much of the Southern Ocean. The surface salinity biases were again predominantly zonal, being up to 0.2 psu too salty close to the Equator and in subpolar regions and the Arctic, and too fresh in the subtropics. In the Labrador Sea and in the North Atlantic subpolar gyre the surface waters are between 2 and $4\,^\circ\mathrm{C}$ too warm, and around 1 psu too salty.

Both GO1 and GO5.0 model configurations showed good skill in simulating oceanic exchanges between North Atlantic, North Pacific and Arctic oceans. The net oceanic

exports from the Arctic Ocean and the contributions from the individual straits are within the uncertainties of the observational estimates. The main model bias is a more vigorous exchange between the Atlantic and Arctic oceans manifesting itself in too strong (compared to observations) a northward flow of the buoyant warm Atlantic water and too strong a return flow of the dense Arctic water as the overflows across the Greenland–Scotland Ridge. The overturning circulation at 26° N in the Atlantic was correspondingly stronger than that observed, at 21 Sv. The transport in the Antarctic Circumpolar Current was 124 Sv, close to observed estimates, while the Indonesian Throughflow was significantly higher than observations, most likely because of insufficient mixing at the critical straits.

Comparison of the sea ice in the Northern Hemisphere in GO5.0 and observations show that the model simulates the annual means, the interannual trend and the seasonal cycle well, although the model underestimates summer sea ice extent. In the Southern Hemisphere the sea ice extent again compares well with observations, although the recent rising trend in sea ice cover is not simulated in GO5.0, as is also the case in several other comparable models. Both GO1 and GO5.0 underestimate sea ice volume in the Northern Hemisphere with biases larger in summer than in winter. In the Southern Hemisphere the seasonal cycle of sea ice thickness is simulated correctly, with a moderate underestimation (of 15 % for GO5.0) of the hemisphere-averaged sea ice thickness.

The main differences between GO5.0 and GO1 were seen in the penetration of heat and salt into the interior ocean above the thermocline and in the representation of the seasonal cycle. The global mean warming, with a maximum at 200 m depth, was reduced from 0.7 to 0.3 °C, while the steady freshening trend at the same depth was also reduced by 10–20 %. Although the overall reduction in mixed layer depth from GO1 to GO5.0 did not lead to unequivocal improvements in surface biases, wintertime mixed layers were consistently better represented in GO5.0, while the shallow bias in MLD and consequent warm surface bias in GO1 in tropical latitudes were significantly ameliorated in GO5.0.

To attribute the changes seen between GO1 and GO5.0, the physics modifications were applied incrementally starting from the original GO1 configuration. First of all the NEMO source code was upgraded from v3.2 to v3.4; then the model bathymetry was upgraded; the background vertical diffusivity and viscosity were increased; some of the TKE scheme parameters were adjusted; geothermal heat flux and double diffusion of tracers were added; a scheme was added to represent a bottom boundary layer; and, finally, modifications were made to the ice model. It was found that several of the modifications led to changes with large spatial scales in the model surface and subsurface fields that were distinguishable from the eddy variability, but the dominant effects were traced to the code upgrade and to the TKE changes. These two changes, which both affect mainly vertical mixing in the upper few-hundred metres, were found to produce most of the reduction of the subsurface temperature and salinity biases of the model, along with the reduced errors in the seasonal cycle.

We conclude that GO5.0 represents a significant improvement in realism over the previous configuration of the Met Office ocean model, GO1. In particular, the improvements in the representation of vertical mixing (associated both with the code upgrade from the NEMO v3.2 and in the modifications to the TKE vertical mixing scheme in v3.4) lead to a more faithful simulation of the annual cycle in surface temperature and mixed layer depth, as well as to reduced subsurface drifts in the depth range of 200–400 m.

There are clearly aspects of the GO5.0 configuration that need to be improved further. In particular, the subpolar North Atlantic and the Southern Ocean show substantial errors in both surface and subsurface fields that may be at least partly ascribed to deficiencies in model physics. Process evaluation groups (PEGs) have been set up within the JOMP programme specifically to address issues relating to the two aforementioned regions, and work is ongoing in both cases.

In addition, GO5.0 does not contain several physics upgrades which are currently either available or under development in NEMO, and which offer potentially significant improvements in model realism. These include embedded sea ice (in which the base of the sea ice lies beneath the ocean surface and the ice displaces a non-zero volume of sea water); and the z-tilde modification to the vertical coordinate to reduce numerical mixing from high-frequency vertical motions (Leclair and Madec, 2011). The full non-linear free surface physics is available in NEMO v3.4, but not implemented in GO5.0; it is expected that this, along with z tilde and the embedded ice, will be included in future implementations of the global ocean model.

Appendix A: Code availability and model trunk and branches

The model code for NEMO v3.4 is available from the NEMO website (www.nemo-ocean.eu). On registering, individuals can access the FORTRAN code using the open source subversion software (http://subversion.apache.org/). The revision number of the base NEMO code (trunk) used for this paper is 3424. In addition we apply some modifications to the base code (branches). Please contact the authors for more information on these branches and how to obtain them.

The model code for CICE is freely available from the United States Los Alamos National Laboratory (http://oceans11.lanl.gov/trac/CICE/wiki/SourceCode), again using subversion. The revision number for the version used for this paper is 430 (trunk). Once again there are some additional modifications (branches) made for the purposes of this paper, and interested readers are requested to contact the authors for details.

UK users with access to PUMA (cms.ncas.ac.uk/wiki/PumaService) can copy the job details (job ID xhimo) and submit a duplicate job using the Met Office Unified Model user interface (UMUI).

Appendix B: FPP keys used in GO5.0 (NEMO and CICE)

key_dynspg_flt – filtered free surface

key_ldfslp – rotate diffusion operators
(for tracer isopycnal diffusion)

key_traldf_c2d – geographically varying lateral tracer diffusion

key_dynldf_c2d – geographically varying lateral momentum diffusion

key_zdftke – TKE scheme for vertical mixing

key_zdftmx – include tidal mixing scheme

key_zdfddm – include double diffusive mixing parameterisation

key_trabbl – include bottom boundary layer scheme.

Appendix C: Ocean and ice name lists for GO5.0

These are included as the Supplement.

Appendix D: Surface forcing

These are the CORE-2 forcing data set (Large and Yeager, 2009), available at: http://rda.ucar.edu/datasets/ds260.2/.

Appendix E: Other input files

Other files such as bathymetry, river runoff mask and interpolation weights for the surface forcing are required to run GO5.0. These can be obtained on request from the authors.

The Supplement related to this article is available online at doi:10.5194/gmd-7-1069-2014-supplement.

References

Aagaard, K., Weingartner, T., Danielson, S. L., Woodgate, R. A., Johnson, G. C., and Whitledge, T. E.: Some controls on flow and salinity in Bering Strait, Geophys. Res. Lett., 33, L19602, doi:10.1029/2006GL026612, 2006.

Aksenov, Y., Bacon, S., Coward, A., and Holliday, N. P.: Polar Outflow from the Arctic Ocean: a high resolution model study, J. Marine Syst., 83, 14–37, 2010.

Amante, C. and Eakins, B. W.: ETOPO1 1 Arc-Minute Global Relief Model: Procedures, Data Sources and Analysis, NOAA Technical Memorandum NESDIS NGDC-24, 19 pp., 2009.

Arakawa, A.: Computational design of long-term numerical integration of the equations of fluid motion, J. Comput. Phys., 1, 119–143, 1966.

Arribas, A., Glover, M., Maidens, A., Peterson, K., Gordon, M., MacLachlan, C., Graham, R., Fereday, D., Camp, J., Scaife, A., Xavier, P., McLean, P., Colman, A., and Cusack, S.: The GloSea4 ensemble prediction system for seasonal forecasting, Mon. Weather Rev., 139, 1891–1910, doi:10.1175/2010MWR3615.1, 2011.

Århun, M., Nicholls, K. W., and Boehme, L.: Wintertime Water Mass Modification near an Antarctic Ice Front, J. Phys. Oceanogr., 43, 359–365, doi:10.1175/JPO-D-12-0186.1, 2013.

Axell, L. B.: Wind-driven Internal Waves and Langmuir Circulations in a Numerical Ocean Model of the Southern Baltic Sea, J. Geophys. Res., 107, 3204, doi:10.1029/2001JC000922, 2002.

Barnier, B., Madec, G., Penduff, T., Molines, J.-M., Treguier, A.-M., Le Sommer, J., Beckmann, A., Biastoch, A., Böning, C., Dengg, J., Derval, C., Durand, E., Gulev, S., Remy, E., Talandier, C., Theetten, S., Maltrud, M., McClean, J., and De Cuevas, B.: Impact of partial steps and momentum advection schemes in a global ocean circulation model at eddy permitting resolution, Ocean Dynam., 56, 543–567, doi:10.1007/s10236-006-0082-1, 2006.

Beckmann, A. and Doscher, R.: A method for improved representation of dense water spreading over topography in geopotential-coordinate models, J. Phys. Oceanogr., 27, 581–591, 1997.

Bitz, C. M. and Lipscomb, W. H.: An energy-conserving thermodynamic model of sea ice, J. Geophys. Res., 104, 15669–15677, 1999.

Bitz, C. M., Holland, M., Eby, M., and Weaver, A. J.: Simulating the ice-thickness distribution in a coupled climate model, J. Geophys. Res., 106, 2441–2463, 2001.

Blaker, A. T., Hirschi, J. J.-M., McCarthy, G., Sinha, B., Taws, S., Marsh, R., Coward, A. C., and de Cuevas, B. A.: Historical analogues of the recent extreme minima observed in the Atlantic meridional overturning circulation at 26° N, Clim. Dynam., in review, 2014.

Bourdalle-Badie, R. and Treguier, A.-M.: A climatology of runoff for the global ocean-ice model ORCA025, Report, Mercator-Ocean, MOO-RP-425-365-MER, 2006.

Brown, A., Milton, S., Cullen, M., Golding, B., Mitchell, J., and Shelley, A.: Unified modeling and prediction of weather and climate: a 25-year journey, B. Am. Meteorol. Soc., 93, 1865–1877, 2012.

Calvert, D. and Siddorn, J.: Revised vertical mixing parameters for the UK community standard configuration of the global NEMO ocean model, Hadley Centre Technical Note 95, 74 pp., available at: http://www.metoffice.gov.uk/media/pdf/9/0/HCTN_95.pdf, last access: 21 May 2014, 2013.

Cavalieri, D. J., Parkinson, C. L., Gloersen, P., and Zwally, H.: Sea ice concentrations from Nimbus-7 SMMR and DMSP SSM/I-SSMIS passive microwave data, [indicate subset used], NASA DAAC at the National Snow and Ice Data Center, Boulder, Colorado, USA, 1996 (updated yearly).

Clement Kinney, J., Maslowski, W., Aksenov, Y., de Cuevas, B., Nguyen, A., Osinski, R., Steele, M., Woodgate, R. A., and Zhang, J.: On the Flow Through Bering Strait: A Synthesis of Model Results and Observations, in: The Pacific Arctic Region. Ecosystem Status and Trends in a Rapidly Changing Environment, edited by: Grebmeier, J. M. and Maslowski, W., Springer, 2014.

Collins, W. J., Bellouin, N., Doutriaux-Boucher, M., Gedney, N., Hinton, T., Jones, C. D., Liddicoat, S., Martin, G., O'Connor, F., Rae, J., Senior, C., Totterdell, I., Woodward, S., Reichler, T., and Kim, J.: Evaluation of the HadGEM2 model, Met Office Hadley Centre Technical Note no. HCTN 74, available from Met Office, FitzRoy Road, Exeter EX1 3PB, available at: http://www.metoffice.gov.uk/media/pdf/8/7/HCTN_74.pdf, last access: 18 November 2013, 2008.

Craig, P. D. and Banner, M. L.: Modelling Wave-Enhanced Turbulence in the Ocean Surface Layer, J. Phys. Oceanogr., 24, 2546–2559, 1994.

Cunningham, S. A., Alderson, S. G., King, B. A., and Brandon, M. A.: Transport and variability of the Antarctic Circumpolar Current in Drake Passage, J. Geophys. Res., 108, 8084, doi:10.1029/2001JC001147, 2003.

Cuny, J., Rhines, P., and Kwok, R. R.: Davis Strait volume, freshwater and heat fluxes, Deep-Sea Res. Pt. I, 52, 519–542, 2005.

Curry, B., Lee, C. M., and Petrie, B.: Volume, freshwater, and heat fluxes through Davis Strait, 2004–2005, J. Phys. Oceanogr., 41, 429–462, doi:10.1175/2010JPO4536.1, 2011.

Dai, A. and Trenberth, K. E.: Estimates of freshwater discharge from continents: latitudinal and seasonal variations, J. Hydrometeorol., 3, 660–687, 2002.

Danabasoglu, G., Large, G. W., and Briegleb, B.: Climate impacts of parameterized Nordic Sea overflows, J. Geophys. Res., 115, C11005, doi:10.1029/2010JC006243, 2010.

Dawson, A., Matthews, A. J., Stevens, D. P., Roberts, M. J., and Vidale, P.-L.: Importance of oceanic resolution and mean state on the extra-tropical response to El Nino in a matrix of coupled models, Clim. Dynam., 41, 1439–1452, doi:10.1007/s00382-012-1518-6, 2012.

de Boyer Montégut, C., Madec, G., Fischer, A. S., Lazar, A., and Iudicone, D.: Mixed layer depth over the global ocean: an examination of profile data and a profile-based climatology, J. Geophys. Res., 109, C12003, doi:10.1029/2004JC002378, 2004.

Delworth, T., Rosati, A., Anderson, W., Adcroft, A., Balaji, V., Benson, R., Dixon, K., Griffies, S., Lee, H., Pacanowski, R., Vecchi, G. A., Wittenberg, A. T., Zeng, F., and Zhang, R.: Simulated climate and climate change in the GFDL CM2.5 high-resolution coupled climate model, J. Climate, 25, 2755–2781, 2012.

Farneti, R. and Gent, P. R.: The effects of the eddy-induced advection coefficient in a coarse-resolution coupled climate model, Ocean Model., 39, 135–145, doi:10.1016/j.ocemod.2011.02.005, 2011.

Farneti, R., Delworth, T. L., Rosati, A. J., Griffies, S. M., and Zeng, F.: The role of mesoscale eddies in the rectification of the Southern Ocean response to climate change, J. Phys. Oceanogr., 40, 1539–1557, doi:10.1175/2010JPO4353.1, 2010.

Gammelsrod, T., Leikvin, O., Lien, V., Budgell, W. P., Loeng, H., and Maslowski, W.: Mass and heat transports in the NE Barents Sea: observations and models, J. Marine Syst., 75, 56–69, doi:10.1016/j.jmarsys.2008.07.010, 2009.

Gaspar, P., Grégoris, Y., and Lefevre, J.-M.: A simple eddy kinetic energy model for simulations of the oceanic vertical mixing: tests at Station Papa and long-term upper ocean study site, J. Geophys. Res., 95, 16179–16193, doi:10.1029/JC095iC09p16179, 1990.

Gent, P. R. and Danabasoglu, G.: Response to Increasing Southern Hemisphere Winds in CCSM4, J. Climate, 24, 4992–4998, doi:10.1175/JCLI-D-10-05011.1, 2011.

Gent, P. R. and McWilliams, J. C.: Isopycnal mixing in ocean circulation models, J. Phys. Oceanogr., 20, 150–155, 1990.

Gnanadesikan, A., Griffies, S. M., and Samuels, B. L.: Effects in a climate model of slope tapering in neutral physics schemes, Ocean Model., 16, 1–16, 2007.

Gordon, C., Cooper, C., Senior, C. A., Banks, H., Gregory, J. M., Johns, T. C., Mitchell, J. F. B., and Wood, R. A.: The simulation of SST, sea ice extents and ocean heat transports in a version of the Hadley Centre coupled model without flux adjustments, Clim. Dynam., 16, 147–168, 2000.

Gregg, M. C., Sanford, T. B., and Winkel, D. P.: Reduced mixing from the breaking of internal waves in equatorial waters, Nature, 422, 513–515, 2003.

Griffies, S. M., Pacanowski, R. C., and Hallberg, R. W.: Spurious diapycnal mixing associated with advection in a z-coordinate ocean model, Mon. Weather Rev., 128, 538–564, 2000.

Griffies, S. M., Biastoch, A., Böning, C., Bryan, F., Danabasoglu, G., Chassignet, E. P., England, M. H., Gerdes, R., Haak, H., Hallberg, R. W., Hazeleger, W., Jungclaus, J., Large, W. G., Madec, G., Pirani, A., Samuels, B. L., Scheinert, M., Sen

Gupta, A., Severijns, C. A., Simmons, H. L., Treguier, A.-M., Winton, M., Yeager, S., and Yin, J.: Coordinated Ocean-ice Reference Experiments (COREs), J. Ocean Model., 26, doi:10.1016/j.ocemod.2008.08.007, 2009.

Hallberg, R. and Gnanadesikan, A.: The role of eddies in determining the structure and response of the wind-driven Southern Hemisphere overturning: results from the Modeling Eddies in the Southern Ocean (MESO) project, J. Phys. Oceanogr., 36, 2232–2252, 2006.

Hewitt, H. T., Copsey, D., Culverwell, I. D., Harris, C. M., Hill, R. S. R., Keen, A. B., McLaren, A. J., and Hunke, E. C.: Design and implementation of the infrastructure of HadGEM3: the next-generation Met Office climate modelling system, Geosci. Model Dev., 4, 223–253, doi:10.5194/gmd-4-223-2011, 2011.

Hirschi, J. J.-M., Blaker, A. T., Sinha, B., Coward, A., de Cuevas, B., Alderson, S., and Madec, G.: Chaotic variability of the meridional overturning circulation on subannual to interannual timescales, Ocean Sci., 9, 805–823, doi:10.5194/os-9-805-2013, 2013.

Holland, P. R. and Kwok, R.: Wind-driven trends in Antarctic sea-ice drift, Nat. Geosci., 5, 872–875, doi:10.1038/ngeo1627, 2012.

Houghton, J. T., Ding, Y., Griggs, D. J., Noguer, M., van der Linden, P. J., and Xiaosu, D.: Climate Change 2001: The Scientific Basis, Cambridge University Press, 944 pp., 2001.

Hunke, E. C. and Dukowicz, J. K.: An Elastic–Viscous–Plastic Model for sea ice dynamics, J. Phys. Oceanogr., 27, 1849–1867, 1997.

Hunke, E. C. and Lipscomb, W. H.: CICE: The Los Alamos Sea Ice Model, Documentation and Software User's Manual, Version 4.1, Tech. Rep. LA-CC-06-012, Los Alamos National Laboratory, Los Alamos, New Mexico, available at: http://oceans11.lanl.gov/trac/CICE, last access: 18 November 2013, 2010.

Ingleby, B. and Huddleston, M.: Quality control of ocean temperature and salinity profiles – historical and real-time data, J. Marine Syst., 65, 158–175, 2007.

IOC, IHO and BODC: Centenary Edition of the GEBCO Digital Atlas, published on CD-ROM on behalf of the Intergovernmental Oceanographic Commission and the International Hydrographic Organization as part of the General Bathymetric Chart of the Oceans, British Oceanographic Data Centre, Liverpool, UK, 2003.

Johns, T. C., Durman, C. F., Banks, H. T., Roberts, M. J., McLaren, A. J., Ridley, J. K., Senior, C. A., Williams, K. D., Jones, A., Rickard, G. J., Cusack, S., Ingram, W. J., Crucifix, M., Sexton, D. M. H., Joshi, M. M., Dong, B.-W., Spencer, H., Hill, R. S. R., Gregory, J. M., Keen, A. B., Pardaens, A. K., Lowe, J. A., Bodas-Salcedo, A., Stark, S., and Searl, Y.: The New Hadley Centre Climate Model (HadGEM1): evaluation of coupled simulations, J. Climate, 19, 1327–1353, 2006.

Josey, S. A., Gulev, S., and Yu, L.: Exchanges through the ocean surface, in: Ocean Circulation and Climate: A 21st Century Perspective, 2nd Edn., edited by: Siedler, G., Griffies, S., Gould, J., and Church, J., Oxford, GB, Academic Press, International Geophysics Series, 103, 115–140, 2013.

Kennedy, J. J., Rayner, N. A., Smith, R. O., Saunby, M., and Parker, D. E.: Reassessing biases and other uncertainties in sea-surface temperature observations measured in situ since 1850 – Part 2: Biases and homogenisation, J. Geophys. Res., 116, D14104, doi:10.1029/2010JD015220, 2011.

Koch-Larrouy, A., Madec, G., Blanke, B., and Molcard, R.: Water mass transformation along the Indonesian throughflow in an OGCM, Ocean Dynam., 58, 289–309, 2008.

Large, W. G. and Yeager, S. G.: The global climatology of an interannually varying air-sea flux data set, Clim. Dynam., 33, 341–364, doi:10.1007/s00382- 008-0441-3, 2009.

Leclair, M. and Madec, G.: ž-Coordinate, an Arbitrary Lagrangian–Eulerian coordinate separating high and low frequency motions, Ocean Model., 37, 139–152, doi:10.1016/j.ocemod.2011.02.001, 2011.

Lee, M.-M., Coward, A. C., and Nurser, A. J. G.: Spurious diapycnal mixing of the deep waters in an eddy-permitting global ocean model, J. Phys. Oceanogr., 32, 1522–1535, 2002.

Lohmann, G., Gerdes, R., and Chen, D.: Sensitivity of the thermohaline circulation in coupled oceanic GCM-atmospheric EBM experiments, Clim. Dynam., 12, 403–416, 1996.

Madec, G.: NEMO – the OPA9 ocean engine: Note du Pole de Modelisation, Institut Pierre-Simion Laplace, 1:100, available at: http://www.nemo-ocean.eu, last access: 18 November 2013, 2008.

McCarthy, G., Frajka-Williams, E., Johns, W. E., Baringer, M. O., Meinen, C. S., Bryden, H. L., Rayner, D., Duchez, A., Roberts, C., and Cunningham, S. A.: Observed interannual variability of the Atlantic meridional overturning circulation at 26.5° N, Geophys. Res. Lett., 39, L19609, doi:10.1029/2012GL052933, 2012.

Megann, A. P., New, A. L., Blaker, A. T., and Sinha, B.: The sensitivity of a coupled climate model to its ocean component, J. Climate, 23, 5126–5150, 2010.

Meijers, A. J. S., Shuckburgh, E., Bruneau, N., Sallee, J.-B., Bracegirdle, T. J., and Wang, Z.: Representation of the Antarctic Circumpolar Current in the CMIP5 climate models and future changes under warming scenarios, J. Geophys. Res., 117, C12008, doi:10.1029/2012JC008412, 2012.

Merryfield, W. J., Holloway, G., and Gargett, A. E.: A global ocean model with double-diffusive mixing, J. Phys. Ocean., 29, 1124–1142, 1999.

Munday, D. R., Johnson, H. L., and Marshall, D. P.: Eddy Saturation of Equilibrated Circumpolar Currents, J. Phys. Ocean., 43, 507–532, doi:10.1175/JPO-D-12-095.1, 2013.

Olsen, S. M., Hansen, B., Quadfasel, D., and Østerhus, S.: Observed and modelled stability of overflow across the Greenland–Scotland ridge, Nature, 455, 519–522, 2008.

Østerhus, S., Turrrell, W. R., Jónsson, S., and Hansen, B.: Measured volume, heat, and salt fluxes from the Atlantic to the Arctic Mediterranean, Geophys. Res. Lett., 32, L07603, doi:10.1029/2004GL022188, 2005.

Penduff, T., Le Sommer, J., Barnier, B., Treguier, A.-M., Molines, J.-M., and Madec, G.: Influence of numerical schemes on current-topography interactions in 1/4° global ocean simulations, Ocean Sci., 3, 509–524, doi:10.5194/os-3-509-2007, 2007.

Penduff, T., Juza, M., Brodeau, L., Smith, G. C., Barnier, B., Molines, J.-M., Treguier, A.-M., and Madec, G.: Impact of global ocean model resolution on sea-level variability with emphasis on interannual time scales, Ocean Sci., 6, 269–284, doi:10.5194/os-6-269-2010, 2010.

Rae, J. G. L., Hewitt, H. T., Keen, A. B., Ridley, J. K., Harris, C. M., Hunke, E. C., and Walters, D. N.: Development of Global Sea Ice 5.0 CICE configuration, Geosci. Model Dev., in preparation, 2014.

Rahmstorf, S. and Willebrand, J.: The role of temperature feedback in stabilizing the thermohaline circulation, J. Phys. Oceanogr., 25, 787–805, doi:10.1175/1520-0485(1995)025<0787:TROTFI>2.0.CO;2, 1995.

Rayner, N. A., Parker, D. E., Horton, E. B., Folland, C. K., Alexander, L. V., Rowell, D. P., Kent, E. C., and Kaplan, A.: Global analyses of sea surface temperature, sea ice, and night marine air temperature since the late nineteenth century, J. Geophys. Res., 108, 4407, doi:10.1029/2002JD002670, 2003.

Remy, E., Siefridt, L., Fleury, L., and Bremond, M.: Construction de la bathymetrie pour la configuration modele ORCA025, CERFACS Report, May 2003.

Reynolds, R. W., Rayner, N. A., Smith, T. M., Stokes, D. C., and Wang, W.: An improved in situ and satellite SST analysis for climate, J. Climate, 15, 1609–1625, 2002.

Roberts, C. D., Waters, J., Peterson, K. A., Palmer, M. D., McCarthy, G. D., Frajka-Williams, E., Haines, K., Lea, D. J., Martin, M. J., Storkey, D., Blockley, E. W., and Zuo, H.: Atmosphere drives recent interannual variability of the Atlantic meridional overturning circulation at 26.5° N, Geophys. Res. Lett., 40, 5164–5170, doi:10.1002/grl.50930, 2013.

Roberts, M. J., Clayton, A., Demory, M.-E., Donners, J., Vidale, P.-L., Norton, W., Shaffrey, L., Stevens, D. P., Stevens, I., Wood, R. A., and Slingo, J.: Impact of resolution on the tropical pacific circulation in a matrix of coupled models, J. Climate, 22, 2541–2556, 2009.

Robson, J., Hodson, D., Hawkins, E., and Sutton, R.: Atlantic overturning in decline?, Nat. Geosci., 7, 2–3, 2014.

Saunders, P. P., Cunningham, S. A., de Cuevas, B. A., and Coward, A. C.: Comments on "Decadal Changes in the North Atlantic and Pacific Meridional Overturning Circulation and Heat Flux", J. Phys. Ocean., 38, 2104–2107, 2008.

Scaife, A. A., Copsey, D., Gordon, C., Harris, C., Hinton, T., Keeley, S., O'Neill, A., Roberts, M., and Williams, K.: Improved Atlantic winter blocking in a climate model, Geophys. Res. Lett., 38, L23703, doi:10.1029/2011GL049573, 2011.

Semtner, A. J.: A model for the thermodynamic growth of sea ice in numerical investigations of climate, J. Phys. Oceanogr., 6, 379–389, 1976.

Shaffrey, L. C., Stevens, I., Norton, W. A., Roberts, M. J., Vidale, P. L., Harle, J. D., Jarrar, A., Stevens, D. P., Woodage, M. J., Demory, M. E., Donners, J., Clark, D. B., Clayton, A., Cole, J. W., Wilson, S. S., Connolley, W. M., Davies, T. M., Iwi, A. M., Johns, T. C., King, J. C., New, A. L., Slingo, J. M., Slingo, A., Steenman-Clark, L., and Martin, G. M.: U.K. HiGEM: The new U.K. high-resolution global environment model – model description and basic evaluation, J. Climate, 22, 1861–1896, 2009.

Simmons, H., Jayne, S., Laurent, L. S., and Weaver, A.: Tidally driven mixing in a numerical model of the ocean general circulation, Ocean Model., 6, 245–263, 2004.

Sinha, B., Topliss, B., Blaker, A. T., and Hirschi J. J.-M.: A numerical model study of the effects of interannual timescale wave propagation on the predictability of the Atlantic meridional overturning circulation, J. Geophys. Res., 118, 131–146, doi:10.1029/2012JC008334, 2013.

Sirevaag, A., McPhee, M. G., Morison, J. H., Shaw, W. J., and Stanton, T. P.: Wintertime mixed layer measurements at Maud Rise, Weddell Sea, J. Geophys. Res., 115, C02009, doi:10.1029/2008JC005141, 2010.

Skagseth, Ø., Furevik, T., Ingvaldsen, R., Loeng, H., Mork, K. A., Orvik, K. A., and Ozhigin, V.: Volume and heat transports to the Arctic Ocean via the Norwegian and Barents Seas, in: Arctic–Subarctic Ocean Fluxes: Defining the Role of the Northern Seas in Climate, edited by: Dickson, R. R., Meincke, J., and Rhines, P., Springer, the Netherlands, 45–64, 2008.

Smeed, D. A., McCarthy, G. D., Cunningham, S. A., Frajka-Williams, E., Rayner, D., Johns, W. E., Meinen, C. S., Baringer, M. O., Moat, B. I., Duchez, A., and Bryden, H. L.: Observed decline of the Atlantic meridional overturning circulation 2004–2012, Ocean Sci., 10, 29–38, doi:10.5194/os-10-29-2014, 2014.

Smith, D. M., Cusack, S., Colman, A. W., Folland, C. K., Harris, G. R., and Murphy, J. M.: Improved surface temperature prediction for the coming decade from a global climate model, Science, 317, 796–799, doi:10.1126/science.1139540, 2007.

Solomon, S., Qin, D., Manning, M., Chen, Z., Marquis, M., Averyt, K. B., Tignor, M., and Miller, H. L.: Climate Change 2007: The Physical Science Basis, Cambridge University Press, 996 pp., 2007.

Sprintall, J., Wijffels, S. E., Molcard, R., and Jaya, I.: Direct estimates of the Indonesian Throughflow entering the Indian Ocean: 2004–2006, J. Geophys. Res., 114, C07001, doi:10.1029/2008JC005257, 2009.

Stein, C. A. and Stein, S.: A model for the global variation in oceanic depth and heat flow with lithospheric age, Nature, 359, 123–129, 1992.

Storkey, D., Blockley, E. W., Furner, R., Guiavarc'h, C., Lea, D., Martin, M. J., Barciela, R. M., Hines, A., Hyder, P., and Siddorn, J. R.: Forecasting the ocean state using NEMO: the new FOAM system, Journal of Operational Oceanography, 3, 3–15, 2010.

Tansley, C. E. and Marshall, D. P.: On the dynamics of wind-driven circumpolar currents, J. Phys. Oceanogr., 31, 3258–3273, 2001.

Thomas, M. D. and Zhai, X.: Eddy-induced variability of the meridional overturning circulation in a model of the North Atlantic, Geophys. Res. Lett., 40, 1–6, doi:10.1002/grl.50532, 2013.

Viebahn, J. and Eden, C.: Towards the impact of eddies on the response of the southern ocean to climate change, Ocean Model., 34, 150–165, 2010.

Williamson, D., Goldstein, M., Allison, L., Blaker, A., Challenor, P., and Jackson, L.: History matching for the quantification and reduction of parametric uncertainty in climate model projections, Clim. Dynam., 41, 1703–1729, doi:10.1007/s00382-013-1896-4, 2013.

Woodgate, R. A., Weingartner, T. J., and Lindsay, R.: Observed increases in Bering Strait oceanic fluxes from the Pacific to the Arctic from 2001 to 2011 and their impacts on the Arctic Ocean water column, Geophys. Res. Lett., 39, L24603, doi:10.1029/2012GL054092, 2012.

Worby, A. P., Geiger, C. A., Paget, M. J., van Woert, M. L., Ackley, S. F., and DeLiberty, T. L.: Thickness distribution of Antarctic sea ice, J. Geophys. Res., 113, C05S92, doi:10.1029/2007JC004254, 2008.

Yeager, S. G. and Jochum, M.: The connection between Labrador Sea buoyancy loss, deep western boundary current strength, and Gulf Stream path in an ocean circulation model, Ocean Model., 30, 207–224, 2009.

Zalesak, S. T.: Fully multidimensional flux corrected transport algorithms for fluids, J. Comput. Phys., 31, 335–362, 1979.

Zhang, J., Thomas, D. R., Rothrock, D. A., Lindsay, R. W., Yu, Y., and Kwok, R.: Assimilation of ice motion observations and comparisons with submarine ice thickness data, J. Geophys. Res., 108, 3170, doi:10.1029/2001JC001041, 2003.